

Self-organisation of anisometric particles : statistical theory of shape, confinement and external-field effects

Citation for published version (APA):

Otten, R. H. J. (2011). *Self-organisation of anisometric particles : statistical theory of shape, confinement and external-field effects*. [Phd Thesis 1 (Research TU/e / Graduation TU/e), Applied Physics and Science Education]. Technische Universiteit Eindhoven. <https://doi.org/10.6100/IR716778>

DOI:

[10.6100/IR716778](https://doi.org/10.6100/IR716778)

Document status and date:

Published: 01/01/2011

Document Version:

Publisher's PDF, also known as Version of Record (includes final page, issue and volume numbers)

Please check the document version of this publication:

- A submitted manuscript is the version of the article upon submission and before peer-review. There can be important differences between the submitted version and the official published version of record. People interested in the research are advised to contact the author for the final version of the publication, or visit the DOI to the publisher's website.
- The final author version and the galley proof are versions of the publication after peer review.
- The final published version features the final layout of the paper including the volume, issue and page numbers.

[Link to publication](#)

General rights

Copyright and moral rights for the publications made accessible in the public portal are retained by the authors and/or other copyright owners and it is a condition of accessing publications that users recognise and abide by the legal requirements associated with these rights.

- Users may download and print one copy of any publication from the public portal for the purpose of private study or research.
- You may not further distribute the material or use it for any profit-making activity or commercial gain
- You may freely distribute the URL identifying the publication in the public portal.

If the publication is distributed under the terms of Article 25fa of the Dutch Copyright Act, indicated by the "Taverne" license above, please follow below link for the End User Agreement:

www.tue.nl/taverne

Take down policy

If you believe that this document breaches copyright please contact us at:

openaccess@tue.nl

providing details and we will investigate your claim.

**Self-organisation of anisometric particles:
statistical theory of shape, confinement and
external-field effects**

Ronald H.J. Otten

**Self-organisation of anisometric particles:
statistical theory of shape, confinement and
external-field effects**

PROEFSCHRIFT

ter verkrijging van de graad van doctor aan de
Technische Universiteit Eindhoven, op gezag van de
rector magnificus, prof.dr.ir. C.J. van Duijn, voor
een commissie aangewezen door het College voor
Promoties in het openbaar te verdedigen op
maandag 24 oktober 2011 om 16.00 uur

door

Ronald Henricus Johannes Otten

geboren te Veldhoven

Dit proefschrift is goedgekeurd door de promotoren:

prof.dr.ir. P.P.A.M. van der Schoot

en

prof.dr. M.A.J. Michels

Druk: Universiteitsdrukkerij Technische Universiteit Eindhoven

Omslagontwerp: Joris Otten

A catalogue record is available from the Eindhoven University of Technology Library.

ISBN: 978-90-386-2760-1

This research forms part of the research program of the Dutch Polymer Institute (DPI),
Technology Area Performance Polymers, DPI project #648.

Contents

Contents	5
1 Self-organisation of anisometric particles	9
1.1 Soft condensed matter	10
1.2 Percolation	15
1.3 Connectedness percolation	20
1.4 Nematic liquid crystals	24
1.5 Competing surface and bulk forces	28
1.6 Thesis outline	31
2 Connectedness percolation of polydisperse nanofillers: theory	33
2.1 Introduction	34
2.2 Cluster-size calculation	37
2.3 Application to carbon nanotubes	39
2.4 Tetradisperse distribution	43
2.5 Mixtures of conductive and insulating particles	46
2.6 Discussion and conclusions	50
2.A Second-virial approximation	55
3 Connectedness percolation of polydisperse nanofillers: applications	59
3.1 Introduction	60
3.2 Realistic carbon-nanotube distributions	61
3.3 Graphene size distributions	65
3.4 Discussion and conclusions	68
3.A Symmetric length distributions	71

4	Conductivity of temporal networks of rod-like particles	73
4.1	Introduction	74
4.2	Model	76
4.3	Backbone fraction	79
4.4	Comparison with experiments	81
4.5	Conclusions and discussion	83
5	Connectedness percolation of hard rods in an external field	87
5.1	Introduction	88
5.2	Model ingredients	89
5.3	Results	94
5.4	Conclusions	98
6	Capillary rise of an isotropic-nematic fluid interface	101
6.1	Introduction	102
6.2	Weak surface anchoring	105
6.3	Strong surface anchoring	112
6.4	Discussion and conclusions	116
6.A	Strong surface anchoring	119
7	Deformable homeotropic tactoids in a magnetic field: strong anchoring	125
7.1	Introduction	126
7.2	Model ingredients	128
7.3	Tactoid model	130
7.4	Optimal shape	132
7.5	Comparison with experiments	134
7.6	Discussion and conclusions	136
8	Spherical homeotropic tactoids in a magnetic field	139
8.1	Introduction	140
8.2	Free energy	141
8.3	Intermediates	147
8.4	Comparison to experiments	151
8.5	Conclusions and discussion	154
8.A	Hedgehog point defect	156
8.B	Split-core defect	157
8.C	Oblate drop with boundary hedgehog	160

9 Deformable homeotropic tactoids in a magnetic field	163
9.1 Introduction	164
9.2 Tactoid configurations	165
9.3 Stability diagrams	170
9.4 Comparison with experiments	174
9.5 Conclusions and discussion	178
9.A Wulff construction	180
9.B Cut-sphere lens	183
9.C Split-core defect	185
10 Conclusions and outlook	187
10.1 Aim of the thesis	187
10.2 Build-up of networks of colloidal particles in fluid media	187
10.3 Nematics of colloids under soft confinement	189
10.4 Outlook	191
References	193
Summary	201
Samenvatting	203
List of publications	207
Acknowledgements / Dankwoord	209
Curriculum vitae	211

Self-organisation of anisometric particles

1

A general introduction is given to the rich behaviour of the self-organisation of non-spherical particles in soft condensed matter that provides the motivation for this work. We start with discussing some typical characteristics of soft condensed matter and we describe the phase behaviour of dispersions of spherical colloidal particles. Next, we discuss non-spherical, hard particles with a sufficiently large aspect ratio that may have strong, anisotropic interactions, which leads to even richer behaviour, including liquid-crystalline phases at sufficiently large densities or low enough temperatures. We discuss the different phases of rod-like and plate-like colloidal particles and the effect of size polydispersity and flexibility. In the isotropic phase these particles can form temporal, self-assembled networks that span a macroscopic system at very low loadings. This network formation can be described by connectedness-percolation theory and we outline the concepts of that theory after giving a brief introduction to lattice percolation. Then we focus on the liquid-crystalline nematic phase in which the particles exhibit long-range orientational order but no long-range positional order. We discuss how a competition between surface and bulk forces determines the shape and structure of nematics under soft confinement. Finally, the scope of this thesis is discussed.

1.1 Soft condensed matter

Materials that consist of molecules or small particles of more or less spherical shape exhibit at, say, room temperature only a gas, liquid, and a solid phase, but may form plasmas at high temperatures or exhibit quantum behaviour at low temperatures [1, 2]. The gas phase is characterised by a low particle density and short-range positional order. The liquid phase also has short-range positional order but a density that away from the critical point is roughly a thousand times larger than that of a gas. Ideal gases and liquids flow once a shear stress has been applied. The strain rate is proportional to the shear stress, and the constant of proportionality is called the viscosity. In a solid the particles have long-range positional order because they are confined to a lattice, whereas the mean density is usually close to that of the liquid. Sometimes particles do not form a crystal but are arrested in a glassy state. A solid responds elastically to an applied shear stress with a shear strain. In an ideal solid the shear strain is proportional to shear stress and the constant of proportionality is the shear modulus [3].

There exist also many materials that have both liquid-like and solid-like properties, and the class of these materials is generally referred to as soft (condensed) matter. It includes gels, foams, glues, paints, polymers, granular materials, colloids, and liquid crystals. They are chemically complex and usually contain more than a single component. The materials that can be classified as soft matter have in common that the particles have a size in the mesoscopic range from a few nanometres to a few micrometres, where atomistic details are less important and gravity also plays a subdominant role. Their interactions take place on the energy scale of the thermal energy $k_B T$, which is the energy scale associated with the random Brownian motion of particles, and where k_B is Boltzmann's constant and T the absolute temperature. Associated with this Brownian motion is the Boltzmann statistics that collections of particles obey: spontaneous thermal fluctuations have a probability to overcome an energy barrier ΔF that decays exponentially with $\Delta F/k_B T$.

Another common feature observed in all types of soft matter is their propensity to self-organise into complex structures [3]. The theoretical framework that can be used to describe the self-organisation of this type of material is that of statistical mechanics provided the system is ergodic, i.e., the time average of a system property equals its statistical ensemble average. In statistical mechanics the microscopic interactions of many-particle systems with a huge number of degrees of freedom are described statistically to predict their macroscopic behaviour. Throughout this thesis we make use of the framework of statistical mechanics and we focus on colloidal dispersions in which particles in the mentioned mesoscopic size range are dispersed in a fluid host material. These

colloidal particles move around randomly in the dispersion due to Brownian motion but once they come into contact, they tend to stick together because of strong, short-range van der Waals forces. So, if one aims to stabilise the dispersion against aggregation, a repelling force between the particles is required, which can be the result of electrostatic forces via charge stabilisation, or attaching polymer chains to the surfaces, which is called steric stabilisation [3]. We consider both types of dispersion in chapters 7, 8, and 9 and find that the type of stabilisation can make quite a difference in the particle behaviour.

Hence, in theory the dispersion is stable if the attractive and repulsive forces between the particles are in balance such that thermal fluctuations cannot drive the system to another state, but in practice most dispersions are only kinetically stable, not thermodynamically. If the particles are spherical and there is little variation in their size, they form colloidal crystals in a perfectly organised lattice structure with long-range order if one increases the concentration. However, this only occurs provided the colloids have enough time to adopt the lattice positions. Indeed, if the increase in concentration is very rapid, the particles are not given this time and they form a colloidal glass in a kinetically arrested state. If there is a large variation in particles size, colloidal hard spheres form no crystal either and enter a glassy state [4].

If the particles are rigid and non-spherical, also called anisometric, the analysis of these interactions is much more intricate than in the case of spherical particles, because the relative angles between the particles have a large impact on them. On a positive note, however, the anisometric shape and associated interactions lead to many interesting physical phenomena that in the macroscopic world have led and will undoubtedly lead to many applications in modern technology that are discussed below. These phenomena are particularly observed if the aspect ratio of the particles is large, say, more than a hundred, meaning that they are either very slender or very flat.

Indeed, this anisotropy introduces additional degrees of freedom, e.g., if the non-spherical particles are sufficiently stiff. At low particle concentrations the excluded-volume interactions do allow for an isotropic distribution of orientations. If the aspect ratio is large enough, then the particles can form temporal, connected networks that span macroscopic scales at very low particle loadings. It is important to emphasise that both *transient* and *permanent* networks may form, the latter, e.g., in systems that become in some sense kinetically arrested because the particles stick permanently to each other. In this thesis we shall focus on thermalised, temporal networks that form in thermodynamically stable dispersions. Note that the particles, if electrically conducting and dispersed in a non-conducting medium, need not make actual physical contact to allow for electrical contact via hopping or tunneling of charge carriers from one particle

to another. It turns out that a minimal loading much less than close packing is required for the dispersions to become electrically conducting. This minimal loading is called the percolation threshold.

Above this threshold the particles form a network that spans the whole system. If the fluid carrier phase can be solidified sufficiently quickly, the network gets frozen in the final solid composite, the material properties of which can be significantly improved by the network, despite the low loading of the nanofillers. Colloidal fluid stages in the production are often encountered in the processing of solid functional materials. Hence, this is a field where soft and hard matter connect, and for these cases material properties of the solid composites potentially allow for a theoretical description from the point of view of soft condensed matter.

Besides network formation at very low particle loadings, which parenthetically can be probed by, e.g., dielectric spectroscopy [5], the particle anisotropy also causes ordered, so-called liquid-crystalline phases to become possible different from the usual states of matter. If the interactions between the particles are mainly repulsive, e.g., due to excluded volume, this turns out to occur at somewhat higher particle densities than required for a temporal percolating network to form. These liquid-crystalline phases are often referred to as mesophases because they are found under conditions in between those of liquids and crystalline solids. As is true in general for all soft matter, liquid crystals combine properties characteristic of liquids and solids: they flow like ordinary liquids but at the same time are also able to withstand and respond elastically to certain static deformations, giving them solid-like properties [6].

Liquid crystals are formed in a large range of materials, such as low-molecular-weight fluids, surfactant systems, polymers, colloidal dispersions and so on. There are two classes of liquid crystal, referred to as lyotropic and thermotropic [7]. Lyotropic liquid crystals consist of particles in the colloidal size range dispersed in a fluid. In these systems the control variable is the density, so particle alignment creates the free volume that the system runs out of upon a density increase. Thermotropic liquid crystals are usually single-component systems, and include both low and high molecular-weight compounds or polymers. In this type of system anisotropic attractive interactions induce particle alignment between the particles, and the temperature of the system is the control variable.

The different phases of anisometric particles can be distinguished by the degrees of freedom the particles have. The state of a rigid body can be represented by three positional and two rotational degrees of freedom, provided it is not chiral, meaning that it can be superimposed on its own mirror image. Any combination of the positional and angular degrees of freedom can in principle be frozen in. If the particles are chiral, this

gives rise to even richer behaviour. For rod-like particles the simplest liquid-crystalline phase is the nematic phase in which the particles are aligned along a common axis, but there is no long-range positional order, and we return to this phase in detail in section 1.4. See also Fig. 1.1. If one positional and one orientational degree of freedom are frozen in, the rods are aligned in a single direction like in a nematic, but on top of that, they are positionally ordered in layers. The phase is called smectic-A if the layer is perpendicular to the axis of orientational symmetry, and smectic-C if the layer is tilted with a different angle. If the particle orientation is perpendicular to the smectic plane with liquid-like behaviour in the layers, but the particles have short-range positional and a quasi-long-range orientational order, this is called a hexatic smectic-B phase [6].

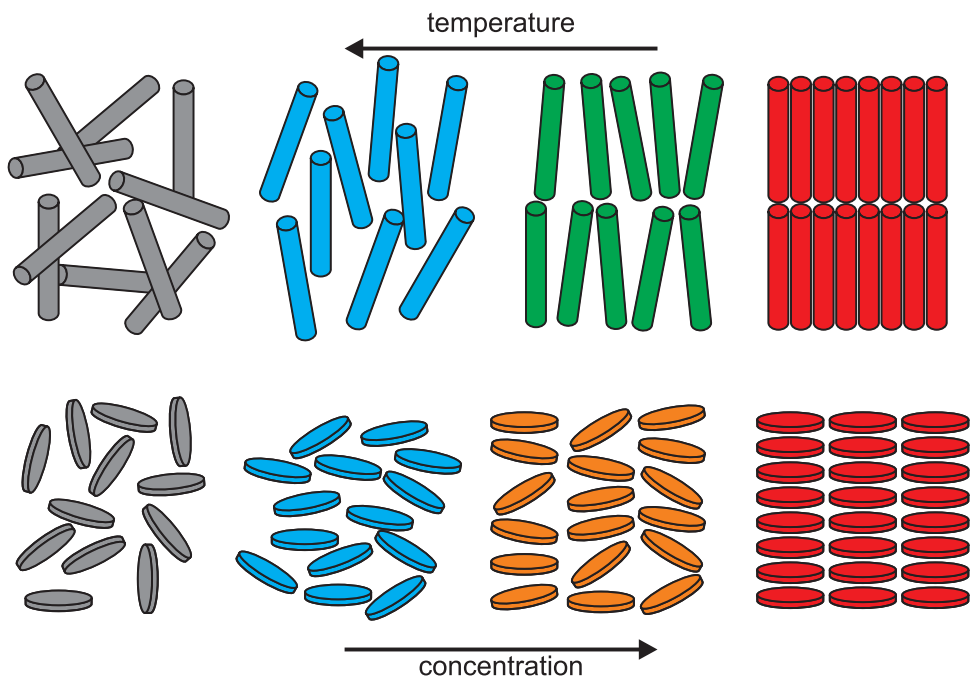


Figure 1.1: With increasing concentration (in entropy-dominated systems) or decreasing temperatures (in energy-dominated systems) rod-like particles become more ordered and normally exhibit an isotropic, a nematic, a smectic, and a crystal phase (top row), whereas plate-like particles usually have an isotropic, a nematic, a smectic, and a crystal phase (bottom row).

For plate-like particles without cylindrical symmetry there is, besides a nematic phase, also a bi-axial nematic, in which two orientational degrees of freedom are frozen in. Moreover, in a columnar phase there is only one unrestrained orientational degree of freedom, like in the nematic and smectic phases, but the particles are arranged in

columns in which there is still liquid-like freedom; the columns can form two-dimensional crystals, e.g., packed hexagonally or in rectangles [7]. See also Fig. 1.1. In a rotator phase, also referred to as a plastic crystal, all positional degrees of freedom are frozen in, so the particles are located on a lattice, but there are still two orientational degrees of freedom. Finally, if all positional and orientational freedom is restricted for both rod-like and plate-like particles they are packed in a crystalline solid. For rod-like particles computer simulations indicate that there are two main types of crystalline packing: in AAA stacking a rod is positioned exactly above a rod in the layer below it, as shown in the top-right corner of Fig. 1.1, whereas in ABC stacking there is a shift in the layers [8].

The above phases emerge if the particles are all of the same size and are perfectly rigid. If there is a significant size polydispersity in the dispersion of rod-like particles, this suppresses the formation of the smectic phase and favours the columnar phase [9], as does a finite flexibility of the rods [10]. In dispersions of plate-like particles a diameter polydispersity causes no such suppression of the columnar phase, but at high concentrations smectic-like ordering is observed, which in turn is suppressed by a polydispersity in the thickness [11, 12].

In this thesis we consider the large-scale self-organisation of elongated and flat colloidal particles, and our aim is to gain a better insight into this self-organisation to predict macroscopic behaviour that results from their anisotropic interactions. More specifically, the purpose is to show how the network formation is affected by the material properties of the nanofillers, such as a size polydispersity and their conductance, particle alignment, and how it competes with the transition to a nematic phase. This nematic phase in turn exhibits interesting phenomena under soft confinement, e.g., in case of the capillary rise of an isotropic-nematic interface up a vertical wall and the formation of nematic droplets.

To study percolation phenomena we invoke a microscopic theory that describes particle interactions at the molecular level, because this allows us to directly incorporate the effect of angular correlations between the particles. These turn out to be very important. For the nematics we could also have used a microscopic Onsager-type theory that is suited for lyotropic nematics of rod-like particles, albeit that it is not as accurate for plate-like particles [13]. However, it turns out to be convenient to use a mesoscopic or even macroscopic Frank-Oseen elasticity theory because it suffices to use the cylindrical symmetry of the nematogens [14]. The reason is that the particle shape is coupled to the (ratios of) values of the elastic constants, surface tension, and anchoring strength, so we need not consider the microscopic details. The common ground of the theories we use for the percolation phenomena and nematic liquid crystals is that the anisotropic,

hard-core interactions dictate the structure of networks and are at the root of the formation of liquid-crystalline phases and the elastic and surface properties of these phases. Both network properties and the properties of liquid crystals under conditions of soft confinement depend crucially on particle shape.

In the remainder of this chapter, we first present a brief introduction to percolation theory in section 1.2 and the elements of connectedness-percolation theory that we use in section 1.3. Next, we give a brief introduction into liquid-crystal theory with in particular the nematic phase in section 1.4, and we discuss the competition between surface and bulk forces characteristic of the nematic in section 1.5. Finally, the scope of the thesis is outlined in section 1.6.

1.2 Percolation

Broadbent and Hammersley coined the term percolation to describe the fluid flow through a porous material consisting of fixed channels (bonds) of which a fraction is randomly chosen to be blocked [15]. They showed that there is no fluid flow if the fraction p of open channels is smaller than some critical fraction p_p . Hence, at a critical fraction of connected channels, they form a network that allows fluid to traverse the whole system, and this critical point is referred to as the percolation threshold [16]. See also Fig. 1.2. For $p > p_p$ the flow increases monotonically, to reach a maximum at $p = 1$. Alternatively, the flow process can be described in terms of valves that may block the flow at the junctions of the pipes. These two types of a flow in terms of open channels and valves on a fixed lattice are referred to bond and site percolation, respectively.

In continuum percolation there is no lattice and the sites are distributed continuously in space. If these sites are molecules or small particles that are dispersed in a host solvent, a certain connectedness criterion has to be defined to determine for what configuration two particles can be considered connected. Analogous to lattice percolation, there is a critical, minimum loading of particles at which they form a connected network that spans the entire system. This allows rod-like and plate-like particles to significantly enhance the properties of the host material after solidification, as already referred to in section 1.1. In practice, carbon nanotubes, graphene sheets, silver nanowires, self-assembled anorganic nanotubes, and fibers of nanowire-forming materials based on transition metal-chalcogenides can be used for this to improve the properties of a host material [17–21]. Experiments on these composites are usually performed on the final solid composites, although percolation of carbon nanotubes in the fluid phase has been studied with dielectric spectroscopy [5], including the role of shear on the insulator-conductor transition [22]. These studies also show the sensitive dependence of the final

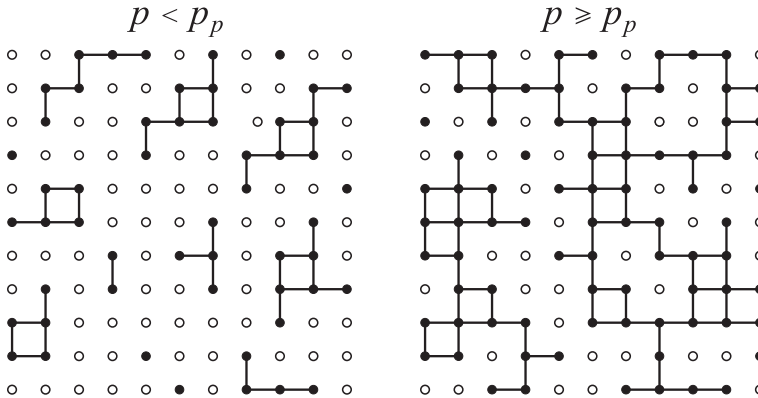


Figure 1.2: The simplest lattice in two dimensions is a square lattice. In bond percolation the bonds are occupied (solid lines) with a probability p . In nearest-neighbour site percolation sites are occupied (filled circles) with a probability p and two neighbouring sites are defined to be connected if both of them are occupied. In both cases there is no network of connected bonds/sites that spans the whole system if the fraction p is smaller than a critical fraction p_p (left), whereas there is one for $p \geq p_p$ (right). For an infinite system $p_p = 1/2$ for bond percolation, whereas $p_p = 0.5927$ for nearest-neighbour site networks [25].

properties on the processing conditions that we discuss in more detail in chapters 2, 3, 4, and 5 [23,24].

We compare our results to experiments on composites containing carbon nanotubes and graphene sheets, in which a so-called Latex technology is applied in the manufacturing steps [26,27]. See Fig. 1.3. The nanofillers are distributed in water and a surfactant is added, after which the dispersion is sonicated to separate stacks and bundles of particles. The next step is to separate the remaining bundles and stacks from the single-walled nanotubes and single-layer graphene sheets by centrifugation. The bundles are removed and the spherical latex particles are added and the next step is to remove the water by freeze drying. This means that only a powder remains, after which the substance is compressed and heated in a compression-moulding step, making the latex particle fuse together to obtain a continuous latex-based matrix as the continuous phase. It may seem that there is no (real) thermodynamics left in the composite because of the powder that remains after freeze drying and the fact that we study a solid final composite. However, the system is allowed to equilibrate when the latex particles are added and during the compression moulding, so the processing in fact contains two equilibration steps.

As a consequence, the formation of the percolating network may allow for a theoretical description in the framework of connectedness-percolation theory if we presume

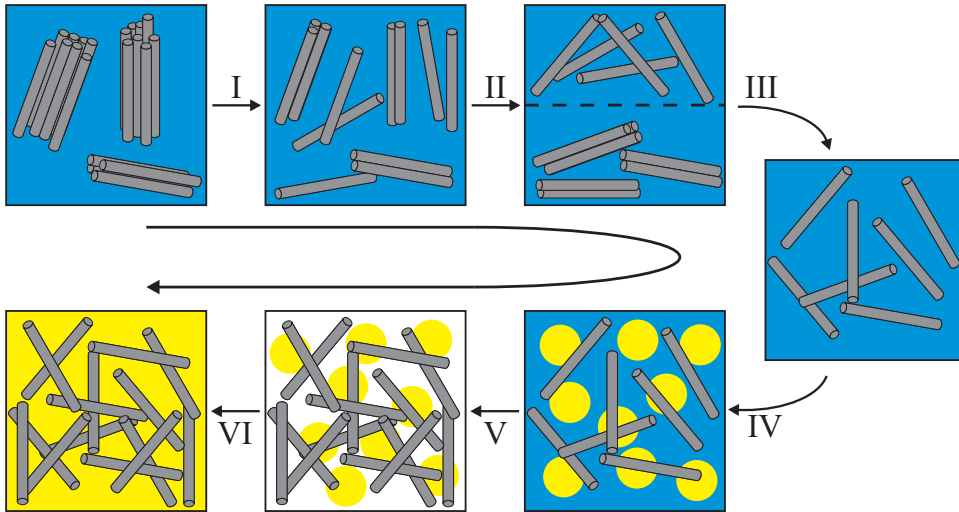


Figure 1.3: The steps in the Latex technology that are used to obtain composite with a random distribution in position and orientation of the carbon nanotubes and graphene sheets. It consists of sonication (I), centrifugation (II), removal of the remaining stacks and bundles (III), adding latex particles (IV), freeze drying (V), and finally compression moulding (VI).

that an equilibrium configuration has solidified in the final composite. As alluded to in section 1.1, in this theory a connectedness criterion has to be defined for what configuration of particles they can be considered to be connected because we consider temporal networks of particles that need not make physical contact. This connectedness criterion is different for different types of percolation and associated properties of interest, such as electrical and mechanical percolation. In this work we focus on the electrical properties so we can compare our results to experiments on the conductivity of composites that have been produced with the Latex technology to enhance the properties of polymeric materials. Theoretical results indicate that the scaling of the percolation threshold for rod-like particles is the same for rigidity percolation and geometric percolation [28].

As already alluded to, it turns out that the carbon nanofillers in the experiments that use the Latex technology do not touch each other in this final product [26], so charge transport occurs by charge tunneling or hopping from one nanofiller to the other, see Figure 1.4. Note that if the criterion was that two particles actually need to touch to be connected, this would statistically happen with vanishing probability, making the percolation threshold diverge. Given that charge-carrier hopping is a quantum-mechanical process that has a probability that decays exponentially with the ratio of the distance between the particles and a typical decay length, or hopping distance, we

would have to incorporate these probabilities in the connectedness criterion. However, if we define a sharp cutoff in the maximum separation allowed for charge transport with a penetrable shell as the connectedness zone around each particle, it turns out that for rod-like particles this so-called cherry-pit model or core-shell model gives the same result as a model with the incorporation of an exponentially decaying hopping probability. Defining such a typical hopping distance as a maximum distance between two connected particles then provides the link between geometrical and electrical percolation that we are interested in in the end.

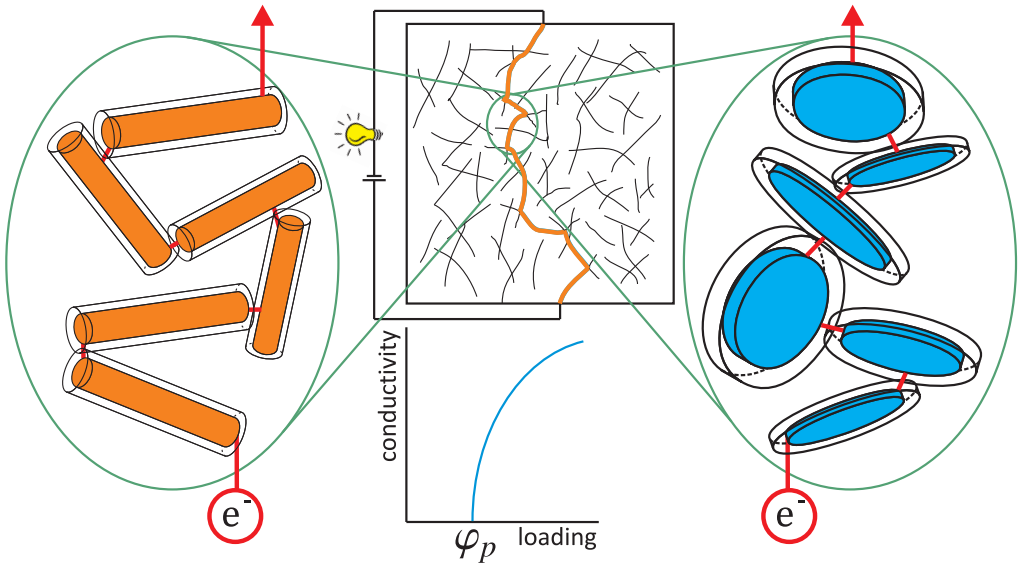


Figure 1.4: Schematic of the percolation process and the cherry-pit model. For a low particle loading the nanofillers are on average too far away from each other to form large clusters. At a critical loading φ_p , referred to as the percolation threshold, the clusters form a network that spans the whole system (the thick path). At this point electrical conductivity of the host material increases with many orders of magnitude. Charge transport from one rod-like or plate-like particle to the other takes place via electron hopping if two nanofillers are sufficiently close to each other, meaning that the transparent cylinders overlap.

As argued above, the hopping probability decays exponentially with the distance between two particles, suggesting that any two particles are always connected and that a well-defined percolation threshold cannot be identified, but this is not the case. In order to understand this we have to take a closer look at the connection between electrical and geometrical percolation. For penetrable spherical particles of a fixed radius in continuum space there is a critical number of contacts (overlaps) between the spheres, and, as a result, a critical volume fraction occupied by the spheres at which the connected spheres

form a percolating network [29]. This geometrical percolation can be translated into electrical percolation if one considers randomly distributed conducting point sites (we extend this to conducting particles below) because it can be shown that even with an exponentially decaying overlap probability, there is still a critical sphere radius R_c and an associated number of contacts (neighbours) that is required for a percolating network in the limit of $R_c \gg L$, with L the localisation length of the host material [30,31]. Computer simulations have shown that this is also true for the special case of variable-range hopping [32]. In the limit of $R_c \approx L$ the sites are much closer to each other and the critical sphere now has an effective radius equal to the localisation length L , which is a material constant. This means that there is a smooth crossover to geometrical percolation of penetrable spheres of radius L . In case of particles of a finite size instead of conducting point sites we have to consider surface-to-surface tunneling instead of centre-to-centre tunneling. Clearly, this changes the geometry of the problem, but the concept remains the same. It is for this reason that we use a model with a constant hopping distance throughout this thesis in a model for the geometrical percolation threshold to predict the electrical percolation threshold of composites containing rod-like and plate-like particles.

The percolation threshold is often expressed in terms of the volume fraction φ_p that the filler particles occupy. Many percolation properties exhibit power-law scaling behaviour close to this critical loading. For instance, for volume fractions φ with $|\varphi - \varphi_p| \ll 1$, we have

$$\begin{aligned} F &\sim |\varphi - \varphi_p|^\beta \\ S &\sim |\varphi - \varphi_p|^{-\gamma} \\ \xi &\sim |\varphi - \varphi_p|^{-\nu} \\ \Sigma &\sim |\varphi - \varphi_p|^t, \end{aligned}$$

where F , S , ξ , and Σ are the percolation probability, the weight-average cluster size, the correlation length, and the conductivity respectively [25]. The quantity F denotes the probability that an arbitrarily chosen particle is part of the percolating cluster. Note that F is only defined for $\varphi < \varphi_p$, whereas ξ and S (if the infinite cluster is excluded) and Σ are defined on both sides of the percolation threshold [25]. The weight-average cluster size S is the average size of a cluster of connected particles that an arbitrarily selected particle is part of. This we discuss in more detail below. The correlation length ξ measures the range of particle correlations and is also a measure of the cluster dimensions as we show in chapter 5, or of the cluster heterogeneity for $\varphi > \varphi_p$ [25].

For both lattice and continuum percolation it has been shown that theoretically the critical exponents β , γ , and ν are universal, meaning that their value only depends on the dimensionality of the system. However, experimentally this is certainly not the

case [33]. The critical exponents β, γ , and ν are coupled by the so-called hyperscaling relation $d\nu = 2\beta + \gamma$, with d the dimensionality of the system, whereas t can be considered as an “independent” exponent [16]. Such a scaling relation is believed to hold for $d \leq d_c$, where d_c is a critical dimension above which the exponents are believed to adopt their dimension-independent mean-field values. For mean-field theories $\beta = \gamma = 1$, and $\nu = 1/2$, so the hyperscaling relation gives $d_c = 6$, so in six or more dimensions mean-field theory is exact [25]. The mean-field exponent of the conductivity is $t = 3$ [25], and we return to this in chapter 4. We find in this work that mean-field connectedness theory is exact for rod-like particles in three dimensions, albeit that this only holds in the limit of infinite aspect ratio. The concepts of this connectedness-percolation theory we discuss in the next section.

1.3 Connectedness percolation

In order to calculate the average cluster size of connected particles, and from that the percolation threshold, we presume that the configuration of dispersed nanofillers that is frozen in, is an equilibrium configuration. This allows us to apply equilibrium connectedness-percolation theory in chapters 2, 3, and 5. Here, we outline the principles of this theory. The weight-averaged cluster size S can be expressed in terms of the number of clusters n_k consisting of k particles, also called a k -mer. Then the probability that an arbitrarily chosen particle is part of a k -mer is $s_k = kn_k/N$, with $N = \sum_k kn_k$ the total number of particles. This gives for $S = \sum_k ks_k = \sum_k k^2n_k / \sum_k kn_k$ [25]. Given the distribution of the cluster sizes n_k we find that the total number of contacts between two particles within the same cluster, defined as the number of pairs of particle that have a direct or an indirect connection within the same cluster, is given by $N_c = \sum_k \binom{k}{2} n_k = \frac{1}{2} \sum_k k(k-1)n_k$. Hence, we deduce that $S = \sum_k (kn_k + k(k-1)n_k)/N = 1 + 2N_c/N$, which is an exact result. The first term, unity, stems from choosing a particle, and the second, $2N_c/N$, from counting the particles it is in contact with in the same cluster.

The number of contacts, N_c , and the weight-average cluster size, S , can also be described in terms of the so-called pair-connectedness function P . For simplicity we consider spherical particles of equal size; the generalisation to anisometric particles is discussed below. P is defined such that $\rho^2 P(\mathbf{r}, \mathbf{r}') d\mathbf{r} d\mathbf{r}'$ is the probability of simultaneously finding a particle in a volume element $d\mathbf{r}$ at position \mathbf{r} and a second particle in $d\mathbf{r}'$ at \mathbf{r}' , given that they are part of the same cluster. Here, ρ is the number density of the particles that we presume to be uniformly distributed. So P decomposes the radial distribution function g into a “connected” and a “disconnected” part: $g(r) = P(r) + D(r)$,

where $\rho^2 D(\mathbf{r}, \mathbf{r}') d\mathbf{r} d\mathbf{r}'$ is the probability of simultaneously finding two particles at \mathbf{r} and \mathbf{r}' that are *not* in the same cluster [34].

The definition of P implies that $N_c = \frac{1}{2}\rho^2 \iint d\mathbf{r} d\mathbf{r}' P(\mathbf{r}, \mathbf{r}')$ must be the total number of pairs of particle that are in contact (either directly or indirectly) in a cluster, where the factor 1/2 corrects for double counting. If we use the property of the translational invariance of P we can write $N_c = \frac{1}{2}\rho N \int d\mathbf{r} P(\mathbf{r}, \mathbf{r}')$, which hence gives for the cluster size,

$$S = 1 + \rho \int d\mathbf{r} P(\mathbf{r}, \mathbf{r}') = 1 + \rho \lim_{q \rightarrow 0} \hat{P}(\mathbf{q}), \quad (1.1)$$

where the hat $(\hat{\cdot}) \equiv \int d\mathbf{r}(\dots) \exp(i\mathbf{q} \cdot \mathbf{r})$ denotes a spatial Fourier transform with \mathbf{q} the wave vector.

The description can straightforwardly be generalised to anisometric particles for which P also depends on their orientations. The weight-average cluster size S then reads

$$S = 1 + \lim_{q \rightarrow 0} \rho \left\langle \left\langle \hat{P}(\mathbf{q}, \mathbf{u}, \mathbf{u}') \right\rangle_{\mathbf{u}} \right\rangle_{\mathbf{u}'}, \quad (1.2)$$

with $\mathbf{u} \equiv (\mathbf{u}_1, \mathbf{u}_2)$ with \mathbf{u}_1 and \mathbf{u}_2 the unit vectors in the direction of the main axes of a particle. For the sake of notational convenience we introduced the notation $\langle \dots \rangle_{\mathbf{u}_n} \equiv \int d\mathbf{u} \psi(\mathbf{u})(\dots)$ to denote the orientational average, with a similar prescription for the primed variables, and where $\psi(\mathbf{u})$ denotes an orientational probability distribution function. In chapters 2 and 3 we consider a uniform distribution of orientations with $\psi = 1/4\pi$, but in chapter 5 we focus on the effect of particle alignment, i.e., a non-uniform distribution on the network formation.

The probability P can be obtained from the orientation-dependent connectedness Ornstein-Zernike equation [34], the Fourier transform of which reads

$$\hat{P}(\mathbf{q}, \mathbf{u}, \mathbf{u}') = \hat{C}^+(\mathbf{q}, \mathbf{u}, \mathbf{u}') + \rho \left\langle \hat{C}^+(\mathbf{q}, \mathbf{u}, \mathbf{u}'') \hat{P}(\mathbf{q}, \mathbf{u}'', \mathbf{u}') \right\rangle_{\mathbf{u}''}. \quad (1.3)$$

Here, C^+ denotes the direct pair-connectedness function that in essence measures short-range correlations, discussed more extensively below. An intuitive interpretation of Eq. (1.3) may be given as follows, where we are ignoring the angular dependence for convenience and write it as $P(\mathbf{r}, \mathbf{r}') = C^+(\mathbf{r}, \mathbf{r}') + \int d\mathbf{r}'' P(\mathbf{r}'', \mathbf{r}') C^+(\mathbf{r}, \mathbf{r}'')$. The functions $P(\mathbf{r}, \mathbf{r}')$ and $C^+(\mathbf{r}, \mathbf{r}')$ describe different kinds of cluster[†] in which two particles at \mathbf{r} and \mathbf{r}' are connected, and the Ornstein-Zernike equation states that all clusters in the fluid described by the probability $P(\mathbf{r}, \mathbf{r}')$, can be subdivided into the sum of clusters with probability $C^+(\mathbf{r}, \mathbf{r}')$ that do not have any bottleneck particles that upon removal

[†]In fact, P and C^+ can be expressed in terms of a sum of graphs and describe average probabilities of having the particles connected in such a graph, which is not an actual cluster.

split a cluster into two disconnected ones, and those clusters that do contain such particles [34]. Clusters from this latter type can then be divided into those that connect the first particle at \mathbf{r} to the closest bottleneck particle at \mathbf{r}'' and another that connects \mathbf{r}'' to the second particle at \mathbf{r}' , giving $C^+(\mathbf{r}, \mathbf{r}'')P(\mathbf{r}'', \mathbf{r}')$. Averaging over all possible positions of \mathbf{r}'' then gives the second term in the Ornstein-Zernike equation.

However, the direct-connectedness function is not known a priori. The closure that we make throughout this thesis is the so-called second-virial approximation. It implies that we consider only linear pair correlations between the particles, i.e., no loop correlations, and it is also referred to as a random-phase approximation [35], or the bare-chain sum approximation [36]. As we show in chapter 2, this absence of loop correlations has a significant consequence for non-additive mixtures. This approximation also allows us to invoke the analogy with percolation on a Bethe lattice. For rod-like particles with a large aspect ratio in excess of 100, such as carbon nanotubes, the approximation is an accurate closure as we show in chapter 2. In the limit of rods with an infinite aspect ratio, the theory becomes even exact. We also show that it may not be very accurate for plate-like particles, but recent calculations show that the topologies of phase diagrams for binary mixtures of hard platelets of different sizes are the same for a second-virial theory and fundamental measure theory [37], which is known to be very accurate. Hence, the second-virial approximation may still provide reasonably accurate results for percolation of plate-like particles.

The second-virial approximation implies that $\hat{C}^+ = \hat{f}^+$ [34,38], with $f^+ = \exp(-\beta u^+)$ the connectedness Mayer function of particles that belong to the same cluster and interact via the connectedness potential u^+ . Here, $\beta^{-1} = k_B T$, with k_B Boltzmann's constant and T the absolute temperature. This definition of f^+ is an extension of the regular Mayer function $f = \exp(-\beta u) - 1$, with u the interaction potential, because of the added constraint in u^+ that particles belong to the same cluster. The potential u for hard, impenetrable particles is infinitely large for all configurations in which two particles intersect and zero otherwise. The two-body connectedness potential u^+ by definition is infinitely large not only for any configuration where two particles overlap, but also if they are not connected. In this thesis we make use of the so-called cherry-pit or core-shell model in which the particles have a penetrable shell of thickness λ around their hard core [39], where λ then denotes a typical hopping distance, but in case of rod-like particles this turns out to be equivalent to an connectedness probability that decays exponentially with decay length λ . See also Figure 1.4. In this cherry-pit model we can define the contact volume, which equals the volume $\langle\langle \hat{f}^+ \rangle_{\mathbf{u}}\rangle_{\mathbf{u}'}$ that the centre of mass of a particle can occupy such that it is in contact with a second particle. For both rod-like and plate-like particles the contact volume to leading order scales with

the sine of the relative angle between the particles, implying that for long rods and large plates the contact volume is much larger for a configuration where the particles are perpendicular to each other than for one where they are parallel.

A direct estimate of the percolation threshold can be obtained by presuming that there is on average one particle per contact volume, giving a critical density of $\rho_p = 1/\langle\langle\hat{f}^+\rangle\rangle$, where we omit the arguments of \hat{f}^+ for the sake of readability. In Eqs. (1.2) and (1.3) this amounts to neglecting angular correlations, meaning that the convolution term in Eq. (1.3) is presumed to be separable and that it can be written as $\langle\hat{f}^+(\mathbf{q}, \mathbf{u}, \mathbf{u}'')\rangle_{\mathbf{u}''}\langle\hat{P}(\mathbf{q}, \mathbf{u}'', \mathbf{u}')\rangle_{\mathbf{u}'}$ if we substitute \hat{f}^+ for \hat{C}^+ . It follows that $\langle\langle\hat{P}\rangle\rangle = \langle\langle\hat{f}^+\rangle\rangle/(1 - \rho\langle\langle\hat{f}^+\rangle\rangle)$. As a result, in this approximation the density where $\langle\langle\hat{P}\rangle\rangle$ diverges, and consequently, S diverges, equals $\rho_p = 1/\langle\langle\hat{f}^+\rangle\rangle$, in agreement with the above result. If we apply this to rod-like particles, we find to leading order $\rho_p = \pi\lambda L^2/2$, so $\varphi_p = D^2/2\lambda L$, with L and D the rod length and diameter. This means that the percolation threshold diverges for a vanishing hopping distance and decreases with increasing aspect ratio L/D of the rods. For plate-like nanofillers of diameter D and thickness L , we have $\rho_p^{-1} = \pi\lambda D^2(5\pi + 6)/8$, so $\varphi_p = 2L/(\lambda(5\pi + 6))$. Again, the percolation threshold scales inversely with the hopping distance, but more importantly, it is independent of the plate diameter D . In chapter 2 we find the same scaling by taking into account the angular correlations, but this is only true in the monodisperse limit. More generally, we show in chapters 2, 3, and 5 that the above results have the correct scaling behaviour, but the contact-volume approach significantly underestimates the effect of a polydispersity in the linear dimensions and of particle alignment, meaning that for anisometric particles the angular correlations between particles are very important indeed.

The reason that we consider this size and connectivity polydispersity is that in practice the composites exhibit these non-ideal characteristics. Indeed, carbon nanotubes and graphene sheets are inherently very polydisperse and the connectivity ranges plausibly depend sensitively on the material properties, e.g., the dielectric constant and the quality of the nanofillers. Therefore, we extend Eqs. (1.2) and (1.3) in chapters 2 to particles with polydispersity in size and connectivity range and find a very sensitive dependence of the percolation threshold. This explains, at least partly, the huge scatter of many orders of magnitude of measured percolation thresholds for carbon-nanotube composites that have been observed experimentally for systems with the same average dimensions. If the length and diameter distributions are independent, we find that a few larger sheets added to a collection of smaller ones can drastically lower the percolation threshold, and the same is true for adding a few longer rods to a set of short ones, whereas adding thicker ones raises the threshold. On the other hand, if the length and diameter distributions are coupled, the situation is completely different and polydispersity raises

the percolation threshold. This coupling may seem plausible if, e.g., a sonication step or ball-milling step, in which the nanofillers are put in a type of grinder that is rotated to separate stacked or bundled particles, is used in the processing because the probability of a thick (multi-walled) carbon nanotube breaking into two shorter particles seems smaller than that for a thin (single-walled) nanotube. This is discussed in chapter 3.

The processing may also lead to a composite with the nanofillers sharing a certain orientation, which is the reason that we study it in chapter 5 by switching on an external alignment field. We find such an orientation to considerably raise the percolation threshold and an infinite network to even be absent in a sufficiently strong field. Interestingly, for a given field strength the percolating network even breaks up at higher particle loadings. At these higher loadings it is more favourable for the particles to align and, as a consequence, the temporal network breaks up because of interaction-induced alignment of the particles. We find the percolation threshold to interfere with a transition to a nematic liquid-crystalline phase, which we discuss in detail in section 1.4.

1.4 Nematic liquid crystals

As mentioned in section 1.1, at sufficiently large nematogen concentrations (lyotropic nematic) or low enough temperature (thermotropic) the particles start to align in a certain preferred direction in the nematic phase, where the particles have liquid-like, short-range positional order and long-range orientational order. As a result, it is a fluid with a broken symmetry because the properties of the material depend on the direction one is viewing. Because of this the material is also optically anisotropic or birefringent, allowing it to be probed by, e.g., polarisation microscopy. This technique makes use of the fact that the refractive index of the nematic is different along the main optical axis from the orientation perpendicular to it. Hence, if a nematic liquid crystal is observed between crossed polarisers, and the particle orientation is not parallel to either polariser, light is transmitted. This property is at the basis of the application of these materials in liquid-crystal displays (LCDs).

The average orientation of the particles is indicated by a normalised vector field \mathbf{n} that is called the director field. The fact that it is normalised means that it obeys $\mathbf{n} \cdot \mathbf{n} = 1$. The director field of a nematic is a local axis of symmetry, around which the field has cylindrical symmetry. It also has up-down or inversion symmetry because it only indicates an orientation and not a direction, so it must be symmetric with respect to the transition $\mathbf{n} \rightarrow -\mathbf{n}$. As introduced in section 1.2, the orientational distribution of anisometric particles is given by a function $\psi(\mathbf{u})$ that describes the probability that the main-axis vector points in a certain direction \mathbf{u} , relative to an axis that here we

take to be the nematic director \mathbf{n} . Given that ψ represents a distribution function, it is normalised such that $\int d\mathbf{u} \psi(\mathbf{u}) = 1$. The cylindrical and inversion symmetry causes ψ to be separable in a product of $\psi_\vartheta(\vartheta)$ and $\psi_\varphi(\varphi)$ of distribution functions of the polar angle ϑ and azimuthal angle φ , respectively.

The cylindrical symmetry causes $\psi_\varphi = 1/2\pi$ to be uniform, so $\psi = \psi(\vartheta)$ only depends on the polar angle. The degree of order in a nematic liquid crystal is usually expressed in terms of an order parameter S_2 that is defined via [6]

$$S_2 = \int_0^\pi d\vartheta \sin \vartheta \psi(\vartheta) P_2(\cos \vartheta) \quad (1.4)$$

where $P_2(x) = (3x^2 - 1)/2$ is the second Legendre polynomial. Eq. (1.4) is used in chapter 5 to determine the degree of alignment of rod-like particles. For perfectly aligned particles $S_2 = 1$, for an isotropic angular distributions $S_2 = 0$, and $S_2 = -1/2$ if all the nematogens point their main axis perpendicular to the director. In the nematic phase $S_2 > 0$ and a typical value of S_2 for the isotropic-nematic transition is between 0.3 and 0.4 in thermotropic systems and between 0.4 and 0.8 in lyotropic systems, showing that it is a first-order phase transition.

The broken symmetry characteristic of a nematic causes the surface properties to be quite complex. Indeed, there are three types of surface tension, where one is the bare, i.e., isotropic surface tension and the other two are called anchoring energies. The latter energies arise from the preference of the director field to align at a certain angle with an interface of a liquid, solid or gas phase. These comprise a polar anchoring energy and an azimuthal anchoring energy along some preferred direction that is usually caused by surface inhomogeneities, and is only present if the surface is solid and has a symmetry axis. Usually, this term is much smaller than the other two energies, so we presume it to be negligible. The polar anchoring of the nematic to a surface can be the result of the particle shape and/or of specific interactions between the surface and nematogens. The interfacial energy then consists of a bare surface energy and the anchoring energy $F_{st} + F_{sa}$ that we take of the Rapini-Papoular type [40],

$$F_{st} + F_{sa} = \int_A dA (\gamma + \zeta \sin^2 \alpha), \quad (1.5)$$

where the integration is taken over the entire surface area A of the drop and α is the angle between the surface normal $\mathbf{q} = \mathbf{q}(\mathbf{r})$ and the director field $\mathbf{n} = \mathbf{n}(\mathbf{r})$ at the interface. See also Figure 1.5. This Rapini-Papoular form of the interfacial energy has been shown to be a very accurate representation for rod-like particles [41], and we presume it to be reasonable for disk-like ones as well.

Generally, we distinguish between planar anchoring, where the director field is parallel to the surface, and homeotropic, in which case the director field is perpendicular to the

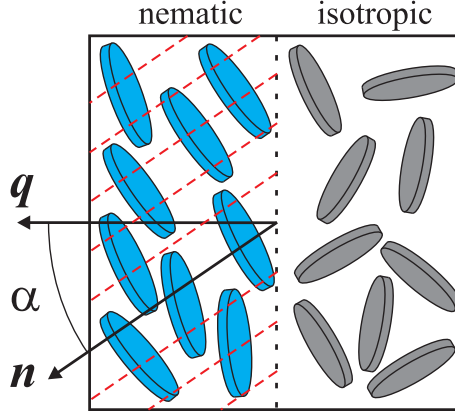


Figure 1.5: Interactions between nematogens and the molecules of another phase (in this case isotropic) they are in contact with favour a particular alignment of the director field (dashed lines) relative to the interface, which is measured by the angle α between the director field \mathbf{n} and the surface normal \mathbf{q} . Phenomenologically, this is usually expressed in a surface tension σ of the Rapini-Papoular type [40], as given by Eq. (1.5) in the main text.

surface. In lyotropic systems plate-like particles for entropic reasons prefer homeotropic anchoring [42], implying $\zeta > 0$ in Eq. (1.5), whereas rod-like particles prefer planar anchoring, giving $\zeta < 0$. Typical values of the surface tension can directly be estimated from a dimensional analysis. The dimension of the surface tension is J/m^2 , so we have to divide a typical energy scale by the square of a relevant length scale. The relevant energy scale is the thermal energy $k_B T$, with k_B Boltzmann's constant and T the absolute temperature, and the relevant length scale depends on the type of nematogen. For rod-like particles these are the length L and the diameter D , giving $\gamma \approx k_B T / LD \approx 10^{-9} - 10^{-7} \text{ J/m}^2$ as a characteristic value for lyotropic nematics [43,44]. For plate-like particles the diameter D is the determining scale, from which we obtain $\gamma \approx k_B T / D^2 \approx 10^{-9} - 10^{-5} \text{ J/m}^2$ as a typical value for homeotropic anchoring [45]. These ultra-low values of the surface tension make surfaces easily deformable and the consequences of this we encounter in chapters 6, 7, 8, and 9.

This surface anchoring of the director field couples the interfacial energy to the bulk elastic energy, for which we can apply the Frank-Oseen elasticity theory [14]. It describes the free-energy cost of deforming a director field away from the ground-state uniform spatial distribution, i.e., a homogeneous director field. The elastic energy F_e comprises three contributions that arise from a splay, twist and bend distortion and have associated elastic constants K_1 , K_2 , and K_3 . See also Fig. 1.6. These constants are linear elastic constants and only apply to small deformations. The elastic deformation energy can

then be written as [6]

$$F_e = \frac{1}{2} \int_V dV (K_1(\nabla \cdot \mathbf{n})^2 + K_2(\mathbf{n} \cdot (\nabla \times \mathbf{n}))^2 + K_3(\mathbf{n} \times (\nabla \times \mathbf{n}))^2), \quad (1.6)$$

where we omitted the splay-bend term $K_{13} \int dV \nabla \cdot (\mathbf{n} \nabla \cdot \mathbf{n})/2$ and the saddle-splay term $K_{24} \int dV \nabla \cdot (\mathbf{n} \nabla \cdot \mathbf{n} + \mathbf{n} \times (\nabla \times \mathbf{n}))/2$. These are often presumed to be subdominant because they can be converted to a surface integral via Gauss's divergence theorem. However, the K_{13} term has been claimed to be problematic because it would not be bounded from below [46]. It is rather contentious because K_{13} has also been asserted to be zero [47] or even negative [48,49]. An additional approximation that is often employed and that we use in chapter 6, is the equal-constant approximation where $K_1 = K_3 = K$ is presumed, with K the average elastic constant. This we use in chapter 6 to model the capillary rise of an isotropic-nematic interface up a solid vertical wall.

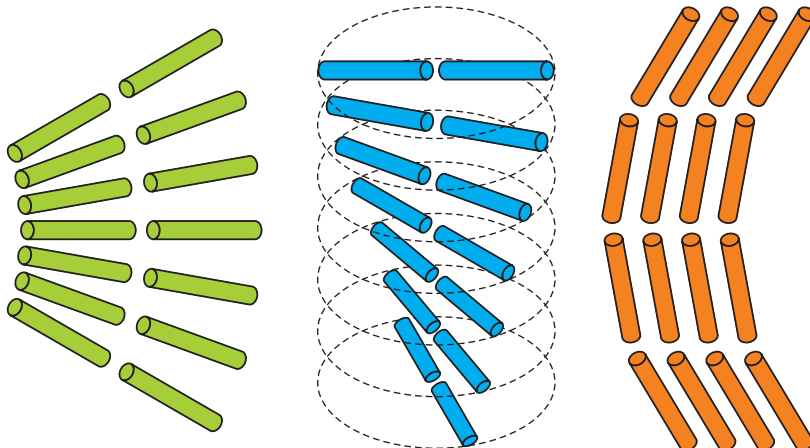


Figure 1.6: The three main types of elastic-energy contributions are associated with director-field deformations of the splay type with elastic constant K_1 (left), the twist type with constant K_2 (middle), and the bend type with constant K_3 (left).

Typical values of the elastic constants can again be estimated from a dimensional analysis. The constants K_i have dimension N, or J/m, and the only relevant energy is again the thermal energy $k_B T$, whereas the relevant length scale depends on the type of particle. For lyotropic hard rods it turns out that $K_i \approx k_B T/D$, with D the rod diameter, giving $K_i \approx 10^{-13} - 10^{-11}$ N [50,51]. For lyotropic hard platelets $K_i \approx k_B T/D$, with D the plate diameter [52], and this provides $K_i \approx 10^{-14} - 10^{-11}$ N.

Both the surface tension, anchoring energy and the elastic constants define an energy cost associated with a deviation from the zero-energy state of a zero surface area, perfect

particle alignment to the interface, and a uniform director field, respectively. This gives rise to a competition between the anisotropic surface tension and bulk elasticity of nematics that governs interfacial phenomena involving liquid-crystalline fluids such as nematic liquid crystals. This competition can be probed, e.g., in a flat-cell geometry in a setup where an external magnetic (or electric) field is applied and the response of the director field measured, providing access to information on the elastic constants and the surface anchoring energies [6]. We discuss it in more detail in the next section.

1.5 Competing surface and bulk forces

The competition between the anisotropic surface tension and bulk elasticity manifests itself in, e.g., nematic droplets, referred to as tactoids, that are often observed in dispersions of sufficiently anisometric colloidal particles under conditions where the isotropic and nematic phase co-exist. Recently, it has been suggested that quantitative information can be obtained on the material parameters of the nematic by studying the shape and director-field structure these tactoids [53–57]. Especially in lyotropic nematics that consist of dispersions of rod-like and plate-like colloidal particles in a fluid host medium this should be the case because of their ultra-low interfacial tensions that we discussed above. Presently, much more information is available (both experimentally and theoretically) on dispersions of rod-like particles [43, 44, 50, 51, 57–77] than on those of plate-like ones [11, 45, 78–83], presumably because plate-like colloids are much more difficult to stabilise [11, 78, 79]. However, recently interesting experiments on tactoids consisting of plate-like gibbsite particles have been carried out in the presence and absence of a magnetic field [84–86] and in chapters 7, 8, and 9 we study the tactoids shapes and director fields theoretically and compare our results with the experiments. Continuum theories [53, 54, 61, 62, 87] have been fitted to experimental results [56, 63–65] on nematic droplets in fluid dispersions of *rod-like* particles, giving anchoring strengths that are at least an order of magnitude larger than theoretical predictions [88, 89], whereas these have proved to be reliable in determining other properties, such as the surface tension and elastic constants [51, 57–60, 66–69]. One could argue that this discrepancy is the result of the quite strong curvature of the droplets relative to the micrometre scale of the rod-like colloidal particles [90], but this is not certain at all.

An alternative method for probing the interfacial properties of nematic liquid crystals that we address here is provided by the examination of their wetting properties if brought into contact with a solid surface, and in particular the capillary rise against a vertical wall. For isotropic fluids, this is caused by differences in interfacial tensions between the solid and fluid phases, and the capillary-rise height (as well as the interface profile) is

determined by the competition between the Laplace pressure associated with the curved surface and the hydrostatic pressure associated with the density difference between the two fluids. If one of the fluid phases is a nematic liquid crystal the situation is more complicated because of the anchoring properties of the director field to the various surfaces. The interface profile (meniscus shape) and the director-field structure in the capillary-rise region are in that case in addition determined by these anchoring strengths and the Frank elasticity due to the response of the director field to the presence of two interfaces [91]. As argued above, the analysis of the capillary rise might in fact be more suitable for finding the anisotropic surface tensions than analysing tactoid shapes, provided that the curvature of the profile is sufficiently small, that is, the radius of curvature of the meniscus shape should be very large compared to the size of the particles. This capillary rise of an isotropic-nematic interface is the topic of chapter 6.

For both the nematic droplets and the capillary-rise profile the minimisation of the sum of free energies as given by Eqs. (1.5) and (1.6) with respect to the director field and interface profile turns out to be a boundary-value problem that is probably impossible to solve analytically, and even quite hard numerically, but straightforward scaling arguments can already provide some insight into different regions where either energy is dominant over the other. The competition between surface tension and anchoring and bulk elasticity expresses itself in a length scale that presents itself naturally from the free energies and must be compared to a length scale that follows from the problem in hand. It follows from Eqs. (1.5) and (1.6) that for nematic droplets the bulk elastic energy scales as K times the volume R^3 times the square of the inverse radius of curvature of the director field, $1/R^2$, with K the relevant elastic constant and R the relevant length scale of the problem at hand that we discuss below, whereas the surface energy scales as ζR^2 . This immediately gives a cross-over scale $\lambda \equiv K/\zeta$, called the extrapolation length, that can be used to estimate the type of director field in the rise region or droplet given the magnitude of the extrapolation length relative to the relevant length scale. For the capillary-rise profile we consider the energies per unit length of the meniscus, and this gives the same cross-over scale.

In case of the capillary rise of an isotropic-nematic interface, the relevant length scale turns out to be the capillary length $\ell_c = \sqrt{2\gamma/\Delta\rho_m g}$, with g the gravitational acceleration and $\Delta\rho_m$ the mass-density difference between the isotropic and nematic phase. This length scale provides a measure of the capillary-rise height and follows from equating the aforementioned hydrostatic pressure associated with lifting the interface and the Laplace pressure associated with the curved interface. If $\lambda \gg \ell_c$, then the director field in the rise region should be approximately uniform on account of the rigidity of the field on that scale. Conversely, if $\lambda \ll \ell_c$, the field in the rise region

also deforms to accommodate the predominance of the surface anchoring. Associated with the hydrostatic pressure is a gravitational free-energy cost of raising the isotropic-nematic interface up the wall. It reads

$$F_g = \Delta\rho_m g \int_V dV y, \quad (1.7)$$

where V is the volume of the nematic phase that is raised above the horizontal reference state $y = 0$. The detailed analysis of the interface profiles and director fields in the capillary-rise region can be found in chapters 6.

In case of the nematic droplets the relevant length scale is simply the drop size R , hence the radius in case of a spherical drop. The drops are presumed to be floating freely in the isotropic phase, so the density difference and gravitational energy play no role. If R is large relative to the extrapolation length λ , the surface anchoring is dominant and the director field has to comply with the preferred anchoring, leading to a curved director field. On the other hand, if R is small compared to λ , then the elasticity is dominant and the director field is more or less uniform. The details of our analysis of the shape and structure of tactoids consisting of plate-like particles can be found in chapters 7, 8, and 9. In these chapters we also study the influence of a magnetic field on these droplets, because it couples to their shape and director field and this may provide access to additional information on the material parameters. Such a magnetic field imposes a certain orientation of the particles, which complicates the competition between the anisotropic surface energy and elastic bulk energy. In this case we have an additional magnetic energy that reads

$$F_m = -\frac{1}{2}\rho\Delta\chi \int_V dV (\mathbf{n} \cdot \mathbf{B})^2, \quad (1.8)$$

where we have dropped a spatially invariant term [6], ρ is the particle number density, $\Delta\chi$ the diamagnetic susceptibility anisotropy (dimensions J/T²), and \mathbf{B} the magnetic field. If $\Delta\chi < 0$, which is the case for gibbsite platelets, the particles have a tendency to orient their director perpendicular to the magnetic field. We compare our results to experiments on tactoids in dispersions of gibbsite particles in chapters 6, 7, 8, and 9. In these chapters we observe that if the field is sufficiently strong, this leads to interesting, non-trivial shapes and director fields. Finally, we summarise our main conclusions from this thesis and suggest a number of theoretical and experimental challenges for future investigation in chapter 10.

1.6 Thesis outline

The general purpose of this work is to gain a better insight into how the large-scale self-organisation of anisotropic particles originates from their anisotropic interactions. More specifically, we aim to understand how the self-assembled system-spanning networks in solution are affected by particle shape and size, and connectivity ranges, and how soft interfaces in liquid-crystalline (symmetry-broken) states are influenced by particle shape, surface properties, and external fields. This understanding then should help in the production of a composite with an as low as possible nanofiller loading and high conductivity, and the comparison of our results on isotropic-nematic interfaces with experimental studies should enable us to extract material properties of the liquid-crystalline materials.

The remainder of this thesis is organised as follows. We start in chapter 2 with studying the effect on the percolation behaviour of a polydispersity in the linear dimensions and connectivity range of rod-like and plate-like particles. Next, we apply the results from this chapter to realistic size distributions of carbon nanotubes and graphene in chapter 3. In chapter 4 we consider the conductivity of the percolating network of rod-like particles beyond the percolation threshold. We then focus on how an externally applied alignment field and excluded-volume interactions conspire against the formation of a percolating network in chapter 5, where the percolation transition is found to interfere with the transition to a uniaxial nematic phase. Such a nematic phase in contact with its isotropic phase gives rise to interesting interfacial shapes and director-field structures. This we show in chapter 6 where we study the rise of an isotropic-nematic interface up a solid vertical wall, and in chapters 7, 8, and 9, where we consider the shape and internal structure of homeotropic nematic droplets in the presence of a magnetic field. In chapters 7 and 8 we consider the limiting cases of strong surface anchoring ($\zeta/\gamma \rightarrow \infty$) and spherical shapes ($\zeta/\gamma \rightarrow 0$), and in chapter 9 we present the general case of imperfect surface anchoring and non-spherical tactoid shapes.

Connectedness percolation of polydisperse nanofillers: theory

2

We present a generalised connectedness-percolation theory reduced to a compact form for a large class of anisotropic particle mixtures with variable degrees of connectivity. Even though allowing for an infinite number of components, we derive a compact yet exact expression for the mean cluster size of connected particles. We apply our theory to rod-like particles taken as a model for carbon nanotubes and find that the percolation threshold is sensitive to polydispersity in length, diameter, and the level of connectivity, which may explain large variations in experimental values for the electrical percolation threshold in carbon-nanotube composites. The calculated connectedness-percolation threshold depends only on a few moments of the full distribution function. If the length and diameter distributions are independent, then the percolation threshold is raised by the presence of thicker rods whereas it is lowered by any length polydispersity relative to the monodisperse one with the same average length and diameter. The effect of connectivity polydispersity is studied by considering non-additive mixtures of conductive and insulating particles. Finally, we present tentative predictions for the percolation threshold of graphene sheets modelled as perfectly rigid, disk-like particles.[†]

[†]The contents of this chapter have been published as:
R. H. J. Otten and P. van der Schoot, Phys. Rev. Lett. **103**, 225704 (2009),
R. H. J. Otten and P. van der Schoot, J. Chem. Phys. **134**, 094902 (2011).

2.1 Introduction

Since their discovery in the early 1990s carbon nanotubes have attracted a lot of attention on account of their excellent mechanical, electrical, and thermal properties. More recently, the arguably even more remarkable characteristics of another carbon allotrope, graphene sheets, were discovered [17]. Both these allotropes manifest their properties on a macroscopic level in, e.g., polymer-based composites through the networks that they form in such media. It is not surprising, then, that the network formation of these nanofillers has also attracted much attention [18, 19]. Indeed, a crucial requirement for obtaining the desired properties of the final composite material is controlling network formation. Provided their level of connectivity meets the criteria set by the physical property of interest, and provided they form a system-spanning network, the nanofillers can considerably improve the physical properties of the host material [16]. For example, in order to enable charge-carrier hopping or tunneling from a particle to a neighbouring one in the network they ought to be sufficiently close to each other. This required proximity sets a connectedness criterion, which in turn determines the so-called percolation threshold, i.e., the minimal loading of nanofillers needed to form a domain-spanning network [16]. Around this critical point, the electrical conductivity increases many orders of magnitude [18, 19].

A considerable research effort has been devoted to determining the percolation threshold of anisometric nanofillers in composites and values as small as or smaller than 10^{-3} , measured in terms of the volume fraction that they occupy, have been found for both carbon nanotubes [26] and graphene [19]. Such small values are not entirely surprising because both for rod-like and plate-like particles the percolation threshold has been predicted to scale inversely with their aspect ratio that typically is on the order of one thousand [38, 92–96]. Indeed, graphene, being a single layer of graphite, has a typical thickness of a few tenths of nanometres and a diameter on the order of a micrometre. For the rod-like carbon nanotubes the diameters range from about one nanometre for single-walled carbon nanotubes to tens of nanometres for multi-walled carbon nanotubes, whereas their lengths are generally on the micrometre scale.

In practice, preparations of nanofillers, including those of the mentioned carbon allotropes, exhibit a number of characteristics that potentially affect network formation in the preparatory stages of the composite material and hence the percolation threshold. These include a size polydispersity and the presence of non-conducting species [19, 26, 97, 98]. In this work we focus attention on these two issues from a theoretical point of view, where we note that both carbon nanotubes and graphene sheets in the final composite normally show a large distribution in their linear dimensions. One cause of

this size polydispersity is that because of strong van der Waals forces they tend to form bundles or stacks that, even after processing, are difficult to exfoliate [26]. Because percolation phenomena are intimately related to phase transitions, which are known to be strongly influenced by polydispersity effects [99], we expect a significant impact of polydispersity on the percolation threshold. As we show in this chapter this turns out to be the case. Whether or not there is a correlation between the diameters and lengths of the nanofillers we find to be a crucial question in this context, and our main claim is that the inverse-aspect-ratio scaling mentioned in section 1.3 is only true if the linear dimensions are independent of each other. A coupling between them leads to completely different behaviour.

The other issue we focus on is non-additivity. Non-additivity of interactions has been shown to have a strong effect on the phase behaviour of hard-rod dispersions [100] and hence could also be important here. As an example, we consider non-additivity of charge transport between different kinds of particle, which implies that the connectivity range of two unlike particles differs from the average of those between pairs of like particles. In particular, we focus on the presence of non-conductive species and again expect a significant impact on the percolation threshold because in practice only one third of the single-walled carbon nanotubes are metallic and two thirds are semi-conducting.[†] This expectation turns out to be correct because we find a percolation threshold that depends very sensitively on the connectivity ranges.

The combined effects of size and connectivity variations in our view may explain, at least in part, the variation of several orders of magnitude observed in percolation thresholds of carbon nanotubes that have approximately the same mean aspect ratio [101]. Theoretically, neither the effect of polydispersity in size nor that of conductivity of the nanofillers is well understood for either allotrope, and often ignored in computer simulations and model predictions. For graphene, and flat particles in general, there is only a limited number of theoretical works devoted to their percolation behaviour for reasons that will become apparent below. For rod-like particles there are indeed numerous predictions but most approaches, including the reference-interaction-site model (RISM) [96] and excluded or contact-value theorems [38, 92–95], preaverage angular correlations or neglect long-range correlations [2, 96]. In this chapter we show, by taking a more fundamental approach, that these correlations can in fact be very important. We demonstrate that a generalised connectedness percolation theory can be reduced to a tractable form for a large class of mixtures of anisometric particles. We make use of the multi-component pair-connectedness Ornstein-Zernike equation, which has an ana-

[†]As produced graphene sheets are conductive but if they are first oxidised and later reduced in the processing of the nanocomposites, their conductivity can be strongly reduced [114].

logue in liquid-state theory [34], where we allow for polydispersity in all three linear dimensions and connectivity ranges of the particles. From this we obtain an explicit expression for the average cluster size, with the underlying assumption that the network is formed in the fluid stages of the nanocomposite production process. This means that we presume an equilibration configuration to be frozen in because of the equilibration steps in the processing, as discussed in section 1.2 [26, 27].

For definiteness, we apply our theory to harshly repulsive (non-overlapping) rod-like carbon nanotubes, invoke a second-virial approximation and use a generalised version of the so-called cherry-pit, or core-shell model that considers two particles to be connected if they are sufficiently close to each other [20, 39]. This is reasonable because nanotubes in conducting networks do not actually touch each other in the final product and charge transport across nanotubes occurs via electron hopping between them. An advantage of the cherry-pit model is that it can straightforwardly be applied to study non-additive mixtures of conductive and non-conductive particles. With these model ingredients we find an analytical expression for the percolation threshold from the nanofiller fraction at which the cluster size diverges. Similar to what was found previously for the geometrically much simpler case of spherical particles [102], the percolation threshold that we obtain is a function only of a few higher-order moments of the full size distribution notwithstanding the presence of angular correlations between the filler particles caused by translation-rotation coupling.

Our findings may be summarised as follows.

1. The percolation threshold of carbon nanotubes only depends on a few moments of the full distribution function of sizes and connectivity ranges, meaning that the details (higher moments) of these distributions are irrelevant. The combined influence of length and width polydispersity on the percolation threshold is a highly non-trivial function of the prevalence of the various species in the mixture;
2. If we assume that all carbon nanotubes are conductive and that the length and width distributions are independent of each other, then the percolation threshold is inversely proportional to the *weight* average of the distribution of rod lengths. This implies that a small fraction of longer rods significantly lowers the threshold of a dispersion of short ones it is added to. This generalises prior calculations and puts these on a much firmer theoretical footing [97, 103]. Thicker carbon nanotubes, on the other hand, have the opposite effect: they raise the percolation threshold and more so than expected from the inverse-aspect-ratio dependence valid for monodisperse tubes;
3. In mixtures of conductive and insulating carbon nanotubes, which are inherently

non-additive, the percolation threshold scales with the inverse fraction of conductive filler implying that the concentration of conductive filler particles determines the percolation threshold and the insulating ones act, in a way, as dead mass. This is specific to rod-like particles and is caused by the predominance of linear chains of interactions in the long-range correlations between them.

In the remainder of this chapter we derive in section 2.2 an equation for the average cluster size of mutually connected nanofillers with arbitrary distributions of their linear dimensions. In section 2.3 we choose an appropriate closure and discuss the connectivity model that we use to derive the percolation threshold for rod-like carbon nanotubes, which, even in the monodisperse limit, is a non-trivial result due to the influence of translation-rotation coupling on the long-range correlations between the particles [97]. In section 2.4 we show the effect on the percolation threshold of a tetradisperse size distribution. For the effect of a size polydispersity on the percolation threshold of several more realistic size distribution functions the reader is referred to chapter 3. In this chapter we apply our model to compute the effect of the presence of non-conductive particles on the percolation threshold in section 2.5. Finally, we draw our conclusions in section 2.6, discuss the applicability of the second-virial approximation to fillers with a different shape, and we make tentative but surprising predictions for the percolation threshold of graphene sheets that we model as idealised mutually repelling (“hard”) disks, because we presume them to be randomly distributed in the final composite.

2.2 Cluster-size calculation

In order to find the percolation threshold from connectedness-percolation theory, we have to find the critical density where the (weight) average cluster size S , as given by Eq. (1.1), diverges. This description can straightforwardly be generalised to polydisperse, anisometric particles for which P and C^+ also depend on their linear dimensions and orientations. To describe these particles with arbitrary linear dimensions, let $x_{i\alpha\ddagger}$ denote the mole fraction of particles of length L_i , width D_α , and height H_\ddagger . In the following, we use indices with Roman symbols to denote length polydispersity, Greek ones for variations in width and the symbols \dagger , \ddagger , and \S to indicate different heights. The weight-average cluster size S is now the sum over the indices of the weight-average “partial cluster sizes” $S_{ij\alpha\beta\dagger\ddagger}$ that contain averages over the orientations

$$S_{ij\alpha\beta\dagger\ddagger} = x_{i\alpha\dagger} \delta_{ij} \delta_{\alpha\beta} \delta_{\dagger\ddagger} + \lim_{\mathbf{q} \rightarrow 0} x_{i\alpha\dagger} x_{j\beta\ddagger} \rho \left\langle \hat{P}_{ij\alpha\beta\dagger\ddagger}(\mathbf{q}, \mathbf{u}, \mathbf{u}') \right\rangle_{\mathbf{u}, \mathbf{u}'}. \quad (2.1)$$

Here, δ_{ij} is the Kronecker delta and $\mathbf{u} \equiv (\mathbf{u}_1, \mathbf{u}_2)$ with \mathbf{u}_1 and \mathbf{u}_2 the unit vectors in the direction of the main axes of a particle. For the sake of notational convenience we

introduced the notation $\langle \dots \rangle_{\mathbf{u}_n} \equiv (4\pi)^{-1} \int d\mathbf{u}_n(\dots)$, $n = 1, 2$ to denote the orientational average, with a similar prescription for the primed variables. The short-hand notation $\langle \dots \rangle_{\mathbf{u}, \mathbf{u}'}$ implies the compound average $\langle \langle \dots \rangle_{\mathbf{u}} \rangle_{\mathbf{u}'}$. The first term of Eq. (2.1) is only nonzero for the particle chosen to start counting the contacts, i.e., $i = j$, $\alpha = \beta$ and $\dagger = \ddagger$, or for two different particles of equal dimensions, because for those $S_{ij\alpha\beta\dagger\ddagger}$ is the same. The second term gives the number of intra-cluster contacts between a particle of dimensions L_i , D_α , and H_\dagger and one of dimensions L_j , D_β , and H_\ddagger , weighted by their mole fractions to give the correct sum.

The probability $\hat{P}_{ij\alpha\beta\dagger\ddagger}$ obeys the multi-component analogue of the pair-connectedness Ornstein-Zernike equation, Eq. (1.3), and its Fourier transform reads

$$\hat{P}_{ij\alpha\beta\dagger\ddagger}(\mathbf{q}, \mathbf{u}, \mathbf{u}') = \hat{C}_{ij\alpha\beta\dagger\ddagger}^+(\mathbf{q}, \mathbf{u}, \mathbf{u}') + \rho \sum_{k, \gamma, \S} x_{k\gamma\S} \left\langle \hat{C}_{ik\alpha\gamma\dagger\S}^+(\mathbf{q}, \mathbf{u}, \mathbf{u}'') \hat{P}_{kj\gamma\beta\S\dagger\ddagger}(\mathbf{q}, \mathbf{u}'', \mathbf{u}') \right\rangle_{\mathbf{u}''}. \quad (2.2)$$

Because the cluster size obeys $S \equiv \sum_p S_p$ with $p \equiv \{i, j, \alpha, \beta, \dagger, \ddagger\}$, we see from Eqs. (2.1) and (2.2) that we need not solve the individual components of \hat{P} but have to obtain information only on a weighted average of \hat{P} over its six indices and four orientations. Therefore, detailed knowledge of the individual components of $\hat{P}_{ij\alpha\beta\dagger\ddagger}$ is not required to calculate the cluster size and the trick to solving Eq. (2.2) is to take averages over j , β , \ddagger , and \mathbf{u}' . For this purpose we now introduce the generalised notation $\langle \dots \rangle_{j\beta\ddagger, \mathbf{u}} \equiv (4\pi)^{-1} \int d\mathbf{u}' \sum_{j, \beta, \ddagger} x_{j\beta\ddagger}(\dots)$ for an average over the size distribution and the orientations of a single particle. We next define the functions $\Pi_{i\alpha\dagger}$ and $\Gamma_{i\alpha\dagger}$ and the operator $O_{i\alpha\dagger}$ as

$$\Pi_{i\alpha\dagger}(\mathbf{q}, \mathbf{u}) \equiv \left\langle \hat{P}_{ij\alpha\beta\dagger\ddagger}(\mathbf{q}, \mathbf{u}, \mathbf{u}') \right\rangle_{j\beta\ddagger, \mathbf{u}'} \quad (2.3)$$

$$\Gamma_{i\alpha\dagger}(\mathbf{q}, \mathbf{u}) \equiv \left\langle \hat{C}_{ij\alpha\beta\dagger\ddagger}^+(\mathbf{q}, \mathbf{u}, \mathbf{u}') \right\rangle_{j\beta\ddagger, \mathbf{u}'} \quad (2.4)$$

$$O_{i\alpha\dagger} f_{k\gamma\S} \equiv \rho \left\langle \hat{C}_{ik\alpha\gamma\dagger\S}^+(\mathbf{q}, \mathbf{u}, \mathbf{u}'') f_{k\gamma\S}(\mathbf{q}, \mathbf{u}'') \right\rangle_{k\gamma\S, \mathbf{u}''}, \quad (2.5)$$

where $f_{k\gamma\S}$ is an arbitrary integrable function. This allows us to rewrite the averaged version of the Ornstein-Zernike equation (2.2) into a more compact form as

$$\Pi_{i\alpha\dagger}(\mathbf{q}, \mathbf{u}) = (I_{k\gamma\S} - O_{k\gamma\S})^{-1} \Gamma_{k\gamma\S}(\mathbf{q}, \mathbf{u}), \quad (2.6)$$

with $I_{i\alpha\dagger}$ an operator that changes the indices of a function, so $I_{i\alpha\dagger} f_{k\gamma\S} = \sum_{k, \gamma, \S} \delta_{ik} \delta_{\alpha\gamma} \delta_{\dagger\S} f_{k\gamma\S} = f_{i\alpha\dagger}$.

According to Eq. (2.1), this gives for the overall average cluster size

$$S = 1 + \lim_{\rho \rightarrow 0} \rho \langle \Pi_{i\alpha\dagger}(\mathbf{q}, \mathbf{u}) \rangle_{i\alpha\dagger, \mathbf{u}}. \quad (2.7)$$

We insert Eq. (2.6) in Eq. (2.7) for the cluster size S , note that $\Gamma_{k\gamma\delta}(\mathbf{q}, \mathbf{u}) = \rho^{-1} O_{k\gamma\delta} \mathbf{1}$, and invoke the identity $1 + (I_{k\gamma\delta} - O_{k\gamma\delta})^{-1} O_{k\gamma\delta} \mathbf{1} = (I_{k\gamma\delta} - O_{k\gamma\delta})^{-1} I_{k\gamma\delta} \mathbf{1} = \left(I_{k\gamma\delta}^{-1} (I_{k\gamma\delta} - O_{k\gamma\delta}) \right)^{-1} \mathbf{1}$. This gives $S = \left\langle (I - O_{i\alpha\uparrow})^{-1} \mathbf{1} \right\rangle_{i\alpha\uparrow, \mathbf{u}}$, with I the identity operator. To solve for S , we write

$$S = \langle T_{k\gamma\delta}(\mathbf{u}) \rangle_{k\gamma\delta, \mathbf{u}}, \quad (2.8)$$

where T must be solved from the following simplified integral equation,

$$T_{k\gamma\delta}(\mathbf{u}) - \rho \left\langle \hat{C}_{km\gamma\delta\uparrow}^+(0, \mathbf{u}, \mathbf{u}') T_{m\delta\uparrow}(\mathbf{u}') \right\rangle_{m\delta\uparrow, \mathbf{u}'} = 1. \quad (2.9)$$

Eqs. (2.8) and (2.9), which represent our central result, involve averages over the indices and orientation of a single particle as opposed to those of two particles in the original Ornstein-Zernike equation (2.2), and it follows that finding certain averages of T over its indices and argument suffices to compute the cluster size. This simplifies the calculation significantly. In section 2.3 we apply our theory, valid for particles of arbitrary linear dimensions, to the rod-like carbon nanotubes. For this we invoke an appropriate closure because the direct-connectedness function \hat{C}^+ is an as yet unknown quantity.

2.3 Application to carbon nanotubes

We now apply our model to carbon nanotubes, which we assume to have perfect cylindrical symmetry, so only two dimensions and a single orientation are required to describe their properties. Carbon nanotubes have a typical aspect ratio of 10^2 to 10^4 and for such slender particles an accurate closure of Eq. (2.9) for the average cluster size is provided by the second-virial approximation [104]. See also Appendix 2.A. This means that we consider only linear pair correlations between the particles, i.e., no loop correlations, which, as is shown below, has a significant consequence for non-additive mixtures. The accuracy of the second-virial approximation and the possible applicability to other types of particle are considered in the discussion in section 2.6. We first elaborate on this approximation and the connectivity model that we use, and compute the percolation threshold using this approximation. To show the strong effect of polydispersity we apply the result to a tetradisperse distribution in section 2.4. Finally, the results are applied to non-additive mixtures in section 2.5.

As already announced in the chapter 1, the second-virial approximation implies that $\hat{C}^+ = \hat{f}^+$ [34, 38], with $f^+ = \exp(-\beta u^+)$ the connectedness Mayer function, u^+ the connectedness potential of particles that belong to the same cluster, and $\beta^{-1} = k_B T$, where k_B is Boltzmann's constant and T the absolute temperature. For any configuration where two rods are not connected this two-body connectedness potential u^+ by

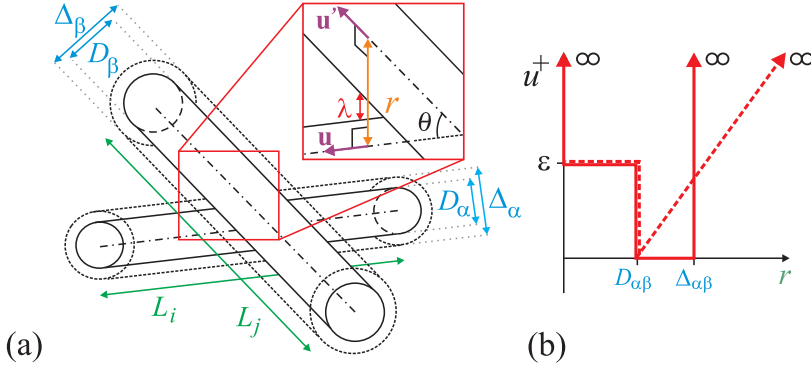


Figure 2.1: (a) Schematic representation of two nanotubes with orientations \mathbf{u} and \mathbf{u}' , lengths L_i and L_j and diameters D_α and D_β , separated by a distance r between their centerlines and skewed at an angle θ . Charge transport between the rods requires r to be smaller than $D + \lambda = \Delta$: the dashed cylinders of diameter Δ enclosing the rods must overlap. (b) Solid line: the connectedness potential u^+ for the idealised “cherry-pit” model between two particles in the same cluster versus their distance r for ideal ($\varepsilon = 0$) and hard particles ($\varepsilon \rightarrow \infty$). The dashed line shows an alternative connectedness potential $\beta u^+ = (r - D)/\lambda$ for $r > D$ that may provide a more realistic description of an exponentially decaying electron-tunneling probability with a decay length λ . Within the second-virial approximation described in the main text, both connectedness potentials produce identical results.

definition is infinitely large. The potential that we use interpolates between ideal, penetrable particles and hard ones that interact via a strongly repulsive excluded-volume interaction, but our final purpose is to model particles of the latter type, see Fig. 2.1. For intersecting particles, for which the distance r between them satisfies $r \leq D_{\alpha\beta}$, we have $u^+ = \varepsilon$, where $\varepsilon \rightarrow \infty$ for impenetrable rods and $\varepsilon = 0$ for ideal (penetrable) ones and where $D_{\alpha\beta} \equiv \frac{1}{2}(D_\alpha + D_\beta)$ denotes their average diameter. In the overlap or connectedness zone $u^+ = 0$ for $D_{\alpha\beta} \leq r \leq \Delta_{\alpha\beta}$ and $u^+ \rightarrow \infty$ for $r \geq \Delta_{\alpha\beta}$ away from it. The length $\Delta_{\alpha\beta}$ is an adjustable parameter in our model and indicates the maximal range for effective charge transport [97]. This means that beyond this range charge transport is neglected and below we discuss the effect of a hopping probability with a longer range. The concept of the connectedness criterion is corroborated by the experimental observation that in practice the nanotubes in conducting networks do not actually touch each other [26]; our model is therefore a generalisation of the so-called cherry-pit model that has earlier been used for spherical particles [36, 39].

The next step is to compute \hat{f}^+ , for which it is convenient to make use of Straley’s oblique coordinate system [105]. This means instead of Cartesian coordinates \mathbf{r} we shift to one that has two axes along the orientations \mathbf{u} and \mathbf{u}' of two test rods and the third

one along the shortest line connecting them,

$$\mathbf{r} = \xi \mathbf{u} + \eta \mathbf{u}' + \zeta \frac{\mathbf{u} \times \mathbf{u}'}{|\mathbf{u} \times \mathbf{u}'|}. \quad (2.10)$$

The associated volume element is $d\mathbf{r} = |\sin \theta| d\xi d\eta d\zeta$, with $\theta(\mathbf{u}, \mathbf{u}')$ the angle between the particles. For slender rods of lengths L_i and L_j we find to leading order [13]

$$\begin{aligned} \hat{f}_{ij\alpha\beta}^+(0, \mathbf{u}, \mathbf{u}') &= \int_{-L_i/2}^{L_i/2} d\xi \int_{-L_j/2}^{L_j/2} d\eta \left(\int_{-\Delta_{\alpha\beta}}^{\Delta_{\alpha\beta}} d\zeta - \int_{-D_{\alpha\beta}^{\text{eff}}}^{D_{\alpha\beta}^{\text{eff}}} d\zeta \right) |\sin \theta| \\ &= 2L_i L_j (\Delta_{\alpha\beta} - D_{\alpha\beta}^{\text{eff}}) |\sin \theta|, \end{aligned} \quad (2.11)$$

where $D_{\alpha\beta}^{\text{eff}} \equiv D_{\alpha\beta}(1 - \exp(-\beta\varepsilon))$ an effective diameter, so $D_{\alpha\beta}^{\text{eff}} = 0$ for ideal and $D_{\alpha\beta}^{\text{eff}} = D_{\alpha\beta}$ for hard rods. See also Fig. 2.1. This figure also shows an alternative potential $\beta u^+ = (r - D)/\lambda$ for $r > D$ that more realistically mimics an exponentially decaying electron-tunneling probability with a decay length λ , because in that case $\hat{f}^+ = \exp(-(r - D)/\lambda)$ [106]. If we use this potential instead of the cherry-pit potential and set $\lambda = \Delta_{\alpha\beta} - D_{\alpha\beta}$ as the characteristic tunneling distance, then this leaves our result Eq. (2.11) for \hat{f}^+ invariant, so our cherry-pit model implicitly takes this effect into account.

We are now in a position to solve Eqs. (2.8) and (2.9) with the closure $\hat{C}^+ = \hat{f}^+$, where \hat{f}^+ is given by Eq. (2.11). Let us first tentatively presume additivity of charge-carrier hopping distances, so $\Delta_{\alpha\beta} = (\Delta_{\alpha} + \Delta_{\beta})/2$. Non-additivity effects caused, e.g., by a fraction of the particles not contributing to charge transport through the network, are extensively discussed in section 2.5. For the case of additive hopping distances the cluster size S for our polydisperse carbon nanotubes can be obtained by substituting \hat{f}^+ into Eq. (2.9), giving

$$\begin{aligned} T_{k\gamma}(\mathbf{u}) - \rho L_k (\Delta_{\gamma} - D_{\gamma}^{\text{eff}}) \langle L_m |\sin \theta| T_{m\delta}(\mathbf{u}') \rangle_{m\delta, \mathbf{u}'} - \\ \rho L_k \langle L_m (\Delta_{\delta} - D_{\delta}^{\text{eff}}) |\sin \theta| T_{m\delta}(\mathbf{u}') \rangle_{m\delta, \mathbf{u}'} = 1, \end{aligned} \quad (2.12)$$

where we have inserted within the second-virial approximation $\hat{C}^+ = \hat{f}^+$ and Eq. (2.11) for \hat{f}^+ , which tacitly presumes the additivity of the overlap distance $\Delta_{\alpha\beta}$. If we average the above integral equation over \mathbf{u} and use that $\langle |\sin \theta| \rangle_{\mathbf{u}} = \langle \langle |\sin \theta| \rangle_{\mathbf{u}'} \rangle_{\mathbf{u}} = \pi/4$ for an isotropic distribution of the orientations [13], then subsequent averaging the resulting equation over the variables k and γ produces an expression for $S = \langle T_{k\gamma}(\mathbf{u}) \rangle_{k\gamma, \mathbf{u}}$ and two of its higher moments,

$$\begin{aligned} \langle T_{k\gamma}(\mathbf{u}) \rangle_{k\gamma, \mathbf{u}} - \rho \frac{\pi}{4} \langle L_k (\Delta_{\gamma} - D_{\gamma}^{\text{eff}}) \rangle_{k\gamma} \langle L_m T_{m\delta}(\mathbf{u}') \rangle_{m\delta, \mathbf{u}'} - \\ \rho \frac{\pi}{4} \langle L_k \rangle_k \langle L_m (\Delta_{\delta} - D_{\delta}^{\text{eff}}) T_{m\delta}(\mathbf{u}') \rangle_{m\delta, \mathbf{u}'} = 1. \end{aligned} \quad (2.13)$$

To solve for S , we repeat this exercise after multiplying the integral equation by L_k and $L_k(\Delta_\gamma - D_\gamma^{\text{eff}})$, respectively.

The solution of the set of three equations that we thus obtain gives an expression for S that diverges at the percolation threshold if the rod volume fraction $\varphi_p = \frac{\pi}{4}\rho\langle L_k D_\gamma^2 \rangle_{k\gamma}$ obeys

$$\varphi_p = \frac{\langle L_k D_\gamma^2 \rangle_{k\gamma}}{\langle L_k^2 \lambda_\gamma^{\text{eff}} \rangle_{k\gamma} + \sqrt{\langle L_k^2 \rangle_k \langle L_k^2 (\lambda_\gamma^{\text{eff}})^2 \rangle_{k\gamma}}}, \quad (2.14)$$

with $\lambda_\gamma^{\text{eff}} \equiv \Delta_\gamma - D_\gamma^{\text{eff}}$. The other two equations from the set of three provide the moments $\langle L_k T_{k\gamma} \rangle_{k\gamma}$ and $\langle L_k (\Delta_\gamma - D_\gamma^{\text{eff}}) T_{k\gamma} \rangle_{k\gamma}$, and these diverge at the same percolation threshold as given by Eq. (2.14). This equation is our main result for dispersions of rod-like particles. We find that the percolation threshold depends only on several higher-order moments of the full distribution function. A similar result was found for spherical particles, although these obviously do not exhibit angular correlations [102]. That these are important for rods is straightforward to illustrate by means of a so-called contact-volume argument [93]. This implies that we presume that percolation requires that there is about one rod per average contact or overlap volume, which is equal to $V_{\text{cont}} = 2 \langle L_k^2 \lambda_\gamma^{\text{eff}} |\sin \theta| \rangle_{k\gamma, \mathbf{u}} = \langle L_k^2 \lambda_\gamma^{\text{eff}} \rangle_{k\gamma} \pi/2$. We then find $\varphi_p = \frac{\pi}{4} \langle L_k D_\gamma^2 \rangle_{k\gamma} / V_{\text{cont}} = \langle L_k D_\gamma^2 \rangle_{k\gamma} / 2 \langle L_k^2 \lambda_\gamma^{\text{eff}} \rangle_{k\gamma}$, so we retrieve Eq. (2.14), except that the denominator now becomes two times the first term of the denominator of Eq. (2.14), so $\langle L_k^2 \lambda_\gamma^{\text{eff}} \rangle_{k\gamma}$. The neglect of translation-rotation coupling between the rods in the ‘‘simple’’ contact-volume argument causes the discrepancy between the two results.

Eq. (2.14) holds for arbitrary length and diameter distributions that are even allowed to be coupled, in which case $\langle L_k D_\gamma^2 \rangle_{k\gamma} \neq \langle L_k \rangle_k \langle D_\gamma^2 \rangle_\gamma$. We shall see later that a positive correlation between the distributions leads to interesting results but we first presume the distributions to be independent. In that case φ_p is inversely proportional to the *weight* average $\langle L \rangle_w \equiv \langle L_k^2 \rangle_k / \langle L_k \rangle_k$ of the distribution of rod lengths. A direct consequence is that a monodisperse system with only very long rods produces the lowest percolation threshold, that is, the lowest absolute value. However, the fact that the percolation threshold scales inversely with $\langle L \rangle_w$, not the number average $\langle L_k \rangle_k$, causes cooperative behaviour between the rods that has a significant impact on the percolation threshold. Indeed, the dependence on the weight average implies that increasing the length polydispersity lowers the percolation threshold for a constant average length because longer rods contribute more to the growing network than shorter ones do, and the effect is stronger for a larger length difference.

In the next two sections, the results from this section are applied to somewhat idealised systems that can be considered as implementations of our model that are intended

to provide some insight into the effect on the percolation threshold of a polydispersity in the linear systems and the degree in which the particles conduct electricity. In section 2.4 we first consider a system of tetradisperse rods that shows a sensitive dependence of the percolation threshold on a size polydispersity. The second application of our model is in section 2.5, where we find a sensitive dependence of the percolation threshold on the presence of non-conductive particles in the distribution. More realistic size distributions are considered in chapter 3, where we demonstrate that a large decrease in the percolation threshold requires a length distribution that is strongly skewed towards shorter lengths.

2.4 Tetradisperse distribution

We first apply our main result for rod-like particles, Eq. (2.14), to a tetradisperse system of long, short, thick, and thin rods, where the thick rods model either multi-walled carbon nanotubes or bundles of carbon nanotubes. This distribution has a very strong effect on the percolation threshold, as is illustrated in Fig. 2.2. We see that the percolation threshold increases linearly with the mole fraction of thick rods, whereas it decreases with the fraction of long rods. The larger the length difference, the smaller the fraction of long rods required to realise a significant reduction in the percolation threshold. For a length ratio of more than 8 the percolation threshold is decreased by a factor of more than 4 by adding only 10 % of long rods, and it is reduced further only slightly by adding long ones. We note that here the distributions are presumed to be independent of each other, which turns out to be an important assumption to be discussed in the next chapter 3.

The reciprocal weight-average length dependence of the percolation threshold that we find agrees with results for interpenetrable sticks [93] and hard rods with monodisperse diameters and connectivity ranges [97], for which we find $\varphi_p = D^2/2 \langle L \rangle_w \lambda$ with $\lambda = \Delta - D$. The value of λ plausibly depends on the dielectric constant of the host medium [97] and can also effectively be manipulated by a penetrable conductive coating of the carbon nanotubes, such as the conductive polymer blend poly(3,4-ethylenedioxythiophene):poly(styrene sulfonate) (PEDOT:PSS) [27, 107], discussed in more detail in section 2.5. In the monodisperse limit we find $\varphi_p = D^2/2\lambda L$ for hard particles, in agreement with recent analytical work [106]. For ideal particles in the same limit we find $\varphi_p = D^2/2\Delta L = D/2L$ with $D_\gamma^{\text{eff}} = 0$, where we put $\Delta = D$ [97]. This is also consistent with computer simulations [108] and with results that were based on geometric arguments [38, 103, 109].

In order to highlight the strong cooperative behaviour between the rods for small

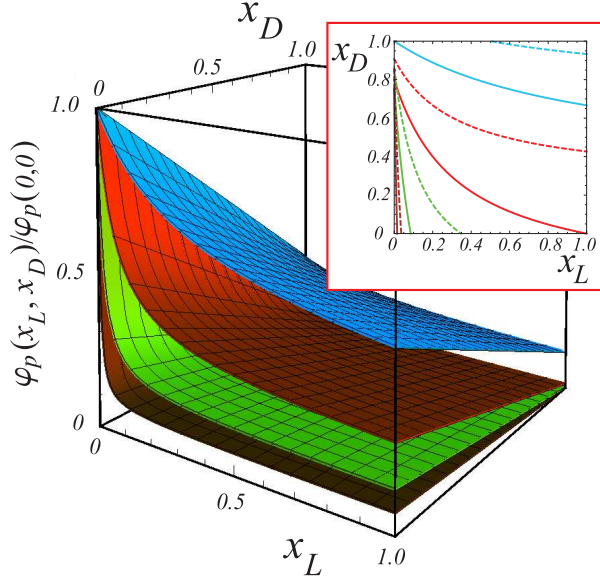


Figure 2.2: For a tetradisperse mixture of thick, thin, long, and short rods the percolation threshold φ_p is shown as a function of the number fractions x_L of long rods and x_D of thin rods. The tunneling length λ is taken as a constant and drops out of the description. The graphs are for different length ratios ($n \equiv L_{\text{long}}/L_{\text{short}}$), and width ratios ($D_{\text{thick}}/D_{\text{thin}}$), which is taken equal to n . From top to bottom: $n = 2, 4, 8$, and 16 . Inset: the non-linear behaviour of φ_p is demonstrated by a cross section for constant $\varphi_p(x_L, x_D)/\varphi_p(0,0) = 0.25$ (0.15) for the solid (dashed) lines. Pairs of line from top right to bottom left: $n = 2, 4, 8$, and 16 .

fractions of long ones and to make the highly non-linear effect of polydispersity more quantitative, we calculate Eq. (2.14) and compare this with that for the monodisperse case for which $\langle L_i^a D_\alpha^b \rangle_{i\alpha} = L^a D^b$ for the powers $a, b = 0, 1, 2 \dots$. We consider polydisperse distributions that obey $\langle L_i \rangle_i^a \langle D_\alpha \rangle_\alpha^b = L^a D^b$, so they have the same *number* averages as the reference monodisperse case. It appears reasonable to presume the hopping distance λ to be an invariant of the dimensions of the carbon nanotubes, so we divide Eq. (2.14) by $\langle D_\alpha \rangle_\alpha^2 / 2\lambda \langle L_i \rangle_i$ and obtain for the ratio of percolation thresholds $\varphi_p(x, y) / \varphi_p(x_0, y_0) = \langle L_i \rangle_i^2 \langle D_\alpha \rangle_\alpha^2 / \langle L_i \rangle_i \langle D_\alpha \rangle_\alpha^2$. Here, x and y are as yet unspecified parameters that depend on the type of length and diameter distribution adopted and that measure the degree of polydispersity; x_0 and y_0 are the values for which the distribution is monodisperse, i.e., very strongly peaked, with the same number average.

We observe that the polydispersity indices $\langle L_i \rangle_i^2 / \langle L_i \rangle_i$ and $\langle D_\alpha \rangle_\alpha^2 / \langle D_\alpha \rangle_\alpha$ of the distributions suffice to determine the effect of polydispersity on the percolation threshold. If we insert the identities $\langle D_\alpha \rangle_\alpha^2 = \text{Var}(D_\alpha) + \langle D_\alpha \rangle_\alpha^2$ and $\langle L_i \rangle_i^2 = \text{Var}(L_i) + \langle L_i \rangle_i^2$,

where Var denotes the variance of a distribution, we obtain

$$\frac{\varphi_p(x, y)}{\varphi_p(x_0, y_0)} = \frac{m + 1}{s + 1}, \quad (2.15)$$

with $m \equiv \text{Var}(D_\alpha) / \langle D_\alpha \rangle_\alpha^2$ and $s \equiv \text{Var}(L_i) / \langle L_i \rangle_i^2$ the relative magnitudes of the variances of the diameter and length distribution.[‡] Eq. (2.15) shows that a small value of m and large value of s are required for a significant reduction of the percolation threshold relative to the equivalent monodisperse distribution. Given that m is positive for any distribution that is not monodisperse, width polydispersity apparently raises the percolation threshold. However, in practice m remains close to unity because for both single-walled carbon nanotubes and multi-walled carbon nanotubes we estimate it to be at most 0.2 [110,111]. As to the influence of a length polydispersity, the fact that a large value of s leads to a low percolation threshold is an important issue that we return to in the discussion.

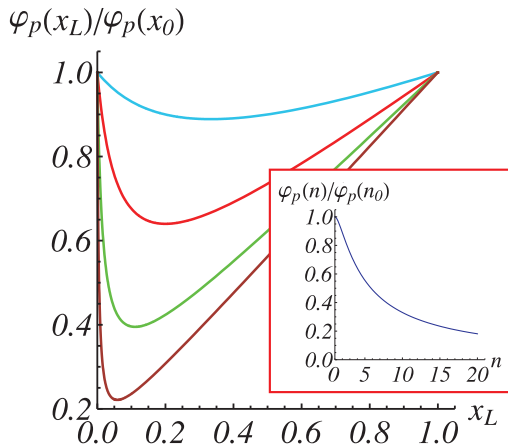


Figure 2.3: For a bidisperse mixture of long and short rods the ratio of the actual percolation threshold $\varphi_p(x_L)$ and that of the corresponding monodisperse solution $\varphi_p(x_0)$ with the same mean length $\langle L_k \rangle_k$ is shown as a function of the number fraction x_L of long rods. The tunneling length λ is taken as a constant and in that case drops out of this ratio. The graphs are for different length ratios $n \equiv L_{\text{long}}/L_{\text{short}}$ and we find $x_0 = nx/(1 + (n - 1)x)$. From top to bottom, $n = 2, 4, 8,$ and 16 . Inset: the largest reduction of the ratio of percolation thresholds is $\varphi_p(n)/\varphi_p(n_0) = 4n/(n + 1)^2$, with $n_0 = (3n - 1)/(n + 1)$, obtained for $x = 1/(n + 1)$, i.e., the minima in the main graph.

If we consider a bidisperse mixture consisting of long and short rods, we find that $x_0 = nx/(1 + (n - 1)x)$, with $n > 1$ the length ratio, and we observe that a large value of

[‡]In probability theory, $\sqrt{s} = \sqrt{\text{Var}(L_i)}/\langle L_i \rangle_i$ is called the coefficient of variation (or variation coefficient) of the distribution of L_i [125].

s is obtained for a large skewness of the distribution, that is, a skewness towards smaller lengths, as is illustrated in Fig. 2.3. Indeed, by adding a small fraction of long rods to a dispersion of short ones that are n times shorter, a significant non-linear reduction can be obtained. This additional reduction decreases again with increasing fraction of long rods, where we note that the absolute minimal percolation threshold is course obtained if all rods are long. The maximal reduction of the percolation threshold relative to the equivalent monodisperse system is reached for a number fraction x_L of long ones that satisfies $x_L = 1/(n + 1)$. So, the larger the length difference, the smaller the number fraction of long rods required to realise a significant reduction of the percolation threshold. At this optimum number fraction the relative percolation threshold equals $\varphi_p(n)/\varphi_p(n_0) = 4n/(n+1)^2$, where, $n_0 = (3n-1)/(n+1)$, see also Fig. 2.3. So, a mixture containing only 11 % of rods that are 8 times longer has a percolation threshold that is more than 60 % lower than the monodisperse system with the same average length. This finding may then provide an explanation for the large scatter in observed percolation thresholds of carbon nanotubes with the same (number) average dimensions [101]. A more generalised analysis that we present in the next chapter 3 teaches us that a length distribution that is strongly skewed towards shorter lengths, as shown in Fig. 2.3, is in fact a *requirement* for a large reduction of the percolation threshold. In chapter 3 we will also consider the impact of polydispersity on the percolation threshold of other length and width distributions inspired by experimental observations.

We next address another form of polydispersity often ignored in theoretical studies, being that in the level of conductance of the carbon nanotubes.

2.5 Mixtures of conductive and insulating particles

In the preceding sections we have tacitly assumed that all carbon nanotubes potentially contribute to the percolating network, and that connectivity is an additive property, i.e., we have $\Delta_{\alpha\beta} = (\Delta_\alpha + \Delta_\beta)/2$. If the nanocomposite contains not only conductive but also semi-conductive or insulating particles, which certainly is true for single-walled carbon nanotubes, then this additivity assumption breaks down because a charge carrier can only move between a pair of conductive particles and its transport is effectively blocked if one or both of them are poor conductors. Fortunately, our theory can quite straightforwardly be adjusted to model a mixture of metallic and electrically insulating rods, at least if they are of equal diameter. This is obviously an idealisation because the single-walled carbon nanotubes that do not possess metallic properties are not perfect insulators and, as already alluded to, exhibit semi-conducting behaviour [18], but for our purposes this model suffices.

In our model description we take our familiar criterion for connectivity of a pair of conductive rods, i.e., $\Delta_{11} = D + \lambda$ with the subscript 1 referring to the conductive species, and we require that particles of any other pair need to touch for charge transport to take place, which statistically occurs with zero probability. This means that $\Delta_{12} = \Delta_{22} = D$, where the subscript 2 indicates an insulating rod. This enforces non-additive charge-transport properties by blocking charge transport if at least one of the particles in a pair is not metallic. We consider a binary mixture of conductive and insulating rods of mole fractions x and $1 - x$, respectively. We then start from Eq. (2.12) that we average over \mathbf{u} , and obtain

$$\langle T_{k\gamma}(\mathbf{u}) \rangle_{\mathbf{u}} - \frac{\pi}{2} \rho L_k \langle (\Delta_{\gamma\delta} - D) L_m T_{m\delta}(\mathbf{u}') \rangle_{m,\mathbf{u}'} = 1. \quad (2.16)$$

If the index $\gamma = 2$ refers to the insulating particles, we have $\langle (\Delta_{2\delta} - D) L_m T_{m\delta}(\mathbf{u}') \rangle_{\delta} = 0$ and for $\gamma = 1$, denoting the conducting particles, we have $\langle (\Delta_{1\delta} - D) L_m T_{m\delta}(\mathbf{u}') \rangle_{\delta} = \lambda x T_{m1}(\mathbf{u}')$. We substitute this in Eq. (2.16) and obtain $\langle T_{k1}(\mathbf{u}) \rangle_{\mathbf{u}} - \frac{\pi}{2} \rho \lambda x L_k \langle L_m T_{m1}(\mathbf{u}') \rangle_{m,\mathbf{u}'} = 1$. We take averages over k after subsequently multiplying it by unity and by L_k . Solving the resulting set of equations for $\langle T_{k1}(\mathbf{u}) \rangle_{k,\mathbf{u}}$ and $\langle L_k T_{k1}(\mathbf{u}) \rangle_{k,\mathbf{u}}$ gives for the former

$$\langle T_{k1}(\mathbf{u}) \rangle_{k,\mathbf{u}} = \frac{1 - \frac{\pi}{2} \rho \lambda x \text{Var}(L_k)}{1 - \frac{\pi}{2} \rho \lambda x \langle L_k^2 \rangle_k}, \quad (2.17)$$

which diverges if the denominator is zero, leading to the critical number density $\rho_p = (\frac{\pi}{2} \lambda x \langle L_k^2 \rangle_k)^{-1}$. From this we find for the percolation threshold

$$\varphi_p = \frac{\pi}{4} \langle L_k \rangle_k D^2 \rho_p = \frac{D^2 \langle L_k \rangle_k}{2 \lambda x \langle L_k^2 \rangle_k}. \quad (2.18)$$

We see that we retrieve our previous result Eq. (2.14) for polydisperse lengths but monodisperse widths, except for an additional factor $1/x$. Hence, we find that the percolation threshold is governed by the fraction $x\varphi$ of conductive particles. This means that if one third of the single-walled carbon nanotubes is conductive, as is believed to be the case [112], then the percolation threshold is three times larger than would have been if all of them had been conductive, implying that increasing the fraction of conductive carbon nanotubes is a useful endeavor if a low percolation threshold is required for the nanocomposite application envisaged [26, 112, 113]. The fact that the percolation threshold is governed completely by the concentration of conductive particles may seem counter-intuitive, the reason being that the presence of non-conductive fillers should cause a disproportionate increase of the percolation threshold because they can take out entire conductive paths in a network that spans the whole system. We surmise

that this effect is counteracted by non-conductive particles that sit in dead branches and would have no contribution to the network anyway. In fact, this prediction can be understood at a deeper level if we consider percolation on a Bethe lattice. A Bethe lattice is a cycle-free tree with z branches per lattice site allowing us to readily deduce that provided a fraction x of these particles contributes to the charge transport, it must have a percolation threshold of $\varphi_p = 1/x(z - 1)$ if expressed in terms of the fraction of occupied sites [16]. From this result we conclude that the $1/x$ scaling in the percolation threshold must be the result of the absence of loop correlations in the Bethe lattice, which it has in common with the second-virial approximation in continuous space.

Another way to achieve the goal of lowering the percolation threshold is to make use of an electrically conducting coating of the carbon nanotubes, replacing the surfactants that often are used to disperse the carbon nanotubes in water in the early stages of the production process of the nanocomposite [27]. This coating then in a way manipulates the (effective) hopping distance λ provided it is in a way soft and physically penetrable to other carbon nanotubes.[§] For such a coating, a polymeric latex known as PEDOT:PSS has been used that also effectively stabilises the carbon nanotubes in solution [27, 107]. We note that the envisaged conduction mechanism of nearest-neighbour hopping in our model may lose its meaning for the rods with the soft conductive coating, because the conduction mechanism could become variable-range hopping [27]. Still, if we presume that the effective hopping distance is much larger for a coated carbon nanotube than for one without a coating, then the probability of charge transport between two carbon nanotubes without a coating is negligible compared to that of a pair with at least one coated particle. This implies that $\Delta_{11} = D + \lambda$, $\Delta_{12} = D + \lambda/2$ and $\Delta_{22} = D$, where the subscript 1 (2) indicates the (non-)conductive particle. In this model conduction takes place via the intersection of two coatings or via the intersection of a coating and a rod.

If this is so, we have for the average $\langle (\Delta_{2\delta} - D)T_{m\delta}(\mathbf{u}') \rangle_\delta = \frac{\lambda}{2} x T_{m1}(\mathbf{u}')$ in Eq. (2.16) for the index $\gamma = 2$ and $\langle (\Delta_{1\delta} - D)T_{m\delta}(\mathbf{u}') \rangle_\delta = \lambda x T_{m1}(\mathbf{u}') + \frac{\lambda}{2}(1 - x)T_{m2}(\mathbf{u}')$ for the index $\gamma = 1$, where x now stands for the mole fraction of coated carbon nanotubes. If we insert this in Eq. (2.16) we obtain the following set of equations

$$\langle T_{k1}(\mathbf{u}) \rangle_{\mathbf{u}} - \frac{\pi}{2} \rho L_k \left(\lambda x \langle L_m T_{m1}(\mathbf{u}') \rangle_{m, \mathbf{u}'} + \frac{\lambda}{2} (1 - x) \langle L_m T_{m2}(\mathbf{u}') \rangle_{m, \mathbf{u}'} \right) = 1, \quad (2.19a)$$

$$\langle T_{k2}(\mathbf{u}) \rangle_{\mathbf{u}} - \frac{\pi}{4} \rho \lambda x L_k \langle L_m T_{m1}(\mathbf{u}') \rangle_{m, \mathbf{u}'} = 1, \quad (2.19b)$$

for the two types of particle in the dispersion. If we take the average of Eqs. (2.19a) and (2.19b) over k after multiplying them by unity and by L_k , we have four equations

[§]This requires the conductive layer to be above its glass temperature in the preparatory phase in the production stages of the composite. This in practice is the case [27].

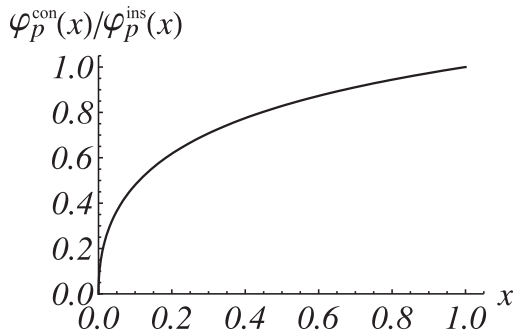


Figure 2.4: The ratio of the percolation thresholds for two systems of rods with a conductive penetrable coating, where one (φ_p^{con}) consists of conductive particles and the other (φ_p^{ins}) of insulating particles, as a function of the fraction x of coated rods. In the non-additive mixture of insulating rods charge transport only occurs between two coated particles, whereas in the additive system of metallic rods, charge transport is possible if at least one of the particles in a pair is coated. This is because we presume the effective hopping distance for a coated particle to be much larger than for one without a coating.

for the four unknowns $\langle T_{k1}(\mathbf{u}) \rangle_{k,\mathbf{u}}$, $\langle T_{k2}(\mathbf{u}) \rangle_{k,\mathbf{u}}$, $\langle L_k T_{k1}(\mathbf{u}) \rangle_{k,\mathbf{u}}$, and $\langle L_k T_{k2}(\mathbf{u}) \rangle_{k,\mathbf{u}}$. We solve these and find that the solutions have as a common denominator

$16 - \pi\lambda\rho x \langle L_k^2 \rangle_k (8 + \pi\lambda\rho(1-x) \langle L_k^2 \rangle_k)$, which vanishes at the critical number density $\rho_p = ((\sqrt{x} + x) \langle L_k^2 \rangle_k \pi\lambda/4)^{-1}$. This then gives

$$\varphi_p = \frac{D^2 \langle L_k \rangle_k}{(\sqrt{x} + x)\lambda \langle L_k^2 \rangle_k}, \quad (2.20)$$

for the percolation threshold. So, we find a non-trivial dependence of the percolation threshold on the fraction of coated rods x . Again, the larger the fraction of coated rods, the lower the percolation threshold, as is to be expected.

One may ask what would be the percolation threshold of PEDOT:PSS-coated nanotubes that are poor conductors instead of metallic ones – an experiment recently conducted by Hermant and co-workers [27, 107]. In that case the particles may only serve as a scaffold that still allows the conductive material to percolate at very low loadings, so charge transport is then only possible provided two coatings intersect. This case is equivalent to the one we discussed earlier, i.e., mixtures of conducting and non-conducting nanotubes. So Eq. (2.18) also gives the percolation threshold for a system of insulating nanotubes, of which a fraction x has been coated. Comparing Eqs. (2.18) and (2.20) we conclude that there is an additional factor $2x/(\sqrt{x} + x)$ determining the percolation threshold that can be gained by taking conductive instead of insulating rods, which is quite significant if x is not very close to unity. See also Fig. 2.4.

Inspired by the experiments of Hermant, we can now perform a thought experiment to demonstrate this effect. We determine the percolation threshold of high-quality (metallic) single-walled carbon nanotubes, and use a small amount of conductive, penetrable coating material that we presume to fully cover a small fraction of the single-walled carbon nanotubes. If we perform the same experiment on poor-quality (insulating) single-walled carbon nanotubes, then, according to the above observation, the percolation threshold should be more than a factor two lower for a fraction of coated carbon nanotubes that is less than only 10 %. Hence, there should be a considerable difference between using conductive and insulating filler particles, suggesting that for incomplete surface coverage the fillers not only serve as a scaffold.

2.6 Discussion and conclusions

In this chapter we have presented a systematic approach to study the effect of size and connectivity polydispersity on connectedness percolation for a large class of particle dispersions. Using the multi-component pair-connectedness Ornstein-Zernike equation that depends on the properties of pairs of particle, we derived an expression for the average cluster size of connected particles requiring as input only some average of a function that depends on the properties of a *single* (test) particle. By choosing an appropriate closure for this expression, we obtained an analytical expression for the percolation threshold of conductive rod-like particles. It turns out to be a non-trivial function of the distribution of lengths, widths and connectivity ranges, yet depends on a few moments of the full distribution. This implies that for the percolation threshold one only needs to know these moments and the details of the distribution are irrelevant.

If the length and width distributions are uncorrelated, which may be quite a strong assumption considering the sonication step often used in the nanocomposite production process, we deduce that the presence of wider rods raises the percolation threshold and slightly more so than based on the inverse-aspect-ratio dependence of it for monodisperse ones, whilst a length polydispersity significantly lowers the percolation threshold at equal number average for small fractions of longer rods because the percolation threshold scales inversely with the weight average of rod lengths. For a bidisperse system this latter effect is very strong indeed provided the length difference is large and the main component of the mixture consists of short rods. In chapter 3 we will consider more realistic length distributions and show that such a skewed distribution towards short rods is in fact required for a low percolation threshold. A reciprocal weight-average length dependence of the percolation threshold was also found for systems of interpenetrable sticks [93, 94]. For hard rods with $D_\gamma^{\text{eff}} = D_\gamma$ we obtain for the case of monodisperse rod widths,

i.e., $D_\gamma = D$ and $\Delta_\gamma = \Delta$, that the percolation threshold $\varphi_p = D^2/(2\langle L \rangle_w(\Delta - D))$, in agreement with earlier work based on a formal mapping of the cluster size to the osmotic compressibility of the rod fluid [97]. For ideal particles with $D_\gamma^{\text{eff}} = 0$ the percolation threshold in the monodisperse limit reduces to $\varphi_p = D^2/2\Delta L = D/2L$, where by convention we put $\Delta = D$, making D the diameter of the penetrable rod [97]. This is also consistent with earlier findings based on geometric arguments [38, 103] and with computer simulations [108].

The other type of polydispersity we considered in this chapter is that in the way that the particles conduct electricity. For a binary mixture of conductive and non-conductive rods of respective number fractions x and $1 - x$, we find that the size of a cluster of conductive particles diverges at a packing fraction $\varphi_p \approx D^2/2x\lambda\langle L \rangle_w \sim 1/x$. Hence, if, say, one third of the carbon nanotubes is conductive, then the percolation threshold is three times higher than would have been if all of them had been conductive. It does indeed seem sensible, then, to select for high fractions of conductive carbon nanotubes if as low as possible a percolation threshold is required for the envisaged nanocomposite application [26]. Our prediction that the percolation threshold is governed solely by the concentration of conductive nanotubes, i.e., $x\varphi$, might appear counter-intuitive because one would expect that if only contacts between conductive rods contribute to the network, the presence of small numbers of insulating ones should raise the percolation threshold disproportionately. The reasoning is that the presence of a single insulating nanotube in it potentially takes out at least one complete conductive path in a system-spanning network. On the other hand, if this nanotube sits in a dead branch its impact is zero, and it is likely this effect that provides the compensation.

Another way to lower the percolation threshold is to make use of a conductive penetrable (“soft”) coating of the rod-like particles to effectively manipulate the hopping distance. In our model description of this we presume the effective hopping distance to be substantially increased by the coating so that charge transport predominantly occurs via the intersection of either the coating and a particle or of two coatings. We find that a significant reduction of the percolation threshold can be gained by taking conductive instead of insulating particles if the fraction of coated rods is not very large. The conductive polymer latex PEDOT:PSS has been used as the coating material for the carbon nanotubes [27] and it was argued that the contribution of the carbon nanotubes could be neglected because the filler particles merely serve as a template for a percolating PEDOT:PSS network. However, we conclude that if the fraction of the particles without a coating is not negligible, then neither is the conductivity of the carbon nanotubes. If the experiments are performed with insulating particles the mixture is non-additive because charge transport is only possible between two coated particles and charge transport is

blocked by any particle in a pair that has no coating. As a consequence, the percolation threshold is governed solely by the concentration of coated particles.

In fact, our prediction can be understood more quantitatively by considering the simplified case of percolation on a Bethe lattice. This connected cycle-free tree, sprouting z branches per lattice site, can straightforwardly be shown to have a conductivity threshold, defined here in terms of the fraction of sites occupied, of $\varphi_p^c = 1/x(z-1)$, if a fraction x of these particles contributes to the charge transport [16]. We conclude that the absence of loop correlations between particles on a Bethe lattice and ones in free space within the second-virial approximation causes the percolation threshold to scale as $1/x$. This corresponds in fact to a mean-field theory and the question is justified how good a mean-field theory is for describing percolation. As is well-known, for percolation on a lattice the upper critical dimension is 6 [25], and one would perhaps naively infer from it that in continuum space this must be true also. However, for rod-like particles this turns out not the case. Indeed, as is well established, the thermodynamics of rod dispersions are well described by the second-virial approximation in the limit of large aspect ratios [104]. To quantify this connection between continuum percolation of rod-like particles and percolation on a Bethe lattice, we can equate $\varphi_p = 1/(z-1)$ for the Bethe lattice to $\varphi_p = D^2/2\lambda L$ in continuum space in the monodisperse limit, if we presume that fraction of sites occupied can be mapped onto the volume fraction φ . This gives $z = 1 + 2\lambda L/D^2$, which is quite a large number for single-walled carbon nanotubes for which $\lambda \approx D$ and $L \gg D$. We again invoke the analogy between percolation on a Bethe lattice with a large coordination number and percolation of rods in continuum space in chapter 4, where we study the conductivity of a percolating network of rods.

It is instructive to explicitly evaluate the accuracy of the second-virial approximation for connectedness percolation also. For this purpose we consider the following (virial) expansion for the direct pair-connectedness function \hat{C}^+ at zero wave vector, $\hat{C}^+(0) = \hat{C}_2^+(0) + \rho \hat{C}_3^+(0) + \rho^2 \hat{C}_4^+(0) + \dots$, where $\hat{C}_n^+(0)$ denotes the n -body contribution, ρ the number density and angular averages are implied [34,38,118]. We refer to Appendix 2.A for details of the diagrammatic contributions to the first-order correction, stemming in effect from the third virial term. For rod-like particles we find that $\hat{C}_2^+ = \mathcal{O}(\lambda L^2)$ and $\hat{C}_3^+ = \mathcal{O}(\lambda^3 L^3)$, so $\hat{C}_3^+ / (\hat{C}_2^+)^2 = \mathcal{O}(\lambda/L)$. This implies that the impact of the three-body virial is indeed negligibly small because the hopping distance λ is much smaller than the rod length L . A similar argument can be shown to hold for the higher-order terms, which justifies the truncation of the virial expansion after the first term, at least for rod-like particles. In practice, the approximation can be considered to be quantitative, meaning that the third-virial contribution is less than 10 % of that of the second virial, if $\langle L \rangle / \lambda > 100$, with $\langle L \rangle$ the mean length, and semi-quantitative for $\langle L \rangle / \lambda > 20$, in

which case the third-virial and second-virial contribution are comparable [104]. Even the former, more strict condition, quite generally holds for individual carbon nanotubes, i.e., collections of exfoliated carbon nanotubes not dominated by bundles.

The second-virial approximation, also sometimes called the bare chain sum approximation [36] and random-phase approximation [35], is as far as we are aware only accurate for rod-shaped particles, even though our central equations (2.8) and (2.9) of our theory apply to other types of particle as well, including spherical and plate-like nanofillers. The latter may serve as a model for graphene. Unfortunately, for these the second-virial approximation should be expected to break down. Indeed, for both plate-like and spherical particles of diameter D we find that $\hat{C}_2^+ = \mathcal{O}(\lambda D^2)$ and $\hat{C}_3^+ = \mathcal{O}(\lambda D^5)$, both to leading order in λ/D . See also Appendix 2.A. Hence, $\hat{C}_3^+ / (\hat{C}_2^+)^2 = \mathcal{O}(D/\lambda)$, which is much larger than 1 for small hopping distances on the scale of the particle size. This means the virials to all orders in the density should contribute to the percolation threshold for both types of particle. On the other hand, and rather surprisingly, it has been shown by means of Monte Carlo simulations that the second-virial approximation is reasonably accurate for spherical particles too, provided that the hopping distance is small relative to the particle size [36]. It is not clear why this is so but presumably this is caused by mutual cancellation of higher-order virials. It is reasonable to presume that this is also the case for plate-like particles. Indeed, recent calculations show that the topologies of phase diagrams of binary mixtures of hard platelets of different sizes are the same for a second-virial theory and fundamental measure theory [37]. The latter is known to be highly accurate.

Because of this our model may within the second-virial approximation still give qualitative results for plate-like particles, where we repeat that in this approximation of the pair-connectedness function P corrections to all orders in the density are included through linear graphs, i.e., all multi-particle correlations that have no loops in them are taken into account. We calculate \hat{f}^+ for hard polydisperse plate-like particles [13] of thickness L and by following a similar procedure as for the rods, we find for the percolation threshold,

$$\varphi_p = \frac{4 \langle L_k D_\gamma^2 \rangle_{k\gamma} (B - \sqrt{B^2 - C})}{\lambda C}, \quad (2.21)$$

with

$$B = 4(\pi + 5) \langle L_k D_\gamma \rangle_{k\gamma} + (5\pi + 6) \langle D_\gamma^2 \rangle_\gamma + (7\pi + 16)\lambda \langle D_\gamma \rangle_\gamma, \quad (2.22a)$$

$$C = (\pi + 6) \left(-16\pi \langle D_\gamma \rangle_\gamma \langle D_\gamma^3 \rangle_\gamma - (\pi + 6) \langle D_\gamma^4 \rangle_\gamma + (17\pi + 6) \langle D_\gamma^2 \rangle_\gamma^2 \right). \quad (2.22b)$$

Eq. (2.21) holds provided $L, \lambda \ll D$ and provided L and λ are of the same order of magnitude. In the monodisperse limit, it reduces to $\varphi_p = 2L/(\lambda(5\pi + 6))$, which,

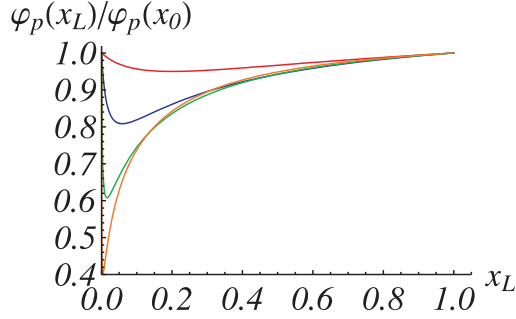


Figure 2.5: The percolation threshold of a binary mixture of large (D_{large}) and small disks (D_{small}) of equal thickness is shown as a function of the mole fraction x_L of large plates relative to its value $\varphi_p(x_0) = 2L/\lambda(5\pi + 6)$ of that of the corresponding monodisperse distribution with equal mean length. The tunneling distance λ is presumed to be a constant and drops out of the equation. From top to bottom: $D_{\text{large}}/D_{\text{small}} = 2, 4, 8,$ and 16 . The ratio of percolation thresholds is lowered substantially by adding a small fraction of large plates to a dispersion of small ones.

interestingly, is independent of the disk diameter D . This may seem surprising but if we again invoke our simple contact-volume argument as we did for the rod-like particles, we obtain a result consistent with it [106]. If we substitute typical values for single-layer graphene, i.e., $L \approx 0.3$ nm and $\lambda \approx 1$ nm [97], we find $\varphi_p \approx 0.03$. This is (considerably) larger than experimental values of $10^{-4} - 10^{-2}$ found in the literature [19, 114, 115], but the discrepancy may partly be explained by polydispersity effects and/or the influence of attractive interactions between them [97]. In spite of the percolation threshold being independent of the diameter in the monodisperse limit, the effect of diameter polydispersity is actually very strong as is shown in Fig. 2.5. Similar to what we found to be the case for bidisperse rods in Fig. 2.3, adding a small quantity of wider sheets to any given collection lowers the percolation threshold and quite considerably so if they are sufficiently large relative to those already present in this collection. The effect wears off with increasing quantities, and our conjecture is that this is because while the small disks can form bridges between the large ones and have a relatively large freedom in their orientations, the large plates have are very restricted in their angular margin due to the excluded-volume interactions. The effect on the percolation threshold of experimentally observed diameter distributions of graphene is discussed in chapter 3.

It appears that any kind of size bidispersity can have a large influence on the percolation threshold of a composite. To see if *shape* polydispersity has a similar impact, we also computed the percolation threshold for a mixture of rod-like and plate-like particles to model a mixture of carbon nanotubes and graphene sheets. See also Fig. 2.6. For

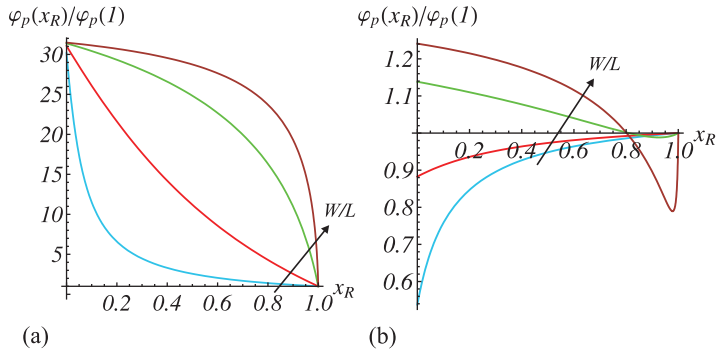


Figure 2.6: For a bidisperse mixture of plates with diameter W and thickness T and rods with length L and diameter D , the percolation threshold φ_p relative to its value of that of the corresponding monodisperse case consisting of only rods is shown as a function of the mole fraction x_R or rods. The arrows indicate increasing values of W/L : 0.1, 0.3, 1 and 3. (a) For typical values for graphene and carbon nanotubes, $L/T = 1500$, $L/\lambda = L/D = 500$, where λ is the hopping distance, a mixture with only rods gives the lowest percolation threshold. For sufficiently large rod aspect ratios L/D , the shape of the curves is almost insensitive to changes in L/T and L/λ , which only change the vertical scale. (b) For rods with a smaller L/D , a mixture with plates can have a lower percolation threshold than the one for only rods, as shown for $L/T = 60$, $L/\lambda = L/D = 15$.

this we used the connectedness Mayer function \hat{f}^+ for the interactions between two rods and two plates as derived before, and computed that of the rod-plate interaction. If we solve Eq. (2.9), we find that for thin rods (say, single-walled carbon nanotubes) the lowest percolation threshold is obtained in a dispersion of only rods but for thicker rods (multi-walled carbon nanotubes), adding a few plates becomes increasingly favourable albeit that the effect is modest. However, it must be noted that we presumed the rods and plates to exhibit cooperative connectivity behaviour, i.e., the hopping distance between a rod and a plate equals that between two rods and between two plates, and this may be a somewhat tenuous supposition [116].

2.A Second-virial approximation

In order to assess the accuracy of the second-virial approximation for several particle shapes, we aim to compute the relative magnitude of the first and second term in the density expansion of the Fourier transform of the direct pair-connectedness function at zero wave vector $\hat{C}^+(0)$, $\hat{C}^+(0) = \hat{C}_2^+(0) + \rho \hat{C}_3^+(0) + \dots$. Here, \hat{C}_2^+ and \hat{C}_3^+ are the two-body and three-body direct-connectedness functions, and we omit the arguments \mathbf{u} and \mathbf{u}' for notational convenience. In order to compare the third virial term with

the second, we note that for the critical number density of particles at the percolation threshold ρ_p we have $\rho_p \langle \hat{C}^+(0) \rangle_{\mathbf{u}, \mathbf{u}'} \approx 1$ [34, 38]. If we truncate the virial expansion after \hat{C}_3^+ , we have $\rho_p \hat{C}_2^+(0) + \rho_p^2 \hat{C}_3^+(0) = 1$. This gives

$$\rho_p \langle \hat{C}_2^+(0) \rangle_{\mathbf{u}, \mathbf{u}'} \left(1 + \rho_p \frac{\langle \hat{C}_3^+(0) \rangle_{\mathbf{u}, \mathbf{u}'}}{\langle \hat{C}_2^+(0) \rangle_{\mathbf{u}, \mathbf{u}'}} \right) = 1, \quad (2.23)$$

so the second-virial approximation is valid if $\langle \hat{C}_3^+(0) \rangle_{\mathbf{u}, \mathbf{u}'} / \langle \hat{C}_2^+(0) \rangle_{\mathbf{u}, \mathbf{u}'}^2 \ll 1$. To evaluate $\hat{C}_3^+(0)$, we follow the approach introduced by Coniglio and co-workers [34]. According to their definition, $C_n^+(\mathbf{r}, \mathbf{r}', \mathbf{u}, \mathbf{u}')$ contains all graphs (diagrams) consisting of n points in a diagrammatic expansion with at least one continuous path of f^+ bonds between the two particles at \mathbf{r} and \mathbf{r}' , so they are part of the same cluster and interact via a potential u^+ . Particles that are not directly connected within the same cluster are said to be “connected” by an f^* bond and interact via the potential u^* . This bond is defined as $f^* \equiv \exp(-\beta u^*) - 1$, such that $f \equiv f^+ + f^*$ is the Mayer function with $\exp(-\beta u^+) + \exp(-\beta u^*) = \exp(-\beta u) = f + 1$ [117]. We consider hard particles in the cherry-pit model, so $f^+ = 1$ for $D < r < \Delta$ and $f^+ = 0$ otherwise, with r the distance between the particles, so it is nonzero only if two particles are connected, i.e., if their connectedness zones overlap. For f^* we have $f^* = -1$ for $r < \Delta$ and $f^* = 0$ for $r > \Delta$, meaning that f^* is nonzero if the particles either intersect or if they are connected. Furthermore $f = f^+ + f^*$, which equals -1 for $r < D$, i.e., if two particles intersect, and zero otherwise.

For the second virial coefficient \hat{C}_2^+ , the diagrams consist only of the points 1 and 2, so only the one with an f^+ bond between these points meets the criterion and $\hat{C}_2^+(0, \mathbf{u}, \mathbf{u}') = \int d\mathbf{r}_{12} f^+(\mathbf{r}_{12})$, with $\mathbf{r}_{12} = \mathbf{r}_2 - \mathbf{r}_1$, which is the contact volume for particles that can be obtained from the excluded volume for cylindrical particles of length L and diameter D [13]. In the case of rod-like particles in an additive system this gives Eq. (2.11), so $\hat{C}_2^+(0, \mathbf{u}, \mathbf{u}') = 2L^2\lambda|\sin\gamma|$ for a constant rod length L and hopping distance λ and where γ is the angle between the orientations \mathbf{u} and \mathbf{u}' . For plate-like particles the excluded volume gives to leading order for large aspect ratios $\hat{C}_2^+(0, \mathbf{u}, \mathbf{u}') = \frac{3}{2}\pi D^2\lambda|\sin\gamma|$, with D the disk diameter.

For the third virial coefficient we can form five diagrams, shown in Fig. 2.7, that meet Coniglio’s criterion [118], which then gives,

$$\begin{aligned} \hat{C}_3^+(0, \mathbf{u}, \mathbf{u}') = & \iint d\mathbf{r}_{12} d\mathbf{r}_{13} (f_{12}^+ f_{13}^+ f_{23}^+ + f_{12}^+ f_{13}^+ f_{23}^* + f_{12}^+ \\ & f_{13}^* f_{23}^+ + f_{12}^* f_{13}^+ f_{23}^+ + f_{12}^+ f_{13}^* f_{23}^*). \end{aligned} \quad (2.24)$$

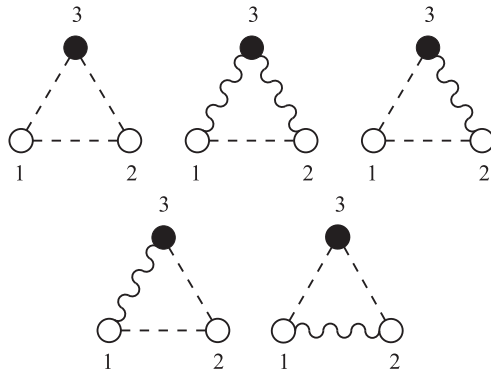


Figure 2.7: Five diagrams consisting of three points can be formed such that point 1 and 2 are connected via a continuous path of f^+ bonds (dashed lines), where the wavy lines represent f^* bonds. This path between 1 and 2 can be either direct, as in the top three and the bottom left diagram, or via a third particle, shown by the bottom right diagram. These diagrams give rise to the five terms in the expression (2.24) for $\hat{C}_3^+(0, \mathbf{u}, \mathbf{u}')$.

To compute this integral we note that $f^* = -1$ if the two particles either intersect or if they are connected, which can be subdivided into the intersection ($f = -1$) and the connection ($f = +1$). We can thus replace f^+ by c and f^* by $s - c$, where c and s indicate a configuration where two particles are connected and intersect, respectively. We then find $\hat{C}_3^+(0, \mathbf{u}, \mathbf{u}') = -c^3 + c^2s + cs^2$, so we have to compute the “volume” of a configuration where the three particles are mutually connected, one where two contacts are connections in the overlap zone and the third is an intersection, and one with two intersections and one connection.

For rod-like particles we obtain the following estimate for the order of magnitude of the different terms. The configuration in which the three particles are mutually connected gives λL^2 for the first contact between two rods, ignoring a constant of the order unity. The third rod needs to be connected to both other rods, which gives an additional volume proportional to λL^2 it can occupy but it has only a very small angle of the order λ/L that it can move, which then gives $\lambda^3 L^3$ in total. The second and third term $cs(s + c)$ can be combined by starting again with two connected rods, giving λL^2 for the c . The third particle then has to intersect one of the first two (a factor D from the s), it has to intersect or make contact with the other (a factor $D + \lambda$ from the $s + d$), and then has a freedom L in the third direction. So we find for this contribution $\lambda D(D + \lambda)L^3$. For single-walled carbon nanotubes D is probably larger than λ and for multi-walled carbon nanotubes it is much larger, so the third virial term is of the order

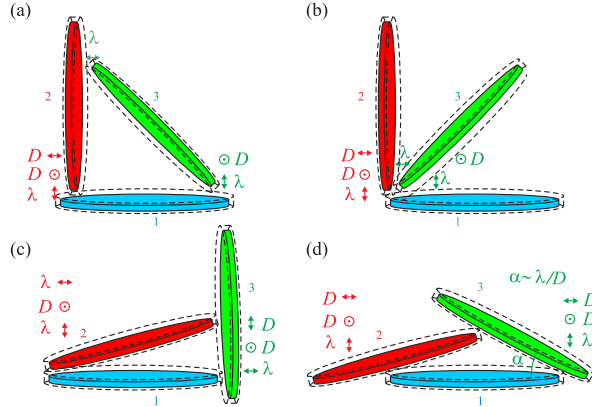


Figure 2.8: Possible configurations of three disks that are mutually connected and that contribute to the three-body direct-connectedness function $\hat{C}_3^+(0)$. The disks have diameter D and the tunneling distance between them is $\lambda \ll D$. If we fix disk 1 and if the difference between the orientations of disk 1 and 2 are almost perpendicular to each other, the overlap criterion is met in a triangle (a) or a branched configuration (b). If this difference is very small, on the other hand, we distinguish between almost complete (c) and limited overlap (d) between particles 1 and 2. In the latter case the angle α that disk 2 and 3 make is of the order λ/D . λ and D denote the ranges of motion in three directions for the disk 2 so that it is connected to disk 1 and for the disk 3 so that it connects to 1 and 2. In all cases we find $\hat{C}_3^+(0) = \mathcal{O}(\lambda^3 D^3)$.

$\lambda D^2 L^3$. Its relative magnitude is then $\lambda D^2 L^3 / (\lambda L^2)^2 = D^2 / \lambda L \ll 1$ because $L \ll D$, and the second-virial approximation is accurate for rod-like particles.

For plate-like particles the situation turns out to be quite different. From a similar argument as that for the rods we find that the c^3 term gives a contribution to \hat{C}_3^+ is of the order $\lambda^3 D^3$, where D now denotes the disk diameter. The way this estimate is obtained is explained in Fig. 2.8. We again take the terms $c^2 s$ and $c s^2$ together, so the two connected plates give λD^2 for the c . The third particle then intersects the first, giving a D , is either connected to the second or intersects it, giving a $D + \lambda$, and has the freedom to move a distance D in the third direction. Hence, for these terms we find a contribution $\lambda(D + \lambda)D^4 \approx \lambda D^5$, which is much larger than the first term from the three mutually connected disks. Compared to the second virial term its magnitude is $\lambda D^5 / (\lambda D^2)^2 = D / \lambda$, which is much larger than unity and would make the truncation of the virial expansion of \hat{C}^+ after the first term unjustified. The scaling for spherical particles gives similar results for \hat{C}_2^+ and \hat{C}_3^+ , where D then denotes the sphere diameter. So for spheres the second-virial approximation would not be suitable either, but it turns out not to be very inaccurate if $\lambda \ll D$, [36] possibly because of cancellation of higher-order virials.

Connectedness percolation of polydisperse nanofillers: applications

3

In this chapter we apply our generalised connectedness percolation theory that we presented in chapter 2 to realistic size distributions for carbon nanotubes and graphene sheets. We show that if the size distribution function of rod-like particles factorises, a length distribution that is strongly skewed to shorter lengths is a requirement for a low threshold relative to the monodisperse one with the same average length and diameter. However, the effect of such realistic size distributions seems not to be strong enough to fully explain the large scatter in observed percolation thresholds of dispersions with approximately the same mean aspect ratio [101]. We show that this may be caused by a coupling of the length and diameter distribution, because this leads to completely different results. Indeed, if the lengths and diameters of the particles are linearly correlated, polydispersity raises the percolation threshold and more so for a distribution skewed towards smaller lengths. Our predictions for the percolation threshold of graphene sheets are applied to distributions that have been experimentally determined by means of dynamic light scattering and the results explain qualitatively the discrepancies in the percolation thresholds of four different dispersions.[†]

[†]The contents of this chapter are based on the following publications:
R. H. J. Otten and P. van der Schoot, *J. Chem. Phys.* **134**, 094902 (2011),
E. Tkalya, M. Ghislandi, R. H. J. Otten, M. Lotya, A. Alekseev, P. van der Schoot, J. Coleman, and C. E. Koning, *Influence of dispersion state of graphene on percolation threshold of conductive graphene/polymer nanocomposites*, submitted.

3.1 Introduction

In chapter 2 we have discussed how rod-like and plate-like particles, such as carbon nanotubes and graphene, after solidification can significantly improve the mechanical, thermal, and electrical properties of the host material they have been dispersed in by forming system-spanning networks at very low particle loadings. We showed how the percolation threshold of rod-like and plate-like particles depends sensitively on polydispersity in their linear dimensions and connectivity ranges. This we demonstrated by considering the idealised case of a bidisperse distribution of either large and small or conductive and non-conductive species, and we found that a distribution that is strongly skewed towards smaller lengths/diameters provides the lowest percolation threshold. In this chapter we consider more realistic size distributions for carbon nanotubes and graphene platelets that follow from experimental observations and determine the impact on the percolation threshold. The graphene distributions have been determined from experiments using dynamic light scattering for four dispersions with different preparation routes. Our findings may be summarised as follows.

1. If we assume that all carbon nanotubes are conductive and that the length and width distributions are independent of each other, then a length distribution that is strongly skewed towards shorter lengths produces the lowest percolation threshold for a fixed mean length. In fact, such a large skewness is a requirement for a large decrease in the percolation threshold relative to the equivalent monodisperse one.
2. If the length and width distributions are coupled, which may be the case because of a sonication step, or, e.g., of a screw-milling procedure in the production process, then neither the length nor the aspect ratio is the determining factor for a low percolation threshold. If this correlation between the length and diameter distribution is linear, the situation is completely the opposite of that of uncorrelated lengths and breadths: polydispersity raises the percolation threshold and very strongly so for a relatively small number of long rods.
3. The model provides a slightly too high prediction for three of the four graphene dispersions under consideration, but the trend in the percolation thresholds agrees with the measured percolation thresholds. For these predictions the thickness of the graphene sheets has to be estimated, and the dispersion with the best theoretical prediction for the experimental percolation threshold presumably has the most accurate fit for the thickness.

In the remainder of this chapter we first show in section 3.2 the effect of realistic length distribution functions on the percolation threshold. We next apply our model

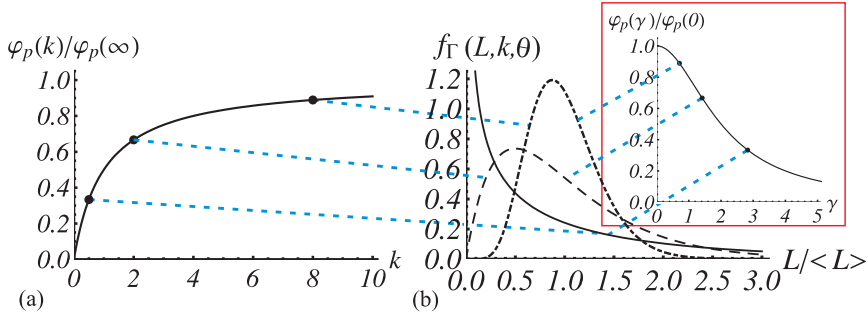


Figure 3.1: (a) The influence of length polydispersity on the ratio of the percolation thresholds of the Gamma distribution and that of the corresponding monodisperse distribution with equal mean length, $\varphi_p(k)/\varphi_p(\infty) = k/(k+1)$. The tunneling length λ is taken as a constant and in that case drops out of the equation. The ratio $\varphi_p(k)/\varphi_p(\infty)$ depends only on the shape parameter k , which is infinitely large for a monodisperse distribution. (b) For $k = 1/2, 2$, and 8 from (a) the distributions are shown for $\varphi_p(k)/\varphi_p(\infty) = 1/3$ (solid), $2/3$ (dashed), and $8/9$ (dash-dotted). Inset: the impact of the length polydispersity as a function of the skewness $\gamma = 2/\sqrt{k}$ of the distribution. The three points marked on the graph correspond to the three distributions.

from chapter 2 to the experimentally determined size distributions of graphene sheets in section 3.3. Finally, we discuss our results and draw our conclusions in section 3.4.

3.2 Realistic carbon-nanotube distributions

In this section we consider more realistic size distributions of carbon nanotubes than the bivalent and tetravalent ones discussed in chapter 2, and for these we compute the effect that they have on the percolation threshold. Because of a lack of experimental data on the covariance of the length and width distributions, we first consider independent distributions; coupled distributions are discussed further on in this section. We showed in chapter 2 that a width polydispersity in practice raises the percolation threshold only marginally, so we take constant carbon-nanotube diameters and we focus on length polydispersity. The experimental determination of the size distribution is difficult, e.g., with electron microscopy it is hard to obtain reliable statistics. Based on the few available experimental measurements of the length distribution of carbon nanotubes we choose a Gamma distribution and the related Weibull distribution [119–122]. A limiting case of both of these distributions is the exponential distribution with a probability density function $f_e(L, \eta) = \eta \exp(-\eta L)$ that has also been measured [123, 124]. If we compute the percolation threshold relative to its value of that of the monodisperse case with the same average length, as was done in chapter 2, we have $\varphi_p(\eta)/\varphi_p(\eta_0) = 1/2$, with

$\eta_0 = \eta/2$, irrespective of the value of the distribution parameter η that takes the form of the inverse mean length [125]. So, an exponential distribution reduces the percolation threshold by a factor two (relative to the equivalent monodisperse case). Parenthetically we note that the exponential distribution is characterised by a single independent moment only.

The Gamma distribution is described by *two* independent moments and obeys a probability density function of the form $f_\Gamma(L, k, \theta) = L^{k-1} \exp(-L/\theta) \theta^{-k} / \Gamma(k)$, with $\Gamma(k)$ the Gamma function [125]. Its first few moments are $\langle L_i \rangle_i = k\theta$, $\langle L_i^2 \rangle_i = k(k+1)\theta^2$, $\langle L_i^3 \rangle_i = k(k+1)(k+2)\theta^3$, where i is a dummy index. The scale parameter θ leaves the shape invariant and only rescales the distribution; k is the shape parameter and for smaller values the spread in the distribution increases because the scaled variance $s \equiv \text{Var}(L_i) / \langle L_i \rangle_i^2$ that was introduced in chapter 2, obeys $s = 1/k$. The monodisperse limit corresponds to $k \rightarrow \infty$, whereas for smaller values of k the distribution becomes more skewed towards smaller lengths. The skewness γ is usually defined as $\gamma \equiv \langle (L_i - \langle L_i \rangle_i)^3 \rangle_i / \langle (L_i - \langle L_i \rangle_i)^2 \rangle_i^{3/2}$ [125], implying that there are many more short carbon nanotubes than long ones for a large positive skewness and *vice versa* for a large negative one. For the Gamma distribution the skewness and shape parameter are related via $\gamma = 2/\sqrt{k} > 0$, which goes to zero for a large value of k . From Eq. (2.15) with $m = 0$ for monodisperse widths and $s = 1/k$, we find that $\varphi_p(k)/\varphi_p(\infty) = k/(k+1)$, which becomes very small for a small k , or, equivalently, a large positive skewness. The results are shown in Fig. 3.1. Given that we consider the distributions at equal first moment $\langle L_i \rangle_i$ and that we have only two independent moments, $\varphi_p(k)/\varphi_p(\infty)$ can also be expressed in terms of the relative magnitude s of the variance because $s = 1/k$ and $\gamma = 2\sqrt{s}$. This agrees with the earlier result, Eq. (2.15), so $\varphi_p(s)/\varphi_p(0) = 1/(s+1)$, and shows that a large value of s is accompanied by a large skewness for this distribution.

The Weibull distribution is defined by the probability density function $f_W(L, a, b) = a b L^{b-1} \exp(-aL^b)$, with $a > 0$ the scale parameter and $b > 0$ the shape parameter. The distribution has as its first moments $\langle L_i \rangle_i = \Gamma(1/b)/(b a^{1/b})$, $\langle L_i^2 \rangle_i = \Gamma(1 + 2/b)/a^{2/b}$, $\langle L_i^3 \rangle_i = \Gamma(1 + 3/b)/a^{3/b}$. The parameter a has no effect on the skewness γ nor on the scaled variance or spread $s = -1 + 2b \Gamma(2/b) / \Gamma(1/b)^2$. The skewness is a complicated expression of Gamma functions and can become negative, unlike that of the Gamma distribution. The monodisperse limit corresponds to a vanishing spread s , which occurs in the limit of $b \rightarrow \infty$, in which case γ converges to the finite value $-12\sqrt{6} \zeta(3) / \pi^3 \approx -1.14$, with ζ the Riemann Zeta function [126].[†] The ratio of the percolation thresholds

[†]The skewness $\gamma \equiv \langle (L_i - \langle L_i \rangle_i)^3 \rangle_i / \langle (L_i - \langle L_i \rangle_i)^2 \rangle_i^{3/2}$ need not go to zero in the monodisperse limit, because both the numerator and the denominator go to zero and the speed of convergence of both determines the monodisperse value of γ .

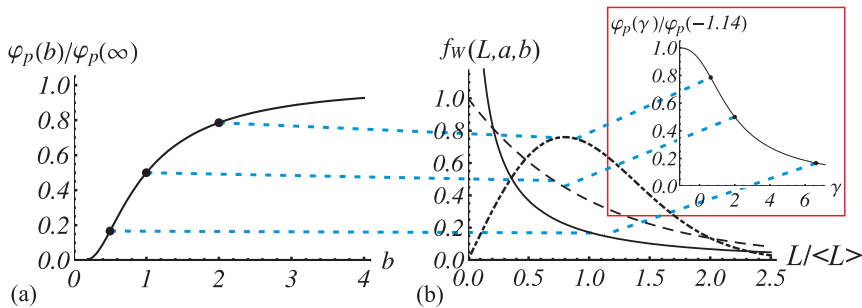


Figure 3.2: (a) For a Weibull distribution the effect of length polydispersity on the ratio of the percolation thresholds of the Weibull distribution and that of the corresponding monodisperse distribution with equal mean length, $\varphi_p(b)/\varphi_p(\infty) = \Gamma(1+1/b)^2/\Gamma(1+2/b)$ with Γ the Gamma function [125]. The tunneling length λ is taken as a constant and in that case drops out of the equation. The ratio depends only on the shape parameter b . The scaled variance s goes to zero in the monodisperse limit that $b \rightarrow \infty$, in which case the skewness $\gamma \rightarrow -1.14$. (b) Three distributions are shown for $b = 1/2, 1$, and 2 , for which $\varphi_p(k)/\varphi_p(\infty) = 0.17$ (solid), 0.5 (dashed), and 0.79 (dash-dotted). Inset: the impact of polydispersity as a function of γ . The three points marked on the graph correspond to the three distributions.

again only depends on the shape parameter via $\varphi_p(b)/\varphi_p(\infty) = \Gamma(1+1/b)^2/\Gamma(1+2/b)$. We have plotted this function in Fig. 3.2, and we again observe that for the polydisperse and equivalent monodisperse cases this ratio decreases for increasing skewness, which also implies an increase of the variance, just as is the case for the Gamma distribution.

In conclusion, we find from Figs. 3.1 and 3.2 that for both the Gamma and the Weibull distributions the non-linearity in the reduction and hence also the absolute reduction of the percolation threshold can be significant, and that a length polydispersity can substantially lower the percolation threshold at equal number-average length. For this to be the case, the distributions need to have a large positive skewness γ (larger than, say, 2), or, equivalently, a large scaled variance s . Clearly, this coupling between the skewness and the spread is not necessarily present for a distribution with more than two independent moments but in the discussion below we show that a large value of s does in fact imply a large skewness, and that a large variance without any skewness is not sufficient to obtain a low percolation threshold. In any event, for those few carbon nanotube systems for which the moments of the length distributions have actually been determined, the skewness and spread seem to be quite small, i.e., $\gamma = 0.40$ and $s = 0.20$, giving $\varphi_p(x)/\varphi_p(x_0) = 0.84$ [120], or $\varphi_p(x)/\varphi_p(x_0) = 0.64$ [127], or $\varphi_p(x)/\varphi_p(x_0) = 0.50$ for an exponential distribution [123, 124], so for these the effect of polydispersity is modest. In view of the very large scatter in measured percolation thresholds of carbon-nanotube composites that we here presume to be caused by polydispersity [101], we

conclude that the skewness in the distributions must usually in fact be much larger than this. In support of this conjecture, we note that it is quite plausible that the sonication of the carbon nanotubes, a necessary exfoliation step in the production process of the nanocomposite, pushes the distribution of carbon nanotubes to become very skewed towards the direction of the shorter rods [26,27]. Indeed, exfoliation goes hand-in-hand with tube scission, and long tubes break more easily than short ones [128]. In fact, wide tubes break less easily than narrow ones, casting doubt on the assumption of independent length and width distributions that we presumed so far. This turns out to be a crucial insight and implies that the length and diameter distributions must be positively correlated.

We saw above that in order to obtain a low percolation threshold, all rods should be thin and the length distribution must have a large positive skewness, so it must decay rapidly with the rod length. However, if the length and width distributions have a positive correlation, then the consequences of such a length distribution are completely different. To estimate the level of correlation, one could argue that the probability of breaking a rod in two is proportional to the required scission energy under sonication, which in turn scales with the area of the cross section of, e.g., multi-walled carbon nanotubes at least if they are sufficiently wide. We recall that multi-walled carbon nanotubes tend to have a broad spread in widths. But if $L_i = \alpha D_\gamma^2$, with α a positive constant, then there would be *no* dependence of the percolation threshold on the size distributions at all because according to Eq. (2.14) the percolation threshold then becomes equal to $\varphi_p = (2\alpha\lambda)^{-1}$, that is, if we presume the tunneling range λ to be constant. (This is by no means certain of course.)

Single-walled carbon nanotubes also exhibit a diameter variation [119,129] and for these the scission energy, which is proportional to the number of bonds that have to be broken, presumably scales linearly with the diameter. If $D_\gamma = \alpha L_i$, we find that $\varphi_p(x) = \alpha^2 \langle L_i^3 \rangle_i / 2\lambda \langle L_i^2 \rangle_i$ and $\varphi_p(x_0) = \alpha^2 \langle L_i \rangle_i / 2\lambda$, so $\varphi_p(x) / \varphi_p(x_0) = \langle L_i^3 \rangle_i / (\langle L_i \rangle_i \langle L_i^2 \rangle_i)$. If we evaluate this for a Gamma, a Weibull and an exponential distribution, we find that the competition between a desired large length and small diameter causes the percolation threshold to be *raised* by polydispersity, not decreased, so the percolation threshold is in that case always higher than that of the corresponding monodisperse distribution, see Fig. 3.3. The effect becomes stronger for smaller values of b and k , i.e., a larger positive skewness and lower spread in the distribution. This result is exactly the opposite of what we obtained for uncorrelated distributions.

In conclusion, we find that the level of correlation between the length and width distributions of rod-like particles is indeed crucial for the dependence of the percolation threshold upon the polydispersity. Depending on the type of coupling, polydispersity

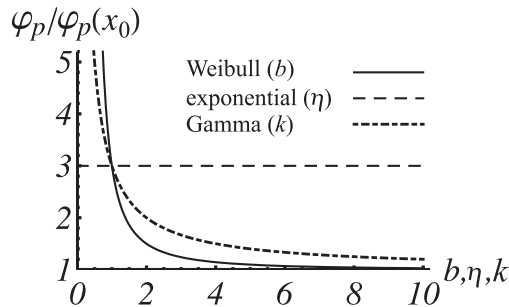


Figure 3.3: The percolation threshold φ_p for a polydisperse distribution relative to its value $\varphi_p(x_0)$ for the corresponding monodisperse case with the same mean length and diameter is shown for a length and diameter distribution that are linearly correlated, i.e., $L_i = \alpha D_i$, with α a constant. For a constant tunneling length λ , polydispersity *raises* the percolation threshold for the Weibull, Gamma and exponential distribution, and most predominantly for small values of the shape parameter b and k of the Weibull and Gamma distribution, meaning a large skewness and large spread. For the exponential distribution the percolation threshold is raised by a factor 3, regardless of the shape parameter η that equals the reciprocal of the mean value of the distribution.

effects may either raise or lower the percolation threshold relative to that of the monodisperse case. We next focus on the applications of our model to experimentally determined diameter distributions of graphene.

3.3 Graphene size distributions

Our model can be applied to any graphene size distribution, as given by Eq. (2.21) from chapter 2, as long as the relevant moments of the distribution are known. In this section we consider four graphene composites with different preparation routes as produced by Tkalya and co-workers [130] and consequently, different size distributions, to determine the effect of size polydispersity. Dispersions A, A-LC (LC being an abbreviation of “low concentration”) and B were prepared out of graphene, preliminary produced by thermal reduction of graphite oxide [131]. Dispersions A and B were prepared under similar conditions, meaning that the same energy was provided per graphene weight unit to both systems during the sonication process (Table 1). The difference between those two relates to the graphene and surfactant concentrations; 1 mg/ml, 1:1 weight ratio graphene/sodium cholate and 0.1 mg/ml, 1:1 weight ratio graphene/sodium cholate for dispersion A and for dispersion B, respectively, meaning that dispersion B was exposed

to a ten times larger amount of energy per graphene flake than dispersion A. Dispersion A-LC with a graphene concentration 0.1 mg/ml and a ratio graphene/sodium cholate 1:1 was exposed to a ten times lower amount of energy than dispersions A and B. This implies that the absorbed amount of energy per graphene unit was the same as in the case of sample A and ten times less than for sample B. Graphene for dispersion C did not have to be sonicated additionally, since it had been obtained in the form of a stable aqueous solution after 100 hours sonication of graphite of concentration 5 mg/ml in 0.1 mg/ml solution of sodium cholate, followed by centrifugation, resulting in a final concentration of graphene of 0.1 mg/ml [132]. The experimental details can be found in [130].

In order to obtain a rough indication of the size distributions in the exfoliated aqueous dispersions of graphene/sodium cholate, dynamic-light-scattering measurements were performed. The graphene platelets can be quite accurately described as two two-dimensional objects, so the data obtained from dynamic-light-scattering measurements are not the real dimensions of the platelets but rather the effective hydrodynamic diameter of an equivalent sphere described by tumbling platelets [133]. From the dynamic-light-scattering measurements the dispersions turned out to have quite some variation in their size distributions, with a difference in the average values as well as a difference in the thickness of the tail of the distribution for large sheets. See Fig. 3.4. In order to rationalise these experimental observations we attempt to assess whether the difference in the percolation thresholds could be explained by the variations in the size distributions. For this we make use of Eq. (2.21).

To determine the required moments of the distribution, we presume the thickness of the graphene sheets to be a constant and, hence, the diameter and thickness distribution to be independent. This may be a tenuous approximation because one might expect that in the sonication process the probability of a thinner sheet to break up into smaller ones to be larger than that of a thicker one. However, due to a lack of experimental information, we for simplicity invoke this approximation that should allow us to assess whether the discrepancies in the observed percolation thresholds are caused by a polydispersity in the diameters. Given the distributions of the diameters, there are two tuneable parameters in the model: the sheet thickness L and the hopping distance λ , which is the largest separation between two particles that still allows a charge carrier to hop from one graphene sheet to the other. We take $L = 0.3$ nm as a typical value and in view of the sensitive dependence of the model on λ and the fact that its exact value is not known accurately, we take three sensible values for λ to fit the data: $\lambda = 0.9, 1.2$ and 1.5 nm [97]. The volume fractions φ_p we find are then converted into weight fractions using a conversion factor of 2, because the density of graphene is twice that of the polymer.

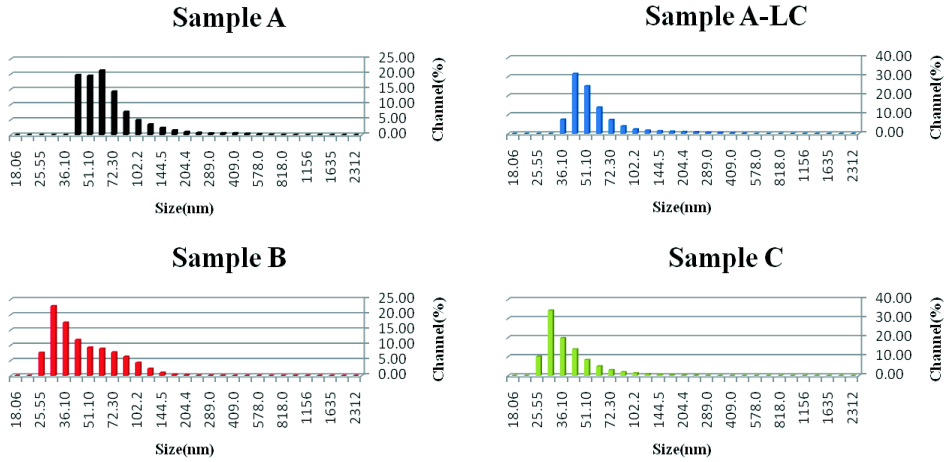


Figure 3.4: The diameter distributions that follow from the dynamic-light-scattering measurements of the four graphene nanocomposites under consideration.

The results are shown in Table 3.1.

Table 3.1: Experimentally determined percolation thresholds for polystyrene/graphene nanocomposites based on the four aqueous graphene dispersions A, A-LC, B and C using sodium cholate as a surfactant and the corresponding theoretical predictions for different values of the hopping distance λ .

dispersion	A (wt %)	B (wt %)	A-LC (wt %)	C (wt %)
experiment	2.0	3.0	2.3	4.5
theory ($\lambda = 0.9$ nm)	3.4	4.9	4.3	4.6
theory ($\lambda = 1.2$ nm)	2.6	3.7	3.2	3.4
theory ($\lambda = 1.5$ nm)	2.0	2.9	2.5	2.7

The agreement between theory and experiment is remarkably good, considering the crudeness of the model. Indeed, for all three values of the hopping distance λ , the trends fully agree. For $\lambda = 1.5$ nm the numerical agreement between theory and experiment is almost perfect for composites A, B, and A-LC, but this value underestimates the experimental value of composite C. For $\lambda = 0.9$ nm nanocomposite C exhibits the best numerical agreement, but for the same λ the other three theoretical values are significantly larger than the corresponding experimental ones. Hence, $\lambda = 0.9$ nm and $\lambda = 1.5$ nm give a lower and upper bound on the hopping distance, whereas the value $\lambda = 1.2$ nm provides a compromise that fits all four systems reasonably well. As already alluded to, we use three values of the hopping distance because its value is not known

accurately, but the lower and upper bound $\lambda = 0.9$ and $\lambda = 1.5$ nm we find are in agreement with the estimate of $\lambda = 1$ nm used in chapter 2 [97]. The thickness of the graphene is not used as a fitting parameter, but it is kept at a constant value $L = 0.3$ nm. However, nanocomposite C shows the highest UV absorbance and therefore has the highest degree of exfoliation [130]. This means that the sheets in dispersion C are presumably thinner than those in the other three dispersions and that $L = 0.3$ nm is quite accurate for dispersion C but it may be too low a value for the other three systems, i.e., the sheets of the other three may consist of a few layers of graphene and are not actually graphene but graphite platelets. However, a larger value of the thickness L as a fit parameter would only raise the theoretically predicted values and make the discrepancy larger for any value of the hopping distance λ . An interesting point to note here is that the graphene sheets are modelled as flat disks in the model, which obviously is not the case in practice. Indeed, if the sheets in aqueous graphene dispersion C are thinner than those in the other three dispersions because of the higher degree of exfoliation, their effective diameter as observed in the dynamic-light-scattering measurements should be smaller, which in fact is the case. The diameter in the model then represents this effective sheet diameter, which leads to a good agreement between experiment and theory for the polystyrene/graphene nanocomposite based on this dispersion.

Again, one could argue that even though the theoretical values of the percolation thresholds for the nanocomposites based on dispersions A, B and A-LC are too high for $\lambda = 1.2$ and $\lambda = 1.5$ nm and would be even higher with a larger thickness as indicated above, the trend in them agrees with that in the experimental values. This means that there could be a systematic deviation in the theoretical predictions, which could, e.g., be due to attractive van der Waals interactions that are not accounted for in the model, and that have been shown to lower the percolation threshold of carbon nanotubes in a polystyrene matrix considerably [97]. Here, it must be noted that the attraction should not be too large because that would lead to stacking of sheets (or bundling of nanotubes), which would raise the percolation threshold of the polystyrene/graphene nanocomposite. So, if the effect of such a systematic deviation in nanocomposites A, A-LC and B is the same, then we could argue that the differences between their percolation thresholds are indeed related to the polydispersities of their sheet diameters.

3.4 Discussion and conclusions

In this chapter we have applied the results from chapter 2 to physically more realistic size distributions of carbon nanotubes and graphene sheets than the binary dispersions from chapter 2 that served as an example to demonstrate the potentially huge impact

of polydispersity on the percolation threshold. We find that the inverse-aspect-ratio scaling of the percolation threshold, although often assumed, only holds if the length and width distributions are uncorrelated, which, as pointed out before, may be quite a strong assumption considering the sonication step often applied in nanocomposite production processes. If the length and width distributions are indeed uncorrelated, we deduce for a binary system that a distribution that is strongly skewed towards the short rods produces the lowest percolation threshold relative to that of the monodisperse one with the same average length. For the plausibly more realistic length distributions such as the Gamma and Weibull distributions, we also find a large decrease in the percolation threshold, again only if the distribution is strongly skewed towards shorter lengths.

This may seem somewhat surprising because $\varphi_p(x)/\varphi_p(x_0) = 1/(s+1)$, with $s \equiv \text{Var}(L_i)/\langle L_i \rangle^2$, depends only on the ratio of the variance and the mean of the rod lengths. However, it so happens that a large positive skewness γ is a necessary condition for a significant decrease of the percolation threshold, and that a large variance is not sufficient to obtain a large value of the parameter s that is required for such a decrease. The reason is that a standard deviation of a positive stochastic variable cannot be large compared to the mean value unless the distribution is strongly skewed. This we cannot prove conclusively from our results for the Gamma and Weibull distributions because these distributions have only two independent moments. For these distributions only one moment can be varied independently, and for a fixed average length a large positive skewness goes hand in hand with a large value of s . On the other hand, for symmetric distributions, so without any skewness, we can show that the one with the largest value of s , which is a bidisperse mixture, has a *maximum* value of $s = 1$. We refer to Appendix 3.A for details. This means that the largest decrease of the percolation threshold as a result of a symmetric length distribution is a factor two.

From the bidisperse mixture in Fig. 2.3 in chapter 2 we have seen that a considerably larger reduction of the percolation threshold can be obtained by taking a distribution that is strongly skewed. Also, from our results for the skewed Gamma and Weibull distributions it follows that polydispersity can cause the percolation threshold to decrease much more than this factor of two. It is for these reasons that a large positive skewness in the length distribution is a requirement for a significant decrease in the percolation threshold. Still, for the realistic distributions with a large skewness we studied, the effect of length polydispersity appears not to be strong enough to explain the scatter of multiple orders of magnitude in observed percolation thresholds of carbon nanotubes with the same average dimensions [101]. We speculate that the few size distributions available in the literature [110, 111, 119–124] are not representative for the actual ones encountered in practice. Although it remains a speculation, we feel it is plausible because

sonication and in some cases other preparation procedures, like screw extrusion [134], cause a larger skewness towards short lengths.

These processing steps may in fact have an additional and rather profound effect on the percolation threshold because the breakup of larger nanotubes into smaller ones may induce a positive correlation between the length and diameter distribution. This leads to a completely different situation from the one where their covariance is zero. Most importantly, we find that neither the aspect ratio nor the length of the carbon nanotubes is the determining factor for the percolation threshold, but there is a sensitive dependence on the coupling of the distribution functions and the relevant higher-order moments. A linear correlation seems plausible for single-walled carbon nanotubes because the probability of breaking is proportional to the scission energy, which in turn scales with the number of bonds to be broken and has a linear relation with the perimeter. In that case the effect of polydispersity is exactly the reverse of what we observe for independent distributions: polydispersity raises the percolation threshold and the effect is stronger for a larger positive skewness in the distribution.

The sensitivity to the coupling is exemplified even more if we assume the length to be proportional to the square of the diameter, which seems more appropriate for multi-walled carbon nanotubes because for those the number of bonds scales linearly with the area of the cross section. This correlation would remove the dependence of the percolation threshold on the distributions altogether. Therefore, control of the break-up process and monitoring the relation between the size distributions could be essential if as low as possible a percolation threshold is required for the envisaged nanocomposite application.

A similar conclusion we can also draw for graphene sheets, not only theoretically but this also follows from the observed sensitive dependence of the percolation threshold on relatively modest variations in the size distribution. Our model seems to explain the trends in the observed percolation thresholds, even though the accuracy of our second-virial approximation should be much lower for plate-like particles than for rod-like ones, as shown in chapter 2. Indeed, the trend in the theoretical predictions for all four graphene nanocomposites is in agreement with percolation thresholds as measured by dynamic light scattering, suggesting that size polydispersity is indeed an important factor determining the electrical percolation threshold. The comparison provides a lower and upper bound for the hopping distance of $\lambda = 0.9$ nm and $\lambda = 1.5$ nm, respectively.

In the next chapters we aim to investigate the impact on the network formation of other aspects that play a role in the nanocomposite processing, such as particle alignment in chapter 5.

We thank Evgeniy Tkalya and Marcos Ghislandi for performing the experiments on graphene.

3.A Symmetric length distributions

We consider symmetric distributions, i.e., with zero skewness, to compute the maximum effect the spread in the length distribution can have on the percolation threshold, i.e., the largest value of s in $\varphi_p(x)/\varphi_p(x_0) = 1/(s+1)$ that was derived in section 2.3. For a truly symmetric distribution we can write

$$\langle L_i \rangle_i = \frac{1}{2} (L_{\text{long}} + L_{\text{short}}), \quad (3.1)$$

with L_{long} (L_{short}) the length of the longest (shortest) rod in the distribution.[‡] In that case we find that the largest value of $s = \text{Var}(L_i)/\langle L_i \rangle_i^2 = 4\text{Var}(L_i)/(L_{\text{long}} + L_{\text{short}})^2$ for given L_{long} and L_{short} is obtained for a distribution with all L_i taking either the value L_{long} or L_{short} , because any rod with a length larger than L_{short} or smaller than L_{long} would lower $\text{Var}(L_i)$. Obviously, the number of rods with length L_{long} and L_{short} must be equal to make the distribution symmetric. This then implies that a bidisperse distribution with a probability density

$$f(L) = \frac{1}{2}\delta(L - L_{\text{long}}) + \frac{1}{2}\delta(L - L_{\text{short}}), \quad (3.2)$$

with δ the familiar Dirac delta function, produces the largest value of s feasible for symmetric distributions. If we write $L_{\text{long}} = nL_{\text{short}}$ with n a real number larger than unity, as we did for the bidisperse mixture in Fig. 2.3, we find $\text{Var}(L_i) = L_{\text{short}}^2(n^2 - 1)/4$, and $\langle L_i \rangle_i = \frac{1}{2}L_{\text{short}}(n + 1)$, and

$$s = \frac{(n - 1)^2}{(n + 1)^2}. \quad (3.3)$$

Expression (3.3) for s is a monotonically increasing function of n and has a *maximum* value of 1 in the limit of $n \rightarrow \infty$, i.e., for an infinite length ratio. With $\varphi_p(x)/\varphi_p(x_0) = 1/(s+1)$ this means that the reduction of the percolation threshold that can be obtained with a symmetric length distribution is *at most* a factor 2 relative to that of the monodisperse case, denoted by x_0 and achieved for the limit $L_{\text{short}} \rightarrow L_{\text{long}}$.

[‡]For a Gaussian distribution centred around $\langle L_k \rangle_k$ this is not strictly the case because by definition $L_k > 0$; however, for $s \ll 1$ it becomes approximately true with $L_{\text{short}} = 0$ and $L_{\text{long}} = 2\langle L_k \rangle_k$.

Conductivity of temporal networks of rod-like particles

4

We present a model for the electrical conductivity of a percolating statistical network of rod-like particles in a solvent. We invoke the analogy between continuum percolation of rod-like particles and percolation on a Bethe lattice, and from that deduce that for particle loadings just above the percolation threshold, the microscopic conductivity should increase quadratically with the concentration albeit that for larger concentrations this crosses over to a linear concentration dependence. The width of the quadratic regime turns out to be the narrower the larger the aspect ratio of the rods. We compare our predictions with experiments on solid-state composites that were produced from dispersions containing carbon nanotubes and electrochemically grown silver nanowires, and find for nanotubes that our prediction for the conductivity exponent of 2 for particle loadings just above the percolation threshold and 1 for larger concentrations seems reasonable. However, the experiments on silver nanowires exhibit much higher exponents with a large scatter for particles with different aspect ratios.

4.1 Introduction

In chapters 2 and 3 we applied continuum connectedness-percolation theory to transient (temporal) networks of anisometric particles and investigated the effect of polydispersity in size and connectivity range on the percolation threshold, i.e., the minimum loading required to form a system-spanning network. Around this critical loading the quantity of interest, e.g., the conductivity of the system, increases many orders of magnitude. In these chapters we limited ourselves to the value of the percolation threshold, as in fact we do in the next chapter 5, where we compute how an externally applied alignment field acts upon it and how this field affects the cluster sizes and shapes upon approach of the percolation threshold. In this chapter we focus on the conductivity itself, that is, *beyond* the percolation threshold, and assess how strongly it increases with increasing particle loadings. The approach we follow is to make use of the analogy between continuum percolation of rod-like particles and site percolation on a Bethe lattice suggested and exploited recently by Chatterjee [109]. Site and bond percolation on Bethe lattices have been studied extensively in the literature, allowing us to translate predictions based on it to conductivity in connectedness-percolation networks of rod-like particles in solution.

In chapter 1 we briefly discussed the critical behaviour of the conductivity Σ of a system of connected particles just above the percolation threshold, a volume fraction φ_p ,

$$\Sigma \sim |\varphi - \varphi_p|^t, \quad (4.1)$$

for volume fractions $\varphi - \varphi_p \ll 1$ and where t indicates a critical exponent. In mean-field theory (supposedly exact for rod-like particles with infinite aspect ratio) $t = 3$, whereas beyond mean-field theory $t = 2$ [25]. The value $t = 3$ is the conductivity exponent in $d_c = 6$ of more dimensions, where d_c is the critical dimension above which mean-field theory becomes exact [25]. For spherical particles, for which the mean-field approximation should not be accurate, experimental values for quite diverse systems such as carbon black, oxide-based thick film resistors, and granular metals exhibit a huge scatter and range from $t = 1$ to $t = 11$ [33]. However, even for rod-like particles such as carbon nanotubes for which mean-field theory should be accurate, no universal behaviour is observed either, because experimental values for the exponent range from 0.9 to 7.6, albeit that most studies do point at a value of about 2 [135]. To explain the discrepancy, theories have been put forward suggesting that the critical conductivity exponent, close to the percolation threshold, consists of the sum of a universal part, t , and a non-universal part often denoted u that depends on the particular system under

study and that depends on, e.g., the distribution of contact resistivities between touching or nearly touching particle parts of the percolating electrical network [30, 144, 145]. In this case Eq. (4.1) transforms to $\Sigma \sim |\varphi - \varphi_p|^{t+u}$. Note that away from the percolation threshold the scaling relation Eq. (4.1) need not hold, although often it seems to do. There is no reason to suspect that the critical exponent t remains the same, and, indeed, many experimental measurements of t in particular in carbon-nanotube composites are done far from rather than close to φ_p .

The formalism of connectedness-percolation theory that we have used in chapters 2 and 3 and that we apply again in the next chapter 5, allows for the computation of the weight-average cluster size S via the connectedness function P , as explained in chapter 1, but provides no information on the full distribution of the cluster sizes. Moreover, continuum connectedness theory breaks down above the percolation threshold, as may be deduced from the fact that $S \propto (\varphi_p - \varphi)^{-1} < 0$ for $\varphi > \varphi_p$. This means that in order to make predictions for the properties of the network beyond the percolation threshold, we should somehow “subtract” the infinite cluster and consider the remaining clusters, which is a non-trivial modification of the theory as we have used it so far. It is for this reason that we take the following alternative approach.

In chapter 2 we showed that the neglect of loop correlations in the second-virial approximation is an accurate closure for rod-like particles, provided the ratio $D^2/\lambda L$ is sufficiently small, with D the rod diameter, L its length, and λ the typical hopping distance. The analogy with percolation on a cycle-free Bethe lattice enabled us to understand the findings we obtained for the presence of non-conducting particles in the dispersion. In this chapter we once again invoke this analogy to predict the conductivity of an infinite network of rod-like particles above the percolation threshold, where we need not limit ourselves to particle loadings that are only slightly higher than the critical value as is the case in Eq. (4.1). We make use of a theory by Stinchcombe [136, 137] for what is often considered to be a microscopic conductivity that gives conductivity exponent of $t = 2$ instead of the mean-field exponent $t = 3$ one expects for the Bethe lattice [138, 139]. We focus on the microscopic conductivity because it allows us to make predictions for the conductivity beyond the critical regime, which in fact is very small and even goes to zero width in the limit of infinite an aspect ratio of the rods. Because the macroscopic conductivity can be calculated, albeit non-trivially, from the microscopic conductivity, we believe that this conclusion transfers to the macroscopic conductivity.

We find that if the contact resistivities of connected rod-like particles are fixed, the conductivity of the network should increase quadratically with the particle loading just above the percolation threshold but linearly beyond that. It is important to emphasise that these values may coincide with the values $t = 2$ close to the percolation threshold for,

e.g., spherical particles [25] and $t = 1$ away from it as follows from an Effective-Medium Approximation [140], but our results are specific for our system of rod-like particles without loop correlations. In section 4.2 we present the model for the conductivity by using established results for cluster growth on the Bethe lattice, and present an intuitive picture for our results in section 4.3. Next, we compare our results to experiments on composites containing carbon nanotubes and silver nanowires in section 4.4. Finally, we draw our conclusions and discuss our results in section 4.5.

4.2 Model

The electrical conductivity Σ and its dependence on the concentration beyond the percolation threshold has been investigated extensively on a Bethe lattice [136, 137], which allows us, as announced in the introduction, to invoke the analogy with percolation of rod-like particles in continuum space. We again emphasise that the type of conductivity our theory predicts is presumably microscopic, but it will turn out to give reasonable results and on top of that it allows for predictions beyond the critical regime. We explicitly make use of the fact that the Bethe lattice is a cycle-free tree, which, again, is analogous to the absence of loop correlations in the second-virial approximation that we used as a closure in these earlier chapters. See also Fig. 4.1. The lattice consists of z branches per site, so in order to translate the results from the Bethe lattice to our rod-like particles, we have to determine the value of z for rod-like particles. The connection between percolation on a Bethe lattice and continuum percolation of *penetrable* rods was recently made by Chatterjee by invoking the contact-volume argument (see chapter 1) [109]. With this approach our Eq. (2.14) can be retrieved for penetrable particles with independent length and diameter distribution to leading order in the coefficient of variation of the diameter distribution (see section 2.4) [109]. Apparently, it is even possible to fully reproduce Eq. (2.14) for hard particles with coupled length and diameter distribution [147].

The mapping Chatterjee makes is as follows. The first step is to compute the average number of contacts $\langle n \rangle$, i.e., intersections, a spherocylinder of length L and diameter D has with other particles of the same length in a dispersion, presuming they are randomly distributed. In the connectedness model that we applied in chapters 2 and 3, we considered two particles to be connected if their connectedness zones overlap. (For rod-like particles this sharp cutoff turned out to be equivalent to an exponentially decaying probability of being connected.) Hence, in order to adapt Chatterjee's theory to our model, we replace the contact volume $\pi L^2 D / 2$ for ideal rods by that of hard rods, $\pi L^2 \lambda / 2$, with λ the connectedness distance presumed fixed and the same for all rods.

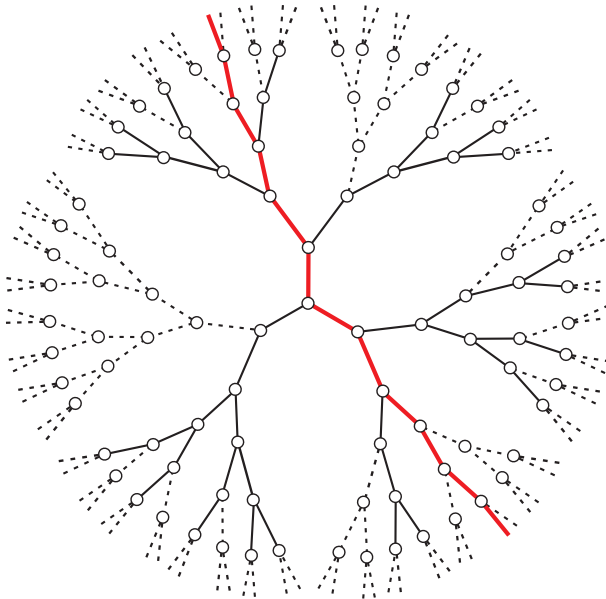


Figure 4.1: A part of a Bethe lattice above the percolation threshold for $z = 3$, so every site has three neighbours. The bonds that are part of the percolating network are shown by the solid lines. The backbone of the percolating path is shown by the thick solid lines, whereas the dangling ends are indicated by the thin solid lines. The former contribute to the charge transport, whereas the latter do not.

This gives to leading order

$$\langle n \rangle = 2\varphi \frac{\lambda L}{D^2} \quad (4.2)$$

for $L/D \gg 1$, with φ the volume fraction of rods [163]. The next step is to equate $\langle n \rangle$ to the average number of occupied neighbours any site has on a Bethe lattice with vertex degree z and probability p of a site being occupied. The average number of occupied neighbouring sites n_p equals pz , because this is simply the average of the binomial probability distribution of n_p with z “trials” a probability p of “success”. Chatterjee finally argues that a rod-like particle in continuum space is analogous to an occupied site on the lattice, implying that a bond in the lattice represents the contact between two rods. Then it follows that $p = \varphi$ and $n_p = \langle n \rangle$ and, as a result, $z = \langle n \rangle / \varphi$ with $\langle n \rangle$ given by Eq. (4.2).

Inserting Eq. (4.2) gives for the equivalent number of branches z per lattice site to leading order

$$z = \frac{2L \lambda}{D D}, \quad (4.3)$$

for large aspect ratios $L/D \gg 1$. Because for percolation on a Bethe lattice $\varphi_p = 1/(z-1) \approx 1/z$ for large z , so we obtain $\varphi_p = D^2/2\lambda L$, consistent with our result of chapter 2. Eq. (4.3) together with the identification $\varphi = p$ constitutes the mapping of percolation on a Bethe lattice on the continuum percolation of rods. It hinges on the second-virial approximation being accurate, which is only true for slender rods. Indeed, z can also be identified as two times the ratio of the second-virial contribution in the expansion of the direct-connectedness function C^+ over the third, as discussed in Appendix 2.A. The second-virial approximation that we make of neglecting this third term is valid for $L/D \gg 1$ or $\varphi \ll 1$, so the larger z , the more accurate it is. For single-walled carbon nanotubes $D \approx \lambda$, whilst for multi-walled nanotubes D is a few times larger than λ [97]. On the other hand, the silver nanowires that we compare our results to in section 4.4 have an aspect ratio 8, 16, and 31, so the approximation of large values of z may not be very accurate.

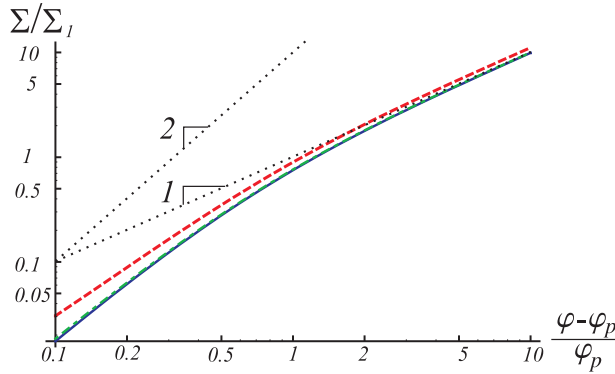


Figure 4.2: The conductivity Σ of the Bethe lattice on a double logarithmic scale, normalised to the value Σ_1 of a bond, as a function of the volume fraction φ relative to the percolation threshold $\varphi_p = 1/9$ (so $z = 10$, dashed line), $\varphi_p = 1/99$ ($z = 100$, dashdotted line), and $\varphi_p = 1/999$ ($z = 1000$, solid line). After a small interval of quadratic increase, the conductivity increases linearly with the concentration φ for large enough coordination number z , as shown by the dotted lines with slopes 1 and 2.

The conductivity of networks on the Bethe lattice can be computed by using the fact that there are no loops, implying that it is a network of parallel paths of resistances that are connected in series [137]. By using moment-generating functions for the distribution of bond resistivities, an implicit equation for the conductivity of the network can be derived. For a binary distribution of conductivities, i.e., only conducting and insulating bonds, and in the limit of large coordination number $z \gg 1$, the resulting microscopic conductivities, defined as that between any node in the network and all nodes at the

end of the tree presumed infinitely large, can be approximated by [137]

$$\frac{\Sigma}{\Sigma_1} \sim -\frac{\varphi}{\varphi_p} \left(\frac{\varphi_p}{\varphi} - 1 + \frac{\varphi_p^2}{\varphi^2} \left(1 - \frac{\varphi_p}{\varphi} \right) (1 - \varphi) \right) + \mathcal{O} \left(\frac{\varphi_p}{\varphi} \right)^3, \quad (4.4)$$

if we express it in terms of our continuum percolation model of hard rods in continuous space, and where Σ_1 is the conductivity of a bond, and $\varphi_p = 1/(z - 1) \approx 1/z$. We neglected higher-order terms in φ_p/φ that are of order $1/z^3$, so very small for large z . We plotted Eq. (4.4) in Fig. 4.2 for three values of z . The conductivity initially increases as $\Sigma \sim (\varphi - \varphi_p)^2$ with exponent $t = 2$ for $\varphi - \varphi_p < \varphi_p$ in the limit of very large z , after which it exhibits a *linear* increase with the concentration φ for $\varphi - \varphi_p \gtrsim 1/z \approx \varphi_p$. For $0 \leq \varphi - \varphi_p < \varphi_p$ the quadratic dependence holds, which indeed is a very small interval for large aspect ratios of rods [137].

The above result may not provide a clear *physical* picture of the origin of the conductivity exponents, so we rationalise it in the next section by computing the fraction of the lattice that contributes to the charge transport, the so-called backbone fraction.

4.3 Backbone fraction

To rationalise the findings of section 4.2, we next present an analysis of the conductivity of networks of rods by considering what fraction of sites on a lattice contributes to the percolating electrical networks. We consider site percolation and not bond percolation, because in our mapping a site is equivalent to the position of a rod-like particle. A percolating cluster is a sparse network, meaning not only that the network occupies only a fraction of three-dimensional space but also that not all particles in the infinite cluster contribute to the charge transport. The branches that have no contribution to the macroscopic charge transport are called dead or dangling ends and the part of the cluster that does contribute is referred to as the backbone. See Fig. 4.1. It is this fraction that contributes to the conductivity, although often the *overall* fraction of sites part of the percolating network, given by the backbone and the dangling ends, is taken as a measure of the level of conductivity produced by the network. As we shall see, only the backbone fraction reproduces the prediction of Eq. (4.4).

The Bethe lattice with z branches per lattices site has a percolation threshold of $p_p = 1/(z - 1)$, where p is the probability of a site being occupied. The percolation probability F is the probability that an arbitrarily selected site is part of an infinite conducting path. If R is the probability that any of the z branches arbitrarily chosen that sprouts from a given site is not infinitely long, then [136, 137]

$$F(p) = 1 - R(p)^z, \quad (4.5)$$

because the probability R for a branch is independent of that of another branch. So, $R(p) = 1$ for $p \leq p_p$ and $0 \leq R(p) < 1$ for $p > p_p$. If the branch that has been chosen is finite, then either the site 1 that begins with it is unoccupied with probability $1 - p$, or if it is occupied (with probability p) the other remaining $z - 1$ branches that sprout from site 1 are finite (with probability R^{z-1}), hence

$$R = 1 - p + pR^{z-1}, \quad (4.6)$$

which provides us with an implicit equation for R , so we can calculate F from that. See Fig. 4.3. F depends differently on p and hence on φ than Σ , telling us indeed that the conductivity is not proportional to the fraction of particles that is part of the percolating network.

The percolation probability determines the percolation fraction P^S , which is the fraction of sites in the Bethe lattice belonging to an infinite cluster of occupied sites. The backbone fraction B^S is then defined as the part of P^S that would carry current if a voltage drop were imposed across the infinite cluster [141]. The percolation fraction P^S is closely related to the percolation probability $F(p)$:

$$P^S = pF, \quad (4.7)$$

because P^S is the probability that a randomly selected is occupied, p , times the probability that it is part of the infinite network, F . One can calculate the tag-end fraction, which is the fraction of occupied sites that are connected to an infinite cluster but are not part of the backbone of that fraction, by considering the sites one must pass to cross the network. It then follows that the backbone fraction B^S obeys [141]

$$B^S = (z - 1)P^S + zp \left(1 - \left(1 - \frac{P^S}{p} \right)^{(z-1)/z} \right) \approx 2zpF, \quad (4.8)$$

where the approximation holds for large values of z . The functional dependence of B^S on the packing fraction is shown in Fig. 4.3 for various values of z , i.e., of φ_p . For $\varphi = p$ close to the percolation threshold $\varphi_p = 1/(z - 1)$, an expansion around φ_p for $\varphi - \varphi_p \ll \varphi_p$ shows that B^S increases with $(\varphi - \varphi_p)^2$, so indeed the exponent for the conductivity Σ that we discussed in section 4.2 [141, 142]. For larger values of φ , B^S increases linearly with $(\varphi - \varphi_p)$ if value of $(\varphi - \varphi_p)/\varphi_p$ exceeds unity, analogous to what we observed above for the conductivity. For large coordination numbers z this also follows from Eqs. (4.5), (4.6), (4.7), and (4.8). Indeed, we find that $F \approx 1$ for $\varphi - \varphi_p > \varphi_p$ because then $R(\varphi) \approx 1$, $P^S \approx \varphi$, and as a result $B^S \propto \varphi$. It also follows from Fig. 4.3 that $B^s/(\Sigma/\Sigma_1)$ depends only very weakly on φ for large values of z ,

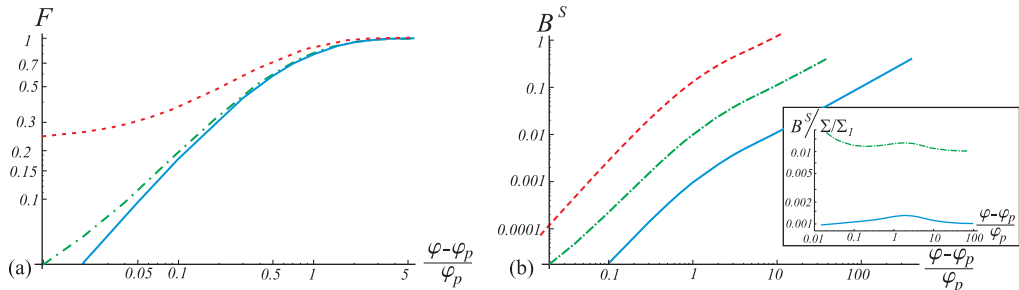


Figure 4.3: The percolation probability F (a) and the backbone fraction B^S (b) of the Bethe lattice, which plausibly is a measure of the conductivity, shown on a double logarithmic scale as a function of the concentration φ relative to the percolation threshold φ_p . The curves are for $\varphi_p = 1/9$ (so $z = 10$, dashed line), $\varphi_p = 1/99$ ($z = 100$, dashdotted line), and $\varphi_p = 1/999$ ($z = 1000$, solid line). Close to the percolation threshold φ_p , B^S grows quadratically with φ for large enough z , after which it increases linearly. The crossover occurs for $(\varphi - \varphi_p)/\varphi_p \approx 1$, as expected. Inset: for $z = 100$ (top) and $z = 1000$ (bottom), $B^S/(\Sigma/\Sigma_1)$ depends only very weakly on φ .

i.e., for large aspect ratios of the rods, so indeed the conductivity seems to be almost proportional to the backbone fraction.

In conclusion, the theoretical result for the quadratic and then linear regime in the conductivity from section 4.2 can be understood by considering the backbone fraction of links. In the next section we compare our predictions with experimental observations.

4.4 Comparison with experiments

In this section we test our predictions from section 4.2 against experimentally determined values of the electrical conductivity of networks or rod-like particles. First we consider composites containing carbon nanotubes that we have considered before in chapters 2 and 3. In Fig. 4.4 a curve fit using Eq. (4.4) is shown to a composite of multi-walled nanotubes and polystyrene stabilised with the surfactant sodium dodecyl sulfate (SDS), with a percolation threshold of $\varphi_p \approx 0.006$. From Eq. (4.3), $\varphi_p \approx 1/z$, and $D \approx 5\lambda$, we find that $L/D \approx 400$ for this composite, which is larger than the observed aspect ratio of 150 in the experiments, but of the same order of magnitude. Our prediction seems to fit the data reasonably well, albeit that the available range of data points for $\varphi - \varphi_p$ is quite narrow and does not quite enter the regime where $t = 1$ is expected. This means that the data seems to obey our prediction of $t = 2$ close to percolation threshold. For the curve fits we have to make a choice for the value of Σ_1 and we return to this in section 4.5.

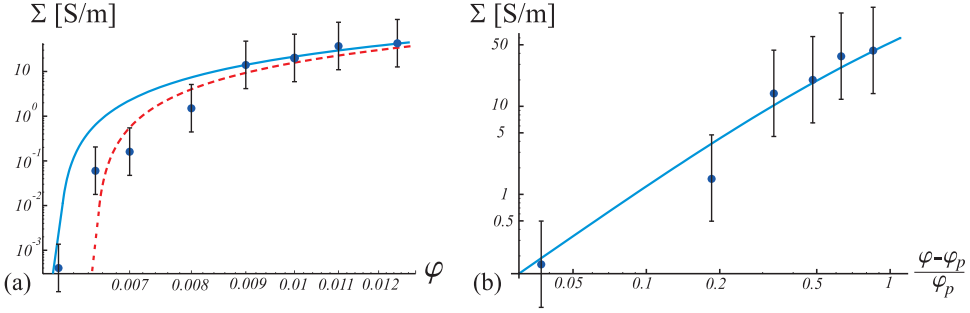


Figure 4.4: Curve fit to experimentally obtained conductivities (dots) for composites of polystyrene and multi-walled carbon nanotubes on a double logarithmic scale, using Eq. (4.4), where $\Sigma_1 = 70$ S/m has been taken to make the best fit. The conductivity Σ/Σ_1 is shown as a function of the concentration φ for $\varphi_p = 0.006$ (solid line) and $\varphi_p = 0.0065$ (dashed line) (a), and as a function of $(\varphi - \varphi_p)/\varphi_p$ for $\varphi_p = 0.006$ (b). The former graph is very sensitive to the choice of φ_p , whereas the latter is not. The error bars are roughly half an order of magnitude in the conductivity.

Fig. 4.5 shows a curve fit to conductivities of composites of single-walled carbon nanotubes in polystyrene, where one dispersion was stabilised using SDS and one using the polymer latex PEDOT:PSS that we discussed in chapter 2 as a conductive coating material [27]. The system with PEDOT:PSS has a percolation threshold of $\varphi_p \approx 0.001$ and the curve fit of Eq. (4.4) matches the data quite well. The percolation threshold gives from Eq. (4.3), and $D \approx \lambda$ for single-walled nanotubes [97], that $L/D \approx 500$, which is in the same order of magnitude as the experimentally determined value of 500 – 1000 [148]. For the system with SDS as stabiliser, the percolation threshold is $\varphi_p \approx 0.0025$, giving an average aspect ratio of $L/D \approx 200$, and the fit of the conductivity using Eq. (4.4) is less accurate than for the system with PEDOT:PSS. It must be remarked that in both cases the uncertainty in the data points is quite large [27]. Note also the large difference in the percolation thresholds of the three systems we consider, which shows the sensitive dependence on the processing conditions [23].

This sensitivity is also observed in different experiments on multi-walled carbon nanotubes, in which the mixture was evaporated and freeze-dried and conductivity exponents of 1.7 and 3.9 have been obtained, respectively [108]. Both of these exponents were obtained in the regime that according to our calculations should give $t = 2$. Conductivity measurements have also been performed with other types of rod-like nanofiller, such as electrochemically grown silver nanowires in polystyrene. For rods with an aspect ratio of 8, 16, and 31, conductivity exponents of $t = 3.3$, 6.7, and 2.8 have been obtained, respectively [20]. These also fall in the regime where we expect $t = 2$, so the

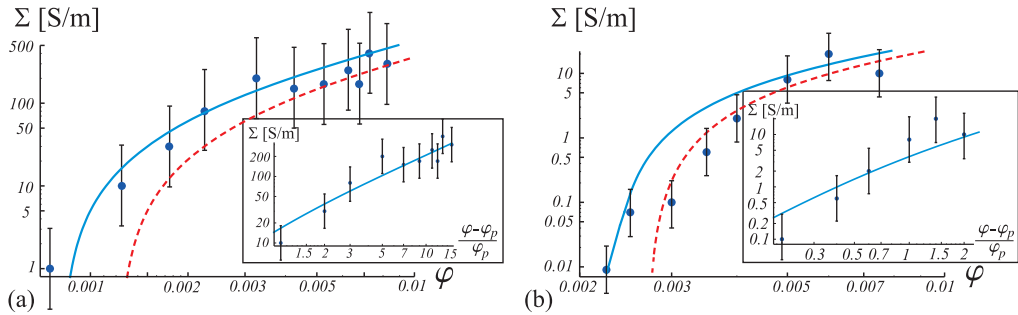


Figure 4.5: Curve fit of Eq. (4.4) to experimentally obtained conductivities on a double logarithmic scale for composites of polystyrene and single-walled carbon nanotubes that were stabilised using the polymer latex PEDOT:PSS (a) and the surfactant sodium dodecyl sulfate (SDS) (b) [27]. The data of PEDOT:PSS is fitted with $\Sigma_1 = 50$ S/m and $\varphi_p = 0.0008$ (solid line) and $\varphi_p = 0.0012$ (dashed line). With SDS the conductivity is fitted with $\Sigma_1 = 20$ S/m, $\varphi_p = 0.0023$ (solid line) and $\varphi_p = 0.0027$ (dashed line). Insets: the conductivity as a function of $(\varphi - \varphi_p)/\varphi_p$, which is not so sensitive to the choice of φ_p . The values $\varphi_p = 0.001$ (a) and $\varphi_p = 0.0025$ (b) have been taken.

range of experimental values is too narrow to verify our prediction of $t = 1$ for larger concentrations.

4.5 Conclusions and discussion

In this chapter we have presented a model for the electrical conductivity of temporal percolating networks of randomly dispersed rod-like particles, where we again invoked the analogy between continuum percolation of rods and percolation on a Bethe lattice that is based on the absence of loop correlations in both. We extended the connection for penetrable rods as made by Chatterjee to hard particles [109], and find that the number of branches per lattice site z , which satisfies $z \approx 1/\varphi_p$, with φ_p the percolation threshold, is of the order of the aspect ratio of the rods. For carbon nanotubes this is a very large number, which allows us to consider the limiting case of very large z and to derive analytical expressions for the conductivity.

According to our predictions, the conductivity should increase quadratically for concentrations that satisfy $\varphi - \varphi_p \leq \varphi_p$, i.e., just above the percolation threshold $\varphi_p \ll 1$ for large z (large aspect ratio). Beyond this regime we find a linear increase of the conductivity with increasing particle loading. We rationalised our findings by noting that the conductivity is governed by the backbone fraction of the percolating network and not by the so-called dangling chains. For this backbone fraction on a Bethe lattice the

exponent is 2 close to the percolation threshold and 1 for $\varphi - \varphi_p > \varphi_p$. We find that the backbone fraction to a very good approximation proportional to the conductivity Σ (see Fig. 4.3), so this supports our results for the conductivity.

We note that the theory in this chapter should be considered as tentative. We presumed that the conductivity on the idealised case of a Bethe lattice can be translated into the conductivity of rods in real three-dimensional space, but it is not obvious that this mapping is so straightforward to make [144]. We assumed a constant junction resistivity of any contact between two rod-like particles, but any distribution in these resistivities possibly has a large impact on the overall conductivity and our simplified model presumably breaks down [137, 146]. More importantly, we focused on the microscopic conductivity that gives a different critical exponent ($t = 2$) than what mean-field theory predicts ($t = 3$) [25]. The main advantage of our approach, though, is that it allows for predictions beyond the critical regime, which we have shown to be very small. Surprisingly, our model for the microscopic conductivity predicts the macroscopic conductivities that are observed in carbon-nanotube composites reasonably well. We speculate that the type of conductivity one measures in an experiment depends on the way in which the experiments are conducted, and perhaps the two-point and four-point measurements often used in the experiments on such composites produce microscopic conductivities.

In fact, results for the Bethe lattice can provide quantitative predictions for continuum percolation of rods, because Chatterjee recently derived our Eq. (2.14) for the effects of length and diameter polydispersity of rod-like particles on the percolation threshold by using the same mapping of the Bethe lattice [147]. Indeed, the comparison with experimentally determined exponents shows reasonable agreement for the first two systems with carbon nanotubes we considered, but strong deviations in the third nanotube composite and the one with silver nanowires. The varying success in the fitting of the three carbon-nanotube composites may be caused by the sensitivity of the material properties on preparation route that we discussed in chapter 3, and the large scatter observed in the exponents may be the result of a crossover from the regime where $t = 2$ to that where $t = 1$. Making these curve fits requires a choice for the reference conductivity Σ_1 that in our mapping represents the conductivity of the bond between two particles where hopping of charge carriers takes place, e.g., the polymer matrix between them in the carbon-nanotube composite. The values we find for Σ_1 for the nanotube composites are of the order of 10 S/m. It is difficult to compare these values to macroscopic conductivities, because our model provides prediction for the microscopic conductivities, as discussed above. In our model we presume the particles to have negligible resistivity, which is of course not completely true, particularly for single-walled carbon nanotubes because in practice only one third of them are metallic and two thirds

are semi-conducting.

Regarding the cited experiments on silver-nanowires, the aspect ratios of the particles ($\mathcal{O}(10)$) are much smaller than, e.g., those of carbon nanotubes, but according to our analysis of the backbone fraction on the Bethe lattice, they should still be large enough to observe the linear dependence of the conductivity on the concentration. We remark, though, that this aspect ratio may not be large enough for the second-virial approximation to be accurate, and, consequently, the neglect of loop correlations that allowed us to invoke the analogy with percolation on the Bethe lattice, to provide quantitative predictions [104]. In addition, the number of data points is very limited in these experiments, so the uncertainty in these measurements is presumably quite large. We note that very few experiments have been done in the range of particle loadings where we expect $t = 1$ to be observed, i.e., for $\varphi - \varphi_p > \varphi_p$. The reason is presumably that the purpose is usually to produce a nanocomposite with a loading of the (expensive) nanofillers that is as low as possible. Also, such high loadings could lead to rheological problems because of very high viscosities.

Hence, this suggests that more experimental data are required to assess whether our theory is valid, and in particular, measurements far beyond the percolation threshold. However, even a sufficiently large number of accurate measurements of the conductivity may still exhibit a large spread in the exponents, as we also noted for the experiments on silver nanowires [20]. This may be the result of the different processing conditions that have been shown to have a large impact on the electrical conductivity and the composite properties in general [23, 108]. However, it has been argued that non-universal behaviour can even be expected in systems that are dominated by tunneling as a charge transport mechanism [143]. The critical conductivity exponent, so close to the percolation threshold, may in that case consist of a universal part t and a non-universal part u that depends on the particular system under study [30, 144, 145], but these theories make no prediction for the conductivity behaviour away from the percolation threshold.

We thank Evgeniy Tkalya for providing us with the experimental data on the carbon-nanotube composites.

Connectedness percolation of hard rod-like particles in an external field

5

An analytical theory is presented of how an external orienting field and excluded-volume interactions conspire against the formation of a percolating network in fluid dispersions of elongated particles. We find the system-spanning network that forms above some very low loading to break up again at higher loadings due to interaction-induced enhancement of alignment of the particles. We also find that upon approach of the percolation threshold the dimensions of the clusters of connected particles diverge differently in the directions parallel and perpendicular to the orienting field. This is caused not by different critical exponents associated with these two directions but by different prefactors.[†]

[†]The contents of this chapter are based on the following publication:
R. H. J. Otten and P. van der Schoot, *Connectedness percolation of elongated nanoparticles in an external field*, submitted.

5.1 Introduction

As discussed in chapters 2 and 3, high-aspect-ratio nanofillers potentially enhance the physical properties of the material they are dispersed in. The main application we focused on were composites containing carbon nanotubes or graphene sheets that acquire (some of) the remarkable thermal, mechanical and electrical properties of these carbon allotropes even at loadings below one volume per cent [18, 19]. In chapters 2 and 3 we have seen how the percolation threshold, i.e., the critical concentration beyond which clusters of connected particles are formed, and beyond which the conductivity of the composite exhibits a massive increase, sensitively depends on the distributions of the linear dimensions and connectivity ranges of the particles.

This polydispersity originates from the nanotube synthesis and the processing that takes place in the fluid stages of the nanocomposite fabrication, e.g., ultrasonication, compression moulding, compounding and extrusion [26, 149, 150]. If the fluid is not allowed to relax post processing, this may not only affect the size distribution of the particles, but also the network structure in the final solid product through alignment of filler particles. In fact, particle alignment has been induced deliberately by electric and magnetic fields to enhance and/or induce anisotropy in the conductivity of the material [95, 151–153, 155]. Naively, one expects the percolation threshold to go up if the particles become mutually aligned, as this increases the shortest distance separating them. This is confirmed by computer simulations for penetrable sticks in two [151] and three dimensions [154], and for impenetrable ones in three [153]. Contact-volume theories confirm this also: the mean volume swept out by the particles decreases with increasing alignment [95, 151, 156, 157]. Unclarified, however, is how this competes with the transition to the nematic liquid-crystalline phase, which takes place in the absence and presence of orienting fields [158].

In order to shed light on this, we present an analytical theory showing how an externally applied alignment field and excluded-volume interactions conspire against the formation of a percolating network in fluid dispersions of elongated particles. Our *anisotropic* continuum percolation theory self-consistently links (i) connectedness-percolation theory for the cluster size and (ii) Onsager theory for the interplay between interactions and the field-induced particle alignment. Angular correlations between the particles, ignored in contact-volume theories, are explicitly taken into account [95, 151, 156, 157]. We find that the system-spanning, self-assembled network forming above some critical loading that depends on the strength of the external quadrupole field, breaks up again at higher loadings. See Fig. 5.1. This kind of re-entrance behaviour is caused by the interaction-induced enhancement of the alignment of the particles and

not unlike disentanglement of rod-like particles in elongational flow fields [159]. For weak fields, the densities at which this happens is preempted by the transition to the uniaxial nematic phase. For sufficiently strong fields, the low-density percolation threshold is suppressed completely.

Finally, according to our calculations the dimensions of the clusters are different parallel and perpendicular to the field direction albeit that both diverge with the same critical exponent. This field-induced cluster anisotropy might in thin-film setups be utilised to fabricate nanocomposites with strongly anisotropic electrical conductivities and with a very low particle loading [152, 155].

5.2 Model ingredients

In our model, we presume the network to be formed in the fluid stages of the composite processing and this network to be frozen in upon solidification. This allows us to invoke the connectedness analog of the Ornstein-Zernike equation of liquid-state theory, and calculate the (weight) average cluster size of connected particles, S . As introduced in chapter 1 and used in chapters 2 and 3, we have within connectedness percolation theory [34]

$$S = 1 + \lim_{\mathbf{q} \rightarrow 0} \rho \langle \langle \hat{P}(\mathbf{q}, \mathbf{u}, \mathbf{u}') \rangle_{\mathbf{u}} \rangle_{\mathbf{u}'}, \quad (5.1)$$

in terms of the Fourier transform $\hat{P}(\mathbf{q}, \mathbf{u}, \mathbf{u}')$ of the pair-connectedness function $P(\mathbf{r}, \mathbf{r}', \mathbf{u}, \mathbf{u}')$ that describes the probability that two particles at positions \mathbf{r} and \mathbf{r}' , and with orientations \mathbf{u} and \mathbf{u}' , are part of the same cluster. In Eq. (5.1), ρ is the overall number density of our particles, presumed cylindrical with a main body-axis vector \mathbf{u} that obeys an as yet unknown orientational probability distribution function $\psi(\mathbf{u})$. As defined before, $\langle \dots \rangle_{\mathbf{u}} \equiv \int d\mathbf{u} (\dots) \psi(\mathbf{u})$ denotes an orientational average, and $(\hat{\cdot}) = \int d\mathbf{r} (\dots) \exp(i\mathbf{q} \cdot \mathbf{r})$ a Fourier transform with \mathbf{q} the wave vector [34, 160].

As introduced in chapter 1, the connectedness function P can be calculated from the connectedness Ornstein-Zernike equation [34], which in Fourier space reads

$$\hat{P}(\mathbf{q}, \mathbf{u}, \mathbf{u}') = \hat{f}^+(\mathbf{q}, \mathbf{u}, \mathbf{u}') + \rho \langle \hat{f}^+(\mathbf{q}, \mathbf{u}, \mathbf{u}'') \hat{P}(\mathbf{q}, \mathbf{u}'', \mathbf{u}') \rangle_{\mathbf{u}''}, \quad (5.2)$$

if we invoke the second-virial approximation that replaces the direct-connectedness function C^+ by the connectedness Mayer function f^+ . As shown in Appendix 2.A, this is accurate provided the rod length is much larger than its width, which we presume to be of the order of the typical distance over which charge transport can take place [160]. We have $f^+ = \exp(-\beta u^+)$, with $\beta = 1/k_B T$, k_B Boltzmann's constant, and T the absolute temperature. Charge transport enters effectively in Eq. (5.2) via u^+ because it is

the connectedness potential that we choose such as to mimic an exponentially decaying conductivity between two rods, presumed impenetrable. This we do below.

Solving Eq. (5.2) for \hat{P} , averaging this function over the orientation distribution $\psi(\mathbf{u})$ and inserting this in Eq. (5.1) gives the cluster size S . The critical density ρ_p for which this quantity diverges we identify with the percolation threshold. The distribution of the particles in the absence of an external field is isotropic, $\psi = 1/4\pi$, at least for densities below which the fluid undergoes a spontaneous transition to the uniaxial nematic liquid-crystalline state. In the presence of an orienting field the distribution function becomes a function of the strength of this field and the density of the particles.

The orientation distribution function we calculate from Onsager's density functional theory for impenetrable rods in an alignment field [13]. The degree of alignment of the rods depends self-consistently on the sum of the external and molecular field strengths, because the latter is a function of excluded-volume interactions that themselves are a function of the degree of alignment. This makes $\psi(\mathbf{u})$ depend on both the field strength and the density. According to Onsager's second-virial theory [13], it obeys the non-linear self-consistent field equation [161, 162]

$$\log \psi(\mathbf{u}) = \mu + \rho \left\langle \hat{f}(0, \mathbf{u}, \mathbf{u}') \right\rangle_{\mathbf{u}'} - U(\mathbf{u}), \quad (5.3)$$

where $\hat{f}(0, \mathbf{u}, \mathbf{u}')$ is the zero-wave vector Fourier transform of the Mayer function $f(\mathbf{r}, \mathbf{r}') = \exp(-\beta u) - 1$ for the inter-particle interaction potential u , μ serves as a Lagrange parameter, and U is the dimensionless external potential.

We presume U to be of the quadrupole type, so $U = \beta K \cos^2 \vartheta$, where K is the field strength and ϑ the polar angle between the field direction and the main body-axis vector. For negative values of K the rods align along the field direction (orienting field), while for positive ones they align perpendicular to it (disorienting). The field strength depends on the type of field that is used to align the particles. If we align them in an electric field of strength E , and they do not have a permanent dipole moment, we have $K = -\Delta\alpha E^2/2$ with $\Delta\alpha$ their electric-polarisability anisotropy. For a magnetic field, then $K = -\Delta\chi H^2/2$ with H the magnetic-field strength and $\Delta\chi$ the diamagnetic susceptibility anisotropy of the rods. If they are coupled to an extensional flow field, $K = -3\dot{\epsilon}/4D_r$, with $\dot{\epsilon}$ the strain rate and D_r the rotational diffusivity [162, 163].

Eqs. (5.1), (5.2) and (5.3) form the basis of our model and connect the cluster size S , the external field strength K , the orientation distribution function ψ , and the particle density ρ . Evidently, the calculation of the particle density at which the mean cluster size diverges (the percolation threshold) requires a self-consistent treatment of this set of three equations. The complicating term here is the interaction term in Eq. (5.3) that makes solving them a non-trivial exercise. To actually perform the calculation, we

need to specify the connectedness potential u^+ and the interaction potential u . Again, we presume the rods to behave as mutually impenetrable, rigid cylinders of length L and diameter D . This implies that $u \rightarrow \infty$ and $u^+ \rightarrow \infty$ for all centreline-to-centreline distances $r < D$ between two rods. Furthermore, $u = 0$ for $r > D$.

As discussed in chapter 2, we effectively incorporate an exponentially decaying probability of charge transport between two rods for distances $r > D$ in our description by taking $\beta u^+ = (r - D)/\lambda$, with λ the typical hopping distance. This produces an exponentially decaying connectedness Mayer function that in our model describes short-range correlations between connected particles. With these ingredients, presuming the rods to be long relative to their width D and to the length λ , and using Straley's [105] oblique coordinate system, we find for nonzero wave vectors

$$\hat{f}_{\mathbf{q}}^+ = 2L^2 \lambda j_0(\mathbf{q} \cdot \mathbf{u}L/2) j_0(\mathbf{q} \cdot \mathbf{u}'L/2) |\sin \gamma| \quad (5.4)$$

and

$$\hat{f}_{\mathbf{q}} = -2L^2 D j_0(\mathbf{q} \cdot \mathbf{u}L/2) j_0(\mathbf{q} \cdot \mathbf{u}'L/2) |\sin \gamma|, \quad (5.5)$$

at least in the slender-rod limit where $L \gg \lambda, D$ and $|\mathbf{q}|D \ll 1$ [160]. Here, $\gamma = \gamma(\mathbf{u}, \mathbf{u}')$ is the angle between two rods with orientations \mathbf{u} and \mathbf{u}' , and $j_0(x) \equiv \sin x/x$. See section 2.3 for the derivation of \hat{f}^+ in the limit of zero wave vector. Here, we relax this condition because we need nonzero wave vectors below in determining the cluster anisotropy.

It turns out not to be necessary to know the full angular and wave-vector dependence of the pair-connectedness function $\hat{P}(\mathbf{q}, \mathbf{u}, \mathbf{u}')$ to calculate the percolation threshold. The reason is that the cluster size can be written as $S = 1 + \rho \langle g(\mathbf{u}) \rangle_{\mathbf{u}}$ with $g(\mathbf{u}) \equiv \langle \hat{P}(0, \mathbf{u}, \mathbf{u}') \rangle_{\mathbf{u}'}$. The latter function we obtain from the Ornstein-Zernike equation Eq. (5.2), which for $\mathbf{q} = 0$ reduces to

$$g(\mathbf{u}) = \left\langle \hat{f}^+(0, \mathbf{u}, \mathbf{u}') \right\rangle_{\mathbf{u}'} + \rho \left\langle \hat{f}^+(0, \mathbf{u}, \mathbf{u}') g(\mathbf{u}') \right\rangle_{\mathbf{u}'} \quad (5.6)$$

that can be viewed as a ‘‘reduced’’ Ornstein-Zernike equation. Because of the cylindrical symmetry of the problem in hand, the angular distribution function $\psi(\mathbf{u}) = \psi(\vartheta)$ depends only on the polar angle ϑ , implying that the integration over the azimuthal angle ϕ involves only the $|\sin \gamma|$ in the connectedness Mayer function that enters the reduced Ornstein-Zernike equation.

Further headway can be made by expressing this integral over φ in terms of the Legendre polynomials P_{2n} [126] by invoking the addition theorem,

$$\frac{1}{2\pi} \int_0^{2\pi} d\phi' |\sin \gamma| = \sum_{n=0}^{\infty} d_{2n} P_{2n}(\cos \vartheta) P_{2n}(\cos \vartheta'), \quad (5.7)$$

with $d_0 = \pi/4$, and

$$d_{2n} = -\pi(4n+1) \frac{(2n-3)!!(2n-1)!!}{2^{2n+2}n!(n+1)!}, \quad (5.8)$$

for $n \geq 1$ [164]. If we use Eq. (5.7) in Eq. (5.6), we obtain an equation for g that depends only on ϑ :

$$\begin{aligned} g(\vartheta) = & 2L^2\lambda \sum_{n=0}^{\infty} d_{2n} P_{2n}(\cos \vartheta) \langle P_{2n}(\cos \vartheta') \rangle_{\vartheta}, \\ & + 2\rho L^2\lambda \sum_{n=0}^{\infty} d_{2n} P_{2n}(\cos \vartheta) \langle P_{2n}(\cos \vartheta') g(\vartheta') \rangle_{\vartheta}, \end{aligned} \quad (5.9)$$

where the brackets denote an orientational average over the polar angle, so $\langle m(\vartheta) \rangle_{\vartheta} = \int d\vartheta \sin \vartheta m(\vartheta) \psi(\vartheta)$. Because of cylindrical symmetry we next write $\psi(\mathbf{u}) = \psi(\vartheta) = (a_0 + a_2 P_2(\cos \vartheta) + a_4 P_4(\cos \vartheta))/2\pi$, where $a_0 = 1/2$ because ψ is normalised. For this expansion to be meaningful the last term needs to be subdominant, i.e., $a_4 \ll a_2$. These expansions we insert in the reduced Ornstein-Zernike equation. Because (i) we are not actually interested in the actual functional form of $g(\vartheta)$ but only in an orientational average of this quantity that determines the cluster size, and (ii) we truncate the expansion of the distribution function after the third term, we find that we only need to account for three moments of the type $\langle P_{2n}(\cos \vartheta) g(\vartheta) \rangle_{\vartheta}$, i.e., those for $n = 0, 1, 2$. To do so, we can use that for the product of two Legendre polynomials we have

$$P_{2k}(x) P_{2\ell}(x) = \sum_n (4n+1) I_{2n,2k,2\ell} P_{2n}(x), \quad (5.10)$$

with $I_{2n,2k,2\ell} = 0$ if $k + \ell - n < 0$, $k - \ell + n < 0$, or $-k + \ell + n < 0$, and

$$\begin{aligned} I_{2n,2k,2\ell} = & \frac{(2n+2k-2\ell)!(2n-2k+2\ell)!(-2n+2k+2\ell)!}{(2n+2k+2\ell+1)!} \times \\ & \left(\frac{(n+k+\ell)!}{(n+k-\ell)!(n-k+\ell)!(-n+k+\ell)!} \right)^2 \end{aligned} \quad (5.11)$$

otherwise. If we compute from Eq. (5.9) $\langle P_{2\ell} g(\vartheta) \rangle_0$, with $\langle \dots \rangle_0 \equiv (4\pi)^{-1} \int d\mathbf{u} (\dots)$, this gives a tri-diagonal matrix. A test of truncating the series after the $\ell = 2$ shows that it gives results for the percolation threshold that are numerically indistinguishable from those found after truncating after $\ell = 3$ and $\ell = 4$, so we ignore the terms of $\langle P_6 g(\vartheta) \rangle_{\vartheta}$

and higher order moments to compute S . We then find

$$\langle g \rangle_0 = 4\tau a_0 d_0 + 2\tau \rho d_0 (a_0 \langle g \rangle_0 + a_2 \langle P_2 g \rangle_0 + a_4 \langle P_4 g \rangle_0), \quad (5.12a)$$

$$\begin{aligned} \langle P_2 g \rangle_0 &= \frac{4}{25} \tau a_2 d_2 + \frac{2}{5} \tau d_2 \rho \left(\frac{1}{5} a_2 \langle g \rangle_0 + \left(a_0 + \frac{2}{7} (a_2 + a_4) \right) \langle P_2 g \rangle_0 \right. \\ &\quad \left. + \left(\frac{18}{35} a_2 + \frac{180}{693} a_4 \right) \langle P_4 g \rangle_0 \right), \end{aligned} \quad (5.12b)$$

$$\begin{aligned} \langle P_4 g \rangle_0 &= \frac{4}{81} \tau a_4 d_4 + \frac{2}{9} \tau \rho d_4 \left(\frac{1}{9} a_4 \langle g \rangle_0 + \left(\frac{2}{7} a_2 + \frac{100}{693} a_4 \right) \langle P_2 g \rangle_0 + \right. \\ &\quad \left. + \left(a_0 + \frac{180}{693} a_2 + \frac{162}{1001} a_4 \right) \langle P_4 g \rangle_0 \right), \end{aligned} \quad (5.12c)$$

with $\tau \equiv 2L^2\lambda$. If we then compute $S = 1 + \rho \langle g \rangle_\vartheta = 1 + \rho (a_0 \langle g \rangle_0 + a_2 \langle P_2 g \rangle_0 + a_4 \langle P_4 g \rangle_0)$, we obtain a fraction with a third-order polynomial in ρ in the denominator. The root ρ_p of this polynomial is the percolation threshold, so it satisfies

$$b_0 + b_1 \pi \tau \rho + b_2 (\pi \tau \rho)^2 + b_3 (\pi \tau \rho)^3 = 0, \quad (5.13)$$

with coefficients

$$b_0 = -2029547520, \quad (5.14a)$$

$$b_1 = -55440(-7865 + 728a_2 + 700a_4), \quad (5.14b)$$

$$b_2 = 630 \left(143 \left(\frac{781}{4} + 109a_2 - 140a_2^2 \right) + 44(342 + a_2)a_4 - 1412a_4^2 \right), \quad (5.14c)$$

$$\begin{aligned} b_3 &= 5 \left(-\frac{1287}{8} (-77 - 84a_2 + 84a_2^2 + 32a_2^3) + 198 (56 - 7a_2 + 41a_2^2) a_4 \right. \\ &\quad \left. + \frac{9}{2} (-1127 + 572a_2) a_4^2 - 3146a_4^3 \right). \end{aligned} \quad (5.14d)$$

It is important to note that the coefficients themselves also depend on the density ρ as well as on the field strength K because they obey Onsager's equation (5.3). To determine the functional dependence of these coefficients on ρ and K , we apply the addition theorem once more in Eq. (5.3), use Eq. (5.10) again, and expand the logarithm for small values of a_2/a_0 and a_4/a_0 . This gives

$$\begin{aligned} \log(a_0) + h_0 + h_2 P_2 + h_4 P_4 &= \mu - 16c(2a_0 d_0 P_0(\cos \vartheta) + \\ &\quad \frac{2}{5} a_2 d_2 P_2(\cos \vartheta) + \frac{2}{9} a_4 d_4 P_4(\cos \vartheta)) - \beta K \cos^2 \vartheta, \end{aligned} \quad (5.15)$$

where we introduced a dimensionless concentration $c \equiv \pi\rho L^2 D/4$, and where

$$h_0 = -\frac{1}{10} \frac{a_2^2}{a_0^2}, \quad (5.16a)$$

$$h_2 = \frac{a_2}{a_0} - \frac{a_2^2}{7a_0^2} - \frac{2}{7} \frac{a_2 a_4}{a_0^2}, \quad (5.16b)$$

$$h_4 = \frac{a_4}{a_0} - \frac{9}{35} \frac{a_2^2}{a_0^2} - \frac{180}{693} \frac{a_2 a_4}{a_0^2}. \quad (5.16c)$$

We write $\cos^2 \vartheta = \frac{2}{3} P_2(\cos \vartheta) + \frac{1}{3} P_0(\cos \vartheta)$ and take the inner product of the result with $P_2(\cos \vartheta)$ and with $P_4(\cos \vartheta)$, giving two equations for a_2 and a_4 ,

$$\frac{a_2}{a_0} - \frac{a_2^2}{7a_0^2} - \frac{2}{7} \frac{a_2 a_4}{a_0^2} = -\frac{16c}{5\pi} d_2 a_2 - \frac{2}{3} \beta K \quad (5.17a)$$

$$\frac{a_4}{a_0} - \frac{9}{35} \frac{a_2^2}{a_0^2} - \frac{180}{693} \frac{a_2 a_4}{a_0^2} = -\frac{16c}{9\pi} d_4 a_4. \quad (5.17b)$$

This fixes a_2 and a_4 , were we note that from the normalisation of ψ it follows that $a_0 = 1/2$. If we put $a_4 = 0$ and insert $a_0 = 1/2$, we find from Eq. (5.17a) that $a_2 = -4\beta K / (3(4 - c))$ for weak fields. Hence, a_2 diverges as $c \rightarrow 4$, which, not surprisingly, coincides with the nematic spinodal where the isotropic phase becomes absolutely unstable [104].

5.3 Results

The polynomial equation (5.13) for the percolation threshold ρ_p needs to be combined with Eqs. (5.17a) and (5.17b). This gives three equations for the three unknowns a_2 , a_4 , and ρ_p in terms of the field strength K and the ratio λ/D that measures how easily charge transport between two rods takes place. The percolation threshold we calculated is plotted for reasonable values of λ/D for single-walled and multi-walled carbon nanotubes [97, 160] in Fig. 5.1. The figure shows that the percolation threshold quite strongly increases with increasing field strengths, irrespective of whether the field is of the orienting or disorienting type. For large enough field strengths $|\beta K| \gtrsim 0.5$ that depends on the precise value of λ/D a percolating network does not form, at least in the low-loading regime where c_p is of the order unity and the volume fraction is of the order $\varphi_p = c_p D/L = \mathcal{O}(D/L) \ll 1$. We return to this below.

Another remarkable result that we read off from Fig. 5.1 is that for values of βK , where a percolating network does form at some low particle concentration, the network dissolves again at higher particle loadings, i.e., exhibits re-entrance behaviour. Interestingly, a similar kind of re-entrance with increasing, imposed alignment was observed

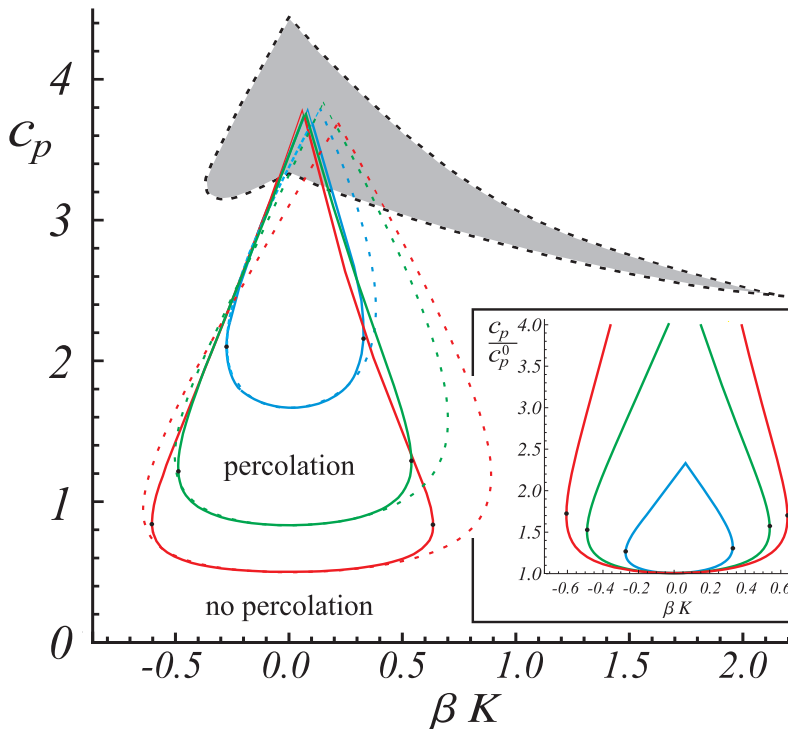


Figure 5.1: Scaled particle concentration $c_p = \varphi_p L/D = \pi D L^2 \rho_p / 4$ at the percolation threshold as a function of the dimensionless field strength βK . Solid lines: connectivity percolation, dashed curves: contact-volume approach for $\lambda/D = 0.3$ (top), 0.6 (middle), and 1 (bottom). Only in the enclosed areas a percolating network exists. The shaded area is the region of co-existing isotropic (paranematic) and nematic phases [161]. Inset: calculated percolation thresholds scaled to the zero-field value c_p^0 . The dots indicate the largest value of $|\beta K|$ that allows for a percolation threshold.

in computer simulations of the electrical conductivity of systems of penetrable rod-like particles [154]. According to our calculations, this is caused by the field-induced alignment that is enhanced by the anisotropic excluded-volume interactions. For small field strengths this causes the re-entrant transition to penetrate the non-percolating regime the region where the transition to a nematic phase occurs [165]. The shape and size of the percolating regime depends sensitively on the ratio λ/D . We see from Fig. 5.1 that the lower percolation threshold decreases with increasing λ/D , whereas the re-entrance threshold depends weakly on λ/D .

If we amend the contact-volume approach [95, 151, 156, 157] with the Onsager theory for the alignment of hard rods in an external field, we presume the convolution of Eq.

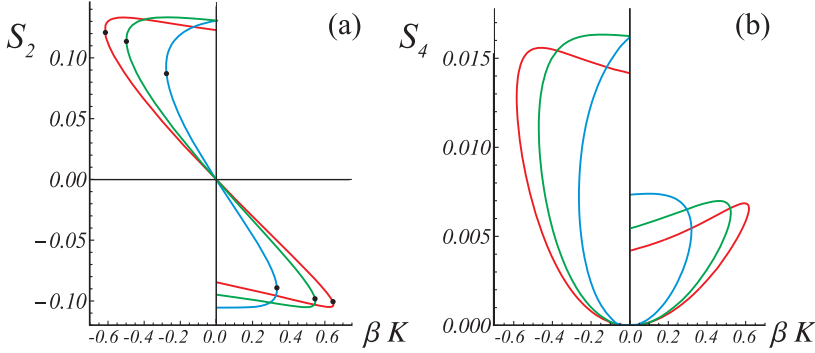


Figure 5.2: The order parameters $S_2 = 2a_2/5$ (a) and $S_4 = 2a_4/9$ (b) as a function of the dimensionless field strength βK at the percolation threshold. From steepest to flattest: $\lambda/D = 0.3, 0.6$ and 1 . A positive βK causes a preference for alignment perpendicular to the field ($S_2 < 0$), whereas a negative βK imposes a preferred orientation along the field direction ($S_2 > 0$). The dots in (a) show the largest value of $|\beta K|$ that allows for a percolation threshold, beyond which $|S_2|$ increases further, see also Fig. 5.1.

(5.2) to be separable, which gives the familiar expression $\rho_p^{-1} = \left\langle \left\langle \hat{f}^+(0, \mathbf{u}, \mathbf{u}') \right\rangle_{\mathbf{u}} \right\rangle_{\mathbf{u}'}$ that was introduced in chapter 1. If we insert our result for $\hat{f}^+(0, \mathbf{u}, \mathbf{u}')$ we find

$$\frac{1}{\rho_p} = 2L^2\lambda \sum_{n=0}^{\infty} d_{2n} \langle P_{2n}(\cos \vartheta) \rangle_{\vartheta}^2 = \frac{L^2\lambda\pi}{1440} (720 - 288\pi^2 a_2^2 - 20\pi^2 a_4^2). \quad (5.18)$$

If we combine this with Eqs. (5.17a) and (5.17b) to find the percolation threshold ρ_p as a function of βK and compare the result to our theory, we have to conclude that the contact-volume approach (dashed lines) significantly underestimates the impact of the external field on the percolation threshold. For small field strengths the underestimation is roughly 10 %, but at re-entrance for high loadings the error can be up to a few 100 %. It appears that ignoring couplings between angular correlations of particles is at the root of this discrepancy [160].

It is instructive to evaluate the relevant order parameters along the stability boundary of our model of electrical percolation in rod dispersions. These are the familiar nematic order parameters $S_2 \equiv \langle P_2(\cos \vartheta) \rangle_{\mathbf{u}} = 2a_2/5$ and $S_4 \equiv \langle P_4(\cos \vartheta) \rangle_{\mathbf{u}} = 2a_4/9$, shown in Fig. 5.2. First, we find S_4 to be always positive and much smaller than the corresponding value of S_2 , justifying our earlier assumption. Second, we find that the order parameter S_2 increases along the curves where the percolation threshold increases, even beyond the inflection point where $|S_2| \approx 0.1$. The curves confirm that for a given field strength, the degree of order increases with increasing density, which is the running variable along the curves. The largest value of S_2 for which percolation occurs is below that of the nematic

phase [161], so there percolation is lost completely.

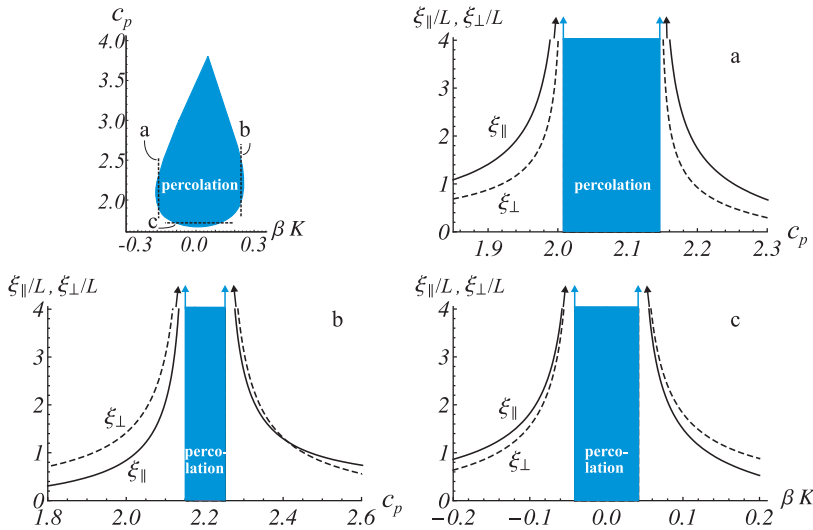


Figure 5.3: Top left: scaled particle concentration $c_p = \pi L^2 D \rho_p / 4$ at the percolation threshold as a function of the dimensionless field strength βK for $\lambda/D = 0.3$ from Fig. 5.1. Paths a, b, and c are traversed in the calculation of the correlation lengths ξ_{\parallel} (solid) and ξ_{\perp} (dashed), as shown in the corresponding graphs on the right for $\beta K = -0.27$ (a), $\beta K = 0.33$ (b), and a horizontal traversal of Fig. 5.1 for $c_p = 1.67$ (c). Away from the percolation threshold the correlation lengths decay to the radius of gyration $L/\sqrt{12}$ of a rod.

In order to investigate the structure of our clusters upon approach of the percolation threshold, we need to probe the wave-vector dependence of the connectedness function $\langle\langle \hat{P}(\mathbf{q}, \mathbf{u}, \mathbf{u}') \rangle\rangle_{\mathbf{u}, \mathbf{u}'} = \langle\langle \hat{P}(0, \mathbf{u}, \mathbf{u}') \rangle\rangle_{\mathbf{u}, \mathbf{u}'} + \langle\langle \mathbf{M}(\mathbf{u}, \mathbf{u}') \rangle\rangle_{\mathbf{u}, \mathbf{u}'} : \mathbf{q}\mathbf{q}/2 + \dots$, with $\mathbf{M}(\mathbf{u}, \mathbf{u}') \equiv \partial^2 \hat{P} / \partial \mathbf{q}^2 |_{\mathbf{q}=0}$ [34]. The linear term in \mathbf{q} drops out for symmetry reasons. From Eq. (5.2) we obtain a self-consistent equation for

$$\begin{aligned} \langle \mathbf{M}(\mathbf{u}, \mathbf{u}') \rangle_{\mathbf{u}, \mathbf{u}'} &= 2\lambda L^2 \rho \langle |\sin \gamma(\mathbf{u}, \mathbf{u}')| \langle \mathbf{M}(\mathbf{u}', \mathbf{u}'') \rangle_{\mathbf{u}', \mathbf{u}''} \rangle_{\mathbf{u}, \mathbf{u}'} \\ &+ \frac{\lambda L^4}{6} \langle |\sin \gamma(\mathbf{u}, \mathbf{u}')| (\mathbf{u}\mathbf{u} + \mathbf{u}'\mathbf{u}') (1 + \rho g(\mathbf{u}')) \rangle_{\mathbf{u}, \mathbf{u}'} \end{aligned} \quad (5.19)$$

This equation for $\mathbf{M}(\mathbf{u})$ is quite analogous to the one for $g(\mathbf{u})$ we found to compute the cluster size (the mean number of particles in a cluster), because only the term that has no dependence on the variable in question (here \mathbf{M} instead of g), is different. As a consequence, the point where the moments of $\mathbf{M}(\mathbf{u})$ diverge, is the same as that for the moments of $g(\mathbf{u})$, i.e., for the isotropic case discussed above [152]. Because of azimuthal symmetry the matrix $\langle\langle \mathbf{M}(\mathbf{u}, \mathbf{u}') \rangle\rangle_{\mathbf{u}, \mathbf{u}'}$ has nonzero elements on its diagonal only, one associated with cluster growth parallel to the field direction and the others with that

perpendicular to it. The wave vector \mathbf{q} separates into components q_{\parallel} parallel and q_{\perp} perpendicular to the field. We compute $\langle\langle \mathbf{M}(\mathbf{u}) \rangle_{\mathbf{u}} \rangle_{\mathbf{u}'}$ in manner similar to that of the cluster size S . Our final result can be expressed as $\langle\langle \hat{P} \rangle_{\mathbf{u}} \rangle_{\mathbf{u}'}/\langle\langle \hat{P} \rangle_{\mathbf{u}} \rangle_{\mathbf{u}'} = 1 + \xi_{\parallel}^2 q_{\parallel}^2 + \xi_{\perp}^2 q_{\perp}^2$, with correlation lengths ξ_{\parallel} and ξ_{\perp} . Values of ξ_{\parallel} and ξ_{\perp} for a vertical and horizontal traversal of the phase diagram of Fig. 5.1 are shown in Fig. 5.3.

Both correlation lengths ξ_{\parallel} and ξ_{\perp} diverge as $1/|\rho_p - \rho|^{1/2}$ for constant K and as $1/|\beta K_p - \beta K|^{1/2}$ for constant ρ , with K_p the critical field strength for a given density. The mean-field exponents $\nu_{\parallel} = \nu_{\perp} = 1/2$ that we find are exact for hard rods in the limit of infinite aspect ratio [160]. However, the prefactors are not equal and depend on the density, the sign and strength of the external field. For a disorienting field, $\beta K > 0$, the clusters are flat because $\xi_{\perp} > \xi_{\parallel}$, while for an orienting field, $\beta K < 0$, they are elongated: $\xi_{\perp} < \xi_{\parallel}$. Although percolation in systems of aligned rods seems superficially related to that of directed percolation, the critical exponents for the latter have been found to be $\nu_{\parallel} = 1$ and $\nu_{\perp} = 1/2$ in three dimensions in mean-field theory [166]. Hence, anisotropic continuum connectedness percolation of elongated particles is not in the universality class of directed percolation.

5.4 Conclusions

In this chapter we have presented an analytical theory that combines Onsager theory and connectedness-percolation theory to show how an externally applied field enhanced by excluded-volume interactions significantly destabilises percolating clusters of hard, rod-like particles. We find that the percolating network is limited to an island of stability in the phase diagram, bounded from above by the isotropic-nematic phase transition. These effects are stronger than predicted by the contact-volume approach because of translation-rotation coupling, similar to what we observed in chapters 2 and 3 for the effect of a polydispersity in size and connectivity range.

Upon approach of the percolation threshold, the size of clusters of connected particles diverges with the same scaling exponent parallel and perpendicular to the field direction. Hence, directed percolation and anisotropic continuum percolation of elongated particles do not belong to the same universality class. Still, due to non-universal prefactors the clusters are anisotropic; they are elongated for orienting and flat for disorienting fields. This suggests that this cluster anisotropy could be used in thin films to fabricate composites with strongly anisotropic electrical conductivities despite the very low particle loading [152, 155].

A limitation of our model is that it only allows for modest degrees of orientation, meaning that the orientation distribution can be written as $\psi(\vartheta) = a_0 + a_2 P_2(\cos \vartheta) +$

$a_4 P_4(\cos \vartheta)$, with $|a_4| \ll |a_2|$. Higher degrees of orientation require more terms in this expansion or a different functional description of ψ , both of which prohibit an analytical solution of the problem. However, the limiting case of perfectly ordered particles can again be dealt with analytically because in that case there is no angular dependence of the distribution function and the Mayer functions. This means that the contact-volume approach can be used, which gives $\langle \langle \hat{f}^+ \rangle_{\mathbf{u}} \rangle_{\mathbf{u}'} = 2\pi\lambda L(2D + \lambda)$ for an orienting field. Hence, in volume fraction $\varphi_p = D^2/8\lambda(2D + \lambda)$, so $c_p = LD/(8\lambda(2D + \lambda))$ for an orienting field, so $c_p \sim L/(D + \lambda)$ because $D/8\lambda = \mathcal{O}(1)$. The reason is that for an orienting field the excluded volume has the same scaling as the rod volume. Such an orientation in the direction of the external field can be the result of a high density or a very strong field, so it is located for negative values of βK at large values of c_p above the island of stability in the phase diagram of Fig. 5.1.

For a disorienting field the situation is different because in this case the excluded volume scales as $L^2 D$ like in the isotropic distribution. This gives $\langle \langle \hat{f}^+ \rangle \rangle' = 2\lambda L^2/\pi$, so $\varphi_p = \pi^2 D^2/8\lambda L$ and $c_p = \pi^2 D/8\lambda = \mathcal{O}(1)$. A perfectly disorienting field can only be caused by a very strong field, so it is located at a value $c_p = \pi^2 D/8\lambda$ for large values of βK in Fig. 5.1. As an explanation for the discrepancy between the values of c_p for both types of field, we note that in an orienting field the rods are all parallel and therefore cannot span large distances, implying small contact volumes, whereas a disorienting field causes the rods to line up in layers in which there is rotational freedom, making the contact volume much larger.

This chapter is the last one of four chapters that deals with the effect that the particle formulation and the processing in the fluid stages of the nanocomposite fabrication has on the network formation of hard rod-like and plate-like particles that have been dispersed in a liquid host material. Clearly, the central message that we obtain from our calculations in this chapter and chapters 2 and 3 is that connectivity percolation is a highly sensitive function of all thinkable system parameters. These include size, shape, connectivity, alignment, and any variation in and correlations between them. This suggests that in order to draw qualitative conclusions from experiments complete control over, or at least a full description of these system parameters is necessary. In this light it seems reasonable to suggest that the processing conditions leading up to the final nanocomposite must be as important as the properties of the nanofillers used in it.

In this chapter we have encountered a competition between the transitions from an isotropic, non-percolation phase to a percolating one and that to a nematic phase, which may or may not percolate. As already alluded to in the Introduction in chapter 1, this nematic phase has cylindrical and inversion symmetry in which the particles exhibit short-range, liquid-like positional order. A nematic is a symmetry-broken fluid, which

makes the elastic and surface properties quite complex. This gives rise to interesting interfacial phenomena because of the competition between the anisotropic surface tension and bulk elasticity of the liquid crystal. This competition manifests itself in, e.g., capillary rise profiles and intriguing shapes and structures of nematic droplets. The capillary rise of an isotropic-nematic interface up a vertical wall is the topic of chapter 6, where we find surprising meniscus profiles. Another manifestation of this competition is in nematic droplets, also called tactoids, that emerge under conditions where the isotropic and nematic phase co-exist and these we focus on in chapters 7, 8, and 9.

Capillary rise of an isotropic-nematic fluid interface

6

A theoretical study is presented on the shape of the interface between co-existing isotropic and nematic phases in contact with a solid vertical wall. The interface profile is determined by a competition between three surface tensions, two anchoring strengths, gravity and the Frank elastic constants of the director field. In the weak-anchoring limit the director field is rigid and uniform, and we find the capillary-rise height to depend non-trivially on the orientation of the director field relative to the solid-fluid interface. For strong surface anchoring the director field adjusts to the preferred homeotropic or planar anchoring at the solid-liquid and liquid-liquid interfaces. The shape of the interface profile is now a function of the balance between the surface energy and the splay and bend elastic-deformation energies. Interestingly, for both weak and strong anchoring the profile decays non-monotonically albeit only very weakly so, in agreement with recent observations. We compare our theory with experimental data on dispersions of gibbsite platelets and are able to extract from them the surface tension and the anchoring strength.[†]

[†]The contents of this chapter have been published as:
R. H. J. Otten and P. van der Schoot, *Langmuir* **25**, 2427 (2009).

6.1 Introduction

As already alluded to in the introduction in chapter 1, the competition between the anisotropic surface tension and bulk elasticity of the liquid crystal manifests itself in the capillary rise of an isotropic-nematic interface up a vertical wall. Clearly, the gravitational force plays an important role as well, and this competition between gravity, surface tension and anchoring, and bulk elasticity in the capillary-rise region, expresses itself in the ratio of two length scales that present themselves naturally for the problem in hand, and that demarcates the boundary between two regimes with different director-field structures, see Fig. 6.1.

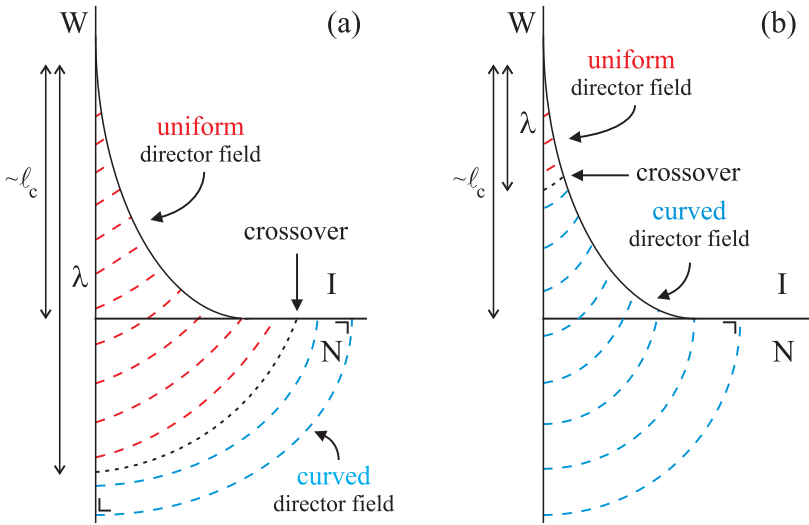


Figure 6.1: Two types of director field in the capillary-rise region enclosed by the isotropic-nematic (IN) interface profile and a vertical wall (W). The field away from this region is dominated by surface anchoring. (a) If the capillary length ℓ_c measuring the rise height is much smaller than the extrapolation length λ that is a measure of the stiffness of the director field, then the field in the rise region is approximately uniform. (b) On the other hand, if the reverse is true and $\lambda/\ell_c \ll 1$, then the field in the rise region is deformed because the surface anchoring is dominant. In these two examples we assume homeotropic anchoring at the IN and the NW interface.

The first length is the extrapolation length $\lambda \equiv K/|\zeta_{\text{IN}}|$, where K is some average of the Frank elastic constants and $\zeta_{\text{IN}} \geq 0$ the anchoring strength of the director field to the isotropic-nematic interface, and the second the usual capillary length $\ell_c \equiv \sqrt{2\gamma_{\text{IN}}/\Delta\rho_m g}$. The sign of the anchoring strength indicates a preference for homeotropic or planar anchoring, see the caption to Fig. 1.5. The capillary length is a function of the “bare”

interfacial tension γ_{IN} between the co-existing isotropic and nematic phases, the mass-density difference $\Delta\rho_m$ between the two phases and the gravitational acceleration g . The rise height is proportional to the capillary length and becomes exactly equal to the rise height for isotropic fluids of which one completely wets the surface and the contact angle is zero [167].

Relying on scaling arguments, Van der Beek and collaborators [45] argued recently that if the extrapolation length greatly exceeds the capillary length, so $\lambda/\ell_c \gg 1$, then the director field in the rise region should be approximately uniform on account of the rigidity of the field on that scale albeit that on large scales (away from the rise region) the director field does deform to accommodate the preferred anchoring. Conversely, if $\lambda/\ell_c \ll 1$ the field in the rise region also deforms to accommodate the predominance of the surface anchoring, see Fig. 6.1. The former regime we refer to as the *weak-anchoring* regime, the latter the *strong-anchoring* regime. In the intermediate case, where $\lambda/\ell_c \approx 1$, the director field crosses over smoothly from uniform to curved in the capillary-rise region. The question arises what in practice is the most prevalent regime, i.e., weak anchoring with $\lambda/\ell_c \gg 1$, intermediate anchoring with $\lambda/\ell_c \approx 1$, or strong anchoring, $\lambda/\ell_c \ll 1$.

Capillary-rise experiments on the lyotropic system of co-existing isotropic and nematic phases of dispersions of gibbsite platelets in the solvent toluene show that $\lambda \approx 70 \mu\text{m}$, whilst $\ell_c \approx 6 \mu\text{m}$, so for this type of system $\lambda/\ell_c \gg 1$ [45]. For thermotropic liquid crystals we would expect the opposite limit to hold, $\lambda \ll \ell_c$, because, e.g., for an interface of water and the thermotropic nematic 5CB (4-cyano-4'-pentylbiphenyl), $K \approx 10^{-12} \text{ N}$, $\gamma_{\text{IN}} \approx |\zeta_{\text{IN}}| \approx 10^{-3} \text{ N/m}$, and $\Delta\rho_m \approx 50 \text{ kg/m}^3$ [168–170], giving $\lambda \approx 10^{-9} \text{ m}$ and $\ell_c \approx 10^{-3} \text{ m}$ and hence $\lambda/\ell_c \ll 1$. We argue that for lyotropic systems generally $\lambda/\ell_c \gg 1$, while for thermotropic systems $\lambda/\ell_c \ll 1$. Simple scaling arguments bear out this fundamental difference in behaviour of lyotropics and thermotropics, which is related to the huge size difference of the nematogens involved.[†]

Theoretically, the capillary rise of the interface between a nematic and an isotropic fluid against a vertical wall has not been studied in detail albeit that several more general aspects of the problem have been discussed in the literature [43–45, 70–74, 91, 171–176]. The purpose of this chapter is to fill in this gap and provide a tool for estimating surface anchoring energies from capillary-rise experiments. This is possible because we obtain analytical expressions for the contact angle and rise height in the relevant limits of weak and strong anchoring. We apply our theory to experimental observations of Van der

[†]Because $K \approx k_B T/\xi$ and $\gamma_{\text{IN}} \approx |\zeta_{\text{IN}}| \approx k_B T/\xi^2$ with ξ the average dimensions of the nematogens, we must have $\lambda/\ell_c \propto \xi^2$. So, the larger the particles, the larger λ/ℓ_c . For thermotropics $\xi = \mathcal{O}(1) \text{ nm}$, whilst for lyotropic $\xi = \mathcal{O}(10^2 - 10^3) \text{ nm}$. Hence, we expect the quantity λ/ℓ_c for the latter to be $\mathcal{O}(10^4 - 10^6)$ times larger than that for the former.

Beek et al. [45], and are able to extract more accurately values for both the interfacial tension and the anchoring strength than provided in that work.

The approach we follow to find the meniscus shape and director field in the capillary-rise region is first to set up an appropriate free-energy functional and subsequently to minimise this with respect to both the profile and the director field. Just as is the case for nematic droplets [53, 54, 88], this produces governing equations that are not easily solved analytically. Hence, we simplify the problem by prescribing plausible director-field geometries inspired by the limiting cases of a uniform and a curved director field. The advantage of our approach is that it is straightforward to apply in arbitrary geometries and, as already announced, produces analytical predictions [91, 171–176].

The main conclusions of our work can be summarised as follows.

1. In the weak-anchoring limit, the capillary-rise height, contact angle as well as the far-field decay length of the profile depend non-trivially on two anchoring strengths and the angle of the nematic director field relative to the bulk interfaces.
2. In the strong-anchoring limit, the capillary-rise height by and large obeys the classical results for isotropic fluids because the surface enslaves the director field. The shape of the interface profile, however, deviates strongly from the classical result, and is due to a competition between surface tension and the splay and bend deformation of the director field.
3. For both weak and strong anchoring we find the interface profiles to be weakly non-monotonic. A closer analysis of polarisation micrographs of the contact-line region in co-existing isotropic and nematic dispersions of gibbsite in toluene confirms this.

The remainder of this chapter is organised as follows. First, we show in section 6.2 how for a nematic liquid crystal with a uniform director field in the capillary-rise region the interface profiles can be obtained from a combination of the surface and gravitational free energies. For the surface free energy we use the familiar expression proposed by Rapini and Papoular [40]. Next, in section 6.3, we adopt the same free-energy-functional approach, where we impose homeotropic anchoring of the director field to both the isotropic-nematic and the nematic-wall interface, and invoke the equal-constant approximation to describe the contribution from the elastic deformation of the director field. Finally, conclusions and a discussion of our findings are presented in section 6.4.

6.2 Weak surface anchoring

Consider an interface between an isotropic (I) and a nematic (N) fluid in contact with a flat vertical wall (W). The fluid interface rises up the wall because the surface tensions between the IW and the NW interfaces are not equal. We consider a nematic fluid domain that is assumed to be large enough not to be influenced by other boundaries and to be denser than the isotropic phase. For lyotropic liquid crystals this is usually the case on account of the larger particle concentration in the nematic phase [6].

The location of the interface is indicated by $y(x)$, where y is the coordinate along the wall relative to a reference plane and x is the coordinate perpendicular to it, see Fig. 6.2. The wall in the z -direction, i.e., perpendicular to the plane of interest, is supposed to be infinitely long so a quasi two-dimensional analysis suffices. The director field in the nematic domain is presumed to be rigid, that is, uniform, and to make a fixed angle ϕ with respect to the normal to the solid wall. So, formally we presume the limit $\lambda/\ell_c \rightarrow \infty$ to hold. Below we relax this condition and discuss what happens when λ/ℓ_c is large but finite.

The (contact) angle that the fluid-fluid interface makes with the wall we denote ϑ . We shall not treat it as a given material parameter but in fact derive the pertinent Young's equation that describes it as a function of the various surface tensions. The surface tensions of the three interfaces we denote σ_{IN} , σ_{NW} , and σ_{IW} , of which σ_{IN} and σ_{NW} are assumed to be of the Rapini-Papoular type [40] that was introduced in chapter 1, so of the generic form $\sigma = \gamma + \zeta \sin^2 \alpha$, with γ the usual (bare) surface tension and ζ the anchoring strength; α is the angle between the field and the normal to the interface, see Fig. 1.5.

We now have to distinguish the NW interface from that of the co-existing isotropic and nematic phases. Let $\alpha = \phi$ denote the angle of the director field and the normal to the NW interface and $\alpha = \beta$ that at the IN interface. These two angles are related to each other if we presume the tangent $y'(x) \equiv dy/dx$ to the profile of the IN interface (the meniscus) to be a known function of the distance x from the wall. Simple geometry then gives $\beta = \pi/2 - \chi - \phi$, with $\chi = -\arctan y'$, see Fig. 6.2. Hence, the surface tensions obey the relations

$$\sigma_{IN} = \gamma_{IN} + \zeta_{IN} \sin^2 \beta = \gamma_{IN} + \zeta_{IN} \frac{(\cos \phi + y' \sin \phi)^2}{1 + y'^2} \quad (6.1a)$$

$$\sigma_{NW} = \gamma_{NW} + \zeta_{NW} \sin^2 \phi, \quad (6.1b)$$

$$\sigma_{IW} = \gamma_{IW}. \quad (6.1c)$$

As already alluded to in chapter 1, the sign of the anchoring strength ζ indicates the preferred type of anchoring. If $\zeta > 0$, the preferred anchoring is homeotropic and if

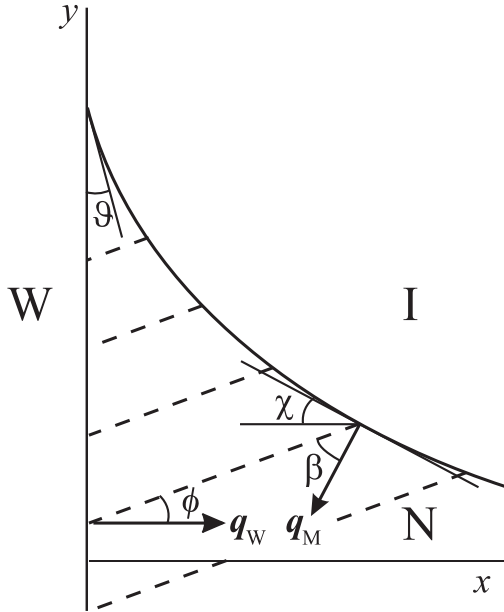


Figure 6.2: The capillary rise of isotropic-nematic (IN) interface up a solid flat wall (W). The director field (dashed lines) is assumed to be homogeneous. It makes an angle ϕ with the normal \mathbf{q}_W to the wall and an angle β with the normal \mathbf{q}_M to the IN interface. The tangent to the profile and the horizontal make an angle χ and θ is the contact angle of the profile with the wall.

$\zeta < 0$, it is planar. Nematic dispersions of rod-like colloids for entropic reasons prefer planar anchoring, whilst in those of disk-like colloids the favoured type of anchoring is homeotropic [80, 81, 87]. This applies to the anchoring at flat walls but also to the interface with the isotropic phase [61, 75]. It is for this reason that we only consider symmetric anchoring conditions.

We presume weak surface anchoring to hold, implying that the director field in the capillary-rise region is rigid and remains uniform, so the elastic energy $F_e = 0$. This must be the case if the extrapolation length $\lambda \equiv K/|\zeta|$ is very much larger than the rise height $h \equiv y(0)$, where we plausibly assume that $\zeta \approx \zeta_{\text{IN}} \approx \zeta_{\text{NW}}$ that for dispersions of hard rods and disks seems to be valid [45, 76, 82, 87]. Refer again to Fig. 6.1. In the weak-anchoring limit, and the excess free energy F per unit length of the meniscus is given by

$$F[y, y'] = \int_0^\infty dx \left(\sigma_{\text{IN}} \left(\sqrt{1 + y'^2} - 1 \right) + (\sigma_{\text{NW}} - \sigma_{\text{IW}}) y \delta(x) + \frac{1}{2} \Delta \rho_m g y^2 \right), \quad (6.2)$$

if we take as a reference a flat interface with $y(x) = 0$ for all $x > 0$, and where we remind

the reader that for now we let $\lambda/h \propto \lambda/\ell_c \rightarrow \infty$. Because of the presence of the Dirac delta “function” $\delta(x)$ in Eq. (6.2), we formally have to extend the integration slightly below zero, so the lower bound should in reality read 0^- . Again, $\Delta\rho_m$ denotes the mass-density difference between the nematic and isotropic fluid and g the gravitational acceleration. The first term in Eq. (6.2) represents the energy associated with the additional length of the IN interface when it creeps up the wall, the second term gives the contribution due to the difference in surface tension between the IW and NW interface when a part of the wall is wet by the nematic and the third term accounts for the gravitational energy.

In equilibrium, the optimal profile $y(x)$ minimises the free energy. Functional minimisation of F with respect to the profile $y(x)$, i.e., putting $\delta F/\delta y = 0$ [177], gives a second-order integral term for the bulk profile and a boundary term that is the generalisation of the familiar Young’s law for the contact angle. The bulk profile we find to

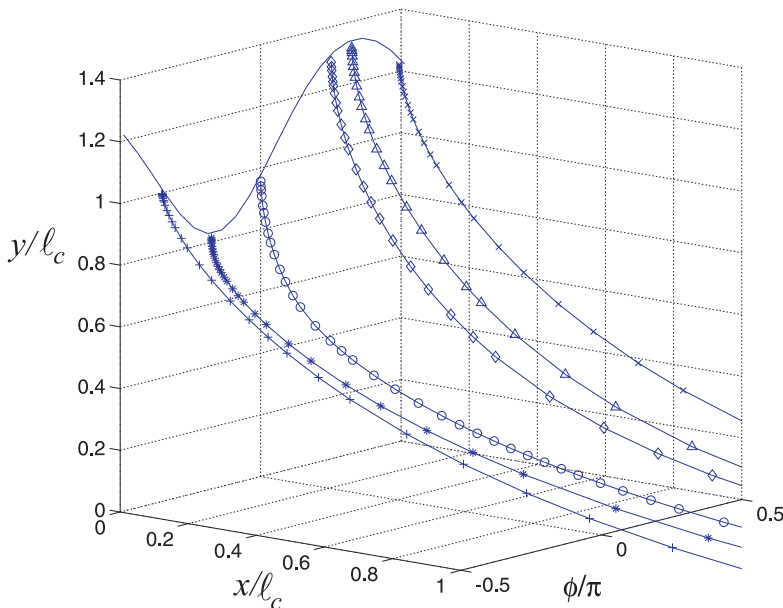


Figure 6.3: The isotropic-nematic interface profile close to the wall for several values of the attack angle of the director ϕ , assuming complete wetting for the weak homeotropic anchoring case with $\omega \equiv \zeta_{\text{IN}}/\gamma_{\text{IN}} = 0.5$. The rise height (solid line) depends on the value of the function $f(\phi) = \sin^2 \phi + \sin 2\phi$, which indicates whether the rise height is smaller, $f < 0$, or larger, $f > 0$, than that of an isotropic fluid, at least if $\omega > 0$. See also the discussion in the main text.

obey the following highly non-linear differential equation,

$$1 + \omega \sin^2 \phi = \hat{y}^2 + \frac{1}{2(1 + \hat{y}'^2)^2} \left((2 + \omega)(1 + \hat{y}'^2)^{3/2} + \omega(-2 + \sqrt{1 + \hat{y}'^2}) \left((1 + 3\hat{y}'^2) \cos 2\phi + 2\hat{y}'^3 \sin 2\phi \right) \right), \quad (6.3)$$

where we have introduced the dimensionless variables $\hat{y} \equiv y/\ell_c$ and $\hat{x} \equiv x/\ell_c$, which are the profile coordinates on the scale of the capillary length ℓ_c , and where we also have introduced the dimensionless IN anchoring strength $\omega \equiv \zeta_{\text{IN}}/\gamma_{\text{IN}}$. To obtain Eq. (6.3), we have multiplied the result of the free-energy minimisation by \hat{y}' , integrated left and right of the equal sign and used the condition that for $\hat{x} \rightarrow \infty$, $\hat{y} = \hat{y}' \rightarrow 0$, to fix the integration constant. A consequence of this is that $\hat{y}' = 0$ can only hold for $\hat{y} = 0$, so for $\hat{x} \rightarrow \infty$. This means that $\hat{y}' < 0$ for all \hat{x} , so the profile decreases monotonically, at least in the limit $\lambda/\ell_c \rightarrow \infty$. As we shall see below, for any finite value of λ/ℓ_c this is strictly not true for $x \gtrsim \lambda$.

In Fig. 6.3 we have plotted our numerically obtained solutions to Eq. (6.3), showing that the capillary-rise height, the far-field decay of the profile and the contact angle of the profile at the wall depend non-trivially on the angle ϕ between the director field and the normal to the wall. The figure shows that the average radius of curvature of the profile is of the order ℓ_c , as to be expected. Referring to the discussion of the Introduction, we estimate that if the radius of curvature is large compared to the size of the particles, i.e., if the capillary length is large compared to the particle size, we need not explicitly consider any impact of curvature on the surface tension.

Salient features of our findings may be summarised as follows. We focus on the capillary-rise height, the far-field profile and the contact angle.

i) Capillary-rise height. We need not solve this Eq. (6.3) in order to obtain an analytical expression for the capillary-rise height $h \equiv y(0)$. By inserting the identity $\vartheta = -\arctan(1/y'(0))$ into Eq. (6.3), we obtain,

$$\left(\frac{h}{\ell_c} \right)^2 = 1 + \omega \sin^2 \phi - \frac{1}{4} \sin \vartheta \left(4 + 2\omega + \omega \left(-2 + \frac{1}{\sin \vartheta} \right) \left(3 \sin(\vartheta - 2\phi) + \sin(3\vartheta - 2\phi) \right) \right), \quad (6.4)$$

which is still a function of the as yet unknown contact angle ϑ . For $\omega = 0$, the classical result $h = \ell_c \sqrt{1 - \sin^2 \vartheta}$ for isotropic fluids is immediately retrieved. We note that our expression for the rise height simplifies enormously in the limit of complete wetting

where $\vartheta = 0$. In that case we obtain,

$$h = \ell_c \sqrt{1 + \omega (\sin^2 \phi + \sin 2\phi)}, \quad (6.5)$$

which, depending on the angle ϕ between the director and the normal to the wall, can be larger or smaller than that of an equivalent isotropic fluid of the same capillary length, and for which $\omega = 0$. If $\omega > 0$, so for homeotropic anchoring, h is larger than ℓ_c if $\phi > 0$ or $\phi < -\arccos(1/\sqrt{5}) \approx -1.11$ radians. The maximal rise height of $h = 1.35 \ell_c$ is for $\phi = \arccos\left(\sqrt{(5 - \sqrt{5})/10}\right) \approx 1.02$ and the minimal rise of $h = 0.83 \ell_c$ is for $\phi = -\arccos\left(\sqrt{(5 + \sqrt{5})/10}\right) \approx -0.55$.

One might wonder what the origin is of the different terms in Eq. (6.5) for the rise height. In fact, one could argue that the rise height seems to contain contributions from both the near- and far-field of the profile. This we deduce from the fact that the $\sin 2\phi$ term is characteristic of the presence of the wall, as can be verified by letting $\hat{y}' \rightarrow -\infty$ in Eq. (6.3), because then the second term in the right-hand-side of Eq. (6.3) reduces to $\omega \sin 2\phi$. The $\sin^2 \phi$ term describes the influence from the profile far from the wall as follows from setting $\hat{y}' \rightarrow 0$, to give $1 + \omega \sin^2 \phi$ for the second term in the right-hand side of Eq. (6.3).

ii) Far field. Away from the wall, i.e., in the far field $\hat{x} \gg 1$, the solution to Eq. (6.3) for the interface profile $y(x) \sim \exp(-x/\ell_\infty)$ turns out not to depend on the angle ϑ , with decay length

$$\ell_\infty = \frac{\ell_c}{\sqrt{2}} \sqrt{1 + \omega \cos^2 \phi}. \quad (6.6)$$

This shows that the profiles for isotropic fluids with $\omega = 0$ and decay length $\ell_\infty = \ell_c/\sqrt{2}$ decay more rapidly than those of nematic fluids if $\omega > 0$ and less rapidly if $\omega < 0$. We are also able to conclude from Eqs. (6.5) and (6.6) that the rise height and the decay length are not symmetric for the cases ω and $-\omega$, so biases for homeotropic or planar anchoring produce quite different interface profiles. In fact, the rise height and the far-field decay depend in very different ways on the angle ϕ , as shown in Fig. 6.4. This means that the profiles for different attack angles ϕ , presented in Fig. 6.3, must intersect if plotted in the same figure, as in fact they do.

iii) Contact angle. From the boundary term we obtain by functionally minimising the free energy, Eq. (6.3), we extract an implicit equation for the contact angle $\vartheta = -\arctan(1/y'(0))$. It reads

$$\cos \vartheta + \omega \left(\cos \vartheta \sin^2(\vartheta - \phi) + (\sin \vartheta - \sin^2 \vartheta) \sin(2\phi - 2\vartheta) \right) + k = 0, \quad (6.7)$$

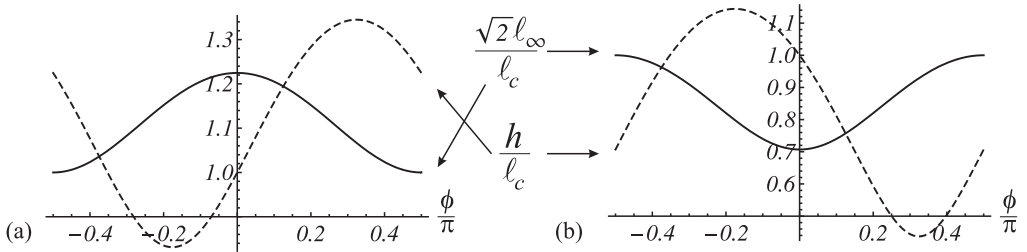


Figure 6.4: The capillary-rise height h (dashed line) and the decay length ℓ_∞ (solid line), as a function of the attack angle ϕ of the uniform director field. (a) $\omega \equiv \zeta_{\text{IN}}/\gamma_{\text{IN}} = 0.5$. (b) $\omega = -0.5$. Complete wetting is presumed.

where $k \equiv (\gamma_{\text{NW}} + \zeta_{\text{NW}} \sin^2 \phi - \gamma_{\text{IW}})/\gamma_{\text{IN}}$. Note that Eq. (6.7) for the contact angle is also asymmetric for the cases of planar ($\omega < 0$) and homeotropic alignment ($\omega > 0$). For isotropic fluids with $\zeta_{\text{IN}} = \zeta_{\text{NW}} = 0$ we retrieve the relation $\cos \vartheta = (\gamma_{\text{IW}} - \gamma_{\text{NW}})/\gamma_{\text{IN}}$, which is the familiar Young's law [178]. Hence, Eq. (6.7) represents a generalisation of Young's law for uniaxial, symmetry-broken fluids. For near-complete wetting, i.e., for small contact angles $|\vartheta| \ll 1$, Eq. (6.7) can be approximated by

$$\frac{\vartheta^2}{2} \sim \frac{1 + \omega \sin^2 \phi + k}{1 + \frac{\omega}{2} (1 + 3 \cos 2\phi + 4 \sin 2\phi)}, \quad (6.8)$$

so that we have complete wetting, $\vartheta = 0$, if the numerator of Eq. (6.8) is zero, that is, if

$$1 + \omega \sin^2 \phi + \frac{\gamma_{\text{NW}} + \zeta_{\text{NW}} \sin^2 \phi - \gamma_{\text{IW}}}{\gamma_{\text{IN}}} = 0, \quad (6.9)$$

as in fact also follows directly from Eq. (6.7) by inserting $\vartheta = 0$.

Our prediction for the rise height h is a real number only for all attack angles $\phi \in [-\pi/2, \pi/2]$ if the dimensionless anchoring strength ω obeys $-0.62 < \omega < 1.62$, implying that for values outside this range not all angles ϕ are permitted. One has to bear in mind, however, that this angle ϕ is not a free parameter but is determined by the various interfacial tensions and the geometry of the entire three-dimensional domain. Presumably, ϕ sets itself so not as to violate the indicated bounds on it.

Computer simulations [43, 62] and theoretical predictions [61, 75, 77] give values of $-0.6 \lesssim \omega \lesssim -0.4$, at least for idealised rod-like model particles. Different values of ω have been extracted from experimental observations on the shape of tactoids by fitting macroscopic theories with similar ingredients as the one we put forward here. For nematic droplets of vanadium-pentoxide ribbons in water, for instance, Prinsen et al. and Kaznacheev and et al. found values in the range of $-1 \lesssim \omega \lesssim -0.83$ [54, 63, 64]. For tactoids of actin fibers in water, Oakes and co-workers [179] were able to get a

good description of their (somewhat noisy) data by presuming rigid parallel anchoring, implying $\omega \rightarrow -1$. In fact, we deduce that any value between $-1 \leq \omega \lesssim -0.8$ should produce a fit consistent with their data [53]. Experimental observations on nematic tactoids in aqueous dispersions of the rod-like feline-distemper (fd) virus mixed with the polymer dextran suggest that for this particular system $-1 \lesssim \omega \lesssim -0.88$ [53]. All these values of ω are quite outside the range predicted by simulations and theory. It is not clear what causes the discrepancy but we speculate that curvature effects on the surface tension may have something to do with it. As already discussed in the introduction, capillary-rise experiments of the sort described here might resolve this issue but these have yet to be performed.

For *disk-like* colloidal particles that are known to favour homeotropic anchoring little is known about what typical values of ω to expect albeit that density functional theory simulations predict a value of $\omega \approx 0.87$ for infinitely thin hard platelets [180]. However, using Eq. (6.5) and the experimental data of Van der Beek et al. we can find an estimate for this quantity for a suspension of sterically stabilised gibbsite platelets in the solvent toluene [45]. From polarisation-microscopy images these authors conclude that $\phi \approx \pi/4$, $\lambda \approx 70 \mu\text{m}$, and $\vartheta \approx 0$. Inserting $K = K_3 \approx 7 \cdot 10^{-14} \text{ N}$, obtained from experiments on the Frederiks transition in the same system [83], we deduce that $\zeta_{\text{IN}} \approx 1 \text{ nN/m}$. The rise height $h \approx 6 \mu\text{m}$ is much smaller than the extrapolation length, λ , so the weak-anchoring limit holds. Inserting $\Delta\rho_m = 20 \text{ kg/m}^3$, we obtain from Eq. (6.5) $\gamma_{\text{IN}} = 2 \text{ nN/m}$. This is comparable to but smaller than the estimate of 3 nN/m cited in the work of Van der Beek et al. [45]. Hence, we find $\omega = 0.5$. This value is quite insensitive for the precise value of the attack angle ϕ , because the values of γ_{IN} for $\phi = \pi/6, \pi/4$, and $\pi/3$ we obtain are $\gamma_{\text{IN}} = 2.0, 2.1$, and 2.5 nN/m , respectively. A point worthy of mention is that the diameter of the platelets is $D = 240 \text{ nm}$, so that $\ell_c \simeq h \gg D$ and the requirement for the negligibility of curvature effects should be fulfilled.

Clearly, in this example $\lambda/\ell_c = 70/6 \approx 11$ is not infinite, implying that for $x \gtrsim 70 \mu\text{m}$ away from the wall the director field is no longer rigid but bends to minimise the surface energy on large scales. The polarisation-microscopy images of Van der Beek et al. [45] confirm this. The far field we discuss is in actual fact an intermediate field, valid if $\ell_c \lesssim x \lesssim \lambda$. For $x > \lambda$, we do have strong anchoring conditions. As we shall explore in the following section in more detail, the actual far field then does not obey $y(x) \sim \exp(-x/\ell_\infty)$, but Eq. (6.14), i.e., $y(x) \propto -(\ell_c/x)^2$. For $x \ll \lambda$, $y(x) > 0$, whilst for $x \gg \lambda$, $y(x) \uparrow 0$, i.e., the profile is non-monotonic in the far field. This remarkable feature of nematic liquid crystals not seen in isotropic fluids we investigate in more detail next.

6.3 Strong surface anchoring

We now consider the limit of strong surface anchoring, as defined in section 6.1, where we formally take the limit $\lambda/\ell_c \rightarrow 0$. The director field deforms and adjusts to accommodate the anchoring conditions that we now presume to be rigid. This implies that there should be an additional elastic free-energy cost associated with the director-field distortion. In our two-dimensional model the energy density associated with the elastic deformation of the director field \mathbf{n} comprises only a splay and a bend contribution, given by $\frac{1}{2}K_1(\nabla \cdot \mathbf{n})^2$ and $\frac{1}{2}K_3(\nabla \times \mathbf{n})^2$, respectively.[‡] Within the equal-constant approximation where the splay and bend elastic constants are presumed to be equal to each other, we have for the elastic deformation energy per unit length [14]:

$$F_e = \frac{K}{2} \int dx dy ((\nabla \cdot \mathbf{n})^2 + (\nabla \times \mathbf{n})^2), \quad (6.10)$$

with $\mathbf{n}(x, y)$ the director field that is a function of the spatial coordinates (x, y) and $K \equiv K_1 = K_3$ the Frank elastic constant. For lyotropic nematic phases of gibbsite platelets dispersed in the solvent toluene $K_3 \approx 7 \cdot 10^{-14}$ N [83], and in chapter 9 we find value for K_1 for these platelets of $K_1 = (1.0 \pm 0.5) \cdot 10^{-13}$ N, suggesting that the equal-constant approximation is acceptable for this kind of material. For stiff rod-like colloids typically $K_3 \gg K_1$ [50, 57, 58], the equal-constant approximation is more tenuous. On the other hand for thermotropic nematics, $K_3/K_1 \approx 1$ –2 and the approximation seems appropriate [182, 183].

The question arises what boundary condition to impose, i.e., homeotropic or planar. In the equal-constant approximation, however, this question is vacuous because it is straightforward to show that for any pair of two-dimensional vector fields \mathbf{n} and \mathbf{n}_\perp that are perpendicular to each other at every point in space and that obey $\mathbf{n}^2 = \mathbf{n}_\perp^2 = 1$, we have $(\nabla \cdot \mathbf{n})^2 = (\nabla \times \mathbf{n}_\perp)^2$ and $(\nabla \times \mathbf{n})^2 = (\nabla \cdot \mathbf{n}_\perp)^2$, so the overall elastic deformation energies are equal in any geometry. This means that both cases of (symmetric) homeotropic-homeotropic and planar-planar anchoring at the isotropic-nematic and the nematic-wall interfaces are captured by a single calculation. However, we note here that this requires that the area of the plane we consider is larger than that of the plane perpendicular to it, because otherwise a homogeneous director field perpendicular to this plane would be the most favourable configuration.

We arbitrarily invoke homeotropic anchoring of the nematic at both interfaces it is in contact with. To simplify the calculations, we now seek to directly connect the director field $\mathbf{n}(x, y)$ to the interface profile $y(x)$. To do this, we have to make a presumption

[‡]The term $(\nabla \times \mathbf{n})^2 = (\mathbf{n} \cdot (\nabla \times \mathbf{n}))^2 + (\mathbf{n} \times (\nabla \times \mathbf{n}))^2$ comprises both the twisting (former) and bending (latter) of the field. In the two-dimensional consideration, we only have the latter.

about the geometry of the director field. Because of the imposed homeotropic anchoring, a plausible ansatz would be to presume the director field lines to be circle sections that intersect both surfaces perpendicularly. This implies that we can uniquely connect the director $\mathbf{n}(x, y)$ at every point (x, y) in the nematic domain to a corresponding point at the fluid–fluid interface and a point at the solid wall.

Referring the interested reader to the Appendix 6.A for details, we merely quote our ansatz for the free energy per unit length for the case of rigid (homeotropic or planar) boundary conditions,

$$F[y, y', y''] = \int_a^\infty dx \left\{ \gamma_{\text{IN}} \left(\sqrt{1 + y'^2} - 1 \right) + (\gamma_{\text{NW}} - \gamma_{\text{IW}}) y \delta(x - a) + \frac{1}{2} \Delta \rho_m g y^2 + \frac{K}{2} \left(\frac{\arctan y'}{x} + \frac{y''(1 + y'(\frac{\pi}{2} + \arctan y'))}{1 + (y')^2} \right) \right\}, \quad (6.11)$$

where again a flat reference profile has been subtracted and a microscopic cut-off length a has been introduced to avoid a divergence of the elastic free energy at the three-phase boundary. We expect $a \approx D$ with D the largest dimension of the nematogen – it is the core size of the defect line that sits at the three-phase contact line. Below we discuss this point in more detail. Variational minimisation of this free energy with respect to y produces the following differential equation for the optimal interface profile,

$$-\frac{\hat{y}''}{(1 + \hat{y}'^2)^{3/2}} + 2\hat{y} + \frac{\hat{\lambda}'}{2} \frac{1 + \hat{y}'^2 + 2\hat{x}\hat{y}'\hat{y}''}{\hat{x}^2(1 + \hat{y}'^2)^2} = 0, \quad (6.12)$$

where we again make use of the dimensionless variables $\hat{y} \equiv y/\ell_c$ and $\hat{x} \equiv x/\ell_c$. We also define a dimensionless length $\hat{\lambda}' \equiv \lambda'/\ell_c$, with $\lambda' \equiv K/\gamma_{\text{IN}}$ that we expect to be of the order of the extrapolation length $\lambda = K/|\zeta_{\text{IN}}|$. In the absence of gravity, or, equivalently, if the density difference is negligible, the second term in Eq. (6.12) is absent, making the equation integrable with respect to x . This gives a differential equation consistent with that found by Poniewierski [172] who studied the wetting of a horizontal substrate by a nematic fluid. (See again Appendix 6.A for details.)

The first two terms of Eq. (6.12) are identical to what one would obtain for isotropic fluids, the last term accounts for the impact of the elastic deformation of the director field. This term should be subdominant because in the limit of rigid anchoring conditions surface tension effects should be stronger than elastic effects. If we ignore this for a moment, then we read off from Eq. (6.12) that the profile $\hat{y}(\hat{x})$ must be non-monotonic. Our numerical solutions to this equation, presented in Fig. 6.6, confirm this. For isotropic fluids with $\hat{\lambda}' = 0$, the minimum is located infinitely far from the wall, and the profile decays monotonically as expected. However, for $\hat{\lambda}' > 0$ the third term of

Eq. (6.12) drives the profile to develop a minimum. With increasing values of $\hat{\lambda}'$, the position of the minimum \hat{x} moves in from infinity and becomes increasingly smaller for larger $\hat{\lambda}'$ to balance the increasing magnitude of the isotropic terms.



Figure 6.5: Polarisation micrographs of an isotropic-nematic (I-N) interface of charge-stabilised gibbsite platelets, dispersed in a 10^{-2} M NaCl solution. Indicated are the orientations of the polarisers (arrows at right angles in the top left-hand corner) [202].

The non-monotonic profiles may seem physically unrealistic but we have a direct experimental observation of the capillary-rise profile of a sterically stabilised dispersion of gibbsite platelets, see Fig. 6.5. In fact, if one takes a very close look at the capillary-rise profile presented in the experiments we referred to above [45], one can also observe a shallow minimum in the profile of Fig. 1 of that paper. However, we note that the capillary-rise profile seems to be quite sensitive to the experimental procedure [181]. This is an important point that we return to in the discussion in section 6.4 and in the next chapters. In the discussion we also provide arguments to rationalise these profiles in terms of competing types of elastic deformation. Note that in agreement with the observations, the depth of the minimum should be expected to be very shallow. Indeed, if $\lambda' \approx \lambda$ and the anchoring is rigid, we have to insist $\lambda' \ll \ell_c$ for the strong-anchoring conditions to hold. In fact, for the theory to be internally consistent we must have $\lambda' < a$, otherwise the (molten) defect core would “escape” into a core with uniform director field. A conservative upper bound for λ' is therefore a , making the minimum in the profile exceedingly shallow.

We now address aspects of the profiles presented in Fig. 6.6 that can be analysed analytically. For details the reader is referred to Appendix 6.A.

i) Capillary-rise height. The capillary-rise height $h/\ell_c \equiv \hat{y}(\hat{a}) \rightarrow \hat{y}(0)$, with $\hat{a} \equiv a/\ell_c$, can be estimated from Eq. (6.12). We discussed above that $\hat{\lambda}'$ must be small, so the rise height cannot deviate strongly from that for $\hat{\lambda}' = 0$, i.e., the equivalent isotropic case. Then we find the familiar result $h_0/\ell_c = \sqrt{1 - \sin \vartheta}$ with ϑ the contact

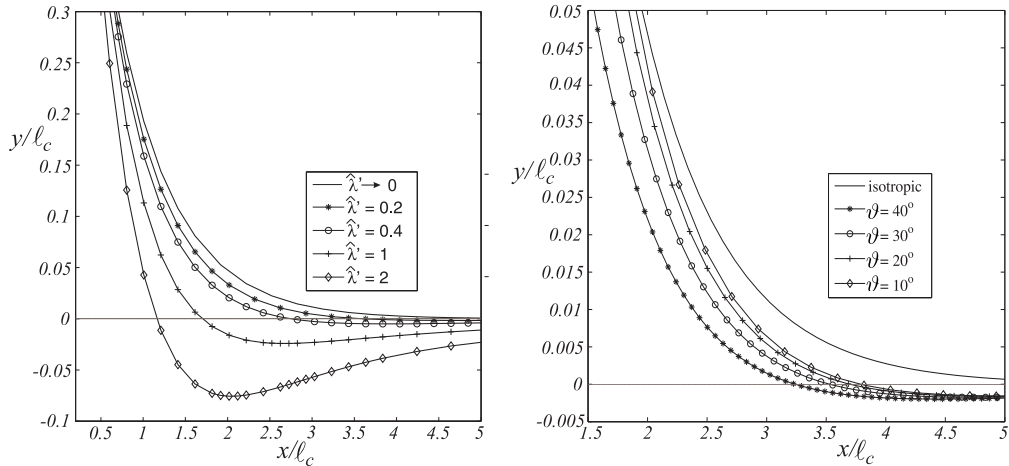


Figure 6.6: Left: fixed contact angle $\vartheta = 25^\circ$, with various values of the parameter $\hat{\lambda}' \equiv \lambda'/\ell_c$. Right: constant values of the parameter $\hat{\lambda}' = 0.2$ for different values of the contact angle ϑ . Profile of an isotropic fluid: $\vartheta = 25^\circ$. The cutoff $a = 0.2 \ell_c$ for both graphs. For any value $\hat{\lambda}' > 0$ the profiles decay more rapidly than that of the isotropic fluid and the profiles drop below zero next to rise again further away from the wall. However, $\hat{\lambda}' \ll 1$ in the rigid anchoring limit so the minima are very shallow indeed.

angle defined at the cutoff. We define h_1 as the first order correction to h_0 for small values of $\hat{\lambda}'$, so $h \equiv h_0 + \hat{\lambda}' h_1$. We then find

$$\frac{h_1}{\ell_c} = \frac{\cos \vartheta \sqrt{1 - \sin^2 \vartheta}}{\hat{a}} - \frac{\sin^2 \vartheta}{4\hat{a}^2}, \quad (6.13)$$

where we have used the identity $\hat{y}'(\hat{a}) = -1/\tan \vartheta$. For complete wetting we then obtain $h/\ell_c = 1 + \hat{\lambda}'/\hat{a} = 1 + \lambda/a$.

ii) Far field. The far-field solution for $\hat{x} \gg 1$ can be found by presuming that the first derivative of the profile is small, giving the following asymptotic relation,

$$\hat{y}(\hat{x}) \sim C \exp(-\sqrt{2} \hat{x}) - \frac{\hat{\lambda}'}{4\hat{x}^2}, \quad (6.14)$$

with C an integration constant. The exponential part is due to the bare surface tension and the algebraic part comes from the deformation of the director field. This means that there is no typical length scale describing the decay. The minus sign in front of the second term indicates that the profile rises to zero at infinity, coming from a negative value.

iii) Contact angle. The boundary condition at the cutoff a that follows from the

minimisation of the free energy, Eq. (6.11), with respect to y we find to obey

$$\cos \vartheta + \frac{\gamma_{NW} - \gamma_{IW}}{\gamma_{IN}} - \frac{\lambda'}{2a} \sin^2 \vartheta = 0. \quad (6.15)$$

Eq (6.15) agrees with earlier work [91, 172, 184] and is a generalised Young's law for the contact angle of a nematic with symmetric homeotropic (or planar) alignment. The first two terms are the usual ones for fluids governed by surface tensions, i.e., isotropic fluids, and the third contribution is that from the elastic deformation that depends explicitly on the cut-off length a . If $\lambda' \ll a$, we retrieve Young's law and the contact angle depends only on the surface tensions. In the (hypothetical) limit of very large $\lambda' \gg a$, we approach $\cos \vartheta = \pm 1$, i.e., complete wetting or dewetting. Again, we expect $\lambda' \ll a$ to hold for internal consistency. If this is not the case, then the defect escapes in a uniform field near to the three-phase contact line. If $\lambda' \approx \lambda \gg \ell_c$, then the theory of the preceding section applies. If $a \ll \lambda' \ll \ell_c$, this requires a description that interpolates between the two presented in this manuscript. We intend to investigate this intermediate regime in future work.

6.4 Discussion and conclusions

We put forward a model for the capillary rise of a semi-infinite isotropic-nematic interface up a single vertical wall, extending earlier work of Rey [91] on a nematic between two walls at very close separation and find that the type of director field in the rise region depends on the relative size of the extrapolation length λ and the capillary length ℓ_c . In the limit that $\lambda \gg \ell_c$, which we claim is generally the case in lyotropic systems, the director field is uniform in the rise region and the capillary-rise height, decay length and contact angle depend in different, non-trivial ways on the angle ϕ that the field makes with the normal to the wall. Moreover, these three properties are not symmetric for positive and negative values of the dimensionless anchoring strength ω , making the cases $\omega < 0$ (corresponding to planar anchoring) and $\omega > 0$ (corresponding to homeotropic anchoring) fundamentally different.

We applied our analytical expression for the rise height to capillary-rise experiments on a suspension of gibbsite platelets, under conditions of co-existing isotropic and nematic phases where conditions of strong surface anchoring and complete wetting were observed [45]. Using our model, we find a very low surface tension of 2 nN/m of the nematic-isotropic interface, and a value for the anchoring strength of $\omega = 0.5$. The value of $\zeta_{IN} = \omega\gamma_{IN}$ that we deduce from this depends rather weakly on the attack angle ϕ of the director field, so the obtained value can be qualified as reliable. Of course, more experimentation is needed in particular on systems of rod-like particles where experimental

and theoretical values of ω disagree quite considerably. Capillary-rise experiments might give more accurate values of ω than studies of tactoid shapes because of the potentially more prominent effects of curvature on the surface free energy.

In the opposite limit with $\lambda \ll \ell_c$, which seems more typical for thermotropic systems, the field in the capillary-rise region deforms to accommodate the predominance of the surface anchoring energy, leading to a curved director field with either homeotropic or planar anchoring at the surfaces. In the equal-constant approximation both types of strong anchoring are equivalent if the anchoring conditions are symmetric on both interfaces, allowing us to capture symmetric parallel and perpendicular alignment in a single calculation. The usual equation describing the meniscus profile contains an additional term that accounts for the distortion of the director field. However, this term is proportional to the ratio of the extrapolation length and capillary length $\lambda'/\ell_c \approx \lambda/\ell_c$, so it should be subdominant because in the limit of rigid anchoring conditions surface tension effects must be stronger than elastic effects. Therefore, the capillary-rise height approximately obeys the classical results for isotropic fluids albeit that the actual profile does deviate from the classical one: we find that the profile exhibits a minimum, i.e., is a non-monotonic function of the distance to the wall. In fact, the minimum that we predict in the strong-anchoring limit persists in the weak-anchoring regime because for large enough $x \gtrsim \lambda$ surface anchoring is always dominant.

The minimum in the profile might seem counter-intuitive but makes perfect sense if, given the rigid homeotropic boundary conditions, locally the bend deformation is relaxed. This is only possible at the expense of a splay deformation of the director field, near a virtual defect centred just above the minimum, see Fig. 6.7(a). Of course, there is a second energy cost associated with the increase of the interface length but there might be an additional energetic advantage because the non-monotonic profile is steeper close to the wall than the corresponding monotonic profile, which makes the field lines less curved in the capillary-rise region. We conclude that these combined effects must lead to a net free-energy gain favouring the non-monotonic profile. The argument for planar anchoring is analogous.

In fact, in order to support this explanation we can visualise the relative magnitudes of the elastic deformation densities. From the numerically obtained solution to Eq. (6.12) we compute the splay and bend deformation density, $f_s \equiv (\nabla \cdot \mathbf{n})^2$ and $f_b \equiv (\nabla \times \mathbf{n})^2$, respectively. We then evaluate the relative contribution of splay deformation to the total director-field distortion, $f_s/(f_s + f_b)$, indicated by the colours in Fig. 6.7(b). We take the rather large value $\hat{\lambda}' = 4$ to clarify the statement, and see that indeed the splay deformation is concentrated near the minimum in the profile, as sketched in Fig. 6.7(a). In that region the splay deformation even dominates, whereas away from it,

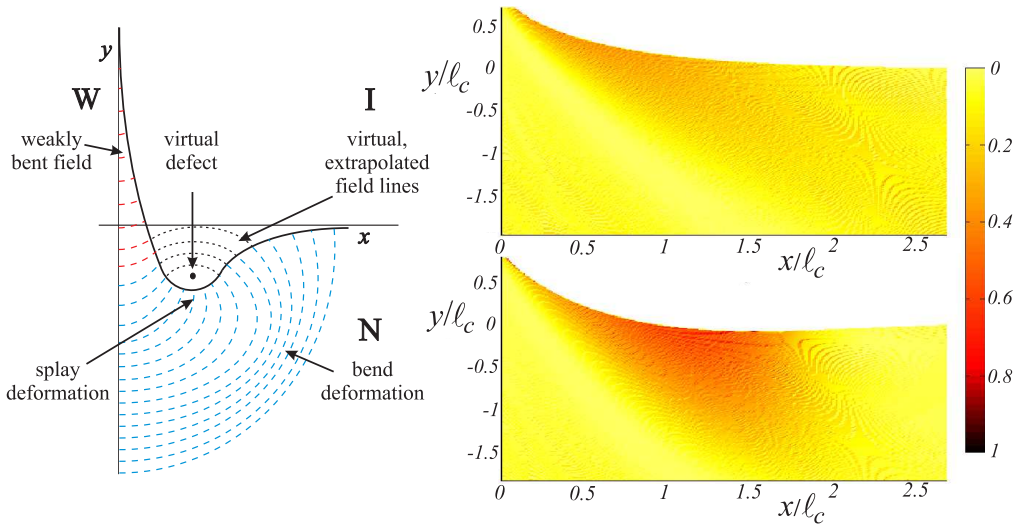


Figure 6.7: (a) Schematic representation of the deduced director field with fixed homeotropic anchoring. The minimum develops to minimise the bend distortion at the expense of an elastic splay and surface deformation. The envisaged field-line pattern gives rise to a virtual defect line indicated by the dot at the centre of the radius of curvature associated with the minimum of the profile. (b) The relative contribution of the splay deformation to the total director-field distortion for a monotonic profile with $\hat{\lambda}' = 0$ (top) and a non-monotonic profile with $\hat{\lambda}' = 4$ (bottom). The splay deformation is significant only near the minimum in both cases and it is even dominant for $\hat{\lambda}' = 4$.

the bend deformation is completely dominant. The distribution of splay deformation is asymmetric with respect to the minimum, just as the profile itself is, see Fig. 6.6. Note that for $\hat{\lambda}' = 0$, for which case the interface profile is monotonic, there is also some splay deformation in the bulk nematic but it is nowhere dominant.

A point worthy of mention is that for plate-like particles theoretical estimates predict that $K_1 > K_3$ [185], implying that the exchange of bend for splay distortion is energetically more expensive than one leads to suspect on the basis of the equal-constant approximation, presumably partially undoing the effect that we think causes the minimum in the capillary profile. On the other hand, for gibbsite platelets the two Frank constants differ not by much, $K_1 \approx 1.5 \cdot 10^{-13}$ N and $K_3 \approx 7 \cdot 10^{-14}$ N [83, 181, 186], explaining why the minimum can clearly be observed in Fig. 6.5. However, the rise height and depth of the minimum as well as the director field are very sensitive to the experimental procedure because, e.g., surface inhomogeneities in the capillary wall might lead to pinning of the three-phase contact line. This is not too far-fetched a possibility on account of the very low interfacial tensions. For rod-like particles it is well established

that $K_3 \gg K_1$ [50,57,58], so for these it might be quite difficult to observe the minimum in the profile.

The question remains what the influence of elasticity is in the intermediate regime where λ and ℓ_c are of the same order of magnitude, and the anchoring is moderately strong. This influence must evidently be there, as outside these limits it is absent or quite weak. We leave it for future investigation. In the next three chapters we focus on another manifestation of the competition between elastic and anchoring forces characteristic of isotropic-nematic interfaces, namely that in nematic droplets.

We would like to thank Lia Verhoeff for the capillary-rise experiments on gibbsite platelets and for providing us with the experimental value of the elastic constant K_1 of the nematic phase of gibbsite platelets.

6.A Strong surface anchoring

In the strong-anchoring limit we for simplicity but without loss of generality presume symmetric homeotropic anchoring because it allows for a convenient mathematical construction of the director field, which is worked out in this Appendix. As explained in section 6.3, the invoked equal-constant approximation makes the result also valid for planar anchoring, provided that the area of the plane we consider is larger than that of the plane perpendicular to it. From the profile equation we next derive interesting properties such as the decay length and the contact angle.

i) Parametrisation. For a point (\tilde{x}, \tilde{y}) in the bulk of the rise region, we find the section of a circle that has its centre on the y -axis, and intersects the profile $y(x)$ perpendicularly in (x_0, y_0) , see Fig. 6.8. The line tangent to this point intersects the vertical axis at height $\xi = y_0 - y'(x_0)x_0$. The profile is assumed to decay completely within a finite distance R from the wall. We formally let $R \rightarrow \infty$ at the end of the calculation. The points (\tilde{x}, \tilde{y}) satisfying $\tilde{x}^2 + (\tilde{y} - \xi)^2 = x_0^2 + (y_0 - \xi)^2 = x_0^2(1 + (y'(x_0))^2)$ are on the same distance from $(0, \xi)$, so they are on the same field line. We then find for the director field at (\tilde{x}, \tilde{y}) :

$$\mathbf{n}(\tilde{x}, \tilde{y}) = \left(-\frac{\tilde{y} - \xi}{\sqrt{\tilde{x}^2 + (\tilde{y} - \xi)^2}}, \frac{\tilde{x}}{\sqrt{\tilde{x}^2 + (\tilde{y} - \xi)^2}} \right), \quad (6.16)$$

where ξ depends on \hat{x} and \hat{y} implicitly. In order to find the elastic energy, we must perform an integration over the domain, for which a suitable parametrisation is chosen. Let the parameter x pass through the profile y , taking on values between 0 and R . So we have $x_0 = x, y_0 = y(x)$. For every x we then integrate over the azimuthal director

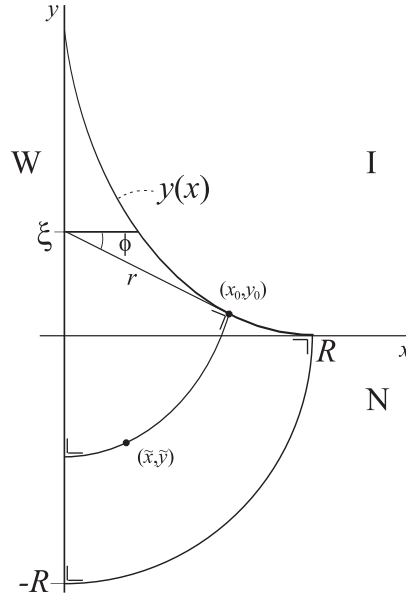


Figure 6.8: Explanation of the parametrisation of the surface that is used in order to calculate the elastic deformation energy for the prescribed director field. The director field in a point (\tilde{x}, \tilde{y}) in the bulk lies on the circle section that intersects the profile $y(x)$ perpendicularly in (x_0, y_0) . This circle has centre $(0, \xi)$ and radius r . ϕ is the angle that the line connecting a point on the circle section and $(0, \xi)$ makes with the horizontal. $y'(R) = 0$ is presumed, giving $\xi = 0$ and $\phi \in (0, \pi/2)$ for points on the bottom circle section.

field from the profile to the vertical axis. This means crossing the circle section, the centre of which is at $(0, \xi)$, with $\xi(x) = y(x) - y'(x)x$. The radius r of the circle then obeys $r^2 = x^2(1 + y'(x)^2)$. The angle that the tangent makes with the horizontal is ϕ . We now shift from the coordinates \tilde{x} and \tilde{y} to coordinates x and ϕ . These are not the usual polar coordinates because the origin is not fixed. Abbreviating y' for $y'(x)$, we find

$$\tilde{x} = r \cos \phi = x\sqrt{1 + y'^2} \cos \phi, \quad (6.17a)$$

$$\tilde{y} = \xi - r \sin \phi = y - y'x - x\sqrt{1 + y'^2} \sin \phi. \quad (6.17b)$$

The Jacobian of our coordinate transformation is

$$\left| \frac{\partial(\tilde{x}, \tilde{y})}{\partial(x, \phi)} \right| = x(1 + y'^2) + x^2 y'' \left(y' + \sqrt{1 + y'^2} \sin \phi \right). \quad (6.18)$$

The boundaries for x are $(0, R)$, the upper bound for ϕ is $\phi = \pi/2$; the lower bound follows from Fig. 6.8: $\tan \phi = (\xi - y)/x = -y'$, so $\phi = -\arctan y'$.

ii) Elastic free energy. The director field can easily be expressed in terms of the new variables, which gives for the elastic energy density

$$f_e = (\nabla \cdot \mathbf{n})^2 + (\nabla \times \mathbf{n})^2 = \frac{1}{x^2(1+y'^2)}. \quad (6.19)$$

f_e diverges for $x \rightarrow 0$, so we introduce a cut-off radius a to avoid this divergence. The cut-off radius can be estimated as follows. The elastic energy F_e in the reference state is $F_e = \vartheta K \log(R/a)/2$, which follows from the elastic energy of a wedge with angle ϑ and multiplied by R [187]. The difference in free energy when replacing the volume that has been cut off of the nematic phase by the isotropic phase is equal to $F_c = -\vartheta a^2(f_N - f_I)/2$, where f_N and f_I are the energy densities of the nematic and isotropic phases. The length scale a is found by minimising $F_e + F_c$ with respect to a , which gives $a = \sqrt{K/(2f_I - 2f_N)}$, independent of the opening angle ϑ . The order of magnitude of a we estimate by assuming that $f_N - f_I \sim k_B T/D^3$, D being the length (diameter) of a particle, as $k_B T$ is the only energy scale and D the only suitable length scale in the system. Furthermore, $K \sim k_B T/D$ for the same reasons. This then gives $a \sim D$.

For an arbitrary shape of the interface we have for the Frank elastic energy per unit length

$$\begin{aligned} F_e &= \frac{K}{2} \int_a^R dx \int_{-\arctan y'}^{\pi/2} d\phi \left| \frac{\partial(\tilde{x}, \tilde{y})}{\partial(x, \phi)} \right| \frac{1}{x^2(1+y'^2)} \\ &= \frac{K}{2} \int_a^R dx \left(\frac{\pi}{2x} + \frac{\arctan y'}{x} + \frac{y''(1+y'(\frac{\pi}{2} + \arctan y'))}{1+y'^2} \right). \end{aligned} \quad (6.20)$$

After noting that the first term of the last integrand of Eq. (6.20) gives the deformation energy in the reference state, Eq. (6.11) then follows for the excess free energy per unit length, F , when going from a flat interface to the capillary rise, where the limit $R \rightarrow \infty$ has been taken. For this the weight of a column of width a and height $y(a)$ must be neglected in order to obtain an expression within one integral, which seems acceptable given that $a \sim D$. Note that this excess free energy is zero for a flat interface.

iii) Free energy minimisation. To functionally minimise F , we compute $\delta F \equiv F[y + \delta y, y' + \delta y', y'' + \delta y''] - F[y, y', y''] = 0$ with the boundary condition $\delta y(R) = 0$ to first order in δy . We note that last term in the last integrand of Eq. (6.20) can be integrated explicitly, meaning that this term only has a contribution in the boundary

condition. This gives for δF

$$\begin{aligned} \delta F = & \gamma_{\text{IN}} \int_a^R dx \frac{y'}{\sqrt{1+y'^2}} \delta y' + (\gamma_{\text{NW}} - \gamma_{\text{IW}}) \int_{a-c}^{a+c} dx \delta(x) \delta y + \Delta \rho_m g \int_a^R dx y \delta y + \\ & \frac{K}{2} \int_a^R dx \frac{1}{x(1+y'^2)} \delta y' + \frac{K}{2} \frac{1+y'(\frac{\pi}{2} + \arctan y')}{1+y'^2} \delta y' \Big|_{x=a}^{x=R} = 0, \end{aligned} \quad (6.21)$$

with c a positive constant. The last boundary term with $\delta y'$ can be rewritten in terms of δy by integration by parts. Therefore, both resulting terms must be equal to zero. The integrands containing $\delta y'$ in Eq. (6.21) can be integrated by parts to give

$$\begin{aligned} \delta F = & -\gamma_{\text{IN}} \frac{y'(a)}{\sqrt{1+y'(a)^2}} \delta y(a) - \gamma_{\text{IN}} \int_a^R dx \frac{y''}{(1+y'^2)^{3/2}} \delta y + (\gamma_{\text{NW}} - \gamma_{\text{IW}}) \delta y(a) \\ & + \Delta \rho_m g \int_a^R dx y \delta y + \frac{K}{2} \frac{1}{x(1+y'^2)} \delta y \Big|_{x=a}^{x=R} + \frac{K}{2} \int_a^R dx \frac{1+y'^2+2xy'y''}{x^2(1+y'^2)^2} \delta y = 0. \end{aligned} \quad (6.22)$$

This equation must hold for arbitrary functions δy and $\delta y'$, so that the terms proportional to $\delta y'$ produce a boundary condition and the collection of the δy terms gives a differential equation for y . For the boundary condition we have, using that $\delta y(R) = 0$ and approximating $y'(0)$ by $y'(a)$,

$$-\gamma_{\text{IN}} \frac{y'(a)}{\sqrt{1+y'(a)^2}} + (\gamma_{\text{NW}} - \gamma_{\text{IW}}) - \frac{K}{2} \frac{1}{a(1+y'(a)^2)} = 0. \quad (6.23)$$

With $y'(a) = -1/\tan \vartheta$, this gives Eq. (6.15).

For the profile $y(x)$ we obtain Eq. (6.12). The far-field behaviour of the profile is computed by solving the differential equation that remains after taking the limit $\hat{y}' \rightarrow 0$ in Eq. (6.12). The solution reads

$$\hat{y}(\hat{x}) \approx C \exp(-\sqrt{2}\hat{x}) - \frac{\hat{\lambda}'}{4} \left(\exp(\sqrt{2}\hat{x}) I(-\sqrt{2}\hat{x}) + \exp(-\sqrt{2}\hat{x}) I(\sqrt{2}\hat{x}) \right), \quad (6.24)$$

with C an integration constant, $\hat{\lambda}' \equiv \lambda'/\ell_c = K/(\gamma_{\text{IN}}\ell_c)$, and $I(z) = -\int_{-z}^{\infty} dt \exp(-t)/t$. For large \hat{x} the solution obeys Eq. (6.14), showing a combination of exponential and algebraic decay.

iv) Comparison with earlier work. In the absence of gravity, Eq. (6.12) can be integrated with respect to x ,

$$-\gamma_{\text{IN}} \frac{y'}{\sqrt{1+y'^2}} - \frac{K}{2} \frac{1}{x(1+y'^2)} = C \quad (6.25)$$

with C an integration constant equal to $-K/(2R)$ because of the boundary condition that $y'(R) = 0$. Eq (6.25) is consistent with Eq. (40) of work by Poniewierski [172]

for $\ell = a$, where wetting of a horizontal substrate is considered and $\ell(x)$ is the distance between the IN interface and the substrate as a function of the horizontal coordinate x . This equation follows from our Eq. (6.25) by substituting $\ell(x)$ for $x(-y)$ and $\ell' = -1/y'$. The constants appearing in that equation follow from boundary conditions and are incorporated in our integration constant. The boundary condition, Eq. (41) in the paper mentioned [172], for the contact angle (or the local tilt angle) is in agreement with our Eq. (6.15), assuming that $V(a) = \gamma_{\text{IN}}$ with $V(\ell)$ the excess free energy per unit area of a uniform nematic film of thickness ℓ . Here, $V(\infty) = \gamma_{\text{IN}} + \gamma_{\text{NW}} - \gamma_{\text{IW}} = -S$, where S is the spreading coefficient [178]. Our boundary condition is also in accord with Eqs. (58) and (85) in papers by Rey [91,184], where it must be noted that in those papers the cut-off distance is measured radially, explaining why those equations have $\sin \vartheta$ instead of $\sin^2 \vartheta$ in the last term.

Deformable homeotropic nematic droplets in a magnetic field: strong surface anchoring

7

We present a simple Frank-Oseen elasticity theory to study the effect of a magnetic field on the shape and director field of nematic droplets, also known as tactoids, with homeotropic surface anchoring. In the model we presume a spherocylindrical droplet shape, strong anchoring of the director field to the surface of the tactoid, and a negative diamagnetic susceptibility of the nematogens. We find that above a critical field strength spherical tactoids with a radial director field undergo a drastic reorganisation of the director field and the drop shape as a split-core line defect develops in an elongated tactoid. We compare our results with experiments on droplets in sterically stabilised dispersions of gibbsite platelets that indeed have a negative magnetic susceptibility, allowing us to extract values for the interfacial tension and the splay elastic constant.[†]

[†]The contents of this chapter have been published as:
A. A. Verhoeff, R. H. J. Otten, P. van der Schoot, and H. N. W. Lekkerkerker, *Journal of Physical Chemistry B* **113**, 3704-3708 (2009).

7.1 Introduction

In chapter 6 we considered the competition between the anisotropic surface tension and bulk elasticity of a nematic liquid crystal in the capillary rise of an isotropic-nematic interface up a vertical wall. In this and the next two chapters we focus on a different manifestation of this competition, namely that in the shape and structure of nematic droplets. These droplets are often observed in dispersions of sufficiently anisometric colloidal particles under conditions where the isotropic and nematic phases co-exist [41,55,63,64,179,188,190]. Nematic droplets, also called tactoids, have been investigated quite intensively over the last few decades, not least because of their interesting and sometimes unusual shapes and internal structures. These include oblate and prolate droplet shapes with round and sharp edges, and director-field structures involving surface and bulk point defects as well as ring-shaped disclination lines and bipolar twisted “parity-broken” director fields, all depending the size of the drops and the shape of the colloids [41, 53, 54, 63, 64, 179, 188, 190].

Because the shape and structure of tactoids result in effect from a competition between surface and elastic forces, studying them provides quantitative information on material properties, including the elastic constants, surface tension and anchoring strength of the director field to the interface between the co-existing isotropic and nematic phases [6, 41, 53, 54, 56, 57, 63, 64, 190]. Tactoids in lyotropic systems are more suitable for this purpose than those in thermotropic ones because of the extremely low surface free energies typical of lyotropics [45,66,67].

Studies on tactoids in dispersions of *rod-like* colloidal particles such as vanadium pentoxide [63,64,191], f-actin [179], tobacco mosaic virus [192], boehmite [193], and fd virus [65], have shown that these drops tend to have a bipolar director field, in which the curved field lines run from one virtual surface point defect (boojum) to another on the other side of the drop. The cause of this tendency for bipolar director fields is that rod-like particles for entropic reasons prefer planar alignment of the director to the interface. Theoretically one only expects this to be so if the drops are sufficiently large relative to some length scale set by the elastic and interfacial properties of the nematic drops [87]. Tactoids with uniform director fields have been observed in computer simulations and recently also in dispersions of carbon nanotubes [41, 62, 194]. The structure of tactoids with planar anchoring conditions have been studied theoretically in great detail [41, 53, 54, 63, 64, 179, 193].

Tactoids of *plate-like* colloids seem to have a very different director field from those of rod-shaped ones, although it has to be said that to date much fewer systems have been studied. The rather intricate stabilisation of plate-like colloids is presumably the reason

for this [11, 42, 78, 79, 195]. Tactoids have been observed in dispersions of sterically stabilised and charge-stabilised gibbsite platelets [78, 84–86]. For these systems both uniform and radial director fields have been observed, the latter a result of the tendency of plate-like particles to align homeotropically to interfaces, again for entropic reasons [85]. The radial director field is characterised by a hedgehog point defect in the centre of the drop [55, 84, 196, 197], which could also be a small ring defect [198, 200].

As already alluded to, quantitative information can be obtained on the material parameters by fitting theoretical models to experimental results on tactoids. Additional information on the material properties can be obtained by means of an externally applied electrical or magnetic field because these couple to the shape and director field of tactoids [63]. In recent experiments on tactoids in suspensions of sterically stabilised plate-like gibbsite particles in bromotoluene, it was shown that these tactoids respond to an increasing magnetic field not by a continuous deformation but by a sudden rearrangement of the director field if the field strength exceeds a critical value, a phenomenon reminiscent of a Frederiks transition in which the director field of a thin layer of a well-aligned nematic between parallel plates suddenly changes at a critical magnetic-field strength [199]. Free-floating bipolar tactoids in colloidal dispersions of rod-like colloidal particles have been shown to orient and stretch under the influence of a magnetic field, but do not exhibit a Frederiks transition [63]. This observation can be understood by applying standard elastic theory and by realising that the drops are freely suspended in solution.

Interestingly, such a split-core line defect was predicted theoretically about a decade ago by Mkaddem and Gartland [200], suggesting that the split-core defect could be stabilised by an externally applied magnetic field but only if the nematogens have a negative diamagnetic susceptibility. Gibbsite has a negative diamagnetic susceptibility, so this corresponds exactly to the situation that was experimentally investigated in dispersions of gibbsite platelets [84, 86], and confirmed that this configuration can be stabilised by the magnetic field. Inspired by these experiments, we present in this chapter a Frank-Oseen elasticity theory for the shape and structure of nematic droplets with homeotropic surface anchoring in the presence of a magnetic field, and we focus on negative values of the diamagnetic susceptibility. For a positive value we expect completely different behaviour, because in that case the magnetic field would presumably drive the radial director field with point defect into a uniform orientation via the formation of a ring defect rather than into a split-core defect [201]. We use a simple model that presumes a spherocylindrical droplet shape and strong anchoring of the director field to the surface. In chapters 8 and 9 we relax this condition and consider imperfect surface anchoring. With our simple model in this chapter a spherical drop with a radial director field

stretches to an elongated drop with a split-core line defect at a critical magnetic-field strength. This is in agreement with the experiments on tactoids consisting of sterically stabilised gibbsite platelets in an organic solvent [84], and the comparison allows us to extract values for the splay elastic constant from the critical magnetic-field strength at which the director field starts to change, and the interfacial tension from the degree of deformation of the tactoid at higher magnetic-field strengths.

In the remainder of this chapter, we first present in section 7.2 the theoretical ingredients, which we use in this chapter and the next chapters, and discuss our simple model for the tactoid deformation in section 7.3. From this we derive the optimal shape in section 7.4 and we compare our results with the experiments on tactoids consisting of gibbsite platelets in section 7.5. Finally, we discuss our results in section 7.6.

7.2 Model ingredients

In this section we present the ingredients of our macroscopic Frank-Oseen elasticity theory that should enable us to rationalise the experimental observations described in the introduction and that we also use in the next two chapters [14]. The basics of this theory were described in chapter 1, and we here discuss the free-energy contributions that we deal with in our case. The free energy $F = F_{st} + F_{sa} + F_e + F_m$ of a tactoid of volume V consists of four contributions associated with the bare surface tension (subscript st) and surface anchoring (sa), the elastic deformation (e) and the magnetic field (m).

1. The bare surface energy and the anchoring energy form the surface energy $F_{st} + F_{sa}$ that we take is of the Rapini-Papoular type [40],

$$F_{st} + F_{sa} = \int_A dA (\gamma + \zeta \sin^2 \alpha), \quad (7.1)$$

where the integration is taken over the entire surface area A of the drop and α is the angle between the surface normal $\mathbf{q} = \mathbf{q}(\mathbf{r})$ and the director field $\mathbf{n} = \mathbf{n}(\mathbf{r})$ at the interface. Eq. (7.1) comprises a contribution from the bare surface tension γ and one from the surface anchoring, where ζ is the surface-tension anisotropy, i.e., the anchoring free energy per unit area of the drop interface. As already announced, platelets for entropic reasons prefer homeotropic alignment of the director field to the interface [42], implying $\zeta > 0$. This form of the interfacial energy has been shown to be a very accurate representation for rod-like particles [41], and we presume it to be reasonable for disk-like ones as well;

2. The Oseen-Frank free energy of elastic deformation reads

$$F_e = \frac{1}{2} \int_V dV \left(K_1 (\nabla \cdot \mathbf{n})^2 + K_3 (\nabla \times \mathbf{n})^2 \right), \quad (7.2)$$

if we ignore any twist deformation, where the integration is over the volume V of the drop, and K_1 and K_3 are the splay and bend elastic constant, respectively. In Eq. (7.2) we omitted the splay-bend term with constant K_{13} and the saddle-splay term with constant K_{24} , and we discuss this in section 7.6. Inspired by the experimental observations, we ignore any contributions from bend deformations,[†] and we return to this in the discussion;

3. The magnetic energy of a nematic drop is given by [6]

$$F_m = -\frac{1}{2} \rho \Delta\chi B^2 \int_V dV (\mathbf{n} \cdot \mathbf{e}_x)^2, \quad (7.3)$$

where we have dropped a spatially invariant term [6], ρ is the particle number density, $\Delta\chi$ the diamagnetic susceptibility anisotropy (dimensions J/T²), and B the magnitude of the magnetic field that we choose to be in the x -direction with unit vector \mathbf{e}_x . As our theory intends to explain the observations on dispersions of gibbsite platelets that have a negative magnetic susceptibility, we presume $\Delta\chi < 0$ [42,83,84,86], so the particles have a tendency to orient their director perpendicular to the magnetic field.

Clearly, we should simultaneously minimise the free energy F with respect to both shape and director field of a tactoid to obtain the optimal structure of the tactoid. However, this is a formidable constrained-free boundary-value problem that is most probably impossible to solve analytically, and even hard to solve numerically. Therefore, in section 7.3 we first presuppose a particular shape and internal structure of the elongated droplet that permits a straightforward calculation of the magnitude of the deformation of the director field and the computation of the overall surface area. This approach should then allow us to explain the director-field transition and the accompanying tactoid elongation for a sufficiently strong magnetic field. In chapters 8 and 9 we present a more sophisticated model with a more realistic tactoid shape and more realistic anchoring conditions. The approach we follow here is first to minimise the free energy with respect to a variational parameter that describes the elongated shape of the tactoid, as is done in section 7.4. The application of this model to the experimental data in section 7.5 then enables us to extract values for the splay elastic constant and the surface tension.

[†]In section 8.3 we consider a ring defect that has a director field with both a splay and a bend deformation, but in the parameter range where this configuration is most favourable, it has hardly any bend deformation.

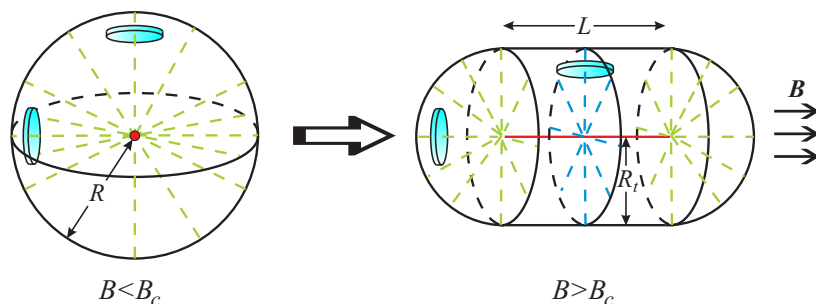


Figure 7.1: Left: for a magnetic field \mathbf{B} with a magnitude B smaller than a critical value B_c , the droplet is spherical with radius R : the director field (dashed lines) is radial in three dimensions (pure splay) with a point defect in the centre (dot). Right: for a magnetic field larger than B_c , the tactoid adopts an elongated shape that we model by a cylinder of length L and radius R_t with hemispherical end caps. In the cylinder, the field is radial in two dimensions with a defect line on the axis and in the caps the field is radial in three dimensions, originating from the ends of the defect line.

7.3 Tactoid model

The strong-anchoring condition expresses itself in a radial director field characterised by a hedgehog point defect at the centre of a spherical drop. For a sufficiently strong magnetic field, its influence on the orientation of the particles becomes significant. This field biases a certain orientation of the platelets, determined by the sign of the diamagnetic susceptibility anisotropy $\Delta\chi$. In the spherical droplet with radially symmetric director field, the orientation of the particles does minimise the surface energy but not their magnetic energy. Therefore, by way of compromise a non-spherical shape, elongated in the direction of the magnetic field, allows more particles to align with the magnetic field and yet retain their homeotropic alignment to the surface.

In our model we presume the droplet shape to be described by a cylinder of length L and radius R_t with two hemispherical end caps, see Fig. 7.1. In addition, we suppose the director field in the end caps to be of the same type as in the spherical tactoid, i.e., radial in three dimensions, and in the cylindrical part to be radial in two dimensions with the cylinder axis as the axis of symmetry. This implies that the point defect in the spherical configuration is stretched to a line (or disclination) defect of topological charge $+1$, as predicted by Mkaddem and Gartland [200]. Associated with the formation of the line defect from the point defect is an increase of the elastic free energy of the director field. Furthermore, the surface area increases with the elongation, giving rise to an additional surface free-energy cost. These two effects are compensated for by the free-energy gain on account of an increase of the number of particles aligning with the

magnetic field.

For the magnetic energy we find from Eq. (7.3)

$$F_m = \frac{2}{9}\pi\Sigma R_t^3, \quad (7.4)$$

with $\Sigma \equiv -\rho\Delta\chi B^2$. This contribution comes from the end caps, since the director field is perpendicular to the magnetic field in the cylinder. The elastic energy F_e associated with the distortion of the director field has contributions from the hemi-spherical end caps and from the cylindrical mid section. The contribution of the cylindrical part can in turn be divided into a part from the bulk and a part from the core containing the defect line on the cylinder axis. This gives an elastic free energy proportional to $f_{\text{core}}La^2$, with f_{core} the energy density of the core of the defect and a the core diameter of the defect line. We absorb this contribution into the bulk free energy of the cylindrical portion of the drop by introducing an effective defect core diameter b that we expect to be of the order of the diameter of the platelets because defects have been observed to be of the size of the nematogens in lyotropic nematics [203]. Note that in this study this contribution is not important for the transition because we compare a spherical drop and an elongated one that both have this core.

A radial director field in the cylinder portion and in the end caps implies that it is irrotational in the entire droplet. In the cylindrical part we have $\nabla \cdot \mathbf{n} = 1/\hat{r}$ with \hat{r} the radial coordinate in two dimensions, whereas in the end caps $\nabla \cdot \mathbf{n} = 2/r$, with r the radial coordinate in three dimensions. Using cylindrical coordinates for the axis part and spherical coordinates for the ends caps we conclude that the elastic energy of our model tactoid must obey

$$F_e = \pi K_1 L \log\left(\frac{R_t}{b}\right) + 8\pi K_1 R_t. \quad (7.5)$$

The interfacial energy has only a contribution F_{st} from the bare surface tension because $F_{sa} = 0$, so it is proportional to the surface area of the elongated droplet, and

$$F_{st} = \gamma(2\pi R_t L + 4\pi R_t^2). \quad (7.6)$$

In the next section we compute the optimale shape by minimising the total free energy, equal to the sum of $F \equiv F_m + F_e + F_{st}$, with respect to the shape.

7.4 Optimal shape

By introducing the dimensionless variables $r \equiv R_t/R$, $b_0 \equiv b/R$, and $\ell \equiv L/R$, the Helmholtz free energy F can be rewritten as

$$F = \frac{2}{9}\pi\Sigma R^3 r^3 + K_1\pi R\ell \log\left(\frac{r}{b_0}\right) + 8\pi K_1 Rr + 2\pi\gamma R^2(r\ell + 2r^2). \quad (7.7)$$

The free energy is made dimensionless by division by K_1R , giving $f \equiv F/K_1R$, and we subtract the reference energy of the spherical droplet with $r = 1$ and $\ell = 0$, to find the excess free energy Δf :

$$\Delta f = \frac{2\pi\Sigma R^2}{9K_1}(r^3 - 1) + \pi\ell \log\left(\frac{r}{b_0}\right) + 8\pi(r - 1) + 2\pi\frac{\gamma R}{K_1}(r\ell + 2(r^2 - 1)). \quad (7.8)$$

We introduce the dimensionless variables $\mathfrak{R} = R\gamma/K_1$ and $\beta^2 \equiv \Sigma K_1/\gamma^2$, and use that the variable ℓ depends on r via volume conservation,

$$\frac{4}{3}\pi R^3 = \pi R^3 r^2 \ell + \frac{4}{3}\pi R^3 r^3, \quad (7.9)$$

so $\ell = (4/r^2 - 4r)/3$. This enables us to express the shape in terms of a single parameter, i.e., the radius r of the cylinder, so the minimisation of F can be performed by differentiation with respect to r .

This gives the excess free energy Δf that we then differentiate with respect to r to find for the optimal shape

$$\frac{2}{3}\pi\beta^2\mathfrak{R}^2 r^2 + \frac{4\pi}{3}\left(\left(-\frac{2}{r^3} - 1\right)\log\left(\frac{r}{b_0}\right) + \frac{1}{r^3} - 1\right) + 8\pi + \frac{8\pi}{3}\mathfrak{R}\left(r - \frac{1}{r^2}\right) = 0. \quad (7.10)$$

If the optimal value of R_t is larger than R , or $r > 1$, then by construction $R_t \equiv R$ because the model allows for negative values of the length of the cylindrical part of the drop. This is the case for magnetic-field strengths smaller than a critical value. This critical value B_c , where the director-field transition occurs, can be obtained from Eq. (7.10) by insisting that $r = R_t/R = 1$, giving $\beta_c^2 = -6(\log b_0 + 2)/\mathfrak{R}^2$, or

$$B_c^2 = \frac{6K_1}{\rho\Delta\chi R^2}\left(\log\left(\frac{b}{R}\right) + 2\right). \quad (7.11)$$

In order to have a positive B_c , Eq. (7.11) requires that $b/R < \exp(-2) \approx 0.14$. Hence, if b is of the order of a platelet diameter (~ 200 nm), this gives $R > 1.5$ μm . For such a small droplet size one may wonder whether a macroscopic theory is still meaningful. This critical magnetic field is independent of the surface tension γ because at the onset of the transition the droplet is not deformed yet. This allows us to determine K_1 from Eq. (7.11), which can then be used to find γ by fitting Eq. (7.10) to the experimental

data of the tactoid size for different magnetic fields. This we do in the next section. The fact that a minimum magnetic-field strength is required agrees with the experiments on the sterically stabilised gibbsite platelets that we mentioned in section 7.1. Eq. (7.11) is reminiscent of a Frederiks transition because it describes a critical field strength that is required for a sudden change in the director field and that scales with $K/\Delta\epsilon R^2$, with $\Delta\epsilon$ the dielectric anisotropy [199], but the type of director-field distortion is different and here we have no solid boundary.

In Fig. 7.2 the degree of tactoid elongation, expressed by r , is shown as a function of β^2 , for various values of \Re . These values have been chosen such that $\Re > 3$, because for smaller values a homogeneous director field is formed instead of a radial one, as we will show in chapter 8.

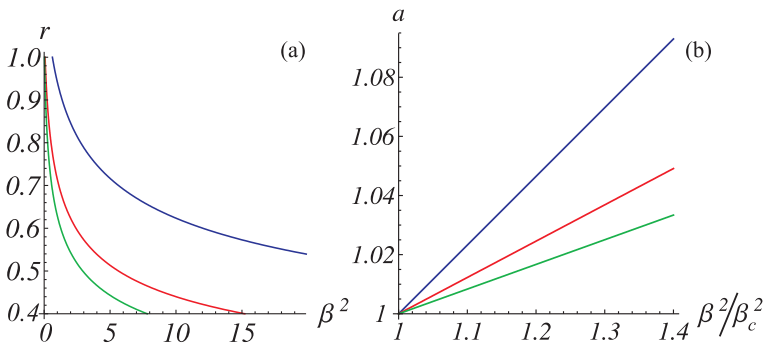


Figure 7.2: (a) The radius of the cylinder relative to that of the initial spherical tactoid $r \equiv R_t/R$, which is a measure of the degree of tactoid elongation, as a function of the dimensionless magnetic-field strength β^2 for $\Re = 5$ (top), 15, and 25 (bottom). (b) The increase in the aspect ratio a as a function of the dimensionless magnetic-field strength β^2 for $\Re = 5$ (top), 15, and 25 (bottom).

As already alluded to in section 7.1, the simple model allows use to find analytical predictions for the transition that follows from the model. Indeed, if we consider small deviations δ from the spherical shape with $r = 1$ and ϵ from the critical magnetic-field strength B_c , so we substitute $r = 1 - \delta$ and $\beta^2 = \beta_c^2(1 + \epsilon)$ in Eq. (7.10), with $0 < \delta \ll 1$ and $0 < \epsilon \ll 1$ as perturbation parameters, we find

$$\delta = \frac{6 - 2\Re + 4 \log\left(\frac{b}{R}\right)}{\log\left(\frac{b}{R}\right) + 2} \epsilon, \quad (7.12)$$

to first order in δ and ϵ . Again, this poses the restriction that $b/R < \exp(-2)$ to make this a meaningful expression. By using volume conservation, Eq. (7.9), we find for

$a = 1 + \ell/2r$ that

$$a = 1 + \frac{2}{3} \left(\frac{2}{r^3} - 1 \right). \quad (7.13)$$

If we substitute $r = 1 - \delta$, we find as a first-order approximation that $a = 1 + 2\delta$. We combine this with Eq. (7.12) to determine how rapidly the aspect ratio increases with increasing magnetic-field strength, just above the critical value. The result is shown in Fig. 7.2. In section 7.5 we find that such a linear approximation for the shape deformation is quite accurate.

A second analytical result is that we can determine the scaling of r that follows from Eq. (7.10) in the limit of very strong magnetic field where the tactoid is strongly elongated. Clearly, r cannot become smaller than b_0 as the cylinder must be larger than the core of the defect, so we cannot simply take a limit $r \rightarrow 0$. If we assume that r can still be so small that $r < 1/\mathfrak{R}$, we find as a first approximation from that

$$\beta^2 \mathfrak{R}^2 r^2 \approx \frac{4}{3r^3} \log \left(\frac{r}{b} \right). \quad (7.14)$$

So, $r \propto \beta^{-2/5} \mathfrak{R}^{-2/5}$ up to logarithmic corrections, which gives for the aspect ratio a according to Eq. (7.13) that $a \propto \beta^{6/5} \mathfrak{R}^{6/5}$. This is a testable result amenable to experimental verification.

7.5 Comparison with experiments

The theoretical predictions from the previous section can be tested against experimental results on tactoids in sterically stabilised dispersions of gibbsite platelets with homeotropic anchoring [84]. From the fact that there is rotational symmetry and from the observed interference colours, the director field can be deduced. For weak magnetic fields the tactoid has a radial director field with a hedgehog point defect of topological charge +1 in its centre. From a certain critical field strength on the dark cross inside the tactoid (where the platelets are oriented along the polarisers) transforms into a dark line along the magnetic field, as depicted in Fig. 7.3. Platelets in this dark region are oriented with their director perpendicular to the focal plane, and therefore do not exhibit birefringence. This implies that the point defect in the centre of the tactoid is stretched to a line defect along the direction of the magnetic field, from which the director lines go to the surface, as illustrated in Fig. 7.1. When the magnetic field is increased further, the tactoid becomes discernably elongated with its long axis in the direction of the magnetic field. Upon decreasing the magnetic field the tactoid relaxes back to its original configuration within a few minutes, so the process is reversible.

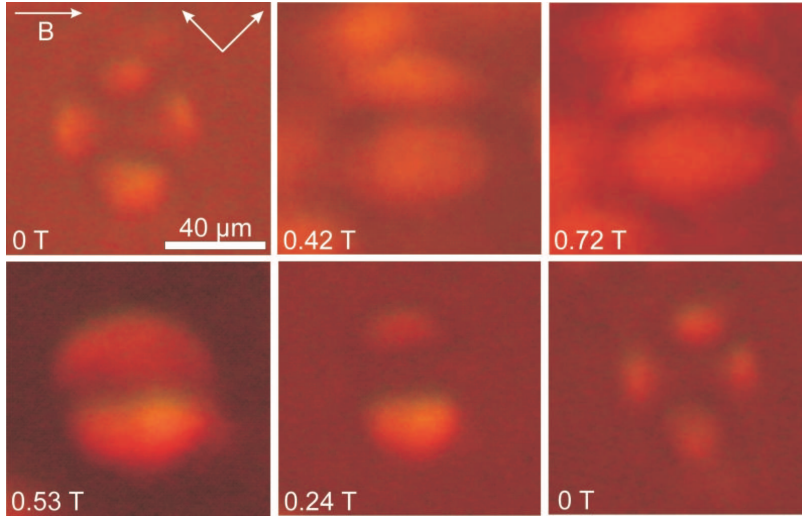


Figure 7.3: Polarisation-microscopy image of the deformation of a tactoid of colloidal gibbsite platelets in a magnetic field [84, 202]. The white arrows indicate the polarisers, meaning that platelets in a dark region are oriented with their director perpendicular to one of the polarisers. The point defect is stretched to a line defect, and the tactoid becomes elongated. When the field is decreased the tactoid relaxes back to its original configuration.

Fig. 7.4 shows the degree of deformation as a function of magnetic-field strength of two different tactoids in terms of the aspect ratio $a = (L + 2R_t)/2R_t$, and the fits of our model that follow from Eq. (7.10). This comparison enables us to extract material parameters of the liquid crystal from the deformation of the tactoid in the magnetic field. First of all, from the critical magnetic field, where the deformation starts, we obtain the splay elastic constant K_1 . From Fig. 7.4 we find for the tactoid with $R = 28 \mu\text{m}$ a critical field strength $B_c = 0.3 - 0.4 \text{ T}$ and for the tactoid with $R = 31 \mu\text{m}$ a critical field strength $B_c = 0.2 - 0.3 \text{ T}$. Using Eq. (7.11), with $\Delta\chi = -10^{-22} \text{ J/T}^2$, $\rho = 4 \times 10^{20} \text{ m}^{-3}$ [42, 83], and $b_0 = 10^{-2}$, where we assume that the size of the defect is of the order of the platelet diameter, we find $K_1 = (1.4 - 2.6) \times 10^{-13} \text{ N}$ for the $28 \mu\text{m}$ tactoid and $(0.9 - 2.0) \times 10^{-13} \text{ N}$ for the $31 \mu\text{m}$ tactoid. From the deformation of the shape above the critical field strength the interfacial tension γ can be determined. Fig. 7.4(a) depicts a fit of the deformation of the $28 \mu\text{m}$ tactoid with Eq. (7.10), using $\gamma = 5 \times 10^{-7} \text{ N/m}$. The dashed lines, representing theoretical results for $\gamma = 3 \times 10^{-7} \text{ N/m}$ and $\gamma = 7 \times 10^{-7} \text{ N/m}$, show that the shape is strongly dependent on the interfacial tension where a lower interfacial tension results in a stronger deformation, and the value we find for γ is therefore robust. A similar fit for the $31 \mu\text{m}$ tactoid, depicted in Fig.

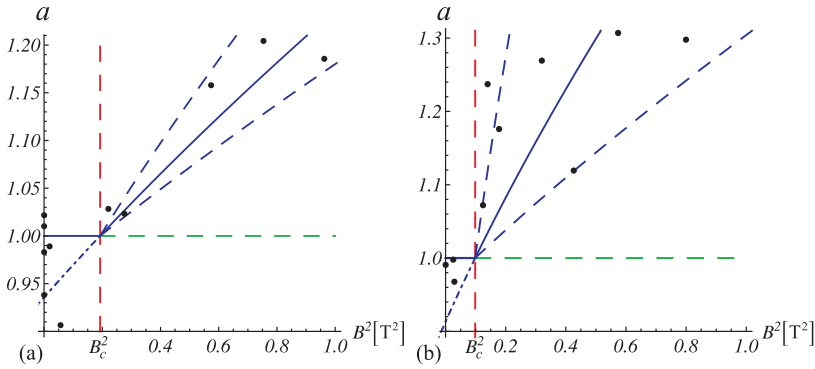


Figure 7.4: Aspect ratio $a = (L + 2R_t)/2R_t$ of tactoids of plate-like gibbsite particles as a function of the square of the magnetic-field strength. The points depict the experimental data and the lines our theoretical model. (a) Fit of the deformation data of the $28 \mu\text{m}$ tactoid, using $K_1 = 3 \times 10^{-13} \text{ N}$, and for the solid line $\gamma = 5 \times 10^{-7} \text{ N/m}$. Dashed lines represents theoretical results with lower and higher values for the interfacial tension ($\gamma = 3 \times 10^{-7}$ and $7 \times 10^{-7} \text{ N/m}$). (b) The same results for the $31 \mu\text{m}$ tactoid with $K_1 = 2 \times 10^{-13} \text{ N}$ and $\gamma = 2 \times 10^{-7} \text{ N/m}$ (solid line), and 0.2 and 5 (dashed lines) $\times 10^{-7} \text{ N/m}$. The steepest lines correspond to the smallest γ . The measured aspect ratio smaller than unity presumably arise from fluctuations or the fact that the tactoid is creaming or sedimenting. The value for B_c follows from the best fit to the data as given by Eq. (7.10).

7.4(b), gives an interfacial tension of $2 \times 10^{-7} \text{ N/m}$, with the dashed lines representing 0.2 and $5 \times 10^{-7} \text{ N/m}$. As argued in section 7.4, such a value can also be obtained by using Eq. (7.12) and the observation that $a = 1 + 2\delta$ for small values of deviations δ in the value of $r = 1$ for the spherical drop.

7.6 Discussion and conclusions

In this chapter we have presented model for nematic droplets with perfect homeotropic anchoring in a magnetic field. We focused on negative values of the magnetic susceptibility $\Delta\chi$ because this is the case for gibbsite platelets, but in case of a positive $\Delta\chi$ the point defect presumably transforms into a ring defect in the plane perpendicular to the magnetic field [201]. The ring increases in size with increasing field strength and gives a uniform director field inside the ring to minimise the magnetic energy cost. For negative $\Delta\chi$ the magnetic field imposes an orientation of the particles perpendicular to that field. If the magnetic field is sufficiently strong, the magnetic energy cost becomes so large that a configuration with split-core line defect is more favourable, because it allows more particles to comply with the magnetic field. Therefore, at this critical field strength the

radial director field with hedgehog point defect in the centre transforms to an elongated shape with split-core line defect. The observed transformation is a Frederiks-like transition, and we have also derived an analytical expression for the critical magnetic-field strength. Our results are confirmed by experiments on tactoids of plate-like particles in a magnetic field [84], where indeed a minimum magnetic-field strength was required to observe the Frederiks-like transition in these dispersions. This is in agreement with the prediction by Mkaddem and Gartland that such a line defect could be stabilised by a magnetic field in case of a negative value of $\Delta\chi$.

From a comparison our of theory and these experiments we have been able to determine both the splay elastic constant and the interfacial tension. The value we find for the splay elastic constant $K_1 = (0.9 - 2.6) \times 10^{-13}$ N should be compared to the value for the bend elastic constant K_3 measured by Van der Beek and co-workers, $K_3 = (7 \pm 1) \times 10^{-14}$ N [83]. We see that K_1 is 2 to 3 times larger than K_3 , in agreement with theoretical predictions by Osipov and Hess [189] and recent computer simulations by O'Brien and co-workers [52]. As expected for these large particles, the interfacial tension is low [6], though recent capillary rise experiments resulted in an even lower value for the interfacial tension of $\gamma = 7 \times 10^{-9}$ N/m [42]. In chapter 6 we found values for γ of the same order of magnitude by fitting our model for the capillary rise to these experiments.

In order to understand this rather significant difference it should be noted that in our analysis of the elastic free energy we ignored the so-called saddle-splay deformation of the field [14], which is nonzero for a three-dimensional radial director field. This means that the second term of Eq. (7.5), originating from the elastic deformation in the end caps, actually contains a renormalised elastic constant $K_1 - K_{24}$. Here, K_{24} is the saddle-splay deformation constant that is unknown, although $K_{24} = (K_{11} - K_{22})/2$ has been estimated from a molecular approach. We note that the saddle-splay deformation is zero for the two-dimensional radial around the defect line. Still, even invoking a renormalised splay elastic constant cannot quite account for the discrepancy because the corresponding third term of Eq. (7.10) is relatively small compared to the first and second term with $b_0 \approx 10^{-2}$. So the shape is determined primarily by a balance between the magnetic contribution and the term associated with the director field deformation in the cylinder.

A moot point in our model is that we neglected the effect of the magnetic field on the material parameters in this work, which may be questionable because of, e.g., the alignment of the background isotropic phase for with increasing field strength. The alignment of the isotropic phase must affect the values of the surface tension and anchoring strength that presumably become smaller due to the alignment. Moreover, the magnetic field increases the order parameter S_2 of the nematic phase, defined in Eq.

(1.4), which should affect the splay elastic constant K_1 and the anchoring strength ζ . The elastic force together with surface anchoring force compete with the magnetic force against the deformation, so an underestimation of K_1 would lead to a too large value of the surface tension. Still, it is not certain by any means that this effect is strong enough to explain the large difference in the values of the surface tension.

A possible explanation for the discrepancy may lie in the imperfect surface anchoring that is neglected in the theory, which may be too strong an assumption both in the cylinder and the end caps. In the end caps, this assumption implies that there are relatively many particles that show (almost) perpendicular alignment with the magnetic field, which is expensive energetically. In the cylinder, complete anchoring is imposed by choosing a cylindrical tactoid shape, whereas a shape with nonzero curvature of the tactoid surface along the direction of the magnetic field, e.g., an ellipsoid, is probably a more realistic model of a tactoid. A model with imperfect surface anchoring is dealt with in the next two chapters. The interfacial energy in Eq. (7.1) then contains not only a contribution originating from the bare surface tension γ , but also one associated with the anchoring strength ζ of the director field to the tactoid interface. In chapter 8 we focus on the limiting case of very small $\omega \equiv \zeta/\gamma$, meaning that surface tension dominates the anchoring strength and the droplets remain spherical. In chapter 9 we combine the approach of this chapter and chapter 8 and allow for non-spherical shapes as well as split-core defects within a spherical shape. This difference in the value of the dimensionless anchoring strength ω is reflected in the experiments in two types of solvent: an aqueous one in the next chapter for $\omega \rightarrow 0$ and the one with bromotoluene with $\omega > 0$ that we considered in this chapter and return to in chapter 9.

We thank Lia Verhoeff for performing the experiments on the tactoids.

Spherical homeotropic nematic droplets in a magnetic field

8

We present a Frank-Oseen elasticity theory for the effect of a magnetic field on homeotropic nematic droplets in a different regime from that of chapter 7, namely that of weak anchoring, where the surface tension dominates over the anchoring of the director field to the drop interface. This implies that the drops remain spherical and, as a result, they have imperfect surface anchoring. We find that small drops have a homogeneous director field for any magnetic field strength, whereas larger drops have a radial director field in a weak magnetic field. We discuss two cross-over routes from the homogeneous director field to the radial configuration: (i) via the gradual displacement of the central hedgehog to infinity, and (ii) via the formation of a ring defect that increases its radius to far outside the drop where it becomes virtual. In both cases an energy barrier has to be overcome to complete the crossover. For strong magnetic fields the hedgehog point defect transforms into a split-core line defect to reduce the magnetic energy cost. We present a phase diagram that shows the director field for a given tactoid size and magnetic field strength. Our findings rationalise the different structures that have been observed experimentally in charge-stabilised dispersions of gibbsite platelets, and the comparison allows us to extract values for the splay elastic constant and the anchoring strength.[†]

[†]The contents of this chapter are based on the following publications:
A. A. Verhoeff, I. A. Bakelaar, R. H. J. Otten, P. van der Schoot, and H. N. W. Lekkerkerker, *Langmuir* **27**, 116-125 (2011),
A. A. Verhoeff, R. H. J. Otten, P. van der Schoot, and H. N. W. Lekkerkerker, *Journal of Chemical Physics* **134**, 044904 (2011),
R. H. J. Otten and P. van der Schoot, in manuscript.

8.1 Introduction

In chapter 7 we presented a model for a drastic change in the director field and shape of tactoids with homeotropic anchoring in a sufficiently strong magnetic field. The model presumed the limiting case of strong anchoring of the director field to the tactoid surface and that the change in director field is accompanied by an elongation of the drop itself. These model ingredients were inspired by recent experimental observations in dispersions of sterically stabilised gibbsite particles in an organic solvent. In this chapter we present a model for a different limiting case, namely where the surface tension dominates the anchoring strength, meaning that the drops are spherical because an increase in the surface area of the drop is prohibitively large. The fact that the drops remain spherical implies that the director field exhibits imperfect surface anchoring. With this model we aim to rationalise different experiments on the same gibbsite particles, but in this case in a charge-stabilised dispersion, in which a similar Frederiks-like transition of the director field was observed as in the sterically stabilised dispersion, but the drops showed no discernable deviation from the spherical shape [85, 86].

A second interesting observation in these experiments is that the crossover from a radial director field to a uniform one with decreasing drop size seems to occur via two different routes. In one route the point defect transforms into a small ring defect that increases its radius until it has left the confines of the drop and becomes virtual, and in the second route, the point defect is displaced from the centre and also becomes virtual when it is outside the drop.

In this chapter and the next chapter we present a macroscopic theory that rationalises these experimental observations, where we presume surface tension to be the dominant force, so we focus on spherical drops. We describe how the director-field configuration is governed by a competition between the anchoring strength, bulk elastic properties of the nematic, and the magnetic field. Based on the experimental observations, we consider a homogeneous and a radial director field, and one with a split-core defect, and we determine the director field with the lowest free energy for given values of the material parameters. We assemble our results in a stability diagram and find that small drops have a homogeneous director field for any magnetic-field strength and larger drops have a hedgehog point defect for weak or zero magnetic field. If the magnetic field is strong enough, a split-core line defect in the direction of this field becomes more favourable than the point defect.

We also discuss the crossovers between the different director fields. The crossover from point defect to line defect is smooth and we find an analytical expression for the critical magnetic-field strength that is reminiscent of the Frederiks transition. For the

transition from radial field to to split-core defect we consider two conceivable cross-over routes, as observed in the experiments mentioned above. A point defect that is located off-centre is not a free-energy minimum, so it cannot be a stable situation, whereas a small ring defect in the centre could be stable. However, in both hypothetical cross-over routes in the phase diagram an energy barrier must be overcome. This means that both crossovers are abrupt and that the intermediates cannot occur in a stable dispersion. Our results agree with the experiments on tactoids in charge-stabilised dispersions of gibbsite platelets and the comparison allows us to extract values for the splay elastic constant and the anchoring strength.

In the remainder of this chapter we first discuss the free energies of the possible director fields in section 8.2. Then we present our phase diagram for the optimal tactoid structure and the cross-over routes from a uniform to radial director field in section 8.3. Next, we compare these results with experimental observations in section 8.4 and finally, we discuss our model and the results in section 8.5.

8.2 Free energy

From Eqs. (7.1), (7.2), and (7.3) as presented in chapter 7 we deduce that the four free energies scale as $F_{st} \sim \gamma R^2$, $F_{sa} \sim \zeta R^2$, $F_e \sim K_1 R$, and $F_m \sim \Sigma R^3$, with $\Sigma \equiv -\rho \Delta \chi B^2$ a measure of the strength of the magnetic field \mathbf{B} , and R the radius of the drop. We immediately see that for sufficiently small tactoids the elastic deformation must be dominant, giving rise to a uniform director field irrespective of the magnetic-field strength. On the other hand, for very large drops the magnetic energy becomes dominant, forcing the particles to comply with the orientation imposed by this field. If we ignore the prefactors for a moment, the relative magnitude of these free-energy scalings provides us with more information in terms of three dimensionless groups that follow naturally from this comparison and turn out to be important for the remainder of this chapter and the next one.

1. If we compare both surface terms, we find a dimensionless anchoring strength $\omega \equiv \zeta/\gamma$. For large values of ω the anchoring is dominant over the bare surface tension, indicating a preference to deform the interface over an unfavourable surface anchoring of the director field to the drop interface.
2. Combining F_e with F_{st} or F_{sa} gives a scaled droplet size $\mathfrak{R} \equiv R\gamma/K_1$ or $R\zeta/K_1 = \mathfrak{R}\omega$. For small values of \mathfrak{R} and $\mathfrak{R}\omega$ the elastic energy dominates over the surface and anchoring energy, leading to a homogeneous director field at the expense of a deformed droplet and imperfect surface anchoring, respectively.

3. Taking the ratio of F_m and F_{st} gives $\Sigma R/\gamma = \beta^2 \mathfrak{R}$, where we defined $\beta^2 \equiv \Sigma K_1/\gamma^2$. The square of β is taken because it has a factor B^2 in it, making it a positive quantity, at least for $\Sigma > 0$, i.e., $\Delta\chi < 0$. We can write $\beta^2 \sim F_m F_e/F_{st}^2$, so a large value of β^2 means either a dominant magnetic field or dominant elasticity. As we will see below, this leads to the director field either becoming uniform or forming a split-core line defect in the direction of the magnetic field.

As already alluded to in chapter 7, the simultaneous minimisation of the free energy F with respect to both shape and director field is a constrained-free boundary-value problem that is virtually impossible to solve analytically, and even hard to solve numerically. Hence, the approach we adopt here is to impose four types of director field and three types of tactoid shape based on the experimental observations and then to calculate the combinations of a shape and a director field that have the lowest free energy for given value of our dimensionless parameters ω , \mathfrak{R} , and β^2 .

From the analysis above it follows that for a sufficiently small spherical drop the zero energy cost associated with the elastic deformation and the magnetic field outweighs the surface anchoring cost of the uniform field. This argument is valid regardless of the magnetic-field strength. This means that there is only an interfacial energy $F_{st}^u = 4\pi\gamma R^2$, with R the drop radius, and an anchoring energy F_{sa}^u . The superscript indicates the type of director field, which is in this case u for uniform. Using spherical coordinates we find $F_{sa}^u = 8\pi\zeta R^2/3$, so

$$F^u = 4\pi\gamma R^2 + \frac{8}{3}\pi\zeta R^2. \quad (8.1)$$

Recall that in this chapter we consider the case of $\omega = \zeta/\gamma \ll 1$, so the surface-tension term is dominant in Eq. (8.1). For larger tactoids the anchoring conditions become increasingly important, so the uniform director field can no longer be maintained. The strong anchoring requirements are fulfilled by a three-dimensional radial director field with a hedgehog point defect in the centre of the tactoid. Its free energy has contributions associated with a director-field distortion and the magnetic field. In the case of a three-dimensional radial director field with a hedgehog point defect (superscript h), there is perfect anchoring to the tactoid surface, so $F_{sa}^h = 0$ and the only contribution from the interfacial energy is $F_{st}^h = 4\pi\gamma R^2$. Using spherical coordinates, the elastic deformation energy and magnetic energy are directly found to be

$$F_e^h = 8\pi K_1 R, \quad (8.2)$$

because $(\nabla \cdot \mathbf{n})^2 = 4/r^2$, with r the radial coordinate in three dimensions, and

$$F_m^h = \frac{2}{9}\pi\Sigma R^3, \quad (8.3)$$

with $\Sigma \equiv -\rho\Delta\chi B^2$ as introduced before. Note that we ignored the free energy associated with the core of the defect. This contribution will become significant in the analysis of the split-core defect.

The total free energy of the spherical tactoid with radial director field becomes

$$F^h = 4\pi\gamma R^2 + 8\pi K_1 R + \frac{2}{9}\pi\Sigma R^3. \quad (8.4)$$

In the absence of a magnetic field, we can estimate for what droplet size R the hedgehog is energetically more favourable than the uniform field. A comparison with experimental data can then provide a lower bound for ζ . We see from Eqs. (8.1) and (8.4) that $F^h < F^u$ gives $8\pi K_1 R < \frac{8}{3}\pi\zeta R^2$, or $\Re\omega > 3$. Hence, for droplets with a radius larger than $3K_1/\zeta$ anchoring has the upper hand such that the surface-anchoring forces drive the director field into the hedgehog configuration. In chapter 9 we will see that for $\omega > 0$ the drops are lens-shaped, and the cross-over value can be very well described by $\Re\omega = 3 + 4\omega/5$, but in order to determine an approximate lower bound for the value of ζ from the experimental data the estimate $\Re\omega > 3$ will do.

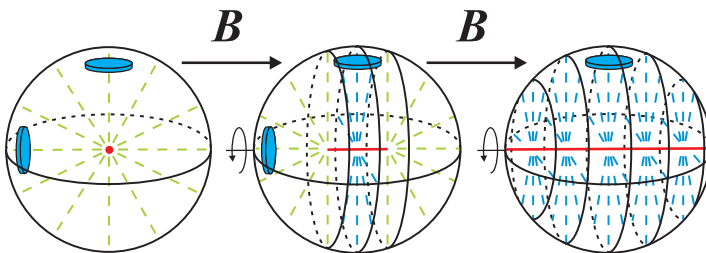


Figure 8.1: In order to lower the magnetic energy of the drop in a sufficiently strong magnetic field, the point defect (left) can stretch to a split-core line defect in the direction of the magnetic field \mathbf{B} . Middle: the field around the defect has a two-dimensional splay deformation with zero magnetic energy cost, whereas the director field is radial in three dimensions emanating from the ends of the defect line. Right: for a line defect throughout the entire tactoid the magnetic energy attains its minimum value.

For large enough tactoids the hedgehog configuration is more favourable than the homogeneous one, but for a sufficiently strong magnetic field it cannot be maintained either because in that case the magnetic energy becomes too large. To comply with the orientation imposed by the magnetic field for a larger fraction of the particles that make up the drop, the tactoid can, besides adopting a uniform director field, stretch the point defect to a line defect of topological charge $+1$ in the direction of the magnetic field. See Fig. 8.1. This in turn goes at the expense of the perfect homeotropic surface anchoring, which can be reduced by elongating the drop (see chapter 9). Note that this

anchoring cost is low relative to the bare surface energy, because we consider the case where $\zeta \ll \gamma$. If the point defect stretches to a line defect and we presume the director field around this line to be radial in two dimensions, the volume around the defect line has minimal magnetic energy penalty. In the remainder of the tactoid the director field is presumed to have a three-dimensional splay deformation. In summary, compared to the hedgehog this configuration has a lower magnetic energy penalty, which is even zero for a defect throughout the entire tactoid, but it has a higher elastic deformation energy and nonzero anchoring cost.

The derivation of the free energy

$$F^{sc} = F_{st}^{sc} + F_{sa}^{sc} + F_e^{sc} + F_m^{sc} \quad (8.5)$$

is quite technical and the details of the calculation can be found in Appendix 8.B. Here, we only give the result for the components of F^{sc} that read $F_{st}^{sc} = 4\pi\gamma R^2$ for the bare surface energy,

$$F_{sa}^{sc} = \frac{\pi\zeta L^3}{6R} + \frac{\pi\zeta}{16LR} \left(16LR^3 + 4L^3R - 4L^4 - 2(L^2 - 4R^2)^2 \coth^{-1} \left(\frac{2R}{L} \right) \right) \quad (8.6)$$

for the surface energy, where L is the as yet unknown line-defect length to be determined a posteriori, and

$$F_e^{sc} = \frac{\pi K_1}{L} \left((8R^2 - 2L^2 + 2LR) \coth^{-1} \left(\frac{2R}{L} \right) + 4LR - 3L^2 + L^2 \log \sqrt{\frac{4R^2 - L^2}{4b^2}} \right) \quad (8.7)$$

for the elastic energy, with b the diameter of the core of the line defect that we presume to be of the order of the nematogens, because it must be a microscopic length in lyotropic nematics [203, 205]. Given that b enters only logarithmically in our equations, its value has only a very limited effect on our results. For the magnetic energy we find

$$F_m^{sc} = \frac{\pi\Sigma}{576L^3} (L - 2R)^3 \left(4L(L^2 + 9LR + 6R^2) - 6(L + 2R)^3 \coth^{-1} \left(\frac{2R}{L} \right) \right). \quad (8.8)$$

For $L/R \rightarrow 0$ of zero line-defect length we retrieve $F^{sc} \rightarrow F^h$, with F^h the free energy of the central hedgehog as given by Eq. (8.4). In the limit of $L \rightarrow 2R$, so a line defect throughout the entire tactoid, we find

$$F^{sc} \rightarrow 4\pi\gamma R^2 + \frac{4}{3}\pi\zeta R^2 + 2\pi K_1 R \left(\log \left(\frac{R\omega}{b} \right) - 1 \right). \quad (8.9)$$

This requires an infinitely strong magnetic field, as we will also see below, and which is also reflected in the leveling off of the curves of L/R to the value 2 with increasing value

of B in Fig. 8.2. If $L/R = 2$ the drop only has energetic costs associated with elastic deformation and surface anchoring (and the irrelevant surface energy). By equating Eqs. (8.9) and (8.1) we obtain an equation for the tactoid size R beyond which the drop with split-core defect throughout the drop is more favourable than the homogeneous one. We find

$$\log\left(\frac{R\omega}{b}\right) - 1 = \frac{2\zeta R}{3K_1}. \quad (8.10)$$

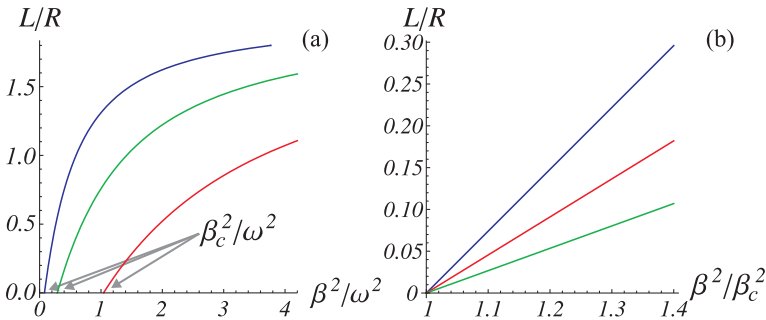


Figure 8.2: (a) The length of the line defect L relative to the tactoid radius R as a function of the magnetic-field strength β^2/ω^2 as given by minimising Eq. (8.5) with respect to L . The line defect starts to grow at a critical magnetic-field strength $\beta_c^2/\omega^2 = \Sigma B_c^2 K_1/\zeta^2$, where B_c is given by Eq. (8.16), and levels off to $L/R = 2$ for larger field strengths. (b) For field strengths a little larger than B_c^2 a linear approximation is accurate. In both graphs: $\Re = 5$ (left), 10, and 20 (right).

We compute the optimal length of the line defect by putting $\partial F^{sc}/\partial L = 0$. The resulting equation, which is given by Eq. (8.30) in Appendix 8.B, is used to eliminate the variable L from the free energy F^{sc} , giving a too large expression to show here, but it enables us to compare the free energy of the split-core configuration with the hedgehog and the drop with uniform director field. The length of the line defect that follows from this minimisation is shown in Fig. 8.2. The line defect starts to grow at a critical field strength from a zero value, showing that it is a second-order transition.

If the field strength is slightly larger than B_c , we can approximate Eq. (8.30) by making a Taylor expansion around B_c as given by Eq. (8.16) and $L = 0$. We substitute $B^2 = B_c^2(1 + \varepsilon)$, with $0 < \varepsilon \ll 1$, and find for small L that

$$L = \frac{15(4 + 2\log(\frac{b}{R}))}{72 - 40\Re\omega + 16\log(\frac{b}{R})} R\varepsilon, \quad (8.11)$$

to first order in ε . As in chapter 7, we have the restriction that $b/R < \exp(-2)$. Eq. (8.11) is shown in Fig. 8.2 together with the full dependence of L on β as follows from Eq. (8.30).

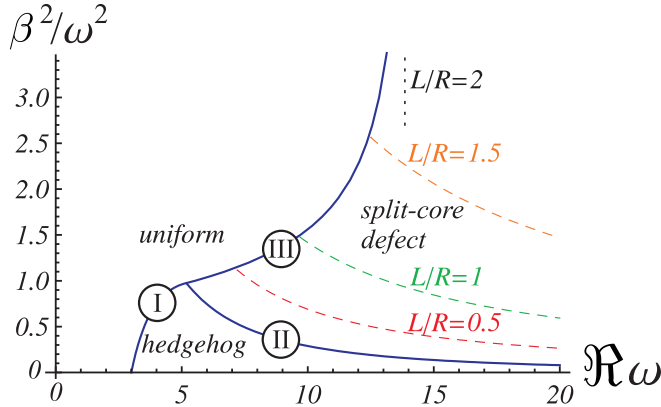


Figure 8.3: Stability diagram for the type of director field in the limit of $\omega \rightarrow 0$ where the tactoid is spherical, as a function of $\Re\omega \equiv R\zeta/K_1$ and $\beta^2/\omega^2 \equiv -\rho\Delta\chi B^2 K_1/\zeta^2$ that indicate the drop size and the magnetic-field strength, respectively. For sufficiently small tactoids the field is uniform, regardless of the magnetic-field strength. Larger tactoids have a hedgehog field but for a strong enough magnetic field this becomes a drop with a split-core line defect. The dashed lines show a constant line-defect length L relative to the drop radius R . The vertical asymptote (dotted line) shows the limit of $L = 2R$, i.e., a line defect throughout the entire tactoid, as given by Eq. (8.10). The crossovers I, II, and III are discussed in section 8.3.

In the limit of $\omega \rightarrow 0$ the surface anchoring plays a subdominant role relative to the bare surface tension γ , making the tactoids spherical and, perhaps counter-intuitively, making the problem independent of γ . This means that the relevant dimensionless groups are given by $\Re\omega = R\zeta/K_1$ and $\beta^2/\omega^2 \equiv -\rho\Delta\chi B^2 K_1/\zeta^2$. The director field is then determined by a balance between the anchoring energy, the elastic deformation energy, and the magnetic energy.

The results that follow from comparing the free energies of the three director fields from section 8.2 are shown in Fig. 8.3. As already expected from the scaling argument in section 8.2, small tactoids have a uniform director field irrespective of the magnetic-field strength, whereas larger tactoids have a hedgehog point defect, provided the magnetic-field strength is small. For larger field strengths this configuration can no longer be maintained because of a prohibitively large magnetic energy, and the point defect stretches to a split-core line defect to allow more particles to align in the direction imposed by the magnetic field. The length of the line defect increases with increasing magnetic-field strength. In the limit of an infinitely strong field the line defect even stretches through the entire drop to minimise the magnetic energy cost, see also Figs. 8.1. This leads to the vertical asymptote in the phase diagram, and the value of the drop size R associated with it satisfies Eq. (8.10).

8.3 Intermediates

The crossovers in the stability diagram of Fig. 8.3 raises two interesting questions that we discuss in this section.

1. If we examine crossover I from uniform to radial field more closely, what happens to two small drops with a uniform director field in zero or weak magnetic field that coalesce to form one that is larger than the cross-over value, so how does the resulting drop acquire the point defect that it should have according to the phase diagram?
2. Are the crossovers I, II, and III between the three type of director field gradual or sharp?

To answer these questions, we consider the intermediates below.

In order to answer question 1, we note that in the experiments on aqueous dispersions of gibbsite platelets, the population distribution of director fields for different drop sizes is almost bimodal, i.e., its shows predominantly uniform and radial director fields, and very few intermediates [85]. Moreover, these intermediates are configurations with a point defect close to the tactoid boundary. This means that the coalescence of two uniform drops would give a drop that according to its size, cannot be uniform anymore. So, this analysis suggests that the intermediates cannot be stable configurations and we support this by a calculation next.

Hence, we first focus on the first part of question 2, and we note that the intermediates between a uniform and a radial director field, shown by crossover I in Fig. 8.3, may involve off-centre hedgehog defects. To investigate their stability, we compute the free energy of this configuration for an arbitrary location of the defect. Details of our calculations can be found in Appendix 8.A. We compute the free energy $F^h(f)$ of the hedgehog at an arbitrary location, with its distance f from the centre acting as the continuous variable, expressed in units of the drop radius. See Fig. 8.4.

gives $F_{sa}^h(f) = 0$, as is the case for the central hedgehog. If the hedgehog is displaced from the centre of the tactoid but retains its three-dimensional radial director field, this introduces an additional anchoring cost and changes the elastic and magnetic energy. Inspired by the experimental observations on tactoids in dispersions of gibbsite, we presume the defect to be located on the z -axis at $(x, y, z) = (0, 0, -fR)$ for a magnetic field in the x -direction, where $f < 1$ ($f > 1$) represents a defect inside (outside) of the droplet. See also Fig. 8.4. The total free energy $F^h(f)$ is given by $F^h(f) = F_{st}^h(f) + F_{sa}^h(f) + F_e^h(f) + F_m^h(f)$, which by construction obeys $F^h(f) = F^h(-f)$. We

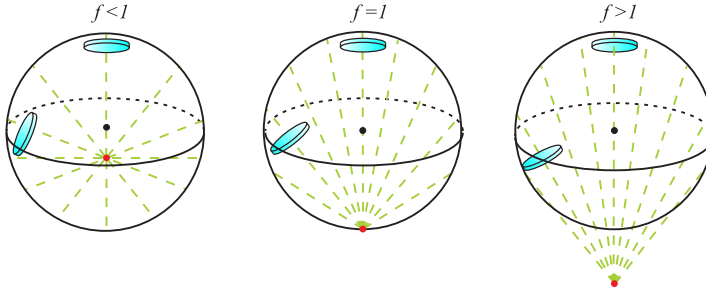


Figure 8.4: A possible cross-over route from a radial to uniform director field. The hedgehog is located at a distance fR from the centre of the tactoid of radius R , so $f > 0$ introduces an additional anchoring cost compared with the central hedgehog ($f = 0$). For $f < 1$ the defect is inside the drop (left), the hedgehog on the boundary follows from putting $f = 1$ (middle), and for $f > 1$ it is virtual, meaning located outside the tactoid (right), with the limit $f \rightarrow \infty$ giving a homogeneous director field.

find $F_{st}^h(f) = 4\pi\gamma R^2$,

$$F_{sa}^h(f) = \pi\zeta R^2 \left(f^2 + 1 + \frac{(f^2 - 1)^2}{4f} \log \left(\frac{f - 1}{f + 1} \right)^2 \right), \quad (8.12)$$

$$F_e^h(f) = 4\pi K_1 R \left(1 + \frac{f^2 - 1}{4f} \log \left(\frac{f - 1}{f + 1} \right)^2 \right), \quad (8.13)$$

and

$$F_m^h(f) = \frac{\pi\Sigma R^3}{288f^3} \left(4f(3 + 8f^2 - 3f^4) - 3(f^2 - 1)^3 \log \left(\frac{f - 1}{f + 1} \right)^2 \right). \quad (8.14)$$

In the limits of $f \rightarrow 0$ and $f \rightarrow \infty$ of $F_m^h(f)$, we recover the known results for a uniform director field and the central hedgehog, as given by Eqs. (8.1) and (8.4). Equating $\lim_{f \rightarrow \infty} F^h(f)$ and $F^h(1)$ retrieves the crossover I in Fig. 8.3. If we take the limit $f \rightarrow 1$ we find for the free energy of a hedgehog point defect located on the surface of the drop

$$F^h(1) = 4\pi\gamma R^2 + 2\pi\zeta R^2 + 4\pi K_1 R + \frac{\pi}{9}\Sigma R^3. \quad (8.15)$$

This means that the director field associated with the hedgehog on the surface has an anchoring cost that is absent for the centrally positioned hedgehog, but this is compensated by an elastic deformation and magnetic penalty that are exactly half of those in the central hedgehog. If we compare the free energy to that of the central hedgehog

and the uniform director field, we find that no configuration with the hedgehog defect at a finite distance from the centre can be a free-energy minimum, meaning that either the central hedgehog or the uniform field is always more favourable for given values of the parameters \Re and β^2 . See also Fig. 8.5. The fact that for a fixed value of \Re an energy barrier must be overcome, means that it is a first-order transition. We remark that putting $\partial F^h(f)/\partial f = 0$ and requiring $\partial^2 F^h(f)/\partial f^2 > 0$ to find the value of f with the lowest free energy, provides only $f = 0$ as an analytical solution.

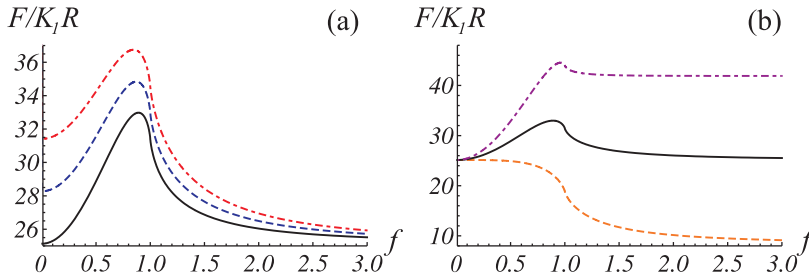


Figure 8.5: The free energy F of a spherical drop of radius R with a point defect with radial director field, with K_1 the splay elastic constant, is shown as a function of the distance f between the defect and the centre of the drop, expressed in units of R . See also Fig. 8.4. (a) For $\Re\omega = R\zeta/K_1 = 3$ and from top to bottom $-\rho\Delta\chi B^2 K_1/\zeta^2 = \beta^2/\omega^2 = 1, 0.5$ and 0 . (b) For zero magnetic field the three curves show the free energies for $\Re = 1$ (dashed), 3 (solid) and 5 (dot-dashed). For $\Re\omega = 3$ the free energy of the central defect and the uniform director field ($f \rightarrow \infty$) are the same.

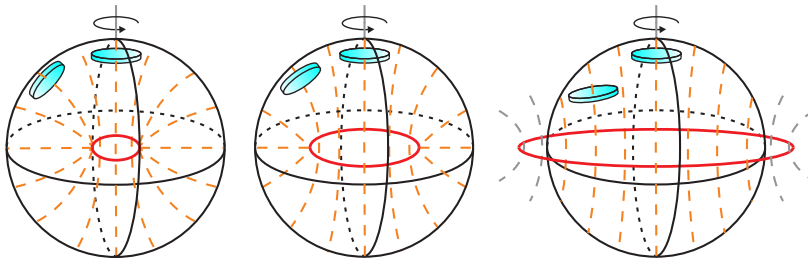


Figure 8.6: The second conceivable cross-over route from radial to uniform director field. The hedgehog point defect develops into a small ring defect that introduces a bend deformation and an anchoring cost, but this is compensated for by a smaller splay deformation and a lower magnetic energy cost than in the hedgehog configuration. A large ring radius compared to the sphere radius leads to a uniform director field within the drop.

We note that in the experiments on the charge-stabilised system it seems that the observed tactoid with hedgehog point defect close to the boundary is somewhat oblate

rather than spherical. However, a perturbation calculation shows that even such an oblate shape cannot have a lower free energy than both the central hedgehog and the uniform droplet for any values of the material parameters. See also Appendix 8.C. Therefore, we conclude that any hedgehog configuration off-centre in general, and the boundary hedgehog in particular, must be an unstable configuration, at least for pure splay fields. We surmise that its occurrence must be caused by the effects of the flow field around the creaming tactoid [85], and we return to this point in the discussion in section 8.5.

The second scenario for crossover I in the phase diagram from a central point defect with radial director field to a uniform director field is by means of the formation of a ring defect that with an increasing radius leads to a homogeneous field inside the tactoid if the ring is much larger than the drop. See also Fig. 8.6. It turns out that this route has in fact been analysed by Terentjev [201], although he did ignore the impact of imperfect anchoring. Terentjev considered a positive diamagnetic susceptibility and a magnetic field parallel to the ring axis, and this symmetry makes the problem equivalent to ours. He showed that in the equal-constant approximation $K_1 = K_3$ a small ring defect can be stable in a magnetic field. For small rings on the scale of the drop the director field is predominantly of the splay type, so the assumption of negligible anchoring energy is reasonable. For larger ring defects this configuration is more favourable than the hedgehog only for large magnetic fields, for which we have seen in Fig. 8.3 that neither configuration has the lowest free energy. We see from Fig. 4 in that paper that an energy barrier has to be overcome for $\Re^2\beta^2 \lesssim 15$ [201]. From Fig. 8.3, we deduce that this condition is met for a spherical drop for almost any cross-over values of $\Re\omega$ and β^2/ω^2 . Moreover, if we incorporate the anchoring energy cost, this makes the energy barrier even higher. So we conclude that only a ring defect that is small on the scale of the tactoid radius can be energetically more favourable than the hedgehog in a spherical drop. For such a small ring defect there is little deviation from the radial director field emanating from the hedgehog point defect, so we chose to omit this configuration in the phase diagram.

Next, we consider transition II from a spherical tactoid with a central hedgehog to one with a split-core disclination, which is reminiscent of a Frederiks transition. It requires the magnetic field to be sufficiently strong in order to allow more particles to comply with orientation imposed by the field. The critical magnetic-field strength B_c associated with this transition reads

$$B_c^2 = -\frac{4K_1}{\rho\Delta\chi R^2} \left(\log\left(\frac{b}{R}\right) + 2 \right). \quad (8.16)$$

The expression (8.16) for B_c is a factor of exact two thirds smaller than what we found earlier in our cruder model, Eq. (7.11), where we presumed perfect surface anchoring and the elongation of the defect to be simultaneously accompanied by a stretch of the drop itself that we presumed to be spherocylindrical [84]. The discrepancy can be explained from the difference in magnetic energy between the two different shapes.

The last crossover from Fig. 8.3 is III from uniform field to split-core defect. The cross-over line follows from equating the free energies of the uniform drop and the one with a split-core, Eqs. F^u and F^{sc} , with the added constraint the line-defect length obeys $\partial F^{sc}/\partial L = 0$. Similar to the radial-to-uniform crossover discussed above, we imagine it to occur via the formation of a ring defect out of the line defect that with increasing size gives a homogeneous director field inside the ring. Given the barrier to be overcome that we discussed above, we expect crossover III also to be abrupt.

In conclusion, there are three crossovers in the stability diagram of Fig. 8.3 between the uniform director field, radial director field with point defect, and field with split-core defect. Crossover II from point defect to line defect is gradual and therefore a second-order one, and the critical magnetic-field strength is given by Eq. (8.16). By contrast, crossovers I and III from uniform field to radial field and from uniform field to split-core defect, are abrupt and, as a result, of first order. Neither cross-over route from uniform to radial director field seems to be a favourable one, and we return to this in the discussion in section 8.5. How exactly two coalescing small drops with a homogeneous director field acquire a hedgehog point defect that the resulting drop should have according to the stability diagram is not obvious, and we leave it for future work.

8.4 Comparison to experiments

We can directly apply the theoretical model described in the previous section to experimental data on tactoids in charge-stabilised aqueous dispersions of gibbsite platelets, and extract material parameters relating to our liquid crystal droplets. Of particular use here are the length of the split-core defect, obtained as a function of the magnetic-field strength, and the critical magnetic-field strength at which this line defect starts to grow. Because of the numerous ways in which the parameters can be determined, we first give an outline of the approach that we have taken, and then present the resulting curve fits and parameter values.

In the limit of $\omega = \zeta/\gamma$, the model is independent of the surface tension γ and the relevant dimensionless groups are $-\rho\Delta\chi B^2 K_1/\zeta^2 \equiv \beta^2/\omega^2$ and $R\zeta/K_1 = \Re\omega$, as shown on the axes of Fig. 8.3. The data of both the length of the split-core defect are a function of the magnetic-field strength, which means that for the curve fits we

have to traverse the phase diagram vertically for a chosen scaled drop size $\Re\omega$ for the charge-stabilised system that has the best match with the data points of the line-defect length. The quality of this match is then determined by choosing the value of the dimension-bearing quantity $\omega^2 B^2 / \beta^2 = \zeta^2 / (-\rho \Delta \chi K_1)$ and the curve fitting amounts to finding a compromise between the best fit to the critical magnetic-field strength B_c where the split-core defect starts to grow, and the best fit to the data beyond those critical field strengths. These two choices then produce a value for ζ / K_1 and ζ^2 / K_1 for the charge-stabilised gibbsite, from which both individual parameter values can be deduced.

We remark that even though a line defect running throughout the entire tactoid was observed at very high field strengths, we omit these last few data points from our curve-fitting procedure, not least because we found in section 8.2 that according to our calculations this requires an infinitely strong magnetic field. A second reason is that including these points would make the general fit to the other points very poor indeed, e.g., with a critical magnetic-field strength that vanishes almost completely and, more worryingly, give the fitted curve the wrong curvature. See also Fig. 8.7. On the other hand, and in support of this choice, it is also true that the experimental points at high magnetic-field strength have a large degree of uncertainty because the contrast strongly diminishes as the “isotropic” (or rather, paranematic) background also aligns in the magnetic field. By way of consistency check, we use the analytic Eq. (8.16) for B_c in combination with the experimental data to derive a value for K_1 that we compare with the values found from our curve fitting procedure.

Finally, as already alluded to in section 8.2, the emergence of a radial hedgehog director field in the absence of a magnetic field produces a lower bound for the anchoring strength, because this happens according to our theory only if $\zeta > 3K_1/R$. Strictly speaking this is true only for the crossover from a spherical drop with a uniform field to a radial field; a slightly sharper, i.e., higher, lower bound can be found if we allow for the equilibrium lens shape, which we discuss in chapter 9. For convenience we here use the simple, but very accurate result that follows from the spherical drops, so then the choice for ω and \Re requires that $\Re\omega > 3$. The values for ω, γ and ζ that follow from these choices and the lower bound mentioned, above should then all be internally consistent. Because uniform tactoids have been observed in the aqueous gibbsite system, we have yet another check for the obtained values for K_1 and ζ , because we can independently determine the ratio of K_1/ζ from the tactoid size where the cross-over from a uniform to a radial director field takes place.

As explained above, we have to find the value of $\Re\omega$ that gives the best agreement with the critical magnetic-field strength B_c , where we again disregard the points at

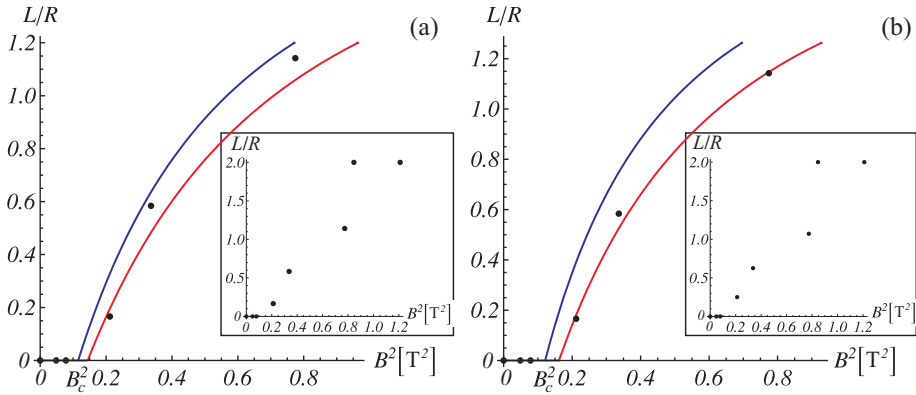


Figure 8.7: Ratio of the length of the split-core defect relative to the tactoid radius, L/R , as a function of the square of the magnetic-field strength B^2 for the case of a charge-stabilised gibbsite in water. Experimental data: points, the left and right drawn curves: theoretical curves, optimised with respect to the critical magnetic-field strength B_c and to the experimental values of L/R at larger field strengths. (a) Tactoid of $R = 30 \mu\text{m}$ with $\omega^2 B^2/\beta^2 = 0.4 \text{ T}^2$ and $B_c = 0.34 \text{ T}$ (left drawn curve) and $\omega^2 B^2/\beta^2 = 0.5 \text{ T}^2$ and $B_c = 0.38 \text{ T}$ (right drawn curve). (b) Tactoid of $R = 19 \mu\text{m}$ with $\omega^2 B^2/\beta^2 = 0.18 \text{ T}^2$ and $\omega^2 B^2/\beta^2 = 0.24 \text{ T}^2$, giving $B_c = 0.35 \text{ T}$ and $B_c = 0.40 \text{ T}$, respectively. Inset: the full set of experimental data [86]. See also the main text.

very high field strengths where $L/R \approx 2$. The fits give a lower and upper bound for $\omega^2 B^2/\beta^2 = \zeta^2/(-\rho\Delta\chi K_1)$. We use the measured length of the split-core defect of two tactoids of radius 30 and 19 μm , respectively [86]. For the drop with $R = 30 \mu\text{m}$ we obtain the value $\Re\omega = 10$, and the fits with the best curvature and the best fit to the data give a lower and upper bound for ζ of $\zeta = 4.8 \cdot 10^{-8} \text{ N/m}$ and $\zeta = 6.0 \cdot 10^{-8} \text{ N/m}$, and K_1 between $1.4 \cdot 10^{-13} \text{ N}$ and $1.8 \cdot 10^{-13} \text{ N}$, where the critical magnetic-field strengths vary between $B_c = 0.34 \text{ T}$ and $B_c = 0.38 \text{ T}$, see Fig. 8.7. If we use Eq. (8.16) with the data for the line-defect length we find $B_c = 0.3 \pm 0.2 \text{ T}$, which results in a value for $K_1 = (3.5 \pm 0.4) \cdot 10^{-13} \text{ N}$. For the smaller drop with $R = 19 \mu\text{m}$ we obtain $\Re\omega = 6.3$, and we find from the best fit to the data bounds of ζ of $\zeta = 2.2 \cdot 10^{-8} \text{ N/m}$ and $\zeta = 2.9 \cdot 10^{-8} \text{ N/m}$, and K_1 between $6.5 \cdot 10^{-14} \text{ N}$ and $8.7 \cdot 10^{-14} \text{ N}$, and B_c between 0.35 T and 0.40 T. From Eq. (8.16) and data for the line-defect length we find $B_c = 0.3 \pm 0.2 \text{ T}$ and $K_1 = (1.4 \pm 0.2) \cdot 10^{-13} \text{ N}$. These values for K_1 are again reasonably consistent with each other.

The values for K_1 and ζ in aqueous gibbsite that we obtained from the fits of the theoretical model to the experimental data are summarised in Table 8.1. If we average the obtained values we find for K_1 a value of $(2 \pm 1) \cdot 10^{-13} \text{ N}$, and for ζ a value of $(4 \pm 2) \cdot 10^{-8} \text{ N/m}$. As explained in the previous section, we can also independently

Table 8.1: Values for the splay elastic constant K_1 and the anchoring strength ζ of the charge-stabilised gibbsite, obtained by fitting our theory to the experimental data for droplets of radius 30 and 19 μm . Values for K_1 are obtained individually from the critical magnetic-field strength, B_c , and together with values for ζ from fit to the magnetic-field dependence of the dimensionless length of the line defect L/R in Figure 8.7, i.e., from the choice of \mathfrak{R} as well as from the curvature fits. The values from the fits of L/R are averaged over the values obtained from the upper and lower bound fits. See also the main text.

	K_1 [10^{-13} N]		ζ [10^{-8} N/m]
	B_c	fit L/R	fit L/R
$R = 30 \mu\text{m}$	3.5 ± 0.4	1.6 ± 0.2	5.4 ± 0.6
$R = 19 \mu\text{m}$	1.4 ± 0.2	0.8 ± 0.1	2.5 ± 0.4

determine a value for the ratio of K_1/ζ from the cross-over tactoid size of the crossover from a uniform to a radial director field with increasing tactoid size. Tactoids with a uniform director field with size up to about 40 μm have been observed, while the smallest tactoid with a radial director field measured 38 μm in diameter. As the cross-over tactoid radius is determined by $R = 3K_1/\zeta$, this provides us with a value of K_1/ζ of 6.5 μm . The value for K_1/ζ that follows from our curve fitting is 5 μm , which is surprisingly close. It is, we repeat, not possible to extract a value for γ in aqueous gibbsite suspensions because the tactoids remain spherical, at least to within the measurement error. What we can say, though, is that ω must be at least smaller than 1, and γ therefore larger than $4 \cdot 10^{-8}$ N/m, because if this had not been the case, it would have led to a tactoid elongation of 10%, which should have been perceptible in the experiments. These elongated drops are discussed in chapter 9.

8.5 Conclusions and discussion

In this chapter we have presented a theoretical study of the shape and internal structure of nematic droplets with preference for homeotropic interfacial anchoring of the director field to the surface. If the drops are subject to a magnetic field that imposes a perpendicular orientation of the particles relative to that field, which is the case for a negative diamagnetic susceptibility, this complicates the competition between surface and bulk elastic forces characteristic of isotropic-nematic interfaces. We focused on the case where surface tension dominates over the surface anchoring, such that the energetic cost of any deviation from the spherical shape is prohibitively large. By minimising the free energies of different director fields in a Frank-Oseen elasticity theory, we have computed the most favourable one for a given value of the interfacial anchoring strength, the

magnetic-field strength, and the tactoid size. The stability diagrams confirm the scaling argument that in small tactoids the bulk elasticity of the director field is dominant, giving the drop a homogeneous director field, regardless of the magnetic-field strength.

For larger tactoids in a weak magnetic field, a hedgehog point defect develops for weak magnetic field because of the predominance of surface anchoring over the bulk elasticity of the director field. As has recently been observed in experiments on tactoids in dispersions of gibbsite plate-like particles, the crossover from a radial to a uniform director field may occur via the formation of a ring defect that increases to infinite radius or via a dislocation of the point defect from the centre to the boundary and eventually, to infinity [85, 86]. We found that neither intermediate configuration can be a stable configuration because in both cross-over routes there is an energy barrier that has to be overcome, as is already suggested by the few intermediates in the experimental population distribution. Substituting typical values into the free energies shows that the height of both energy barriers ranges from hundreds to thousands times the thermal energy $k_B T$, ruling out the option of completing the crossover spontaneously in a single drop via thermal fluctuations. We surmise that the occurrence of the transient configurations in the experiments must be the result of the flow field in the sedimentation process of the phase separation of the isotropic and nematic phase where the droplets emerge. This conjecture is corroborated by the observation that the boundary defects are always observed on the same (far) side of the tactoids [86]. In fact, flow fields are known to affect director fields in nematic droplets [204].

For strong enough magnetic fields the hedgehog configuration with a radial director field has such a high magnetic energy cost that the point defect stretches to a split-core line defect that allows more particles to comply with the orientation imposed by the magnetic field. The crossover from the drop with a hedgehog point defect to a split-core defect is a continuous, i.e., second-order one, and reminiscent of a Frederiks transition. Finally, the transition from a uniform field to the split-core defect is an abrupt one, and we imagine it to occur, in analogy with the uniform-to-radial crossover, via the formation of a ring defect that with increasing radius becomes virtual outside the drop and gives a homogeneous field inside the ring. Given that the intermediates between a uniform and a radial director field cannot be stable, we expect the same to be true for intermediates between a uniform director field and one with a split-core defect.

The prediction that intermediates between a uniform and radial director field are unstable is not the only one confirmed by experiments, because many more of our theoretical results are borne out by the experiments that were conducted recently. Firstly, a uniform director field was observed for small enough droplets that for a weak or no magnetic field turn into a spherical hedgehog defect with a radial director field in a

spherical drop [85, 86]. Secondly, for sufficiently large drops in a weak or no magnetic field, a hedgehog point defect with radial director field develops. Thirdly, in the split-core configuration for even stronger fields the length of the line defect increases with increasing magnetic-field strength up to a point where the defect line runs through the entire tactoid. We note that such a large line defect case requires a very strong field such that the alignment of the isotropic background becomes significant, making it difficult to observe the details of the drop experimentally.

As mentioned in chapter 7, we neglected this alignment of the isotropic background by the magnetic field in the model. If we had taken this into account, this probably would have given lower values of the surface tension and anchoring strength than what we find here. A second caveat is that we neglected the energy associated with the core of the hedgehog point defect and the split-core line defect. In chapter 7 this was irrelevant because we only focused on these two configurations, whereas in this chapter we also considered a uniform field that has no such core.

In chapter 9 we release the constraint of a dominant surface tension over anchoring strength, implying that we extend our model to non-spherical particles. There we also discuss the possible caveats of our model more extensively.

We express our gratitude to Lia Verhoeff for conducting the experiments.

8.A Hedgehog point defect

In this appendix we aim to determine the free energy of a spherical tactoid with hedgehog point defect at an arbitrary location. The free energy of the oblate shape with boundary defect then follows from a perturbation calculation. Let the point defect with any loss of generality be located on the z -axis at $(x, y, z) = (0, 0, -fR)$, such that $f > 1$ ($f > 1$) represents a defect inside (outside) of the droplet. The bare surface energy is simply $F_{st}^h(f) = 4\pi\gamma R^2$. For the anchoring energy, we have to integrate $\sin^2 \alpha$ over the surface A of the tactoid, with α the angle between the director and the surface normal. $\cos \alpha$ is given by the inner product of the normal and the director. From this we find

$$\sin^2 \alpha = \frac{f^2 R^2 (x^2 + y^2)}{(x^2 + y^2 + z^2)(x^2 + y^2 + (z + fR)^2)} = \frac{f^2 \sin^2 \vartheta}{1 + f^2 + 2f \cos \vartheta}. \quad (8.17)$$

This then gives

$$F_{sa}^h(f) = \pi\zeta R^2 \left(f^2 + 1 + \frac{1}{4f} (f^2 - 1)^2 \log \left(\frac{f-1}{f+1} \right)^2 \right). \quad (8.18)$$

In the limit $f \rightarrow \infty$ we retrieve $F_{sa}^h(f) = \frac{8}{3}\pi\zeta R^2$, i.e., the result for a homogeneous director field. The limits $f \rightarrow 0$ and $f \rightarrow 1$ give $F_{sa}^h(f) = 0$ and $F_{sa}^h(f) = 2\pi\zeta R^2$, which are the values for the central and the boundary hedgehog, respectively.

For the elastic energy we have to integrate $(\nabla \cdot \mathbf{n})^2 = 4/(x^2 + y^2 + (z + fR)^2)$ over the tactoid volume, which gives

$$F_e^h(f) = 4\pi K_1 R \left(1 + \frac{1}{4f}(f^2 - 1) \log \left(\frac{f-1}{f+1} \right)^2 \right). \quad (8.19)$$

In the limits of $f \rightarrow 0$, $f \rightarrow 1$, and $f \rightarrow \infty$, we recover the known results $8\pi K_1 R$, $4\pi K_1 R$, and 0 for the hedgehog in the centre, on the boundary and for the uniform director field, respectively.

For the magnetic energy we assume that the magnetic field is in the x -direction, as follows from the experimental observations. We then must integrate $(\mathbf{n} \cdot \mathbf{B})^2$ over the tactoid volume, with

$$(\mathbf{n} \cdot \mathbf{B})^2 = B^2 \frac{r^2 \cos^2 \phi \sin^2 \vartheta}{r^2 + f^2 R^2 + 2rfR \cos \vartheta}. \quad (8.20)$$

Integration then gives

$$F_m^h(f) = \frac{\pi \Sigma R^3}{288 f^3} \left(4f(3 + 8f^2 - 3f^4) - 3(f^2 - 1)^3 \log \left(\frac{f-1}{f+1} \right)^2 \right), \quad (8.21)$$

with $\Sigma \equiv -\rho\Delta\chi B^2$. In the limits of $f \rightarrow 0$, $f \rightarrow 1$, and $f \rightarrow \infty$, we recover the known results $2\pi\Sigma R^3/9$, $\pi\Sigma R^3/9$, with $\Sigma \equiv -\rho\Delta\chi B^2$, and 0 for the hedgehog in the centre, on the boundary and for the uniform director field, respectively.

8.B Split-core defect

The split-core line defect configuration has a director field with a two-dimensional radial field around the defect and a three-dimensional radial field that originates from the ends of the defect line. The drop is initially presumed to be spherical, giving a surface energy of $4\pi\gamma R^2$; the free energy of the prolate drop with line defect is then computed from a perturbation of the spherical tactoid because the experimentally observed deviation is small. The computation of the anchoring, elastic and magnetic energies is separated into a part from the ‘‘axis’’ with the two-dimensional splay deformation, and a part from the ends with the three-dimensional splay deformation.

For the anchoring energy we use spherical coordinates, where R is constant. The azimuthal angle $\phi \in (0, 2\pi)$ and the polar angle ϑ runs from $\arccos(L/2R)$ to $\pi/2$ and the result is then doubled because of symmetry. We split it into a part from the axis

and a part from the ends. For the axis part we have to integrate $\sin^2 \alpha$ over the surface area A of the axis part of the tactoid, with $\alpha = \pi/2 - \gamma$ the angle between the normal and the director field, see Fig. 8.8. The cosine of this angle is the inner product of the radial unit vectors in two and three dimensions, equal to $\sin \vartheta$, so we have to integrate $\cos^2 \vartheta = \cos^2 \gamma$. This gives

$$F_{sa,ax}^{sc} = \frac{\pi \zeta L^3}{6R}. \quad (8.22)$$

For the part in the ends we have to integrate $\sin^2 \beta$ over the surface of the ends of the

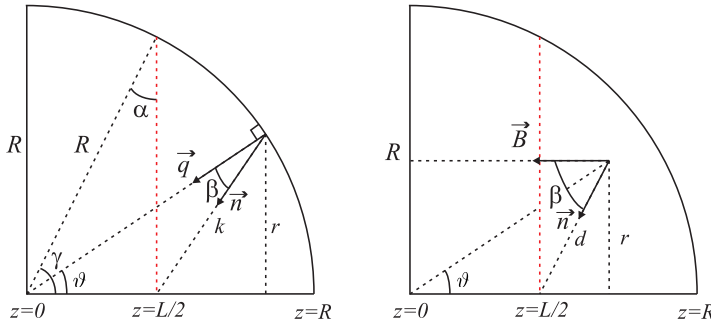


Figure 8.8: Explanation of the boundaries of the polar angle ϑ for a quarter of a spherical droplet for the anchoring energy (left) and the magnetic energy (right).

tactoid, see Fig. 8.8. If we use the sine rule, we see that $\sin \beta / (L/2) = \sin \vartheta / k$, with $k^2 = r^2 + (z - L/2)^2 = R^2 - z^2 + (z - L/2)^2 = R^2 + L^2/4 - zL$. We then use that $z = R \cos \vartheta$, so

$$\sin^2 \beta = \frac{L^2}{4} \frac{\sin^2 \vartheta}{R^2 - RL \cos \vartheta + L^2/4}. \quad (8.23)$$

Note that this expression becomes zero in the limit that $L/R \rightarrow 0$, as in that case we have perfect anchoring in the entire droplet. We then have for the anchoring energy

$$F_{sa,ends}^{sc} = \frac{\pi \zeta}{16LR} \left(16LR^3 + 4L^3R - 4L^4 + (L^2 - 4R^2)^2 \log \left(\frac{2R - L}{2R + L} \right) \right). \quad (8.24)$$

The total anchoring energy is then $F_{sa}^{sc} = F_{sa,ax}^{sc} + F_{sa,ends}^{sc}$, which goes to zero in the limit that $L/R \rightarrow 0$, because then we retrieve the director field with hedgehog point defect that has perfect anchoring.

We divide the calculation of the elastic deformation energy into a part from the axis a part from the ends. In the axis part we have a two-dimensional splay deformation for which we use cylindrical coordinates. $z \in (-L/2, L/2)$, $\phi \in (0, 2\pi)$ and

$r \in (b, \sqrt{R^2 - z^2})$, with b the radius of the defect line. Note that in two dimensions $\nabla \cdot \mathbf{n} = 1/r$, whereas in three dimensions $\nabla \cdot \mathbf{n} = 2/\rho$ with $\rho^2 = r^2 + z^2$. We find for the axis part

$$F_{e,\text{ax}}^{sc} = 2\pi K_1 R \coth^{-1} \left(\frac{2R}{L} \right) + \pi K_1 L \left(-1 + \log \sqrt{\frac{4R^2 - L^2}{4b^2}} \right), \quad (8.25)$$

which goes to zero for $L \rightarrow 0$. In the ends we have a three-dimensional splay deformation so $\nabla \cdot \mathbf{n} = 2/\rho'$, with $\rho' = \sqrt{x^2 + y^2 + (z \pm L/2)^2}$ for the left (+) and right (-) end. Using again cylindrical coordinates we have for the right end: $z \in (L/2, R)$, $\phi \in (0, 2\pi)$, $r \in (0, \sqrt{R^2 - z^2})$. This gives

$$F_{e,\text{ends}}^{sc} = \frac{\pi K_1}{L} (2R - L) \left(L + (L + 2R) \coth^{-1} \left(\frac{2R}{L} \right) \right) \quad (8.26)$$

The contribution from the left end is the same because of symmetry. This gives for the total deformation energy

$$F_e^{sc} = \frac{\pi K_1}{L} \left\{ (8R^2 - 2L^2 + 2LR) \coth^{-1} \left(\frac{2R}{L} \right) + 4LR - 3L^2 + L^2 \log \sqrt{\frac{4R^2 - L^2}{4b^2}} \right\}. \quad (8.27)$$

In the limit of $L/R \rightarrow 0$ we retrieve the familiar result $F_e^{sc} = 8\pi K_1 R$ for the hedgehog.

The magnetic energy is also divided into an axis part and a part from the ends. The axis part is immediately seen to be zero because the magnetic field is perpendicular to the two-dimensional radial director field. For the part from the ends we use the azimuthal symmetry around the z -axis, so we need to compute the integral of $\cos^2 \beta$ over the volume of the ends, see Fig. 8.8. We take the right end for the calculation, but the answer for the left end is the same because of symmetry. With cylindrical coordinates we have for the right and $\phi \in (0, 2\pi)$, $z \in (L/2, R)$, and $r \in (0, \sqrt{R^2 - z^2})$. We have $\cos \beta = (z - L/2)/d$ with $d^2 = r^2 + (z - L/2)^2$. We find

$$F_{B,\text{ends}}^{sc} = \frac{\pi \Sigma}{576L^3} (L - 2R)^3 \left(4L(L^2 + 9LR + 6R^2) + 3(L + 2R)^3 \log \left(\frac{2R - L}{2R + L} \right) \right). \quad (8.28)$$

If we then take the limit that $L/R \rightarrow 0$, we find the expected result $F_B = \frac{2}{9}\pi \Sigma R^3$. Furthermore, in the limit $L \rightarrow 2R$, i.e., a line defect through the entire tactoid, $F_{B,\text{ends}}^{sc} \rightarrow 0$. In this case the ends have zero volume and the director field is two-dimensional splay in the whole tactoid, which is perpendicular to the magnetic field everywhere.

The total free energy F^{sc} of the tactoid with split-core line defect now reads

$$F^{sc} = 4\pi \gamma R^2 - \frac{\pi \zeta L^3}{12R} + \frac{\pi \zeta}{16LR} \left\{ 4LR(L^2 + 4R^2) + (L^2 - 4R^2)^2 \log \left(\frac{2R - L}{2R + L} \right) \right\}$$

$$\begin{aligned}
& + \frac{\pi K_1}{L} \left\{ (8R^2 - 2L^2 + 2LR) \coth^{-1} \left(\frac{2R}{L} \right) + 4LR - 3L^2 + L^2 \log \sqrt{\frac{4R^2 - L^2}{4b^2}} \right\} \\
& + \frac{\pi \Sigma}{576L^3} (L - 2R)^3 \left\{ 4L(L^2 + 9LR + 6R^2) + 3(L + 2R)^3 \log \left(\frac{2R - L}{2R + L} \right) \right\}. \quad (8.29)
\end{aligned}$$

For $L/R \rightarrow 0$ we retrieve Eq. (8.4) for the hedgehog. We compute the optimal length of the line defect by putting $\partial F^{sc}/\partial L = 0$. The resulting equation is used to determine the value of L , enabling us to compare the free energy of the split-core configuration with the hedgehog and the drop with uniform director field.

The optimal value of the line-defect length L is computed by computing $\partial F^{sc}/\partial L = 0$, which gives

$$\begin{aligned}
& 12\zeta L^2 \left(4L(L - 2R)^2(L + R) + (16R^4 - 3L^4 + 8L^2R^2) \log \left(\frac{2R - L}{2R + L} \right) \right) \\
& + 192KL^2R \left(2(L^2 + 4R^2) \coth^{-1} \left(\frac{2R}{L} \right) + 2L^2 - 4RL - L^2 \log \sqrt{\frac{4R^2 - L^2}{4b^2}} \right) \\
& \quad - \Sigma R \left(4L(L - 2R)^2(L^3 + 7L^2R + 12LR^2 + 12R^3) \right. \\
& \quad \left. + 3(L^2 - 4R^2)^2(L^2 + 4R^2) \log \left(\frac{2R - L}{2R + L} \right) \right) = 0. \quad (8.30)
\end{aligned}$$

In the limit of $L \rightarrow 0$ we find B_c as given by Eq. (8.16). To find the computation of the crossover from uniform director field to the one with the split core we put $F^{sc} = F^u$ and use Eq. (8.30) to eliminate the dependence on L . The lines of constant $L/R = c$ in Fig. 8.3 are determined by directly plotting Eq. (8.30) for $L = cR$.

8.C Oblate drop with boundary hedgehog

In the experiments on aqueous dispersions of gibbsite platelets it seems that the drop with hedgehog point defect close to the boundary is slightly oblate rather than spherical [85]. Because the deviation from the sphere is small, we perform a perturbation calculation to the free energy $F^h(f)$ for $f = 1$ as given by Eq. (8.15). This means that we presume the tactoid to be slightly elongated in the x and y direction and slightly compressed in the z direction, thereby keeping the volume fixed. So we relax the condition of a spherical droplet for a moment for the sake of the argument. We start from an oblate ellipsoid that is compressed in the z -direction,

$$\left(\frac{x}{a} \right)^2 + \left(\frac{y}{a} \right)^2 + \left(\frac{z}{c} \right)^2 = 1, \quad (8.31)$$

where we take $a = (1 + \varepsilon)^{1/3}R$ and $c = (1 + \varepsilon)^{1/3}R/(1 + \varepsilon) = R(1 + \varepsilon)^{-2/3}$ so the volume is kept the same as that of the sphere and the drop has an aspect ratio of $1/(1 + \varepsilon) \approx 1 - \varepsilon$.

For this perturbed shape we compute the contributions to the free energy for a radial director field point defect the tactoid boundary at $(x, y, z) = (0, 0, -R/(1 + \varepsilon)^{2/3})$. We then find for the free energy

$$F_{\text{obl}}^h(1) = F^h(1) + \left(\frac{4}{3}\pi K_1 R - \frac{8}{3}\pi\zeta R^2 + \frac{1}{9}\pi\Sigma R^3 \right) \varepsilon + \left(-\frac{10}{9}\pi K_1 R + \frac{152}{45}\pi\zeta R^2 + \frac{32}{45}\pi\gamma R^2 - \frac{1}{30}\pi\Sigma R^3 \right) \varepsilon^2 + \mathcal{O}(\varepsilon^3), \quad (8.32)$$

where $0 < \varepsilon \ll 1$ is the perturbation parameter that equals the inverse drop aspect ratio minus one. For ellipsoids the aspect ratio is defined as the ratio of the axis of cylindrical symmetry and the one perpendicular to it, so it is smaller than unity for oblate shapes and larger than for prolate ones. The latter type we encounter in chapter 9.

We find that the surface anchoring to the interface relaxes the oblate shape because its anchoring energy is lower than in the spherical drop $(-\frac{8}{3}\pi\zeta R^2)$, but this goes at the expense of a larger magnetic $(+\frac{1}{9}\pi\Sigma R^3)$, and elastic $(+\frac{4}{3}\pi K_1 R)$ energy. The increase in surface area is a second-order effect, so this effectively has no additional energy cost in a first approximation. To find the optimal value of the ε that by construction needs to be positive, we take $\partial F_{\text{obl}}^h(1)/\partial\varepsilon = 0$ in Eq. (8.32). However, if we substitute the result for ε , we find that there are no values of ω , \mathfrak{R} and β^2 for which the oblate shape has a lower free energy than the central point defect with radial director field *and* the lens shape with a homogeneous field. Hence, in order to make the crossover from the radial to the uniform director field a free-energy maximum has to be overcome that is associated with a configuration with the defect close to the surface of the tactoid.

Deformable homeotropic nematic droplets in a magnetic field

9

We generalise our macroscopic elasticity theory from chapters 7 and 8 for the effect of a magnetic field on nematic droplets with homeotropic surface anchoring to the case where the shape and structure of the tactoids are dominated by neither the surface anchoring, nor the surface tension. This means that we allow for imperfect surface anchoring and non-spherical droplet shapes. We again focus on the case where the magnetic susceptibility is negative and find that small drops have a homogeneous director field and a lens shape for any magnetic field strength. Larger drops have a radial director field with a hedgehog point defect in weak magnetic fields, whereas for stronger magnetic fields it transforms into a split-core line defect. For even stronger magnetic fields the tactoid itself stretches to a prolate shape. We present a three-dimensional phase diagram that shows the tactoid shape and director field for a given anchoring strength, tactoid size and magnetic field strength. Our findings rationalise the different shapes and structures that recently have been observed experimentally for nematic droplets in sterically stabilised and charge-stabilised dispersions of gibbsite platelets. From a comparison with these experiments we are able to extract values for the splay elastic constant, the surface tension and anchoring strength.[†]

[†]The contents of this chapter are based on the following publications:
A. A. Verhoeff, I. A. Bakelaar, R. H. J. Otten, P. van der Schoot, and H. N. W. Lekkerkerker, *Langmuir* **27**, 116-125 (2011),
A. A. Verhoeff, R. H. J. Otten, P. van der Schoot, and H. N. W. Lekkerkerker, *Journal of Chemical Physics* **134**, 044904 (2011),
R. H. J. Otten and P. van der Schoot, in manuscript.

9.1 Introduction

In this chapter we consider the general case of nematic droplets with a preference for homeotropic surface anchoring of the director field, and again focus on the case of a negative diamagnetic susceptibility. As we have shown in chapter 8, the ground state of the director field is uniform in small drops and radial with a hedgehog point defect in larger drops. In this chapter we examine how these ground states respond to the presence of a magnetic field and what the associated drop shape is.

In chapters 7 and 8 we presented a macroscopic theory for the shape and structure of nematic droplets with homeotropic surface anchoring in a magnetic field. In these chapters we considered two limiting cases: in chapter 7 we presumed strong anchoring of the director field to the interface and the formation of a split-core defect that goes hand-in-hand with an elongation of the droplet, whereas in chapter 8 we focused on a dominant surface tension relative to the anchoring strength, such that the droplets remain spherical and the formation of a line defect is decoupled from the drop shape. These two limiting cases were inspired by experiments on sterically stabilised and charge-stabilised dispersions; both systems exhibit a Frederiks-like transition via the formation of a split-core line defect, in the former system this is accompanied by an elongation of the tactoid itself, whereas in the latter it is not.

In this chapter we release these constraints and consider the general case where we allow for imperfect surface anchoring of the director field and non-spherical droplet shapes. Based on the experiments mentioned above, we consider three director fields and three tactoid shapes: a uniform director field, a radial director field with point defect, and one with a split-core defect, and spherical, prolate, and oblate shapes. We then calculate which combination of director field and shape has the lowest free energy for a given magnetic-field strength, drop size and anchoring strength, and these results we assemble in a three-dimensional stability diagram.

For the homogeneous tactoids we use the so-called Wulff construction that provides the optimal shape that only depends on the ratio ω of the anchoring strength and surface tension. As announced above, the split-core defect is allowed to develop independently of the drop shape. Hence, we consider the split-core defect in spherical drops, as was done in chapter 8, but also in prolate shapes. To model a more realistic shape than the spherocylinder from chapter 7 we study a prolate ellipsoid that we compute by a perturbation calculation of the sphere with line defect from chapter 8. Such a perturbation calculation is permitted because the deviations from the spherical shape observed in the experiments on sterically stabilised dispersions are not very large. We are able to extract values for the splay elastic constant, the surface tension and anchoring strength

from a comparison with the experiments of the critical magnetic-field strength where the split-core defect develops, the length of this line defect and the degree of tactoid elongation.

We again find that small droplets have a uniform director field for any magnetic-field strength, and larger droplets in a weak or zero magnetic field are again spherical with a radial director field with a hedgehog point defect in the centre. Salient features of our findings that were not obtained in chapters 7 and 8 may be summarised as follows.

1. Small drops have a lens shape that becomes flatter with increasing values of ω . For small ω their shape is smooth, but for large values they have a sharp rim.
2. In a strong enough magnetic field, a split-core defect develops inside a spherical drop. At a stronger magnetic field, the tactoid itself stretches to a prolate shape.
3. The elongation disappears again for even strong magnetic fields, whereas the line-defect length keeps increasing with increasing field strength.
4. The larger the value of ω , the larger the regime where elongated tactoids with a split-core defect are stable.

In the next sections of this chapter we first discuss the free energies of the possible shapes and corresponding director fields in section 9.2. Then we present our phase diagrams for the optimal tactoid shape and structure in section 9.3 and compare our results with experiments in section 9.4. Finally, we discuss the validity of our model and the results in section 9.5.

9.2 Tactoid configurations

As discussed in chapters 7 and 8, minimising the free energy $F = F_{st} + F_{sa} + F_e + F_m$, with the components as given by Eqs. (7.1), (7.2), and (7.3), with respect to the tactoid shape and director field, is a formidable free-boundary value problem. In chapter 7 we presumed strong surface anchoring of the director field and the formation of the split-core to be coupled to a shape deformation. In chapter 8 we imposed a spherical shape, but even then finding the optimal director field is difficult, so we chose to consider certain different types of director field. In this chapter we allow for non-spherical tactoid shapes and the approach we adopt is to impose the same types of director field (uniform, radial, and split-core) and three types of tactoid shape based on the experimental observations and then to calculate the combinations of a shape and a director field that have the lowest free energy for given value of our dimensionless parameters ω , \mathfrak{R} , and β^2 . See also Fig. 9.1.

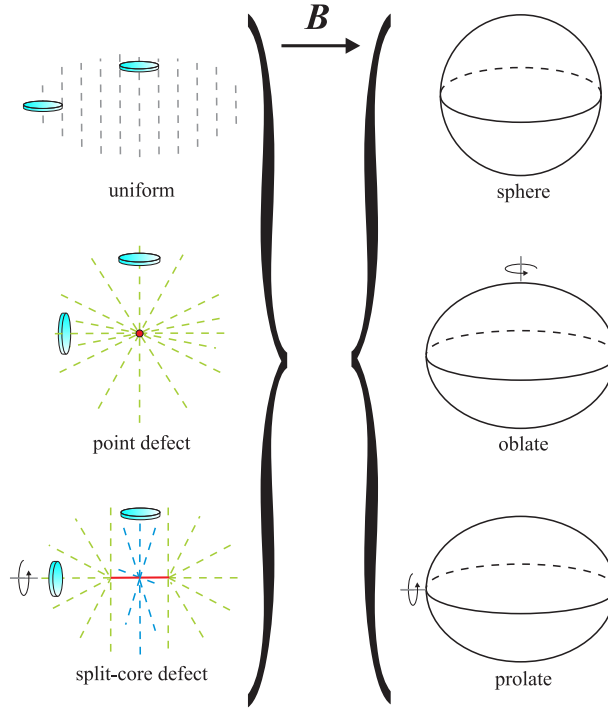


Figure 9.1: Based on recent experimental observations [84–86] we consider three types of director field: a homogeneous field, a three-dimensional radial field, and a two-dimensional radial field around a split-core line defect, capped by a three-dimensional radial field. The uniform field only has an interfacial energy, whereas the other three also have elastic and magnetic energy costs. These three director fields can occur in spherical, oblate and prolate shapes and by taking a free-energy approach, we compute which combination of director field and shape are energetically most favourable for given magnetic field \mathbf{B} . The disks are not drawn to scale and merely serve to indicate the platelet orientation.

From the scaling argument presented in the previous chapter it follows that for sufficiently small tactoids the surface energy and magnetic energy are dominated by the rigidity of the director field, making it uniform, provided the elastic constants are positive. Based on the experimental observations, we presume the drop to orient such that it minimises the magnetic energy cost, so it only has a bare surface energy and an anchoring energy contributing to the free energy F^u . The superscript u indicates the type of director field, which is in this case u for uniform. We make use of the so-called Wulff construction that provides the (exact) optimal shape for a homogeneous director field [206]. This has been worked out for the case of planar anchoring, i.e., $\zeta < 0$ [53], and we extend it here to homeotropic anchoring, so $\zeta > 0$. An approximate and somewhat

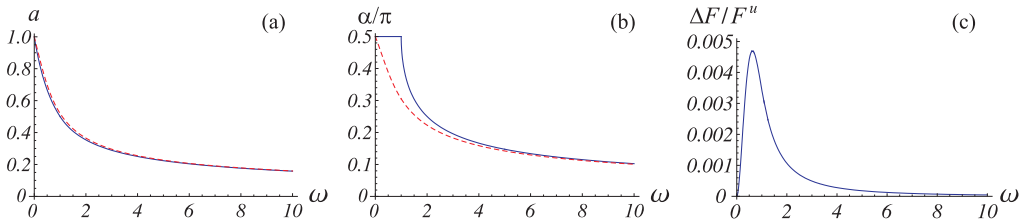


Figure 9.2: The aspect ratio a (a), i.e., the ratio of the short and long axis of the lens shape, the opening angle (b), and the energy difference ΔF of the lens shapes that follow from the Wulff construction and cutting a sphere (c), as a function of the anchoring strength ω . The dashed lines are the results for the cut-sphere lens. The aspect ratio is a smoothly decreasing function of ω , whereas the opening angle shows a non-differentiable cross-over from a smooth to a sharp boundary. The free-energy difference is at most 0.5 %.

simpler shape optimiser may be based on lenses constructed from cut-spheres. We find that, although the shape is different (see Fig. 9.2), the difference in the free energy of both types of lens is negligible. We refer the interested reader to Appendix 9.B for details.

For a homogeneous director field the optimal shape can be obtained from a geometrical construction called the Wulff construction [206]. The derivation is quite technical and the details can be found in Appendix 9.A. Here we only present the main results. The shape that follows from this construction is completely governed by the dimensionless anchoring strength ω . The aspect ratio a is defined as the ratio of the drop size in the direction of the axis of rotational symmetry and that perpendicular to it, so it is a number smaller than unity for oblate ellipsoids and larger than unity for prolate ones. We find

$$a = \begin{cases} \frac{1}{1 + \omega}, & 0 \leq \omega \leq 1 \\ \frac{1}{2\sqrt{\omega}}, & \omega \geq 1. \end{cases} \quad (9.1)$$

It is shown in Fig. 9.2 together with that of the lens that follows from cutting a part from a sphere. The difference in the aspect ratios is very small. See Appendix 9.B for details.

The opening angle α of the Wulff shape satisfies

$$\alpha = \begin{cases} \pi/2, & 0 \leq \omega \leq 1 \\ -\arctan(-\sqrt{\omega - 1}), & \omega \geq 1. \end{cases} \quad (9.2)$$

So for $0 \leq \omega \leq 1$ the boundary is smooth, but for $\omega > 1$ it has a sharp rim. The opening angle is shown in Fig. 9.2. The free energy is a rather large expression and can be found in Appendix 9.A.

As follows from the scaling argument from chapter 8, for larger tactoids the interfacial energy becomes so large that the uniform director field cannot be maintained. As argued in that chapter, for $R\zeta/K_1 > 3$ the radial director field with hedgehog configuration becomes more favourable for weak magnetic fields, at least for spherical droplets. For such a radial director field a spherical shape is indeed the most favourable one because it allows for perfect homeotropic anchoring, and its free energy F^h is given by Eq. (8.4).

As discussed in chapter 8, for a sufficiently strong magnetic field the hedgehog configuration cannot be maintained because in that case the magnetic energy becomes too large. To comply with the orientation imposed by the magnetic field for a larger fraction of the particles, the tactoid can stretch the point defect to a line defect of topological charge +1 in the direction of the magnetic field. The free energy of this configuration is given by $F^{sc} = 4\pi\gamma R^2 + F_{sa}^{sc} + F_e^{sc} + F_m^{sc}$, with F_{sa}^{sc} , F_e^{sc} , and F_m^{sc} given by Eqs. (8.6), (8.7), and (8.8), respectively.

The formation of this split-core defect in turn goes at the expense of the perfect homeotropic surface anchoring, which can be reduced by elongating the drop. This has been observed to be the case in sterically stabilised dispersions of gibbsite platelets, for which we presented a simple model with strong anchoring conditions in chapter 7. As announced in section 9.1, we perform a perturbation calculation to determine the free energy of the prolate drop with line defect because the experimentally observed deviation from the spherical shape is small [86]. Such a perturbation calculation implies that we write the solution in terms of a formal power series in a parameter that quantifies the deviation from the exactly solvable problem. This perturbation we perform in both the shape and the line-defect length, so one perturbation parameter is the deviation in the aspect ratio from that of the sphere, i.e., unity, and the other is the deviation from the line-defect length in the sphere. It is a highly non-trivial calculation and the details can be found in Appendix 9.C.

The free energies of the spherical drop with point defect and split-core split-core line defect are given by Eqs. (8.4) and (8.5), respectively. In the experiments of [86] on gibbsite platelets that we referred to before, the tactoids in dispersions of sterically stabilised gibbsite were observed to stretch to a prolate shape in a sufficiently strong magnetic field. To rationalise this observation, we perform a perturbation calculation of the free energy mentioned above to compute the free energy of a prolate ellipsoid of revolution with line defect, which is reasonable given that the observed aspect ratio was always smaller than 1.3 [86]. This amounts to a perturbation both in the shape, i.e.,

aspect ratio, and the split-core defect length. The reason that we perform a perturbation calculation instead of a full calculation for a prolate ellipsoid of revolution is that in the latter case neither the bare surface energy nor the anchoring energy can be evaluated analytically. The free energy $F_{\text{pr}}^{\text{sc}}$ of the prolate shape we find from the free energy $F^{\text{sc}}(L_s, \varepsilon = 0)$ for the sphere with defect length L_s and deviation $\varepsilon = 0$ from the aspect ratio of unity of the sphere. The equation for $F_{\text{pr}}^{\text{sc}}$ reads

$$F_{\text{pr}}^{\text{sc}}(L, \varepsilon) = F^{\text{sc}}(L_s, 0) + \varepsilon \frac{\partial F^{\text{sc}}}{\partial \varepsilon} \Big|_{(L_s, 0)} + \delta L \frac{\partial F^{\text{sc}}}{\partial L} \Big|_{(L_s, 0)} + \frac{1}{2} \varepsilon^2 \frac{\partial^2 F^{\text{sc}}}{\partial \varepsilon^2} \Big|_{(L_s, 0)} + \frac{1}{2} (\delta L)^2 \frac{\partial^2 F^{\text{sc}}}{\partial L^2} \Big|_{(L_s, 0)} + \varepsilon \delta L \frac{\partial^2 F^{\text{sc}}}{\partial \varepsilon \partial L} \Big|_{(L_s, 0)} + \mathcal{O}(\varepsilon^3, (\delta L)^3), \quad (9.3)$$

where $L = L_s + \delta L$ is the length of the line defect in the prolate ellipsoid. We optimise $F_{\text{pr}}^{\text{sc}}$ with respect to the parameters ε and δL , so we put $\partial F_{\text{pr}}^{\text{sc}} / \partial L = 0$ and $\partial F_{\text{pr}}^{\text{sc}} / \partial \varepsilon = 0$. The different energy terms of $F_{\text{pr}}^{\text{sc}}$ are found by taking a prolate ellipsoidal drop shape with aspect ratio $1 + \varepsilon$ and by using the cylindrical symmetry of the drop around the line defect, so we use cylindrical coordinates. The details can be found in Appendix 9.C.

On the boundary of the regime of the prolate drop in the stability diagram we have $\varepsilon = \delta L = 0$, so to find that boundary it suffices to compute the values of β^2 and \mathfrak{R} that satisfy $\partial F^{\text{sc}} / \partial \varepsilon \Big|_{(L_s, 0)} = 0$ and $\partial F^{\text{sc}} / \partial \delta L \Big|_{(L_s, 0)} = 0$. The result then gives the critical value B_* of the magnetic-field strength where the prolate drop becomes more favourable than the spherical one for a given value of \mathfrak{R} . Inside the area where the prolate drop has the lowest free energy, we need the full equations that result from minimising with respect to $F_{\text{pr}}^{\text{sc}}$ to find the optimal value of ε and δL , plus the added constraint that L_s is still the optimal solution for the spherical shape, hence $\partial F^{\text{sc}} / \partial L \Big|_{(L_s, 0)} = 0$. So we have three equations for the three unknowns ε , L_s , and δL , where a value for the fourth unknown, ω , is selected for every diagram. The lines of constant aspect ratio and constant line-defect length in the stability diagram we then compute by fixing the values of ε and $L = L_s + \delta L$, respectively.

We find that the growth of the line defect is indeed decoupled from the elongation of the tactoid because the former starts at lower magnetic-field strength than the latter, i.e., $B_c < B_*$, albeit that the difference is small. To compare the approach of a coupled growth of the line defect and the tactoid elongation from chapter 7 with the decoupled growth in this chapter, we show the results for the line-defect length and the aspect ratio as a function of the magnetic-field strength for $\omega = 2$ in Fig. 9.3. We see that initially, i.e., for weak magnetic fields, the growth of the split-core defect and the tactoid elongation have the same growth ‘‘rate’’ with increasing field strength, so the approximation the coupling from chapter 7 is quite accurate. However, for larger field strength

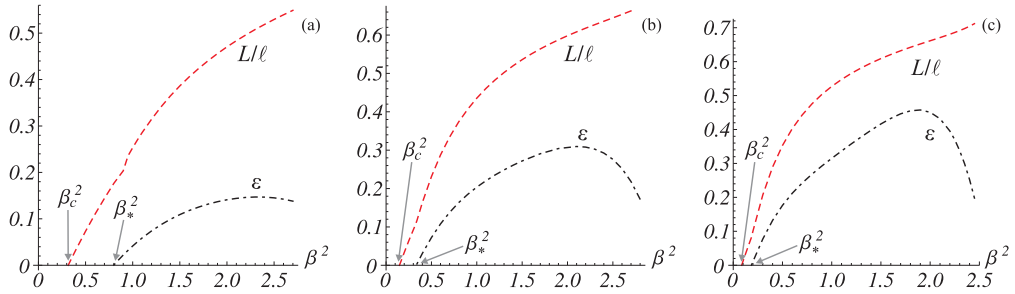


Figure 9.3: The length of the line defect L relative to the tactoid length $\ell = 2R(1 + \varepsilon)^{2/3}$ and the increase ε in the aspect ratio $a = 1 + \varepsilon$ as a function of the dimensionless magnetic-field strength β^2 for $\omega = 2$ and $\Re = 10$ (a), 15 (b), and 20 (c). At the critical magnetic-field strength $\beta_c^2 = \Sigma B_c^2 K_1 / \gamma^2$ the line defect starts to grow, and for $\beta_*^2 = \Sigma B_*^2 K_1 / \gamma^2$ the tactoid itself elongates.

the aspect ratio exhibits re-entrance behaviour because it decreases again, whereas the line defect elongates further. We return to this in section 9.3.

We are now in a position to compare our free energies and assemble the results in a stability diagram that shows the optimal configuration and shape from our class given the dimensionless anchoring strength $\omega \equiv \zeta / \gamma$, drop radius $\Re \equiv R\gamma / K_1$, and magnetic-field strength $\beta^2 \equiv -\rho\Delta\chi B^2 K_1 / \gamma^2$. The results are presented in the next section.

9.3 Stability diagrams

In chapter 8 we considered the limit of $\omega \rightarrow 0$ where the drops are spherical. For nonzero values of ω the surface tension no longer fully dominates the anchoring energy, allowing the drop to deviate from the spherical shape. The results of our numerical calculations are summarised in Fig. 9.4, where we have taken the value of the dimensionless anchoring strength equal to $\omega = 0.25, 0.5, 1$ and 2. A value of approximately $\omega = 0.5$ was found from capillary-rise experiments for gibbsite platelets in toluene that were sterically stabilised [45]. However, to reach the aspect ratios that we observed recently in the experiments on sterically stabilised gibbsite using bromotoluene, a value of $\omega = 2$ is required [86].

The stability diagram shows that we can distinguish four regimes. i) Small drops have a homogeneous director field and a lens shape, irrespective of the magnetic-field strength. ii) Larger drops in a weak magnetic field are spherical with a radial director field and a hedgehog point defect. iii) For stronger magnetic fields the point defect transforms into a split-core line defect within the spherical drop. iv) For even stronger

magnetic fields the tactoid itself stretches to a prolate shape.

The larger the anchoring strength $\omega = \zeta/\gamma$, the larger the area occupied by the prolate drop with split-core defect in the stability diagram. The reason is that a higher value of ω means a larger energetic penalty for imperfect surface anchoring, making the prolate drop more favourable than the spherical drop with split-core defect. With increasing ω , the scale of the horizontal axis decreases, whereas that of the vertical axis increases, but the topology of the diagrams is the same as that of the spherical drop in Fig. 8.3 for all values of ω , except for the invasion of the phase diagram by the prolate drop. That is, small drops again adopt a uniform director field, and the shape is now that of a lens that becomes more oblate for larger values of ω . Larger drops adopt a hedgehog configuration in weak magnetic fields, for which the cross-over size for zero field is shown in Fig. 9.5, whereas in stronger magnetic fields the split-core line defect develops. See also Appendix 9.B.

For $\omega = 2$ the length of the line defect L relative to the drop size R , which is the radius of the spherical drop determining the volume that is the same for all configurations, shows a remarkable re-entrance for an increasing magnetic-field strength. Note, however, that there is quite a large gradient in the aspect ratio a close to the second crossover from prolate ellipsoid to the sphere with line defect and that for values $a \gtrsim 1.4$ our perturbation approximation loses its accuracy.

The split-core configuration also occurs in prolate drops because for all values of the anchoring strength ω that we take, there are values of the dimensionless radius \mathfrak{R} and magnetic-field strength β^2 for which it is the most favourable one of all configurations. For this the tactoid must be sufficiently large to make surface anchoring dominant over elasticity in order to rule out the homogeneous drop, and the magnetic field must be strong enough to force more particles to comply with the orientation imposed by this field than in the hedgehog configuration. The magnetic field must be stronger than a critical value B_* larger than B_c to make the elongated drop with split-core defect more favourable than the spherical one. The value of B_* that follows from it provides the boundary of the area in the phase diagrams in Fig. 9.4 where the prolate drop with split core has the lowest free energy and the way it is computed is explained in Appendix 9.C. At this transition the length L of the line defect is approximately $L \approx R/2$, see Fig. 9.4. In that figure we plot the lines of constant L/R in the ellipsoid region that have a small downward deflection, implying that the line-defect length in the prolate drop is larger than that in equivalent spherical tactoid. See also Fig. 9.3. For a given value of \mathfrak{R} the line-defect length increases with increasing magnetic-field strength until it runs throughout the entire tactoid to minimise the magnetic energy cost. However, we have seen in chapter 8 that in theory this requires an infinitely strong magnetic field.

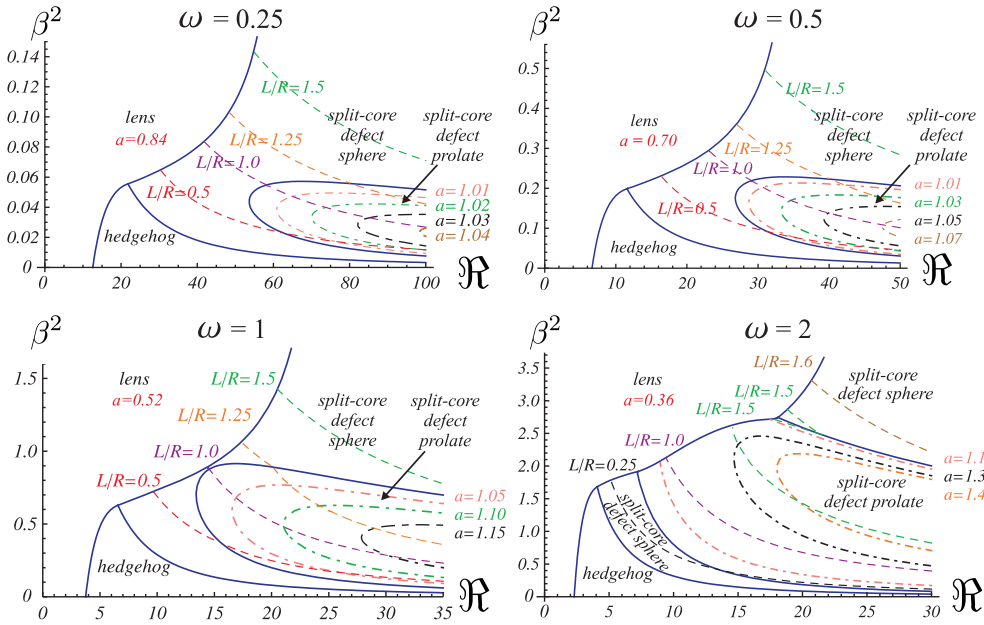


Figure 9.4: The stability diagrams for dimensionless anchoring strength $\omega = 0.25$ (top left), $\omega = 0.5$ (top right), $\omega = 1$ (bottom left), and $\omega = 2$ (right) as a function of the dimensionless radius $\mathfrak{R} \equiv R\gamma/K_1$ and $\beta^2 \equiv -\rho\Delta\chi B^2 K_1/\gamma^2$ that measure the drop size and the magnetic-field strength. The volume is constant for all shapes and equals that of the sphere with radius R . The dashed lines indicate a constant split-core defect length L relative to R . The dashdotted lines show a constant aspect ratio a of the prolate ellipsoid, where $a = 1$ at the crossover from sphere to prolate ellipsoid.

The aspect ratio initially also increases with increasing field strength, but, surprisingly, according to our model the aspect ratio should decrease again to unity for very strong fields, so the spherical tactoid with a split-core defect should re-appear for even larger magnetic-field strengths. See also Figs. 9.3 and 9.4. The reason is that the length of the line defect affects the balance between the magnetic and anchoring energy. That is to say, the additional free energy of the ellipsoid compared to the sphere with line defect contains mainly a competition between the magnetic energy and the anchoring energy, i.e., the elastic deformation is subdominant. The prolate ellipsoid has a lower anchoring energy throughout the entire tactoid than the sphere, whereas its magnetic energy is higher. Note that this magnetic energy comes only from the ends of the tactoid, and not from the axis part where the director field is radial in two dimensions and has minimal magnetic energy cost. For a weak magnetic field $B < B_{*,1}$, with $B_{*,1}$ the smallest of the two values of B_* for given \mathfrak{R} , the line defect is small and almost the en-

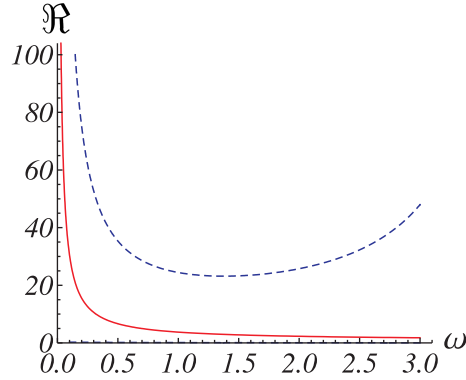


Figure 9.5: The critical value of the dimensionless drop size $\mathfrak{R} \equiv R\gamma/K_1$ for the crossover from a uniform director field in the lens to a radial director field in the sphere as a function of the dimensionless anchoring strength $\omega \equiv \zeta/\gamma$. The solid line shows the critical value at zero magnetic field with $\beta^2 \equiv -\rho\Delta\chi B^2 K_1/\gamma^2 = 0$, and the dashed line indicates the limit for a very strong magnetic field where the defect is stretched through the entire tactoid ($L/R = 2$), which is the vertical asymptote (dotted line) in the phase diagram in Fig. 9.4.

tire volume of the tactoid is in the ends, which makes the prolate ellipsoid energetically expensive compared to the spherical drop. The larger magnetic energy outweighs the gain in anchoring energy of the elongated drop relative to the spherical one because this is mainly caused in the ends, which is small because of the small line defect.

For a stronger magnetic field $B > B_{*,1}$ the line-defect length is about the size of the tactoid radius and the difference in magnetic energy between the prolate ellipsoid and the sphere becomes even larger than for a smaller value of B . However, this is compensated for by the gain in anchoring energy because of the longer line defect that is mainly due to the better anchoring in the ends. For even stronger magnetic fields $B > B_{*,2}$ with $B_{*,2}$ the largest of the two values of B_* for the same value of \mathfrak{R} , there comes a point where the magnetic energy of the prolate drop is too expensive to be compensated for by the more favourable anchoring than in the sphere, which is now mainly in the axis part. This is because the line defect is larger than half the size of the tactoid. In the experiments this re-entrance of the spherical drop with line defect turned out not to be observable because of the poor contrast due to alignment of the isotropic phase in the strong magnetic field [86]. With $\omega \approx 2$, $\beta^2 \approx 3$, $\Delta\chi = -10^{-22}$ J/T², $\rho = 4 \cdot 10^{20}$ m⁻³ [42, 83], and $K_1 \approx 0.8 \cdot 10^{-13}$ N and $\gamma = 1.3 \cdot 10^{-7}$ N/m that we find in section 9.4, we estimate the required magnetic-field strength for this to be observed to be 4 T.

In the next section we compare our results to experiments on tactoids in sterically

stabilised dispersions of gibbsite platelets.

9.4 Comparison with experiments

Just as in the case of the aqueous gibbsite in chapter 8, we can directly apply the theoretical model from the previous sections to the experimental data, and extract material parameters relating to our liquid crystal droplets. Here we not only use the length of the line defect and the critical magnetic-field strength B_c where it starts to grow, but also the degree of tactoid elongation as a function of the magnetic-field strength. The fitting procedure is similar to the one described in section 8.4, except that the relevant variables are $\beta^2 \equiv -\rho\Delta\chi B^2 K_1/\gamma^2$ and $\mathfrak{R} \equiv R\gamma/K_1$, as shown on the axes of Fig. 9.4. The fitting procedure amounts to finding a compromise between the best fit to the critical magnetic-field strengths where the aspect ratio (B_*) or split-core defect (B_c) starts to grow, and the best fit to the data beyond those critical field strengths. This compromise then produces values for γ/K_1 and for γ^2/K_1 , from which we deduce both individual parameter values.

For the curve fitting to the tactoid elongation data that we have obtained for the sterically stabilised system, there is an additional constraint compared to the aqueous system that we require a minimum value of ω for the observed aspect ratios to occur in the phase diagram. This value turns out to be higher than expected from previous experiments in gibbsite platelets [42], which, in fact, is an important observation that we return to later. A value of $\omega = 1.5$ turns out not to suffice, but $\omega = 2$ does and gives a good fit, so we choose to take this value, which agrees with density functional simulations on hard rectangular platelets [80]. Here, it must be noted that a value that is, say, 10 % smaller or larger presumably also allows for an acceptable fit, and that it agrees with the lower bound of $\omega > 1$ that was obtained from comparing the aspect ratio of lens-shaped tactoids with a homogeneous director field with Eq. (9.8) [85].

We rely on the same data for the tactoid elongation as in our chapter 7, where we presumed perfect homeotropic surface anchoring [84]. Hence, we reanalyse these data in the light of our more accurate model described in this chapter, allowing us to assess the effect of imperfect anchoring on the value of the obtained surface tension, γ . We begin with a curve fit of our model to the measured length of the split-core defect of a tactoid with an initial radius of 32 μm in this system. Similar to the charge-stabilised system, a line defect running throughout the entire tactoid was also observed at very high field strengths, but again omit these last few data points from our curve-fitting procedure for the same reasons as mentioned in section 8.4. The value of \mathfrak{R} that produces the best fit to the critical magnetic-field strength turns out to be $\mathfrak{R} = 100$, which is rather large, as

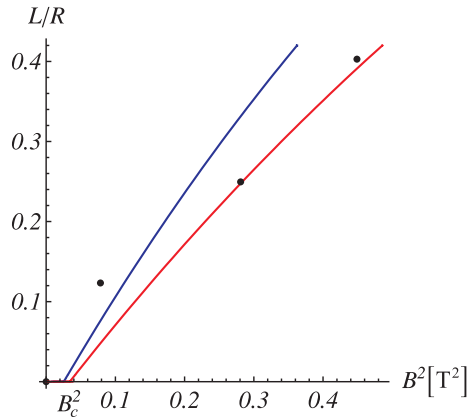


Figure 9.6: Ratio of the length of the split-core defect and the radius of the drop, L/R , as a function of the square of the magnetic-field strength B^2 for a tactoid in a suspension of sterically stabilised gibbsite in bromotoluene. Tactoid radius: $R = 32 \mu\text{m}$. Experimental data: points, theoretical fits to the data: drawn lines. In order to get good agreement for both the critical magnetic-field strength and the ratio L/R , we derive a lower and upper bound for $B^2/\beta^2 = \gamma^2/(-\rho\Delta\chi K_1)$. We find $B^2/\beta^2 = 25 \text{ T}^2$ (left drawn curve) and $B^2/\beta^2 = 35 \text{ T}^2$ (right drawn curve), respectively. See also the main text.

we will see later. We obtain lower and upper bounds for the interfacial tension γ and the elastic constant K_1 , of $\gamma = 2.1 \cdot 10^{-7} \text{ N/m}$ and $\gamma = 2.8 \cdot 10^{-7} \text{ N/m}$, and $K_1 = 0.4 \cdot 10^{-13} \text{ N}$ and $K_1 = 0.6 \cdot 10^{-13} \text{ N}$ respectively, with $B_c = 0.16 \text{ T}$ and $B_c = 0.18 \text{ T}$, see Fig. 9.6. From Eq. (8.16) we can obtain another value for K_1 by determining B_c from the data for the defect length. We determine $B_c = 0.18 \pm 0.2 \text{ T}$, which results in a value for $K_1 = (1.1 \pm 0.5) \cdot 10^{-13} \text{ N}$. These values agree reassuringly well, implying that we believe them to be robust.

Next, we attempt to confirm the previous analysis by a curve fit of our model this time to the aspect ratio of two elongated tactoids with an initial radius of 28 and 31 μm respectively, again for the system of sterically stabilised gibbsite. In order to obtain the correct aspect ratio of $a \approx 1.3$ for the tactoids, we have to take $\omega = 2$ as described above. The value of \Re that produces the best fit to the critical magnetic-field strength is smaller than in our curve fitting to the length of the split-core line defect, because the critical field strength B_c needed to elongate a tactoid is larger. For the tactoid of 28 μm we take $\Re = 25$, and the condition that $\Re\omega > 3$ is then also satisfied. See Fig. 9.7.

From the fit we find $B_* = 0.47 \text{ T}$ and a value of $\gamma = 0.9 \cdot 10^{-7} \text{ N/m}$ with a lower and upper bound of $\gamma = 0.6 \cdot 10^{-7} \text{ N/m}$ and $\gamma = 1.2 \cdot 10^{-7} \text{ N/m}$. The same fit gives $K_1 = 1.0 \cdot 10^{-13} \text{ N}$, with bounds $K_1 = 0.7 \cdot 10^{-13} \text{ N}$ and $K_1 = 1.3 \cdot 10^{-13} \text{ N}$. For the drop

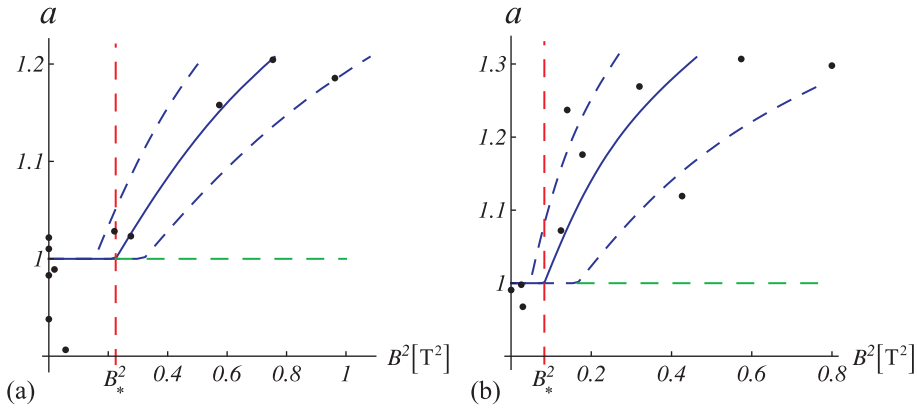


Figure 9.7: The aspect ratio a of two tactoids in the sterically stabilised gibbsite dispersion in bromotoluene as a function of the square of the magnetic-field strength B^2 , where both the critical magnetic-field strength B_* and the values of a are fitted. The points represent experimental data and the solid lines are fits to our model. For both fits $\omega = 2$ has been taken to reach the desired aspect ratios. The fit gives a value for $B^2/\beta^2 = \gamma^2/(-\rho\Delta\chi K_1)$ and the dashed lines indicate a lower and upper bound (see the main text). (a) Tactoid with $R = 28 \mu\text{m}$ with $B^2/\beta^2 = 1.9 \text{ T}^2$, giving $\gamma = 0.9 \cdot 10^{-7} \text{ N/m}$ and $K_1 = 1.0 \cdot 10^{-13} \text{ N}$. (b) Tactoid with $R = 31 \mu\text{m}$ with $B^2/\beta^2 = 0.7 \text{ T}^2$ (solid line), giving $\gamma = 0.4 \cdot 10^{-7} \text{ N/m}$ and $K_1 = 0.5 \cdot 10^{-13} \text{ N}$.

with a radius of $31 \mu\text{m}$ we take $\mathfrak{R} = 23$ and the best fit then produces $B_* = 0.30 \text{ T}$ and values of γ and K_1 of $\gamma = 0.4 \cdot 10^{-7} \text{ N/m}$ with a lower and upper bound of $\gamma = 0.2 \cdot 10^{-7} \text{ N/m}$ and $\gamma = 0.7 \cdot 10^{-7} \text{ N/m}$, and $K_1 = 0.5 \cdot 10^{-13} \text{ N}$, with bounds $K_1 = 0.3 \cdot 10^{-13} \text{ N}$ and $K_1 = 1.0 \cdot 10^{-13} \text{ N}$. Again, these values are quite consistent with those obtained for the smaller drop.

Comparison of the found values for B_c (the critical field strength at which the line defect starts to grow) and B_* (the critical field strength at which the tactoid elongation starts) shows that $B_c < B_*$, in agreement with what was found in the theoretical model: upon an increase of the magnetic field first the point defect stretches to a line defect and subsequently at higher magnetic-field strength the tactoid is elongated in the field direction. The theory also predicts that the tactoid should become spherical again at an even higher magnetic-field strength, but this was not confirmed by the experiments. It must be noted, though, that at high magnetic-field strength a precise measurement of the tactoid properties becomes increasingly difficult, due to alignment of the isotropic background.

All the obtained values for γ and K_1 are summarised in Table 9.1, which also shows the values from chapter 7, obtained with the model that assumes complete anchoring. If

Table 9.1: Results of the fitting procedure for sterically stabilised gibbsite in bromotoluene. The first three columns of the table give values for K_1 from Eq. (8.16) for B_c and average values for K_1 and γ that follow from the upper and lower bound fits of the model to the relative split-core-defect length L/R , as depicted in Fig. 9.6. The next two columns give the best fit values for K_1 and γ that follow from the fits of the model to the elongation of the tactoid, i.e., the aspect ratio a , as depicted in Fig. 9.7. The last column presents results obtained with the old model from chapter 7 involving complete anchoring ($\omega \rightarrow \infty$). All values for K_1 are in units of 10^{-13} N and those of γ in units of 10^{-7} N/m.

$R[\mu\text{m}]$	$\omega = 2$					$\omega \rightarrow \infty$
	line defect			elongation		elongation
	K_1	K_1	γ	K_1	γ	γ
	B_c	fit L/R		fit a		fit a
32	1.1 ± 0.5	0.5 ± 0.1	2.5 ± 0.4	-	-	-
28	-	-	-	1.0 ± 0.3	0.9 ± 0.3	5 ± 2
31	-	-	-	$0.5 \pm 0.5^\dagger$	0.4 ± 0.3	3 ± 2

[†]This rather large value of the error is a consequence of the fact that the upper and lower bounds are asymmetrically deviating from the best fit, thus the lower bound is not zero, but $0.3 \cdot 10^{-13}$ N.

we compare the values for γ obtained from the tactoid elongation with both models, it is clear that significantly lower values are obtained when incomplete anchoring is taken into account, $(0.4 - 0.9) \cdot 10^{-7}$ N/m versus $(2 - 5) \cdot 10^{-7}$ N/m, in agreement with the expectation put forward in the chapter 7 [84]. However, the value we obtained with the new model by the fitting of the length of the line defect as a function of magnetic-field strength is somewhat larger, namely $(2.5 \pm 0.4) \cdot 10^{-7}$ N/m, which results in an average value for the interfacial tension of sterically stabilised gibbsite in bromotoluene of $\gamma = 1.3 \cdot 10^{-7}$ N/m. So, all of the values of the surface tension we extract from the tactoid experiments are much larger than the value of $\gamma = 3 \cdot 10^{-9}$ N/m obtained from capillary-rise experiments, in the comparable system of sterically stabilised gibbsite in toluene as opposed to bromotoluene [42]. We come back to some of the drawbacks of our tactoid model below, although we do not believe these drawbacks can actually explain this discrepancy. The values for the elastic splay constant K_1 of both the fits to the line-defect length and the aspect ratio and B_c produce an average of $(0.8 \pm 0.3) \cdot 10^{-13}$ N, which is somewhat smaller than the values that we established in chapter 7 of $K_1 = (0.9 - 2.6) \cdot 10^{-13}$ N, yet still consistent.

Even though we claimed in chapter 8 that the tactoids in the charge-stabilised system showed no deviation from the spherical shape for sufficiently large tactoids with a split-core defect, i.e., $\omega \rightarrow 0$, for smaller tactoids a non-spherical shape with a uniform director field was observed in the absence of a magnetic field in this system [85]. In agreement

with our predictions, the drops were observed to be lens-shaped with an aspect ratio that is independent of the drop size, as predicted by Eq. (9.8). From this aspect ratio a value $\omega = 0.6$ was readily deduced, so this suggests the aqueous system is not characterised by $\omega \rightarrow 0$. If we reconsider the calculated phase diagram of Fig. 9.4 for $\omega = 0.5$, close to what we find here, a tactoid elongation of 3 to 5 % is expected, which could have easily been missed in the experiments [86]. So, the apparent discrepancy does not seem to be a real one.

9.5 Conclusions and discussion

In this chapter we have extended our theoretical study from chapters 7 and 8 of the shape and internal structure of spherical nematic droplets to the general case of imperfect surface anchoring and non-spherical droplets, so neither the surface anchoring, nor the surface tension is the dominant force. By minimising the free energies of shapes and director fields in a Frank-Oseen elasticity theory, we have computed the most favourable combination of shape and director field for a given value of the interfacial anchoring strength, the magnetic-field strength, and the tactoid size. The stability diagrams confirm the scaling argument that in small tactoids the bulk elasticity of the director field is dominant, giving the drop a homogeneous director field, regardless of the magnetic-field strength. The shape associated with this uniform director field is that of a lens, and its aspect ratio, defined as the ratio of the axis of rotational symmetry and the one perpendicular to it, decreases with increasing anchoring strength to accommodate with the preferred homeotropic surface anchoring.

For larger tactoids in a weak magnetic field, a hedgehog point defect develops in a spherical drop for a weak magnetic field because of the predominance of surface anchoring over the bulk elasticity of the director field. For strong enough magnetic fields the hedgehog configuration with radial director field has such a high magnetic energy cost that the point defect stretches to a split-core line defect that allows more particles to comply with the orientation imposed by the magnetic field. We showed here that also in a sterically stabilised dispersion a split-core defect can be stabilised by a magnetic field for particles with a negative diamagnetic susceptibility anisotropy, again confirming the prediction by Mkaddem and Gartland [200].

Our calculations predict that for positive values of the dimensionless anchoring strength $\omega \equiv \zeta/\gamma$ the tactoid stretches to a prolate shape and that this occurs for stronger fields than that at which the split-core defect starts to grow and this is confirmed by the experiments on sterically stabilised dispersions of gibbsite platelets. For even stronger fields the aspect ratio of the prolate shape should decrease again to unity.

This presumably requires such a strong magnetic field that the contrast is too low for this re-entrance of the spherical shape to be observable experimentally. Our stability diagrams show that the larger the value of ω , the larger the regime for which elongated tactoids with a line defect are stable.

We have demonstrated the effect of decoupling of the elongation of the line defect and that of the tactoid, and find that for weak magnetic fields the approximation of coupling both elongations, as done in chapter 7, is an accurate approximation because the defect length and tactoid length grow equally rapidly with increasing magnetic-field strength. However, for stronger magnetic fields the defect keeps growing until it runs throughout the entire tactoid, whereas the aspect ratio decreases again to unity.

By fitting the observed aspect ratio of the drops and line-defect length in the sterically stabilised system to our theoretical predictions, we extracted values of $K_1 \approx (1.0 \pm 0.5) \cdot 10^{-13}$ N, $\gamma = (2 \pm 1) \cdot 10^{-7}$ N/m, and $\omega \approx 2$ [85, 86]. The values of K_1 are in agreement with earlier results from a much cruder model [84] and also with capillary rise experiments [45], but the value of the surface tension of $\gamma = 3 \cdot 10^{-9}$ N/m in that work is much smaller than what we find here.

There are two possible caveats of our model one could imagine to be responsible for this discrepancy. The first is that we neglected the influence of the magnetic field on the material parameters and this we return to below. The second is that except for the configuration with a ring defect, we only consider splay deformations of the director field. Although it might appear that the observed director fields exhibit merely a splay deformation, any bend deformation could give a significant contribution because a value of $K_3 \approx 7 \cdot 10^{-14}$ N has recently been determined for platelets [83], which would favour a bend deformation over a splay distortion because it is lower than the value for K_1 that we extracted above. Although difficult to infer from the polarised-light-microscopy experiments, the curvature in the dark horizontal band might point in that direction. Indeed, for plate-like particles, the bend elastic constant is thought to be smaller than the splay constant [52], so some elastic energy can be gained. An appropriate bend deformation also makes the anchoring less unfavourable, producing an additional reduction of the free energy. At this point, it is difficult to judge in what way that this should influence the results of our curve fitting. However, it seems unlikely that the incorporation of the bend and/or saddle-splay elastic constant can account for the large discrepancy between the calculated values of the anchoring strength and surface tension that follow from the model and the value obtained earlier from capillary rise experiments [45, 84].

Finally, we once again mention the neglect of the effect the magnetic field on the material parameters in this chapter and chapters 7 and 8. Firstly, the magnetic field

aligns the background isotropic phase and presumably lowers the value of the surface tension and anchoring strength. Secondly, the magnetic field raises the order parameter S_2 of the nematic phase, defined in Eq. (1.4), which should affect the splay elastic constant K_1 and the anchoring strength ζ . Quite plausibly, K_1 and ζ depend differently on the order parameter [6]. Because both the elastic constant and the anchoring strength counterbalance the deformation by the magnetic field, an underestimation of K_1 could lead to a too high value for the anchoring strength and interfacial tension. Furthermore, the anchoring strength might also depend on the magnetic-field strength due to alignment of the isotropic phase in the field. However, correction for the latter would lead to an even higher value for the anchoring strength in zero field.

A difference in the order parameter may also partly explain the aforementioned difference of almost two orders of magnitude between the interfacial tension that we find here and the value obtained from capillary rise experiments. This difference may be caused by the different stages in which the respective experiments are carried out. Our tactoid experiments were carried out when the phase separation process is not quite finished, whereas the capillary-rise experiments require a fully equilibrated sample where all tactoids have sedimented and the different domains in the nematic phase have annealed. Such an equilibrated sample might very well have a higher order parameter. This implies that a higher order parameter would lead to a larger value for the extrapolation length. Moreover, during the equilibration, a sedimentation equilibrium might have started to develop, which would change the concentrations in the co-existing phases and, as a consequence, also change the elastic and surface properties of the nematic.

In any event, it seems quite unlikely that these caveats could be responsible for the difference of almost two orders of magnitude between the two types of system.

We thank Lia Verhoeff and Henk Lekkerkerker for their experimental work on tactoids consisting of gibbsite platelets.

9.A Wulff construction

The geometrical Wulff construction provides a polar plot of the interfacial tension, and every point on the surface is connected to the origin of the coordinate system by a radial vector. A plane perpendicular to each of these vectors is defined at their tips, and the convex envelope of these planes then provides the droplet shape. Our problem is cylindrically symmetric with the z -axis as the symmetric axis, so a two-dimensional approach suffices. This means that the shape that we find in terms of the z -coordinate as a function of the radial distance r that must be rotated around the z -axis. If we

consider the plane of positive z and r values, the line perpendicular to the radial vector of an arbitrary point on the polar plot of the interfacial tension obeys [53]

$$z_{\vartheta}(r, \vartheta) = -r \tan \vartheta + \frac{1}{\cos \vartheta} - \frac{\omega}{1 + \omega} \cos \vartheta, \quad (9.4)$$

where ϑ is the angle between the vector and the z -axis and where z and r have been made dimensionless by dividing them by a scale that fixes the volume of a spherical drop of radius R . We return to this below.

The envelope of the lines for $z(r, \vartheta) \geq 0$ is found from minimising z with respect to the polar angle ϑ for every r , giving $z(r) \equiv \min_{\vartheta \in [0, \pi/2]} z_{\vartheta}(r, \vartheta)$. With $u \equiv \sin \vartheta$, this gives [53]

$$z(r) = \frac{1 - \frac{\omega}{1 + \omega}(1 - u^2) - ur}{\sqrt{1 - u^2}}. \quad (9.5)$$

The optimal value of u satisfies

$$-\frac{\omega}{1 + \omega}u^3 + \frac{1 + 2\omega}{1 + \omega}u - r = 0. \quad (9.6)$$

The shape is now defined for $r \in (0, r_0)$, with r_0 the smallest zero of $z(r)$. To find r_0 we combine Eqs. (9.5) and (9.6), giving

$$z(r) = \sqrt{1 - u^2} \left(1 - \frac{\omega}{1 + \omega}(1 + u^2) \right). \quad (9.7)$$

Eq. (9.7) has a zero for $u = 1$ and $u = 1/\sqrt{\omega}$. From Eq. (9.6) this gives $r_0 = 1$ for $\omega \leq 1$ and $r_0 = 2\sqrt{\omega}/(\omega + 1)$ for $\omega \geq 1$.

The aspect ratio a is defined as the ratio of the drop size in the direction of the axis of rotational symmetry and that perpendicular to it, implying that it is a number smaller than unity for oblate ellipsoids and larger than unity for prolate ones. This means that it follows from $a = z(0)/r_0$. For $r = 0$ it we find from Eq. (9.6) that $u = 0$ or $u = \pm\sqrt{1 - 1/\omega}$, but the latter solution has no real solution for $u = \sin \vartheta$. This gives from Eq. (9.7) that $z(0) = 1/(1 + \omega)$. The aspect ratio is then

$$a = \begin{cases} \frac{1}{1 + \omega}, & 0 \leq \omega \leq 1 \\ \frac{1}{2\sqrt{\omega}}, & \omega \geq 1. \end{cases} \quad (9.8)$$

The opening angle α of the Wulff shape satisfies $\alpha = -\arctan(-z_r(r_0))$, with $z_r = \partial z / \partial r$. We have from Eq. (9.6)

$$\left(\frac{\partial u}{\partial r} \right)^{-1} = -\frac{3\omega}{1 + \omega}u^2 + \frac{1 + 2\omega}{1 + \omega} \quad (9.9)$$

that we use in Eq. (9.7) to compute $\partial z/\partial r = \partial z/\partial u \times \partial u/\partial r$. This then gives $\partial z/\partial r = -u/\sqrt{1-u^2}$. For $\omega \leq 1$ we have $r_0 = 1$ and we find from Eq. (9.6) that $u = 1$, so $\alpha = \pi/2$, whereas for $\omega \geq 1$ we have $r_0 = 2\sqrt{\omega}/(\omega + 1)$ and Eq. (9.6) gives $u = 1/\sqrt{\omega}$, so $\alpha = -\arctan(-\sqrt{\omega-1})$. The Wulff shape has a smooth boundary for $0 \leq \omega \leq 1$ and a sharp rim for $\omega > 1$, whereas the cut-sphere shape has a smooth boundary only for $\omega = 0$ and a sharp one for $\omega > 0$. As we show in Appendix 9.B, this difference is not reflected in a significant difference in the free energies of both shapes.

To find the free energy F^u of the drop we first need to compute the volume $V^u = 4\pi R^3 \int_0^{r_0} dr r z(r)$. Using Eqs. (9.6) and (9.9), we remove the dependence on r and switch to u as integration variable. The integration boundaries are $u = 0$ and $u = 1$ for $0 \leq \omega \leq 1$ and $u = 0$ and $u = 1/\sqrt{\omega}$ for $\omega \geq 1$. We find

$$\frac{V^u}{4\pi R^3/3} = \begin{cases} k(\omega), & 0 \leq \omega \leq 1 \\ \frac{8(\omega-1)^{7/2}}{35\sqrt{\omega}(\omega+1)^3} + k(\omega), & \omega \geq 1, \end{cases} \quad (9.10)$$

with

$$k(\omega) \equiv \frac{35 + 70\omega + 28\omega^2 - 8\omega^3}{35(\omega+1)^3}. \quad (9.11)$$

This volume decreases with increasing values of ω , so to ensure that the volume of the drop is kept equal to that of the spherical tactoid that we have for $\omega = 0$, we have to rescale the length scale R with a factor s_1 for $0 \leq \omega \leq 1$ and s_2 for $\omega \geq 1$ in the surface and anchoring energy. Hence, we equate Eq. (9.10) to unity and from that find $s_1 \equiv k(\omega)^{1/3}$ and $s_2 \equiv (8(\omega-1)^{7/2}/(35\sqrt{\omega}(\omega+1)^3) + k(\omega))^{1/3}$.

With the rescaled volume the bare surface energy obeys $F_{st}^u = 4\pi\gamma(R/s_i)^2 \int_0^{r_0} dr r \sqrt{1+z_r^2}$ and the anchoring energy $F_{sa}^u = 4\pi\zeta(R/s_i)^2 \int_0^{r_0} dr r z_r^2/\sqrt{1+z_r^2}$, with $i = 1$ for $0 \leq \omega \leq 1$ and $i = 2$ for $\omega \geq 1$. We find

$$\frac{F_{st}^u}{4\pi\gamma R^2} = \begin{cases} \frac{15 + 20\omega + 4\omega^2}{15(\omega+1)^2 s_1^2}, & 0 \leq \omega \leq 1 \\ \frac{15 - 4c/\omega + 8c - 4c\omega + 4\omega(\omega+5)}{15(\omega+1)^2 s_2^2}, & \omega \geq 1, \end{cases} \quad (9.12)$$

with $c \equiv \sqrt{\omega(\omega - 1)}$, and

$$\frac{F_{sa}^u}{4\pi\gamma R^2} = \begin{cases} \frac{(70 + 56\omega - 24\omega^2)\omega}{105(\omega + 1)^2 s_1^2}, & 0 \leq \omega \leq 1 \\ \frac{\omega}{105(\omega + 1)^2 s_2^2} (70 + 4c/\omega^2 + 16c/\omega - 44c + 24c\omega + 56\omega - 24\omega^2 - 12c) & \omega \geq 1. \end{cases} \quad (9.13)$$

In the limit $\omega \rightarrow 0$ we find a spherical droplet with a free energy that is simply $F^u = 4\pi\gamma R^2$. Note that if we impose a uniform director field in a spherical drop without any restriction on ω , we retrieve Eq. (8.1).

9.B Cut-sphere lens

In this appendix we show how a lens shape associated with the uniform director field can also be constructed from a sphere, and that its free energy is only slightly larger than the exact lens that follows from the Wulff construction [206]. We cut a part from the top for a polar angle $\vartheta = \alpha < \pi/2$ and mirror it in the $r\phi$ -plane with azimuthal symmetry, see Fig. 9.8. This means that the director field is in the z -direction to minimise the magnetic energy and that α is the opening angle of the cut-sphere (superscript *cs*) shape. For the volume we find

$$V^{cs} = \frac{8}{3}\pi R^3 (2 + \cos \alpha) \sin^4 \left(\frac{\alpha}{2} \right). \quad (9.14)$$

For the volume of the lens to be equal to the volume of the sphere with radius R , we need to re-scale the radius R in Eq. (9.14) by a factor $s(\alpha) = ((4 + 2 \cos \alpha) \sin^4(\alpha/2))^{-1/3}$ that can be rewritten as

$$s(\alpha) = \frac{2}{(8 - 9 \cos \alpha + \cos 3\alpha)^{1/3}}, \quad (9.15)$$

which gives $s(\pi/2) = 1$ for the sphere. As already alluded to, we have only the surface energy and the anchoring energy that contribute to the free energy. We find for the bare surface energy

$$F_{st}^{cs} = 4\pi\gamma s(\alpha)^2 R^2 (1 - \cos \alpha). \quad (9.16)$$

For the surface anchoring term F_{sa}^{cs} we have to integrate the square of the sine of the angle between the director field and the tactoid normal, which is the polar angle ϑ , giving

$$F_{sa}^{cs} = \frac{16}{3}\pi\zeta s(\alpha)^2 R^2 (2 + \cos \alpha) \sin^4 \left(\frac{\alpha}{2} \right). \quad (9.17)$$

The total free energy of the lens-shaped tactoid is $F^{cs} = F_{st}^{cs} + F_{sa}^{cs}$. The optimum value of α is found by putting $\partial F^{cs}/\partial\alpha = 0$, which gives

$$\frac{\partial F^{cs}}{\partial\alpha} = \frac{1}{3}\pi s(\alpha)^2 R^2 \left(4\zeta \sin^3 \alpha - 6\gamma \frac{\sin 2\alpha}{2 + \cos \alpha} \right). \quad (9.18)$$

To find the roots of the right-hand side, we need to solve a third order polynomial in $\cos \alpha$, which gives for the optimum α :

$$\alpha_{\text{opt}}(\omega) = \arccos \left(-\frac{2}{3} + \frac{7\omega - 9}{3g(\omega)} + \frac{h(\omega)}{3\omega} \right), \quad (9.19)$$

with $\omega \equiv \zeta/\gamma$ and

$$h(\omega) = \left(\omega^2(10\omega + 27) + 9\sqrt{\omega^3(-3\omega^3 + 23\omega^2 - 12\omega + 9)} \right)^{1/3}. \quad (9.20)$$

The opening angle is shown in Fig. 9.2, and compared to the opening angle of lens that follows from the Wulff construction. The latter has a smooth boundary for $0 \leq \omega \leq 1$, but the cut-sphere lens has one only in the spherical limit of $\omega \rightarrow 0$ and has a sharp rim for $\omega > 0$. Interestingly, this has hardly any consequences for the free energy, because it is at most 0.5% larger than that of the Wulff shape, see Fig. 9.2.

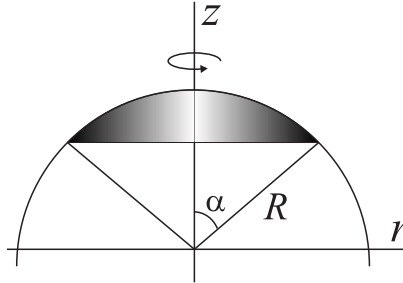


Figure 9.8: The lens shape is constructed by cutting a piece (shaded area) from a sphere of radius R . The cutting angle defines the opening angle α . The relative difference between the free energy of the shape that follows from the Wulff construction F^u and the cut-sphere shape F^{cs} is at most 0.5%, as shown in Fig. 9.2.

Using the optimal value of α as given by Eq. (9.19) we can compute the aspect ratio a of the tactoid, which depends only on ω . It reads

$$a = \frac{\sin \alpha_{\text{opt}}}{1 - \cos \alpha_{\text{opt}}} = \sqrt{\frac{3+y}{3-y}} \quad (9.21)$$

with

$$y = -2 + \frac{7\omega - 9}{h(\omega)} + \frac{h(\omega)}{\omega} \quad (9.22)$$

and $h(\omega)$ given by Eq. (9.20). The aspect ratio is shown in Fig. 9.2.

By comparing the free energy $F_{st}^u + F_{sa}^u$ of the lens shape with uniform director field, where F_{st}^u and F_{sa}^u are given by Eqs. (9.12) and (9.13), and that of the spherical droplet with the central hedgehog in zero magnetic field,

$$F^h = 4\pi\gamma R^2 + 8\pi K_1 R, \quad (9.23)$$

we can determine the drop size R at which the latter becomes more favourable than the former. The energy difference between the lenses that follow from the Wulff and the cut-sphere construction is negligible, as shown in Fig. 9.8, and that of the cut-sphere requires no separation for $\omega < 1$ and $\omega > 1$, so we choose to use the cut-sphere lens with free energy given by $F_{st}^{cs} + F_{sa}^{cs}$ as given by Eqs. (9.16) and (9.17). We find

$$\frac{R_c \zeta}{K_1} = \mathfrak{R}_c \omega = \frac{24\omega}{s(\alpha)^2 (12 + 8\omega(12 + 9\omega) \cos(\alpha) + \omega \cos(3\alpha)) - 12}, \quad (9.24)$$

with α the optimum opening angle given by Eq. (9.19). For the values of ω we consider in this work, i.e., $\omega \lesssim 2$, Eq. (9.24) can be very well approximated by $\mathfrak{R}_c \omega = 3 + 4\omega/5$. See also Fig. 9.5.

9.C Split-core defect

The derivation of the free energy F_{sc} of the sphere with split-core defect is given in Appendix 8.B. The optimal defect length satisfies Eq. (8.30) and to determine the crossover from the lens with uniform field to the sphere with split-core defect in the stability diagram of Fig. 9.4, we put $F^{sc} = F^u$ and use Eq. (8.30) to eliminate the dependence on L . The lines of constant $L/R = c$ in Fig. 9.4 are determined by directly plotting Eq. (8.30) for $L = cR$.

To find the free energy F_{pr}^{sc} of the prolate shape with split-core defect, we perform a perturbation in both in the shape, i.e., aspect ratio, and the split-core defect length of the sphere with line defect. The free energy then follows from the free energy $F^{sc}(L_s, \varepsilon = 0)$ of the sphere with defect length L_s and deviation $\varepsilon = 0$ from the aspect ratio of unity of the sphere, giving Eq. (9.3). Hence, $\delta L = L - L_s$ is the perturbation in the defect length and ε that in the aspect ratio. We optimise the free energy of the prolate shape with respect to the parameters ε and δL , so

$$\left. \frac{\partial F^{sc}}{\partial \varepsilon} \right|_{(L_s, 0)} + \varepsilon \left. \frac{\partial^2 F^{sc}}{\partial \varepsilon^2} \right|_{(L_s, 0)} + \delta L \left. \frac{\partial^2 F^{sc}}{\partial \varepsilon \partial L} \right|_{(L_s, 0)} = 0, \quad (9.25a)$$

$$\left. \frac{\partial F^{sc}}{\partial L} \right|_{(L_s, 0)} + \delta L \left. \frac{\partial^2 F^{sc}}{\partial L^2} \right|_{(L_s, 0)} + \varepsilon \delta L \left. \frac{\partial^2 F^{sc}}{\partial \varepsilon \partial L} \right|_{(L_s, 0)} = 0. \quad (9.25b)$$

To calculate the different terms in the expansion, we note that the derivatives with respect to L can be found by direct differentiation; the derivatives with respect to ε we obtain by performing a perturbation of each of the free-energy terms of the spherical tactoid. This we do as follows. We start from equation of a prolate ellipsoid that is elongated in the z -direction,

$$\left(\frac{x}{a}\right)^2 + \left(\frac{y}{a}\right)^2 + \left(\frac{z}{c}\right)^2 = 1, \quad (9.26)$$

where we take $a = R/(1 + \varepsilon)^{1/3}$ and $c = R(1 + \varepsilon)/(1 + \varepsilon)^{1/3} = R(1 + \varepsilon)^{2/3}$ to keep the volume the same as that of the sphere and to give the shape an aspect ratio of $1 + \varepsilon$. For this perturbed shape we compute the contributions to the free energy for a given director field with line-defect length L_s , so the same director field as in the spherical shape with two-dimensional radial field around the defect line and a three-dimensional field originating from the ends of the defect line. So we write

$$\left.\frac{\partial F^{sc}}{\partial \varepsilon}\right|_{(L_s, 0)} = F_{st, \varepsilon}^{sc} + F_{sa, \varepsilon}^{sc} + F_{e, \varepsilon}^{sc} + F_{m, \varepsilon}^{sc}. \quad (9.27)$$

We find $F_{st, \varepsilon}^{sc} = 0$ because the effect on the bare surface energy is of second order,

$$\begin{aligned} F_{sa, \varepsilon}^{sc} &= \pi \zeta \left(\frac{3L^5}{40R^3} - \frac{11L^3}{18R} \right) \\ &+ \frac{\pi \zeta}{768L^3R^3} \left(i(9L^8 - 80L^6R^2 - 160L^4R^4 + 768L^2R^6 + 2304R^8) \left(\pi + i \log \left[\frac{L+2R}{L-2R} \right] \right) \right. \\ &\left. + 4L(-24L^7 + 9L^6R + 224L^5R^2 - 68L^4R^3 - 384L^3R^4 + 240L^2R^5 + 576R^7) \right), \quad (9.28) \end{aligned}$$

$$\begin{aligned} F_{e, \varepsilon}^{sc} &= \frac{\pi K_1}{3L^3} \left(\left(6L(L^3 - L^2R - 4R^3) + (3L^4 + 8L^2R^2 + 48R^4) \coth^{-1} \left[\frac{2R}{L} \right] \right) \right. \\ &\quad \left. + \left(3L^4 + L^3R \left(2i \coth^{-1} \left[\frac{2R}{(i + \sqrt{3})L - 2\sqrt{3}R} \right] + \right. \right. \right. \\ &\quad \left. \left. 2i \coth^{-1} \left[\frac{2R}{(i + \sqrt{3})L + 2\sqrt{3}R} \right] + \log \frac{(L + i\sqrt{3}L - 4R)(L - 2R)}{(L + i\sqrt{3}L + 4R)(L + 2R)} \right) \right) \right), \quad (9.29) \end{aligned}$$

and

$$\begin{aligned} F_{m, \varepsilon}^{sc} &= -\frac{\rho \Delta \chi B^2}{384L^5} \left(\pi(L^2 - 4R^2)^2 (12LR(L^2 + 4R^2) + i(3L^4 + 8L^2R^2 + 48R^4) \right. \\ &\quad \left. \left(\pi + i \log \left[\frac{L+2R}{L-2R} \right] \right) \right). \quad (9.30) \end{aligned}$$

Note the appearance of the imaginary unit i in the equations, but their values are real. The second-order terms in ε are the second terms in the perturbation as described above and give very large expressions.

Conclusions and outlook

10

10.1 Aim of the thesis

The general aim of this work has been to gain a better insight into the large-scale self-organisation of anisometric colloidal particles dispersed in a solvent. We considered two prototypes of this self-organisation, namely the formation of system-spanning networks of loosely connected particles and the response of nematic liquid-crystalline (symmetry-broken) states to hard and soft confinement. To investigate the former, we applied a microscopic, particle-based theory and studied the effect of particle shape and dimensions and external fields. For the latter we made use of a mesoscopic, structure-based theory to study how surface and elastic properties, which depend crucially on the particle shape, affect how the liquid-crystalline fluid in contact with its isotropic phase creeps up a solid wall, and how droplets of that liquid-crystalline phase respond to magnetic fields. The common denominator of both problems is that the same anisotropic interactions dictate the structure of particle networks and drive the formation of liquid-crystalline states, and determine their elastic and surface properties.

In the remainder of this chapter we summarise our main results on connectedness percolation in section 10.2 and on nematics under soft confinement in section 10.3, and we propose a number of issues for future research in section 10.4.

10.2 Build-up of networks of colloidal particles in fluid media

In the first part of this thesis we focused on the formation of temporal networks in dispersions of rod-like and plate-like particles interacting by a harshly repulsive excluded-volume interaction. The work was inspired by electrical-conductivity measurements on composites containing carbon nanotubes and graphene sheets, which turn out to be quite sensitive to their formulation and processing. To gain understanding of this,

we calculated within the framework of connectedness-percolation theory how having a distribution of particle shape, size and, loosely speaking, ease of charge transport, affects the *percolation threshold*, i.e., the minimal particle loading required for the onset of conduction. We mimicked some of the potential effects of processing by allowing for particle alignment due to, e.g., an elongational flow field, and calculated not only the percolation threshold, but also the size and shape of the clusters upon approach of this percolation threshold. Finally, the conductivity of the network of rod-like particles *above* the percolation threshold was computed by making use of a connection between connectedness-percolation theory for rods and percolation on a particular kind of lattice.

The main conclusions of this part of the thesis are as follows.

1. The often-assumed inverse-aspect-ratio scaling of the percolation threshold for anisometric filler particles is modified both by hard-core interactions and by polydispersity. This explains, in part, large variations in measured values.
2. Whether the percolation threshold in- or decreases relative to that of the idealised case of monodisperse, non-interacting particles, depends in a complicated way on the effective range of electron transport, the shape of the length and width distributions, and whether these are coupled.
3. The lowest percolation threshold for rod-like particles is obtained for uncoupled length and width distributions, provided the length distribution is strongly skewed towards shorter lengths. The presence of thicker-than-average rods always raises the percolation threshold.
4. For monodisperse, mutually avoiding plate-like particles the inverse-aspect-ratio scaling fails completely and for these low percolation thresholds are not to be expected. If a low threshold is required, then rods (carbon nanotubes) are in principle better suited than platelets (graphene). For platelets low percolation thresholds are only possible in mixtures containing a small quantity of much wider particles or rod-like ones.
5. For rods, the percolation threshold is governed solely by the fraction of conductive ones. Insulating rods act as dead mass, so removing them improves percolation. A soft conductive coating potentially improves the contribution of already conductive ones and certainly that of insulating ones.
6. Alignment fields raise the percolation threshold of rod-like particles. Percolating networks in external fields disintegrate due to interaction-induced alignment at sufficiently high concentrations in the region where the isotropic-nematic transition

occurs. This limits the existence of percolating networks to relatively weak fields and a range of concentrations.

7. Particle alignment affects cluster shapes off percolation. Orienting fields give rise to elongated clusters and disorienting fields to flat ones. However, the size of clusters diverges with the same scaling exponent parallel and perpendicular to the field direction upon approach of the threshold.
8. If the electrical conductivity of a percolating network of rod-like particles is governed by the microscopic conductivity and proportional to the backbone fraction, then it increases quadratically with the particle loading just above the percolation threshold and linearly away from it.
9. Connectedness-percolation theory for infinitely many components involving cylindrical particles, elongated and/or flat, can be solved exactly within the second-virial approximation.
10. The percolation threshold depends on a few moments of the length and width distribution only, which are relatively straightforwardly accessible experimentally, implying that the theory itself can relatively straightforwardly be applied in practice.

10.3 Nematics of colloids under soft confinement

In the second part of this thesis we focused on providing a theoretical understanding of experimental findings relating to the interface between co-existing isotropic and nematic phases of dispersions of colloidal clay platelets in two different kinds of solvent, requiring different kinds of colloidal stabilisation. We considered i) the capillary rise of that interface and ii) the shape and structure of nematic droplets, the latter also in the presence of a magnetic field. In both the competition between surface and bulk elastic forces gives rise to unusual interface shapes and spatial distributions of the local symmetry axis of the liquid crystal, the so-called director, observed in experiment. Comparison of our theory with polarisation-microscopic images enabled us to extract material constants including surface free energies and elastic constants of the colloidal liquid crystal of the clay. Our main conclusions pertaining to the second part of the thesis are the following.

1. The competition between surface free energy and bulk elasticity expresses itself in a length scale. On length scales below this *extrapolation length* elasticity wins

out and above it surface forces are predominant. This causes large-scale structural reorganisations of the interface shape and director field of the nematic liquid crystal.

2. The capillary-rise profile of the interface between co-existing nematic and isotropic phases in contact with a vertical wall is a non-monotonic function of the distance to the wall. Near the wall the director field is rigid, distances further away than the extrapolation length the surface anchoring is rigid.
3. The depression in the interfacial profile is stabilised by the presence of a virtual disclination defect line parallel to the wall. The virtual disclination lowers the overall elastic deformation of the nematic at the expense of an additional interfacial area.
4. Nematic droplets with a preferential perpendicular alignment of the director to the interface tend to be flat and have a uniform director field if they are smaller than the extrapolation length. The larger the anchoring strength, the flatter the drop.
5. Droplets larger than the extrapolation length are spherical with a radial field emanating from a point defect, also in the presence of a weak magnetic field. The crossover from the uniform to radial director field is discontinuous, i.e., of first order.
6. In a stronger magnetic field, and provided the diamagnetic susceptibility anisotropy is negative, the radial field transforms to a split-core disclination line but only if this field is sufficiently strong. This transformation resembles a Frederiks transition. The length of the defect increases with increasing magnetic-field strength.
7. For strong fields the droplet itself stretches to a prolate shape if the anchoring strength is sufficiently large relative to the surface tension. For very strong fields it reverts to the spherical shape, whereas the line defect grows further until it runs throughout the entire drop.
8. The transition from spherical to prolate and back to spherical occurs at a well-defined magnetic-field strength and is of second order. The range of magnetic fields over which that this happens, depends on droplet size and anchoring strength.
9. Our variational theory produces approximate but analytical expressions for the crossovers between uniform and radial and between radial and split-core configurations. This allows us to extract from experimental data values for the anchoring strength, surface tension, and an elastic constant.

10. By comparing theory to experimental data, it appears that the interfacial properties of the co-existing isotropic and nematic phases depend rather strongly on the type of solvent, i.e., on the type of stabilisation. The elastic constant, however, turns out to be insensitive to that.

10.4 Outlook

Our generalisation of connectedness-percolation theory applied to rods and disks shows that the percolation threshold depends sensitively on the size and connectivity distributions as well as the degree of alignment of the particles. In practice, these are connected with the formulation and processing of the composite. Therefore, it would be most useful to gain further insight experimentally and theoretically into how the percolating network is affected by each step in the processing. Therefore, we suggest the following avenues of follow-up investigation.

1. It is of crucial importance to obtain quantitative data on the coupling between the length and breadth distributions of, e.g., carbon nanotubes. An obvious way to do this is, is by electron microscopy and/or atomic-force microscopy. Another is to investigate in more detail the break-up mechanism of carbon nanotubes during sonication theoretically and experimentally.
2. Comparison of experimentally determined percolation thresholds of carbon nanotubes and graphene is only possible if their dimensions are known, as well as the degree of polydispersity in them and their degree of alignment in the composite. The latter can be probed by, e.g., radiation-scattering techniques and Raman spectroscopy [207].
3. Systematic probing of alignment should be possible by making use of an externally applied electric field during compression moulding. Experimental equilibration studies are sorely needed to ascertain whether the theory described in this thesis actually applies.
4. The dynamics in the initial stages of the network formation could also be modelled. Starting point of such a theory could be the two-particle Smoluchowski equation [163] from which, in analogy with the Ornstein-Zernike equation, a connectedness counterpart should be derived.
5. A potentially more accurate theory for connectedness percolation in systems of plate-like particles requires a different closure of the Ornstein-Zernike equation

from the one that we have used. Inspiration may be drawn from closures that have been developed for spherical particles.

6. To test our predictions for the electrical conductivity of percolating networks of rod-like particles, more accurate measurements are required with more data points both close to the percolation threshold and away from it.

In the second part of the thesis we found a discrepancy for the same system of gibbsite platelets of more than an order of magnitude between the surface tension and anchoring strength as obtained from the capillary-rise experiments and from studying nematic droplets. Both studies also offer new theoretical and experimental challenges for future research, so here we propose a few issues that would be interesting to investigate.

1. In our calculation of the capillary-rise profile we only considered the limits of weak and strong surface anchoring. A challenge would be to compute the profile without such assumptions to see if the prediction of a non-monotonic profile survives.
2. The few experiments that have been conducted on the capillary-rise profile turned out to be very sensitive to the preparation procedure [181]. More extensive experimentation could provide reliable statistics on the rise height and the interface shape. Moreover, these may provide more conclusive evidence of the non-monotonicity of the profile that we predict.
3. Our tactoid model ignores the effect of the magnetic field on the material parameters and the background isotropic phase. A more sophisticated theory is required to quantify these effects.
4. Our calculations presumed purely radial director fields in the tactoids caused by homeotropic anchoring of the director to the interface. The influence of a potential bend deformation can be investigated by perturbation theory.
5. A precise cross-over mechanism between uniform and radial director fields remains elusive. Experimentally, this should be possible by investigating the director field of a tactoid just large enough to support a radial field in the absence of a magnetic field. At strong enough fields it should become uniform.
6. An interesting but largely unexplored area, theoretically and experimentally, is the coalescence of two nematic drops. For instance, the coalescence of two drops just small enough to have a uniform director field, requires the creation of a hedgehog defect if the anchoring is homeotropic. Theoretically, this may be investigated with the aid of the usual nematodynamic equations, which describe the relaxation of the director field.

References

- [1] P. A. Sturrock, *Plasma Physics: An Introduction to the Theory of Astrophysical, Geophysical & Laboratory Plasmas*, Cambridge University Press (1994).
- [2] J. P. Hansen and I. MacDonald, *Theory of simple liquids*, second edition, Academic Press, London (1986).
- [3] R. A. L. Jones, *Soft Condensed Matter*, Oxford University Press, Oxford, U.K. (2002).
- [4] R. P. Sear, *Europhys. Lett.* **44**, 531 (1998).
- [5] B. Vigolo, C. Coulon, M. Maugey, C. Zakri, and P. Poulin, *Science* **309**, 920 (2005).
- [6] P. G. de Gennes, *The Physics of Liquid Crystals*, Oxford University Press, Oxford, U.K. (1993).
- [7] P. M. Chaikin and T. C. Lubensky, *Principles of soft condensed matter physics*, Cambridge University Press (2010).
- [8] P. Bolhuis and D. Frenkel, *J. Chem. Phys.* **106**, 666 (1997).
- [9] M. A. Bates and D. Frenkel, *J. Chem. Phys.* **109**, 6193 (1998).
- [10] Z. Dogic and S. Fraden *Phys. Rev. Lett.* **78**, 2417 (1997).
- [11] F. M. van der Kooij, K. Kassapidou, and H. N. W. Lekkerkerker, *Nature* **406**, 868 (2000).
- [12] F. M. van der Kooij and H. N. W. Lekkerkerker, *Philos. T. R. Soc. A.* **359**, 985 (2001).
- [13] L. Onsager, *Ann. N. Y. Acad. Sci.* **51**, 627 (1949).
- [14] F. C. Frank, *Discuss. Faraday. Soc.* **25**, 19 (1958).
- [15] S. R. Broadbent and J. M. Hammersley, *Proc. Camb. Phil. Soc.*, **53**, 629 (1957).
- [16] D. Stauffer and A. Aharony, *Introduction to Percolation Theory*, Taylor & Francis, London (1992).
- [17] K. S. Novoselov, A. K. Geim, S. V. Morozov, D. Jiang, Y. Zhang, S. V. Dubonos,

- I. V. Grigorieva, and A. A. Firsov, *Science* **306**, 666 (2004).
- [18] M. Moniruzzaman and K. I. Winey, *Macromolecules* **39**, 5194 (2006).
- [19] S. Stankovich, D. A. Dikin, G. H. B. Dommett, K. M. Kohlhaas, E. J. Zimney, E. A. Stach, R. D. Piner, S. T. Nguyen, and R. S. Ruoff, *Nature* **442**, 282 (2006).
- [20] S. I. White, R. M. Mutiso, P. M. Vora, D. Jahnke, S. Hsu, J. M. Kikkawa, J. Li, J. E. Fischer, and K. I. Winey, *Adv. Funct. Mat.* **20**, 2709 (2010).
- [21] D. Mihailovic, *Prog. Mater. Sci.* **54**, 309 (2009).
- [22] J. Obrzut, J. F. Douglas, S. B. Kharchenko, and K. B. Migler, *Phys. Rev. B* **76**, 195420 (2007).
- [23] N. Grossiord, H. E. Miltner, J. Loos, J. Meuldijk, B. van Mele, and C. E. Koning, *Chem. Mater.* **19**, 3787 (2007).
- [24] P. Pötschke, S. M. Dudkin, and I. Alig, *Polymer* **44**, 5023 (2003).
- [25] S. Torquato, *Random Heterogeneous Materials: Microstructure and Macroscopic Properties*, Springer-Verlag, New York (2002).
- [26] N. Grossiord, J. Loos, O. Regev, and C. E. Koning, *Chem. Mater.* **18**, 1089 (2006).
- [27] M. C. Hermant, B. Klumperman, A. V. Kyrylyuk, P. van der Schoot, and C. E. Koning, *Soft Matter* **5**, 878 (2009).
- [28] A. P. Philipse, *Langmuir* **12**, 1127 (1996).
- [29] G. E. Pike and C. H. Seager, *Phys. Rev. B* **10**, 1421 (1974).
- [30] I. Balberg, *J. Phys. D: Appl. Phys.* **42**, 064003 (2009).
- [31] I. Balberg and M. A. J. Michels, to be published.
- [32] W. F. Pasveer and M. A. J. Michels, *Phys. Rev. B* **74**, 195129 (2006).
- [33] S. Vionnet-Menot, C. Grimaldi, T. Maeder, S. Strässler, and P. Ryser, *Phys. Rev. B* **71**, 064201 (2003).
- [34] A. Coniglio, U. De Angelis, and A. Forlani, *J. Phys. A-Math. Gen.* **10**, 1123 (1977).
- [35] T. Shimada, M. Doi, and K. Okano, *J. Chem. Phys.* **88**, 2815 (1988).
- [36] T. DeSimone, S. Demoulini, and R. M. Stratt, *J. Chem. Phys.* **85**, 391 (1986).
- [37] J. Phillips, M. Schmidt, *Phys. Rev. B* **81**, 041401 (2010).
- [38] A. L. R. Bug, S. A. Safran, and I. Webman, *Phys. Rev. B* **33**, 4716 (1986).
- [39] G. Stell, *Physica A* **231**, 1 (1996).
- [40] A. Rapini and M. Papoular, *J. Phys. (Paris), Colloq.* **30**, C4–54 (1969).
- [41] N. Puech, E. Grelet, P. Poulin, C. Blanc, and P. van der Schoot, *Phys. Rev. E* **82**, 020702 (2010).
- [42] D. van der Beek, A. V. Petukhov, P. Davidson, J. Ferre, J. P. Jamet, H. H. Wensink, G. J. Vroege, W. Bras, and H. N. W. Lekkerkerker, *Phys. Rev. E* **73**, 041402 (2006).
- [43] S. Wolfsheimer, C. Tanase, K. Shundyak, R. van Roij, and T. Schilling, *Phys. Rev. E* **73**, 061703 (2006).

-
- [44] K. Shundyak and R. van Roij, *J. Phys.-Condens. Mat.* **13**, 4789 (2001).
- [45] D. van der Beek, H. Reich, P. van der Schoot, M. Dijkstra, T. Schilling, R. Vink, M. Schmidt, R. van Roij, and H. Lekkerkerker, *Phys. Rev. Lett.* **97**, 087801 (2006).
- [46] V. M. Pergamenschik, *Phys. Rev. E* **48**, 1254 (1993).
- [47] H. Yokoyama, *Phys. Rev. E* **55**, 2938 (1997).
- [48] O. D. Lavrentovich and V. M. Pergamenschik, *Phys. Rev. Lett.* **73**, 979 (1994).
- [49] J. K. Gupta, F. Causo, and N. L. Abbott, *Angew. Chem. Int. Ed.* **48**, 1652 (2009).
- [50] S. D. Lee and R. B. Meyer, *J. Chem. Phys.* **84**, 3443 (1986).
- [51] V. G. Taratuta, F. Lonberg, and R. B. Meyer, *Phys. Rev. A* **37**, 1831 (1988).
- [52] P. A. O'Brien, M. P. Allen, D. L. Cheung, M. Dennison, and A. Masters, *Phys. Rev. E* **78**, 051705 (2008).
- [53] P. Prinsen and P. van der Schoot, *Phys. Rev. E* **68**, 021701 (2003).
- [54] P. Prinsen and P. van der Schoot, *Eur. Phys. J. E* **13**, 35 (2004).
- [55] P. Drzaic, *Liquid Crystal Dispersions*, World Scientific, Singapore (1995).
- [56] J. X. Tang and S. Fraden, *Liquid Crystals* **19**, 459 (1995).
- [57] S. Fraden, A. J. Hurd, R. B. Meyer, M. Cahoon, and D. L. Casper, *J. Phys. (Paris), Colloq.* **46**, C3–85 (1985).
- [58] A. J. Hurd, S. Fraden, F. Lonberg, and R. B. Meyer, *Journal De Physique* **46**, 905 (1985).
- [59] S. Itou, K. Tozaki, and N. Komatsu, *Jpn. J. Appl. Phys. 1* **30**, 1230 (1991).
- [60] V. G. Taratuta, A. J. Hurd, and R. B. Meyer, *Phys. Rev. Lett.* **55**, 246 (1985).
- [61] D. L. Koch and O. G. Harlen, *Macromolecules* **32**, 219 (1999).
- [62] A. Cuetos and M. Dijkstra, *Phys. Rev. Lett.* **98**, 095701 (2007).
- [63] A. V. Kaznacheev, M. M. Bogdanov, and S. A. Taraskin, *J. Exp. Theor. Phys.* **95**, 57 (2002).
- [64] A. V. Kaznacheev, M. M. Bogdanov, and A. S. Sonin, *J. Exp. Theor. Phys.* **97**, 1159 (2003).
- [65] Z. Dogic and S. Fraden, *Philos. T. R. Soc. A.* **359**, 997 (2001).
- [66] W. L. Chen, T. Sato, and A. Teramoto, *Macromolecules* **29**, 4283 (1996).
- [67] W. L. Chen, T. Sato, and A. Teramoto, *Macromolecules* **31**, 6506 (1998).
- [68] W. L. Chen, T. Sato, and A. Teramoto, *Macromolecules* **32**, 1549 (1999).
- [69] W. L. Chen and D. G. Gray, *Langmuir* **18**, 633 (2002).
- [70] E. Velasco, L. Mederos, and D. E. Sullivan, *Phys. Rev. E* **66**, 021708 (2002).
- [71] R. L. C. Vink and T. Schilling, *Phys. Rev. E* **71**, 051716 (2005).
- [72] M. S. Al-Barwani and M. P. Allen, *Phys. Rev. E* **62**, 6706 (2000).
- [73] B. Groh and S. Dietrich, *Phys. Rev. E* **59**, 4216 (1999).
- [74] K. Shundyak and R. van Roij, *Phys. Rev. Lett.* **88**, 205501 (2002).

- [75] Z. Y. Chen and J. Noolandi, Phys. Rev. A **45**, 2389 (1992).
- [76] Z. Y. Chen and S. M. Cui, Phys. Rev. E **52**, 3876 (1995).
- [77] S. M. Cui, O. Akcakir, and Z. Y. Chen, Phys. Rev. E **51**, 4548 (1995).
- [78] F. M. van der Kooij and H. N. W. Lekkerkerker, J. Phys. Chem. B **102**, 7829 (1998).
- [79] A. B. D. Brown, S. Clarke, and A. R. Rennie, Langmuir **14**, 3129 (1998).
- [80] M. Bier, L. Harnau, and S. Dietrich, Phys. Rev. E **69**, 021506 (2004).
- [81] L. Harnau and S. Dietrich, Phys. Rev. E **65**, 021505 (2002).
- [82] A. F. Miller and A.M. Donald, Langmuir **18**, 10155 (2002).
- [83] D. van der Beek, P. Davidson, H. H. Wensink, G. J. Vroege, and H. N. W. Lekkerkerker, Phys. Rev. E **77**, 031708 (2008).
- [84] A. A. Verhoeff, R. H. J. Otten, P. van der Schoot, H. N. W. and Lekkerkerker, J. Phys. Chem. B **113**, 3704 (2009).
- [85] A. A. Verhoeff, I. A. Bakelaar, R. H. J. Otten, P. van der Schoot, and H. N. W. Lekkerkerker, Langmuir **27**, 116 (2011).
- [86] A. A. Verhoeff, R. H. J. Otten, P. van der Schoot, H. N. W. and Lekkerkerker, J. Chem. Phys. **134**, 044904 (2011).
- [87] P. van der Schoot, J. Phys. Chem. B **103**, 8804 (1999).
- [88] E. Virga, *Variational Theories for Liquid Crystals*, Chapman and Hall, London (1994).
- [89] S. Chandrasekhar, Mol. Crystals **2**, 71 (1966).
- [90] R. C. Tolman, J. Chem. Phys. **17**, 333 (1949).
- [91] A. D. Rey, Langmuir **19**, 3677 (2003).
- [92] E. J. Garboczi, K. A. Snyder, J. F. Douglas, and M. F. Thorpe, Phys. Rev. E **52**, 819 (1995).
- [93] I. Balberg, C.H. Anderson, S. Alexander, and N. Wagner, Phys. Rev. B **30**, 3933 (1984).
- [94] I. Balberg, Phys. Rev. B **33**, 3618 (1986).
- [95] A. Celzard, E. McRae, C. Deleuze, M. Dufort, G. Furdin, and J. F. Mareche, Phys. Rev. B **53**, 6209 (1996).
- [96] K. Leung and D. Chandler, J. Stat. Phys. **63**, 837 (1991).
- [97] A. V. Kyrylyuk and P. van der Schoot, P. Natl. Acad. Sci. USA **105**, 8221 (2008).
- [98] Y. R. Hernandez, A. Gryson, F. M. Blighe, M. Cadek, V. Nicolosi, W. J. Blau, Y. K. Gunko, and J. N. Coleman, Scripta Mater. **58**, 69 (2008).
- [99] P. Sollich, J. Phys.-Condens. Matter **14**, R79 (2002).
- [100] K. Shundyak, R. van Roij, and P. van der Schoot, J. Chem. Phys. **122**, 094912 (2005).
- [101] H. Deng, R. Zhang, E. Bilotti, J. Loos, A. A. J. M. Peijs, J. Appl. Polym. Sci.

- 113**, 742 (2009).
- [102] R. Fantoni, D. Gazzillo, and A. Giacometti, *J. Chem. Phys.* **122**, 034901 (2005).
- [103] A. P. Chatterjee, *J. Phys.-Condens. Matter* **20**, 255250 (2008).
- [104] G. J. Vroege and H. N. W. Lekkerkerker, *Rep. Prog. Phys.* **55**, 1241 (1992).
- [105] J. P. Straley, *Phys. Rev. A* **8**, 2181 (1973).
- [106] G. Ambrosetti, C. Grimaldi, I. Balberg, T. Maeder, A. Danani, and P. Ryser, *Phys. Rev. B* **81**, 155434 (2010).
- [107] M. C. Hermant, P. van der Schoot, B. Klumperman, and C. E. Koning, *ACS Nano* **4**, 2242-2248 (2010).
- [108] F. Dalmas, R. Dendievel, L. Chazeau, J.-Y. Cavall e, and C. Gauthier, *Acta Mater.* **54**, 2923 (2006).
- [109] A. P. Chatterjee, *J. Chem. Phys.* **132**, 224905 (2010).
- [110] C. Lu and J. Liu, *J. Phys. Chem. B* **110**, 20254 (2006).
- [111] C. L. Cheung, A. Kurtz, H. Park, and C. M. Lieber, *J. Phys. Chem. B* **106**, 2429 (2002).
- [112] M. S. Arnold, A. A. Green, J. F. Hulvat, S. I. Stupp, and M. C. Hersam, *Nat. Nanotechnol.* **1**, 60 (2006).
- [113] B. Yu, P.-X. Hou, F. Li, B. Liu, C. Liu, H.-M. Cheng, *Carbon* **48**, 2941 (2010).
- [114] E. Tkalya, M. Ghislandi, A. Alekseev, C. Koning, and J. Loos, *J. Mater. Chem.* **20**, 3035 (2010).
- [115] H.-B. Zhang, W.-G. Zheng, Q. Yan, Y. Yang, J.-W. Wang, Z.-H. Lu, G.-Y. Ji, and Z.-Z. Yu, *Polymer* **51** 1191 (2010).
- [116] A. V. Kyrlyuk, M. C. Hermant, T. Schilling, B. Klumperman, C. E. Koning, and P. van der Schoot, *Nat. Nanotechnol.* **6**, 364 (2011).
- [117] T. Hill, *J. Chem. Phys.* **23**, 617 (1955).
- [118] R. Fantoni, D. Gazzillo, A. Giacometti, M. A. Miller, G. Pastore, *J. Chem. Phys.* **127**, 234507 (2005).
- [119] T. Yamada, T. Namai, K. Hata, D. N. Futaba, K. Mizuno, J. Fan, M. Yudasaka, M. Yumura, and S. Iijima, *Nat. Nanotechnol.* **1**, 131 (2006).
- [120] S. Wang, Z. Liang, B. Wang, C. Zhang, *Nanotechnology* **17**, 634 (2006).
- [121] J. Li and J.-K. Kim, *Compos. Sci. Technol.* **67**, 2114 (2007).
- [122] A. F. Holloway, D. A. Craven, L. Xiao, J. Del Campo, G. G. Wildgoose, *J. Phys. Chem. C* **112**, 13729 (2008).
- [123] A. S. Berdinsky, P. S. Alegaonkar, H. C. Lee, J. S. Jung, J. H. Han, J. B. Yoo, D. Fink, and L. T. Chadderton, *Nano* **2**, 59 (2007).
- [124] A. N. G. Parra-Vasquez, I. Stepanek, V. A. Davis, V. C. Moore, E. H. Haroz, J. Shaver, R. H. Hauge, R. E. Smalley, and M. Pasquali, *Macromolecules* **40**, 4043

- (2007).
- [125] R. V. Hogg and A. T. Craig, *Introduction to Mathematical Statistics*, fourth edition, Macmillan, New York (1978).
- [126] M. Abramowitz, I. A. Stegun, *Handbook of Mathematical Functions with Formulas, Graphs, and Mathematical Tables*, Dover, New York (1972).
- [127] Á. Kukovecz, T. Kanyó, Z. Kónya, and I. Kiricsi, *Carbon* **43**, 994 (2005).
- [128] A. Lucas, C. Zakri, M. Maugey, M. Pasquali, P. van der Schoot, and P. Poulin, *J. Phys. Chem. C* **113**, 20599 (2009).
- [129] G.-H. Jeong, S. Suzuki, Y. Kobayashi, A. Yamazaki, H. Yoshimura, and Y. Homma, *J. Appl. Phys.* **98**, 124311 (2005).
- [130] E. Tkalya, M. Ghislandi, R. H. J. Otten, M. Lotya, A. Alekseev, P. van der Schoot, J. Coleman, B. de With, and C. Koning, to be published.
- [131] M. McAllister, J. Li, D. Adamson, H. Schniepp, A. Abdala, J. Liu, M. Herrera-Alonso, D. Milius, R. Car, R. Prud'homme, and I. Aksay, *Chem. Mater.* **19**, 4396 (2007).
- [132] M. Lotya, P. King, U. Khan, S. De, and J. N. Coleman, *ACS Nano*, **4**, 3155 (2010).
- [133] S. Stankovich, R. Piner, S. Nguyen, and R. Ruoff, *Carbon* **44**, 3342 (2006).
- [134] E. T. Thostenson and T.-W. Chou, *J. Phys. D: Appl. Phys.* **35**, L77 (2002).
- [135] W. Bauhofer and J. Z. Kovacs, *Compos. Sci. Technol.* **69**, 1486 (2009).
- [136] R. B. Stinchcombe, *J. Phys. C: Solid State Phys.* **6** L1, (1973).
- [137] R. B. Stinchcombe, *J. Phys. C: Solid State Phys.* **7** 179, (1974).
- [138] J. P. Straley, *J. Phys. C: Solid State Phys.* **10** 3009, (1977).
- [139] P. G. de Gennes, *J. Phys. Lett.* **37**, L1 (1976).
- [140] M. Sahimi, *Heterogeneous Materials I, Linear Transport and Optical Properties*, Springer-Verlag, New York (2003).
- [141] R. G. Larson and H. T. Davis, *Solid State Phys.* **15** 2327, (1982).
- [142] M. E. Fisher and J. W. Essam, *J. Math. Phys.* **2**, 609 (1961).
- [143] N. Johner, C. Grimaldi, I. Balberg, and P. Ryser, *Phys. Rev. B* **77** 174204 (2008).
- [144] P. M. Kogut and J. Straley, *J. Phys. C: Solid State Phys.* **11** 2151, (1979).
- [145] S. H. Feng, B. I. Halperin, and P. N. Sen, *Phys. Rev. B* **35**, 197 (1987).
- [146] P. N. Sen, J. N. Roberts, and B. I. Halperin, *Phys. Rev. B* **32**, 3306 (1985).
- [147] A. Chatterjee, private communication.
- [148] M. C. Hermant, PhD thesis, Eindhoven University of Technology (2009).
- [149] M. C. Hersam, *Nature Nanotechnology* **3**, 387 (2008).
- [150] T. Skipa, D. Lellinger, W. Böhm, M. Saphiannikova, and I. Alig, *Polymer* **51**, 201 (2010).
- [151] I. Balberg and N. Binenbaum, *Phys. Rev. B* **28**, 3799 (1983).

-
- [152] F. Carmona and A. El Amarti, Phys. Rev. B **35** 3284 (1987).
- [153] S. S. Rahatekar, M. Hamm, M. S. P. Shaffer, and J. A. Elliott, J. Chem. Phys. **123**, 134702 (2005).
- [154] S. I. White, B. A. DiDonna, M. Mu, T. C. Lubensky, and K. I. Winey, Phys. Rev. B **79**, 024301 (2009).
- [155] Q. Wang, J. Dai, W. Li, Z. Wei, and J. Jiang, Comp. Sci. Tech. **68**, 1644 (2008).
- [156] S. H. Munson-McGee, Phys. Rev. B **43**, 3331 (1991).
- [157] I. Balberg, N. Binenbaum, and N. Wagner, Phys. Rev. Lett. **52**, 1465 (1984).
- [158] M. P. Lettinga and J. K. G. Dhont, J. Phys.-Condens. Matter **16**, S3929 (2004).
- [159] T. Odijk, Macromolecules **21**, 3511 (1988).
- [160] R. H. J. Otten and P. van der Schoot, J. Chem. Phys. **134**, 094902 (2011).
- [161] A. R. Khokhlov and A. N. Semenov, Macromolecules **15**, 1272 (1982).
- [162] S. Varga, G. Jackson, and I. Szalai, Molecular Physics **93**, 377 (1998).
- [163] M. Doi and S. F. Edwards, *The Theory of Polymer Dynamics*, Oxford University, New York (1986).
- [164] J. D. Jackson, *Classical Electrodynamics*, third edition, Wiley, New York (1999).
- [165] W. Song and A. H. Windle, Macromolecules **38**, 6181 (2005).
- [166] H. Hinrichsen, Adv. Phys. **49**, 815 (2000).
- [167] J. Rowlinson and B. Widom, *Molecular Theory of Capillarity*, Dover, (2003).
- [168] P. K. Rai, M. M. Denn, and C. Maldarelli, Langmuir **19**, 7370 (2003).
- [169] S. DasGupta and S. K. Roy, Phys. Lett. A **306**, 235 (2003).
- [170] J. W. Kim, H. Kim, M. Lee, and J. J. Magda, Langmuir **20**, 8110 (2004).
- [171] A. J. McDonald, M. P. Allen, and F. Schmid, Phys. Rev. E **63**, 010701(R) (2001).
- [172] A. Poniewierski, Liq. Cryst. **27**, 1369 (2000).
- [173] A. D. Rey, J. Chem. Phys. **111**, 7675 (1999).
- [174] A. D. Rey, Liq. Cryst. **27**, 195 (2000).
- [175] A. D. Rey, J. Chem. Phys. **113**, 10820 (2000).
- [176] A. D. Rey, Phys. Rev. E **63**, 032701 (2001).
- [177] A. Forsyth, *Calculus of Variations*, Dover, (1960).
- [178] P. G. de Gennes, Rev. Mod. Phys. **57**, 827 (1985).
- [179] P. W. Oakes, J. Viamontes, and J. X. Tang, Phys. Rev. E **75**, 061902 (2007).
- [180] M. Bier and R. van Roij, Phys. Rev. E **76**, 021405 (2007).
- [181] A. A. Verhoeff, private communication.
- [182] G. Vertogen and W. H. de Jeu, *Thermotropic Liquid Crystals, Fundamentals*, Springer-Verlag, Berlin, (1988).
- [183] A. Scharkowski, G. P. Crawford, S. Žumer, and J. W. Doane, J. Appl. Phys. **73**, 7280 (1993).

- [184] A .D. Rey, Phys. Rev. E **67**, 011706 (2003).
- [185] K. Sokalski and T. W. Ruijgrok, Physica A **113**, 126 (1982).
- [186] M. P. Allen, unpublished results.
- [187] H. D. J. Arodz and W. Zurek, *Patterns of Symmetry Breaking*, Kluwer Academic Publishers, Dordrecht, (2003).
- [188] H. Zocher and K. Jacobsohn, Kolloidchem. Beihefte **28**, 167 (1929).
- [189] M. A. Osipov, S. Hess, Mol. Phys. **78**, 1191 (1993).
- [190] L. Tortora and O. D. Lavrentovich, P. Natl. Acad. Sci. USA **108**, 5163 (2011).
- [191] H. Zocher, Anorg. Chem. **147**, 91 (1925).
- [192] J. D. Bernal and I. Fankuchen, J. Gen. Physiology **25**, 111 (1941).
- [193] H. Zocher and C. Török, C. Kolloid-Z. **170**, 140, (1960).
- [194] Y. Trukhina, S. Jungblut, P. van der Schoot, and T. Schilling, J. Chem. Phys. **130**, 164513 (2009).
- [195] N. Behabtu, J. R. Lomeda, M. J. Green, A. L. Higginbotham, A. Sinitskii, D. V. Kosynkin, D. Tsentalovich, A. N. G. Parra-Vasquez, J. Schmidt, E. Kesselman, Y. Cohen, Y. Talmon, J. M. Tour, and M. Pasquali, Nat. Nanotechnol. **5**, 406 (2010).
- [196] A. Kilian, Liq. Cryst. **14**, 1189 (1993).
- [197] O. D. Lavrentovich, Liq. Cryst. **24**, 117 (1998).
- [198] E. Penzenstadler and H. R. Trebin, J. Phys. France **50**, 1027 (1989).
- [199] V. Frederiks and V. Zolina, Trans. Faraday Soc. **29**, 919 (1933).
- [200] S. Mkaddem and E.C. Gartland, Phys. Rev. E **62**, 6694 (2000).
- [201] E. M. Terentjev, Phys. Rev. E **51**, 1330, (1995).
- [202] This polarisation micrograph was made by A. A. Verhoeff.
- [203] R. B. Zasadzinski and J. Meyer, Phys. Rev. Lett. **56**, 636 (1986).
- [204] A. Fernandez-Nieves, D. R. Link, M. Marquez, and D. A. Weitz, Phys. Rev. Lett. **98**, 087801 (2007).
- [205] W. Song, I. A. Kinloch, and A. H. Windle, Science **302**, 1363 (2003).
- [206] G. Z. Wulff, Kristallogr. **34**, 449 (1901).
- [207] P. Poulin, B. Vigolo, and P. Launois, Carbon **40**, 1741 (2002).

Summary

Colloidal particles dispersed in a fluid exhibit rich and unusual behaviour, in particular if the particles are strongly anisometric, i.e., highly elongated or very flat. Fluid dispersions containing anisometric colloids are, apart from being interesting in their own right, relevant to the industrial production and processing of nanocomposites, high-performance fibers, gels and so on. Their unusual properties result from strongly anisotropic interactions that, amongst others, give rise to the build-up of temporal, system-spanning networks of particles as well as various liquid-crystalline states even at quite low concentrations below one volume per cent. By invoking microscopic and mesoscopic statistical theories, we investigate in this thesis aspects of both network formation and liquid crystallinity as they present themselves on a macroscopic scale. We find that both are strongly affected by the particle shape.

Our work on network formation focuses on the critical concentration where the infinite network forms, and the properties of the clusters at concentrations just below and above this. We investigate how particle shape, variation in the dimensions, externally applied fields, and so on impact upon them. Our calculations, based on so-called connectedness-percolation theory, are inspired by observations of strong variations in the emergence of electrical conduction in composites containing carbon nanotubes and graphene. We make plausible that this is caused by the formulation of the nanocomposite on the one hand and the processing conditions on the other. Our predictions agree favourably with experimental data on polymeric composites containing graphene of known size distribution, and confirm that the presence of very few, very elongated or very flat particles dictate the critical loading.

Our calculations also predict that at higher particle concentrations, the particle network breaks down due to a competition with a transition to the uniaxial, nematic liquid-crystalline phase. This phase presents itself initially in the form of droplets that even-

tually coalesce to become a macroscopic fluid. Properties of both we investigate at the level of Frank-Oseen-Rapini-Papoular theory to describe the competition between elastic and surfaces forces. These determine the interfacial shape and spatial structure of the uniaxial symmetry axis. We predict that under conditions of isotropic-nematic phase co-existence, the capillary rise of a macroscopic nematic fluid up a vertical solid wall produces a non-monotonic isotropic-nematic fluid interface. Our theory allows us to extract from capillary-rise experiments on dispersions of plate-like clay particles estimates for the surface tension and the anchoring strength of the nematic symmetry axis to the interface.

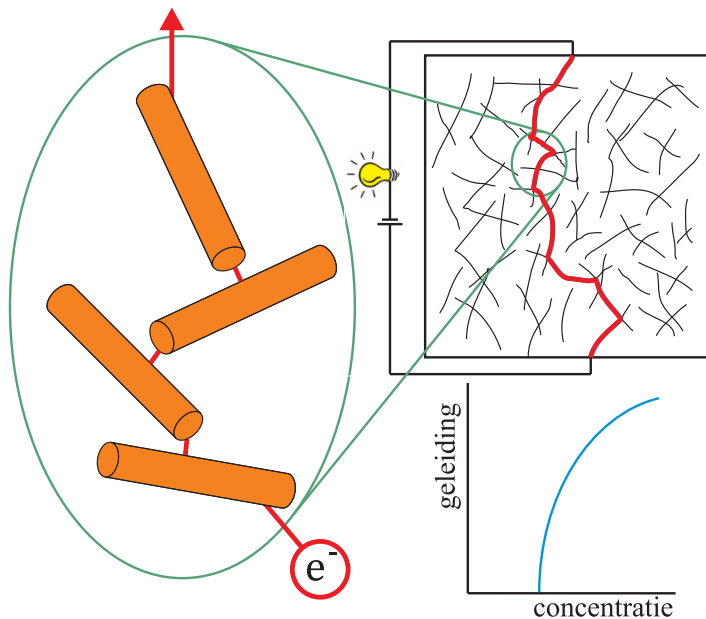
Observations on droplets of the same (gibbsite) clay particles, which have a negative diamagnetic susceptibility and prefer perpendicular anchoring of the symmetry axis to the isotropic-nematic fluid interface, have shown that their internal structure and shape depend strongly on their size and on the strength of an externally applied magnetic field that aligns them. Our calculations show that the transitions between spherical and elongated droplets, and between different kinds of internal organisation of the symmetry axis, are sharp, i.e., resemble phase transitions. By comparing our theory to shape and internal-structure measurements, we have been able to extract values for an elastic constant, the surface tension and anchoring strength. We find that whether or not the droplets elongate under the presence of a magnetic field, depends only on the ratio of the anchoring strength and surface tension.

Samenvatting

Langwerpige of platte deeltjes die opgelost zijn in een vloeistof kunnen zeer interessant en opmerkelijk gedrag vertonen. Als de deeltjes klein genoeg zijn ondergaan ze door thermische fluctuaties een zogeheten Brownse beweging, waarin ze zowel in translatie als in rotatie willekeurig door de vloeistof bewegen in een fase die isotroop wordt genoemd. Deze oplossingen zijn relevant voor industriële toepassingen in bijvoorbeeld versterkte plastics en vezels. Als de deeltjes fijn worden verdeeld zodat ze niet samenklonteren en de concentratie zo laag is dat ze elkaar nauwelijks in de weg zitten, kunnen ze een open netwerk vormen dat het materiaal op macroscopische schaal omvat, dus het hele systeem overspant. Via een ingewikkeld chemisch proces kan zo'n netwerk ingevroren worden, zodat er een vaste stof overblijft die een (nano)composiet wordt genoemd. De thermische, mechanische en elektrische eigenschappen van het composiet kunnen sterk verbeterd worden door de aanwezigheid van het netwerk van nanodeeltjes. Zie ook Figuur 1.

De vorming van dit netwerk wordt percolatie genoemd en de minimale hoeveelheid nanodeeltjes die benodigd is om zo'n systeemoverspannend netwerk te vormen de percolatiegrens, die wordt uitgedrukt in de volumefractie die de deeltjes innemen. Voor de deeltjes kunnen bijvoorbeeld langgerekte koolstofnanobuizen of plaatvormig grafeen gebruikt worden die worden verdeeld in een polymeren (plastic) matrix. Omdat de nanobuizen en grafeen zo enorm langgerekt en plat zijn, is deze grens zeer laag, typisch

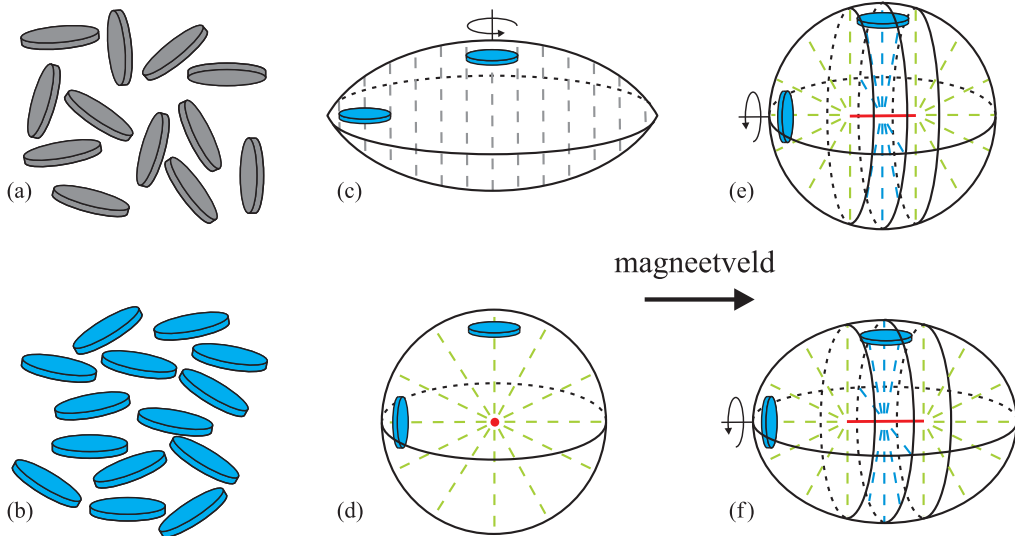
minder dan één procent. Hierdoor is het mogelijk om met zeer kleine hoeveelheden van de dure nanodeeltjes een elektrisch goed geleidend, lichtgewicht en relatief makkelijk te verwerken polymeer te maken. Het optimaliseren van de percolatiegrens en de elektrische geleidbaarheid van het nanocomposiet blijkt echter geen sinecure, omdat er een enorme spreiding is in percolatiegrenzen, zelfs als de productieomstandigheden gelijk lijken te zijn. De eigenschappen van het composiet blijken zeer gevoelig voor eigenschappen van de deeltjes waarmee begonnen wordt en voor de productieprocedure, die bijvoorbeeld zorgen voor een sterke spreiding in de deeltjesgrootteverdelingen, gedeeltelijke ophijning en matige geleiding van een fractie van de deeltjes.



Figuur 1: Als de platte of in dit geval langwerpige deeltjes willekeurig verdeeld zijn in het achtergrondmateriaal is er een kritieke concentratie waarbij er een netwerk ontstaat dat het hele systeem beslaat. Op dat punt schiet de elektrische geleiding met vele ordes van grootte omhoog. Hiervoor hoeven de deeltjes elkaar niet te raken want een lading e^- springt door het achtergrondmateriaal van het ene deeltje naar het andere.

In het eerste deel van dit proefschrift presenteren we een theoretisch model om het effect hiervan op de netwerkvorming te bepalen. Hierbij kijken we naar interacties tussen deeltjes op microscopische schaal (deeltjesniveau) om zo voorspellingen te doen van het composiet op macroscopische schaal. We vinden dat de percolatiegrens sterk afhangt van de lengte- (breedte-) en dikteverdelingen van de deeltjes en of deze gekoppeld zijn, hoe goed ze elektriciteit geleiden en hoe de oriëntaties verdeeld zijn. Ophijning van de

deeltjes verhoogt namelijk de percolatiegrens, omdat ze gemiddeld verder van elkaar verwijderd zijn en extra deeltjes nodig zijn om deze gaten te dichten. Bij nog hogere dichtheden kan het percolerende netwerk zelfs afbreken omdat de deeltjes elkaar zo in de weg gaan zitten dat de oplingning versterkt wordt.



Figuur 2: Als de concentratie groot genoeg is, gaat de isotrope fase (a) over in de nematische fase (b), wat vaak begint met de vorming van nematische druppels. Kleine druppels bestaande uit schijfvormige deeltjes zijn plat met een uniforme oriëntatie (c), terwijl grote druppels rond zijn met een radiële oriëntatie met puntdefect als het magneetveld zwak is (d). Sterke velden rekken het puntdefect uit naar een lijndefect (e) en nog sterkere velden kunnen de druppel zelf langgerekt maken (f). De stippellijnen geven de oriëntatie van de schijfjes weer, die hier niet op schaal zijn weergegeven.

Bij deze hogere dichtheden is er dus geen macroscopisch netwerk meer en komt er een punt (concentratie) dat de langwerpige of platte deeltjes zich spontaan gaan ophijgen in een fase die nematisch wordt genoemd. Zie ook Figuur 2. De nematische fase is de eenvoudigste toestand die een zogeheten vloeibaar kristal kan aannemen. Een vloeibaar kristal is een materiaal dat bestaat uit relatief stijve deeltjes die plat of langgerekt zijn en eigenschappen heeft die typisch zijn voor vaste stoffen (elasticiteit) en vloeistoffen (stromen). In de nematische fase hebben de staafjes of schijfjes allemaal min of meer dezelfde oriëntatie, maar is er nauwelijks positionele ordening, die er bijvoorbeeld wel is in een kristallijne vaste stof. Bij een kritieke concentratie begint de vorming van de nematische fase uit de isotrope fase vaak met de vorming van druppels met deze ordening, die dan zweven in de isotrope fase waarin er geen ordening in de oriëntaties is. De

druppels zakken heel langzaam naar de bodem tot er uiteindelijk totale fasescheiding is met een nematische fase onder een isotrope fase. In het tweede deel van dit proefschrift bestuderen we deze druppels en de vorm van het grensvlak tussen de isotrope en nematische fase. Hierdoor kunnen we informatie verkrijgen over materiaaleigenschappen van het vloeibare kristal.

Geïnspireerd door experimenten aan druppels bestaande uit het schijfvormige gibbsiet, een aluminiumerts, zien we daarin verrassende vormen, waarbij we ook hebben gekeken naar het effect van een magnetisch veld dat ervoor zorgt dat de gibbsietschijfjes zich loodrecht op het magneetveld oriënteren. In overeenkomst met de experimenten vinden we dat kleine druppels afgeplat zijn met een uniforme deeltjesordering, terwijl grotere druppels rond zijn met een driedimensionale radiële ordening in een zwak magneetveld, wat een zogeheten puntdefect geeft. Zie Figuur 2. In een sterker magneetveld rekt dit puntdefect uit tot een lijndefect met tweedimensionale radiële ordening daar omheen. Afhankelijk van de materiaalconstanten kan de druppel zelf ook nog uitrekken in een nog sterker magneetveld. Het bestuderen van het grensvlak tussen de isotrope en nematische fase is niet alleen interessant bij nematische druppels, maar ook vlak bij een vaste wand, waar de vloeistof in de nematische fase omhoog kruipt tegen de wand, zoals water in een glas dat ook doet. Door de ordening van de deeltjes in de nematische fase is het niet evident wat de vorm van het grensvlak dicht bij de wand is en hoe de ordening van de deeltjes er daar uitziet. Uit onze berekeningen vinden we dat deze op een niet triviale manier afhangen van de materiaalparameters, maar bovendien dat het grensvlak een minimum vertoont en dus niet geleidelijk afvalt naar het niveau ver van de wand. Experimenten aan dezelfde gibbsietschijfjes lijken dit te bevestigen.

List of publications

1. R. H. J. Otten and P. van der Schoot, *Capillary rise of an isotropic-nematic fluid interface: surface tension and anchoring versus elasticity*, *Langmuir* **25**, 2427-2436 (2009).
2. A. A. Verhoeff, R. H. J. Otten, P. van der Schoot, and H. N. W. Lekkerkerker, *Shape and director field deformation of tactoids of plate-like colloids in a magnetic field*, *Journal of Physical Chemistry B* **113**, 3704-3708 (2009).
3. R.H.J. Otten and P. van der Schoot, *Continuum percolation of polydisperse nanofillers*, *Physical Review Letters* **103**, 225704 (2009).
4. A. A. Verhoeff, I. A. Bakelaar, R. H. J. Otten, P. van der Schoot, and H. N. W. Lekkerkerker, *Tactoids of plate-like particles: size, shape, and director field*, *Langmuir* **27**, 116-125 (2011).
5. A. A. Verhoeff, R. H. J. Otten, P. van der Schoot, and H. N. W. Lekkerkerker, *Magnetic field effects on tactoids of plate-like colloids*, *Journal of Chemical Physics* **134**, 044904 (2011).
6. R. H. J. Otten and P. van der Schoot, *Connectivity percolation of polydisperse anisotropic nanofillers*, *Journal of Chemical Physics* **134**, 094902 (2011).
7. R. H. J. Otten and P. van der Schoot, *Connectedness percolation of elongated hard nanoparticles in an external field*, submitted.
8. E. Tkalya, M. Ghislandi, R. H. J. Otten, M. Lotya, A. Alekseev, P. van der Schoot, J. Coleman, and C. E. Koning, *Influence of dispersion state of graphene on percolation threshold of conductive graphene/polymer nanocomposites*, submitted.

9. R. H. J. Otten and P. van der Schoot, *Deformable homeotropic nematic droplets in a magnetic field*, in manuscript.
10. R. M. W. van Bijnen and R. H. J. Otten, P. van der Schoot, *Texture and shape of two-dimensional domains of nematic liquid crystal*, in manuscript.

Acknowledgements / Dankwoord

Na vier jaar onderzoek doen is het hoog tijd om een aantal mensen te bedanken, zonder wie er weinig van dit proefschrift terecht was gekomen. Op de eerste plaats natuurlijk mijn eerste promotor en dagelijkse begeleider Paul van der Schoot. Ik heb erg veel van je geleerd, niet alleen over het onderwerp van mijn project, maar ook andere takken van de zachte materie. Zeker niet te onderschatten is wat je me bijgebracht hebt op het gebied van communicatie en presentatie, daar zal ik nog lang van profiteren. Daarnaast heb je ik je altijd aanwezige inspiratie en motivatie altijd enorm gewaardeerd. Mijn tweede promotor Thijs Michels wil ik bedanken voor het klaar staan voor hulp waar nodig en voor de waardevolle bijdrage aan het proefschrift.

I also would like to thank the collaborators in the DPI Graphcom project, Evgeniy Tkalya, Marcos Ghislandi, Charline Sellam, Cor Koning, Joachim Loos, and Ton Peijs for their cooperation, many discussions and understanding of and interest in our theoretical contribution to the project. It has proved to be very difficult to combine experiments and theory on the carbon-nanotube and graphene composites, but I am glad we managed to do so and publish the results in a very nice paper, thanks to a pleasant cooperation. Lia Verhoeff en Henk Lekkerkerker wil ik hartelijk bedanken voor de erg prettige samenwerking aan de vloeibare kristallen. Wat begon met een interessante meting waar jullie theoretische ondersteuning bij zochten, groeide uit tot een zeer vruchtbare samenwerking waarin experiment en theorie elkaar duidelijk versterkten. Dit is terug te zien aan het grote deel van het proefschrift dat te danken is aan deze samenwerking. Alle bezoeken aan jullie lab in Utrecht werkten inspirerend en motiverend en ik heb veel geleerd van de samenwerking.

Avik Chatterjee and Claudio Grimaldi deserve my gratitude for showing much interest in our work and for many stimulating discussions. The same holds for Andriy Kyrylyuk, Menno Lauret, Tanja Schilling, René van Roij, Pavlik Lettinga, and Dirk

Aarts. Dank gaat ook uit naar Rick van Bijnen en Jaap Molenaar voor wat lang geleden begon als een project van drie maanden, maar jaren later afgesloten wordt met een mooi artikel. Het Dutch Polymer Institute wil ik graag bedanken voor het mij de kans geven dit onderzoek uit te voeren.

I am grateful to all the colleagues from the group TPS for the interest they have shown, the discussions during coffee breaks and lunch, and the fun at the movie nights, and during and after the weekly beers at the “borrel”. Met name wil ik Helmi en in de eerste helft van mijn tijd in de groep Clazien bedanken voor hun grote hulpvaardigheid bij alles wat er geregeld moest worden. Helmi maakte het me erg makkelijk op het eind om aan alle regels te voldoen en de formulieren op tijd klaar te krijgen, erg fijn.

Gelukkig had ik ook genoeg vrienden om afleiding bij te zoeken naast het werk. Daarbij noem ik Arjan, Inge, Jasmijn, Jeroen, Joost, Lotte, Lindsey, Mark, Ruud en Ummels die altijd garant staan voor gezelligheid op of naast de tennisbaan, in de kroeg, in de sneeuw, in de zon of waar dan ook. Om niemand te vergeten wil ik daarnaast alle andere vrienden tegelijk bedanken, van wie ik in ieder geval Simon met naam wil noemen vanwege zijn gezelligheid en betrokkenheid al jarenlang.

Daarnaast bedank ik mijn familie en in het bijzonder Joris, Heleen en mijn ouders voor hun steun en interesse. Joris, geweldig dat je zo enthousiast zoveel tijd en moeite in het ontwerpen van de kافت hebt gestoken. Mijn ouders ben ik zeer dankbaar voor hun onvoorwaardelijke steun en het altijd klaar staan.

Ronald

Curriculum vitae

Ronald Otten was born on 9 March 1982 in Veldhoven, The Netherlands. After finishing his pre-university education (gymnasium) at the Van Maerlant lyceum in Eindhoven in 2000, he started studying Applied Physics and Applied Mathematics and in 2007 he obtained both Master's degrees. During his studies he conducted a research internship at the University of Bristol, United Kingdom, in the group of Prof. Jens Eggers, where he worked on the theory of symmetry breaking in the scaling of droplet formation. The Master's project was carried out under the supervision of Prof. Theo Schep, Prof. Mark Peletier, and dr. Leon Kamp. His Master's thesis describes an analysis of mixing and transport in two-dimensional turbulent fluid flows. In October 2007 he started his PhD research under the supervision of Prof. Paul van der Schoot and Prof. Thijs Michels in the group Theory of Polymers and Soft matter. The main results of this research are presented in this thesis.